Atomistic Simulation, Synthesis, and Characterization of 2D Materials for Optoelectronic Device applications

Thesis Submitted by

SAYANTIKA CHOWDHURY

Doctor of Philosophy (Engineering)

Department of Electronics & Telecommunication Engineering
Faculty Council of Engineering &Technology
Jadavpur University
Kolkata, India

2023

JADAVPUR UNIVERSITY

KOLKATA-700032

INDEX NO.: 116/19/E

1. Title of the thesis:

ATOMISTIC SIMULATION, SYNTHESIS, AND CHARACTERIZATION OF 2D MATERIALS FOR OPTOELECTRONIC DEVICE APPLICATIONS.

2. Name, Designation & Institution of the Supervisors:

Prof. P. Venkateswaran

Professor, Department of Electronics and Tele-Communication Engineering (ETCE), Jadavpur University, Kolkata-700032, India

Dr. Divya Somvanshi

(Formerly, DST Inspire Faculty, Dept. of ETCE, JU) Asst. Prof., Department of Physics, School of Basic and Applied Science, Harcourt Butler Technical University (HBTU), Kanpur-208002, India

3. List of Publications:

Journals (6):

[1] S. Chowdhury, A. Mishra, P. Venkateswaran and D. Somvanshi, "Electronic structure and Optical properties of GaTe/$MoTe_2$ based vdW Heterostructure under Mechanical strain and external Electric fields", *Material science in semiconductor processing,* 163 (2023), 107572. DOI: https://doi.org/10.1016/j.mssp.2023.107572 [I.F: 4.644, SCI Journal].

[2] S. Chowdhury, P. Venkateswaran and D. Somvanshi, "Strain-dependent doping and optical absorption in Al-doped graphene-like ZnO monolayer", *Solid State communications,* 365 (2023), 115139. DOI: https://doi.org/10.1016/j.ssc.2023.115139 [I.F: 1.804, SCI Journal].

[3] S. Chowdhury, P. Venkateswaran, D. Somvanshi, "Biaxial strain-modulated electronic and optical properties of transition metals doped-WSe_2 monolayer", *Physica B: Condensed Matter,* 653 (2023) 414668. DOI: https://doi.org/10.1016/j.physb.2023.414668 [I.F: 2.98, SCI Journal].

[4] S. Chowdhury, P. Venkateswaran, D. Somvanshi, "Strain-dependent doping behavior of WSe_2 monolayer: A first-principle calculation", *Europhysics Letters*, 137 (2022) 26004.

DOI: 10.1209/0295-5075/ac4d0c [I.F: 1.95, SCI Journal].

[5] S. Chowdhury, P. Venkateswaran, D. Somvanshi, “A systematic study on the electronic structure of 3d, 4d, and 5d transition metal-doped WSe_2 monolayer”, *Superlattices and Microstructures*, 148 (2020) 106746.
DOI: https://doi.org/10.1016/j.spmi.2020.106746 [I.F: 2.65, SCI Journal].

[6] S. Chowdhury, A. P. Singh, S. Jit, P. Venkateswaran, and D. Somvanshi, “p-WSe_2 Nanosheets/n-WS_2 Quantum Dots/p-Si (2D-0D-3D) Mixed-Dimensional Multilayer Heterostructures Based High Performance Broadband Photodetector”, (Under Review: *IEEE transactions on electron devices*) [I.F: 2.917, SCI Journal].

Conferences (6):

[1] S. Chowdhury and D. Somvanshi, “Electronic Structure and Transport Property of Bilayer $MoSe_2$ with AA and AB Stacking” 66th *DAE Solid State Physics Symposium* (*DAE-SSPS)*, Ranchi, Jharkhand, India, 2022.

[2] S. Chowdhury, P. Venkateswaran and D. Somvanshi, “Strain-Induced Electronic Structure and Bandgap Transition in Bilayer $MoSe_2$ of AB and AA Stacking Order,” *2022 IEEE Calcutta Conference (CALCON)*, Kolkata, India, 2022, pp. 191-195.
DOI: 10.1109/CALCON56258.2022.10060824

[3] S. Chowdhury, P. Venkateswaran and D. Somvanshi, “Interlayer twist angle-dependent electronic structure and optical properties of InSe/WTe_2 van der Waals heterostructure” *2022 IEEE International Conference of Electron Devices Society Kolkata Chapter (EDKCON),* Kolkata, India, 2022, pp. 325-328. **DOI:** 10.1109/EDKCON56221.2022.10032930

[4] S. Chowdhury, P. Venkateswaran and D. Somvanshi, “A comparative study of biaxial strain modulated electronic structure of MSe_2 (M = W, Mo) monolayer,” *2021 5th International Conference on Electronics, Materials Engineering & Nano-Technology (IEMENTech)*, Kolkata, India, 2021, pp. 1-4.
DOI: 10.1109/IEMENTech53263.2021.9614846.

[5] S. Chowdhury, P. Venkateswaran and D. Somvanshi, “Effect of biaxial strain on the electronic structure of Nb-doped WSe_2 monolayer: a theoretical study,” *2021 Devices for Integrated Circuit (DevIC)*, Kalyani, India, 2021, pp. 79-83.
DOI: 10.1109/DevIC50843.2021.9455926.

[6] S. Chowdhury, P. Venkateswaran and D. Somvanshi, "Optical and Electrical Characterization of n-MoS_2/p-Si Heterojunction Diode," *2020 IEEE International IOT, Electronics and Mechatronics Conference (IEMTRONICS)*, Vancouver, BC, Canada, 2020, pp. 1-4. DOI: 10.1109/IEMTRONICS51293.2020.9216399.

4. List of Patents: Nil

5. List of Presentations in National/International/Conferences/Workshops:

[1] Presented a paper entitled "Strain-Induced Electronic Structure and Bandgap Transition in Bilayer $MoSe_2$ of AB and AA Stacking Order," *2022 IEEE Calcutta Conference (CALCON)*, Kolkata, India, 2022.

[2] Presented a paper entitled "A comparative study of biaxial strain modulated electronic structure of MSe_2 (M = W, Mo) monolayer," *2021 5th International Conference on Electronics, Materials Engineering & Nano-Technology (IEMENTech)*, Kolkata, India, 2021.

[3] Presented a paper entitled "Effect of biaxial strain on the electronic structure of Nb-doped WSe_2 monolayer: a theoretical study," *2021 Devices for Integrated Circuit (DevIC)*, Kalyani, India, 2021.

[4] Presented a paper entitled "Optical and Electrical Characterization of n-MoS_2/p-Si Heterojunction Diode," *2020 IEEE International IOT, Electronics and Mechatronics Conference (IEMTRONICS)*, Vancouver, BC, Canada, 2020.

[5] Presented a paper entitled "Electrical characteristics of n-MoS_2/p-Si heterojunction diode", *XXth International Workshop on Physics of Semiconductor Devices (IWPSD)*, Kolkata, India, 2019.

[6] Presented a paper entitled "Optical characterization of n-MoS_2 thin film coated on p-Si substrates for multifunctional heterojunction device applications", *Synthesis, Characterization and Application of Nanomaterials (SCAN),* Kolkata, India, 2019.

“Statement of originality”

I, **Sayantika Chowdhury**, registered on **10th June, 2019** do hereby declare that this thesis entitled **“Atomistic Simulation, Synthesis, and Characterization of 2D materials for Optoelectronic Device applications”** contains literature survey and original research work done by the undersigned candidate as part of Doctoral studies.

All information in this thesis have been obtained and presented in accordance with existing academic rules and ethical conduct. I declare that, as required by these rules and conduct, I have fully cited and referred all materials and results that are not original to this work.

I also declare that I have checked this thesis as per the “Policy on Anti plagiarism, Jadavpur University, 2019”, and the level of similarity as checked by iThenticate software is **2%.**

Sayantika Chowdhury

Signature of Candidate:

Date: 19/05/23

Certified by Supervisor(s):

(Signature with date, seal)

1.

Dr. P. Venkateswaran
PROFESSOR
Dept. of Electronics & Tele-Comm. Engg.
JADAVPUR UNIVERSITY
Kolkata-700 032

2.

Dr. Divya Somvanshi
Assistant Professor
Department of Physics
Harcourt Butler Technical University
Kanpur-208002

JADAVPUR UNIVERSITY
KOLKATA- 700032, INDIA

CERTIFICATE FROM THE SUPERVISOR

This is to certify that the thesis entitled **"ATOMISTIC SIMULATION, SYNTHESIS, AND CHARACTERIZATION OF 2D MATERIALS FOR OPTOELECTRONIC DEVICE APPLICATIONS"** submitted by **Smt. Sayantika Chowdhury**, who got her name registered on **10/06/2019** [**D-7/E/407/19]** for the award of Ph.D. (Engg. Degree of Jadavpur University) is absolutely based upon her own work under the supervision of **Prof. P. Venketswaran**, Department of Electronics and Tele-Communication Engineering, Jadavpur University, Kolkata, India and **Dr. Divya Somvanshi,** (Formerly, DST Inspire Faculty, Dept. of ETCE, JU) Asst. Prof., Department of Physics, School of Basic and Applied Science, Harcourt Butler Technical University, Kanpur, India and that neither her thesis nor any part of the thesis has been submitted for any degree/diploma or any other academic award anywhere before.

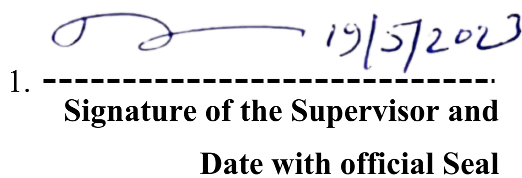

1. ------------------------------

Signature of the Supervisor and Date with official Seal

Dr. P. Venkateswaran
PROFESSOR
Dept. of Electronics & Tele-Comm. Engg.
JADAVPUR UNIVERSITY
Kolkata-700 032

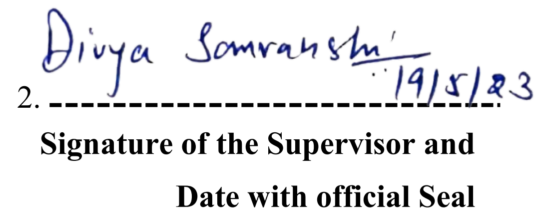

2. ------------------------------

Signature of the Supervisor and Date with official Seal

Dr. Divya Somvanshi
Assistant Professor
Department of Physics
Harcourt Butler Technical University
Kanpur-208002

ACKNOWLEDGEMENTS

The success and final outcome of my thesis required a lot of guidance and assistance from many people and I am extremely fortunate to have got this all along the completion of my thesis work. Whatever I have done is only due to such guidance and assistance and I would not forget to thank them.

First and foremost, I owe my profound gratitude to my project supervisor, **Prof. P. Venketswaran, and** my Joint-supervisor **Dr. Divya Somvanshi** who guided me till the completion of my Ph.D. Thesis work by providing their precious advice and constant support. I would like to express my special appreciation and thanks to **Dr. Divya Somvanshi** for giving her full effort in guiding me to maintain my progress. She has been a tremendous mentor for me because without her invaluable suggestions and her continued motivation, my Ph.D. Work would not have taken a worthwhile shape.

I would like to thank the **DST INSPIRE Faculty Award** (DST/INSPIRE/04/2017/000147) of the Government of India for the financial support.

I am thankful and fortunate enough to get a chance to work under **Dr. Satyabrata Jit**, Department of Electronics and Communication Engg., IIT BHU, Varanasi, India for fabrication and measurements of my thesis work, without this my thesis would not have seen the light of day. He also supported me by sharing important knowledge and resources in many areas relevant to my work. Also, I want to thank all the scholars from CRME lab, and IIT BHU who have supported me to complete my fabrication work.

I also want to thank the Department of Chemical Engineering and Department of Physics, Jadavpur University for helping me to start the initial synthesis processes of my experimental work.

I would like to thank the Head of the Department, Department of Electronics & Telecommunication Engineering, Jadavpur University for providing me with all the facilities for carrying out the entire project work. I would like to express my sincere appreciation to all the teaching and non-teaching staff of the department for providing the necessary support and aid. I also want to thank all the lab members, especially Mr. Ashoke Mondal, and Mr. Bikash Bhowmik of IC Centre, Department of ETCE, Jadavpur University for their help to carry out my some experimental work.

Last but not least, I am immensely thankful to my beloved family members, especially thanks to my dear husband, **Mr. Soham Kanti Bishnu** for his constant support and encouragement. Words cannot express how grateful I am to my parents for all of the sacrifices that they have made on my behalf. Their prayer for me was what sustained me thus far.

Date: 19/05/23

Sayantika Chowdhury

Place: Kolkata

Sayantika Chowdhury

Dedication

To my loving Parents, supportive in-laws, and especially my dear Husband.

PREFACE

Two-Dimensional (2D) Materials are crystalline materials consisting of a single layer of atoms with a thickness of a few nanometers or less. 2D- Transition metal dichalcogenide (TMDCs) are kind of 2D materials such as MoS_2, WSe_2, $MoTe_2$, etc. have a tunable bandgap and are being investigated experimentally and theoretically using density functional theory (DFT) calculations. DFT is a powerful theoretical tool to model the physical, electronic, and optical properties of 2D materials. In this thesis work, using DFT calculations, we systematically explore the possibility of band structure engineering of 2D monolayers by substitutional doping technique using different dopants belonging to 3d, 4d, and 5d groups of the periodic table. Transition metals (TM) are a popular choice of substitutional dopants in TMDCs material. Our results suggest that the **V, Nb, and Ta dopants** are only potential **p-type dopants**, and **Re is an n-type dopant** for the WSe_2 monolayer. In this work, we investigated the band structure, projected density of states (PDOS), and optical spectra of TM- doped 2D semiconductor monolayers such as **WSe_2, and Al-doped g-ZnO (g-AZO) modulated by biaxial strain**. We theoretically investigated the electronic structure and optical properties of Nb, Ta, and Re-doped WSe_2 monolayer by applying biaxial tensile and compressive strain. We also investigated the strain-dependent behaviour of formation energy (E_{form}) for Nb, Ta, V, and Re doped-WSe_2 monolayer using DFT calculations. Further, we systematically studied the strain-dependent doping behavior and optical absorption of the g-AZO monolayer under the application of strain (ε_{xy}) by using Hybrid-DFT calculations. It is observed that **Strain engineering** can be used to **enhance doping concentration** in 2D semiconductors which is useful in **optoelectronic device applications.**

The 2D materials-based heterostructures are highly explored by the device community due to their atomically thin nature, large surface area, and various degrees of freedom. The application of 2D heterostructure mainly depends upon the atomic commensurability, interlayer interaction, charge transfer between constituent 2D materials, and particularly band alignment when heterostructure is formed. Therefore, in this work, we systematically investigated the modulation of electronic structure and optical spectra of **GaTe/$MoTe_2$ van der Waals (vdWs) heterostructure** using Hybrid-DFT calculations. Currently, electronic devices based on these 2D TMDCs materials with Silicon are at the forefront of current research due to their potential applications as p-n junctions, solar cells, LEDs, photodetectors, and photovoltaic cells. A promising approach is to combine two high-performance materials to create a mixed-dimensional heterostructure that performs beyond existing technologies and enables very high sensitivity, low-cost production, and high photodetection gain. A fabricated **2D-0D-3D broadband photodetector** shows an excellent rectifying nature with a **good rectifying ratio and high photoresponse and fast transient time** with significant optoelectronics applications.

CONTENTS

Acknowledgment

Preface

List of Figures………………………………………………………………………...………… **v**

List of Tables…………………………………………………………………………….…... **x**

List of Abbreviations…………………………………………………………………….... **xi**

Chapter 1: Introduction and the basic concept behind the Thesis ……………………………. **1-28**

1.1 Introduction of Two-dimensional (2D) Materials …………………………………………... 1

1.1.1 Graphene ……………………………………………………………........................ 2

1.1.2 Transition metal dichalcogenide (TMDCs) …………………………………………..... 3

1.1.3 Metal monochalcogenides (MMCs) ……………………………………………............. 4

1.2 Doping of 2D Materials …………………………………………………………….............. 4

1.3 Formation of Heterostructures ………………………………………………………………. 7

1.4 Role of external factors on 2D Materials……………………………………………………. 10

1.4.1 Mechanical Strain ………………………………………………………………….. 10

1.4.2 External Electric Field ……………………………………………..…………… 11

1.5 Synthesis of 2D Materials……………………………………………………...………… 11

1.5.1 Micromechanical Exfoliation ……………………………………………………….… 12

1.5.2 Liquid Exfoliations ……………………………………………………………….… 12

1.5.3 Chemical Vapour Deposition (CVD)…………………….………………………….… 13

1.5.4 Hydrothermal and Solvothermal Synthesis method…………………………………… 13

1.6 Characterization Methods ………………………………………………………………… 14

1.6.1 Transmission Electron Microscopy (TEM) …………………………………………… 14

1.6.2 Scanning Electron Microscopy (SEM) ……………………………………………...… 15

1.6.3 Atomic Force Microscopy (AFM) …………………………………………………….. 16

1.6.4 X-ray Diffraction (XRD) ……………………………………………………………..… 18

1.6.5 UV-Visible Spectroscopy ………………………………………………………………… 19

1.6.6 Photoluminescence Spectroscopy (PL) ……………………………………………….… 19

1.6.7 Raman Spectroscopy ……………………………………………………………………. 20

1.7 Basics of Photodetectors ………………………………………………………………….. 21

1.7.1 Photoconductor ……………………………………………………………..……… 22

1.7.2 Photodiode ………………………………………………………………………………. 22

1.7.2.1 p-n junction ………………………………………………………………………… 23

1.7.2.2 Schottky junction ………… 24
1.7.3 MSM photodiode ………… 24
1.8 Performance Parameters of Photodetector ………… 25
1.8.1 Responsivity ………… 25
1.8.2 Detectivity ………… 25
1.8.3 External Quantum Efficiency (EQE) ………… 25
1.8.4 Rise time and fall time ………… 25
1.9 Current-Voltage (I-V) Characteristics ………… 26
1.10 Density Functional Theory (DFT)………… 27
1.10.1 Local Density Approximations (LDA) ………… 28
1.10.2 General Gradient Approximation (GGA) ………… 28

Chapter 2: Literature Review & Organization of the Thesis………… 29-37
2.1 Literature review ………… 29
2.1.1 Substitutional doping of 2D materials ………… 29
2.1.2 Strain engineering of 2D materials ………… 30
2.1.3 2D heterostructures ………… 31
2.1.4 Mixed dimensional (MD) heterostructures-based photodetectors ………… 32
2.2 Motivation ………… 33
2.3 Scope of the Thesis ………… 36

Chapter 3: Electronic structure of 3d, 4d, and 5d transition metal (TM)-doped WSe_2 monolayer ………… 38-51
3.1 Introduction ………… 38
3.2 Computational Methods ………… 39
3.3 Results and discussions ………… 40
3.3.1. Electronic structure of WSe_2 monolayer ………… 40
3.3.2 Formation energy calculations ………… 42
3.3.3. Substitutional doping at W site using 3d, 4d, and 5d transition metals ………… 44
3.3.3.1. 3d TM-doped WSe_2 monolayer ………… 44
3.3.3.2. 4d TM-doped WSe_2 monolayer ………… 46
3.3.3.3. 5d TM-doped WSe_2 monolayer ………… 49
3.4 Conclusions ………… 51

Chapter 4: Strain-dependent doping, electronic structure and optical properties of TM-doped 2D semiconductors ………………………………………..….….............................. 52-77

4.1 Introduction ………………………………………………………………………….…… 52

4.2 Computational Methods ……………………………………………………………….. 55

4.3 Results and discussions …………………………………………….………….…… 55

4.3.1 Electronic structure of pristine and Nb, Ta, and Re-doped WSe_2 monolayer ………… 55

4.3.2. Biaxial strain tuning of the electronic structure of pristine and Nb, Ta, and Re doped WSe_2 monolayer………………………………………………………………………………… 58

4.3.3 Optical properties of pristine and Nb, Re, and Ta-doped WSe_2 monolayer under biaxial strain ………………………………………………………………………… 61

4.3.4 Strain-dependent doping behaviour of TM- doped WSe_2 monolayer ………………….. 64

4.3.5 Electronic structure of Al doped g-ZnO (g-AZO) monolayer …………………………. 69

4.3.6 The formation energy of Al dopant in ZnO monolayer under biaxial strain …………... 71

4.3.7 The electronic band structures of g-AZO monolayer under biaxial strain …………….. 73

4.3.8 The absorption spectra of g-AZO monolayer under application of biaxial strain …….. 75

4.4 Conclusions ………..……………………………………………………………… 77

Chapter 5: Electronic bandstructure and optical properties of GaTe/$MoTe_2$ heterostructure under different biaxial strain and electric fields……………………………………………... 78-90

5.1 Introduction …………………………………………………………..………… 78

5.2 Computational Methods ……………………………………………….………… 79

5.3. Results and Discussions ………………………………………………………………… 80

5.3.1 The atomic and electronic structure of $MoTe_2$ and GaTe monolayer ..………………. 80

5.3.2 Formation and stability of GaTe/$MoTe_2$ heterostructures with different stacking order……………………………………………………………………………………….. 81

5.3.3. The electronic structure and the optical properties of GaTe/$MoTe_2$ vdW heterostructure……………………………………………………………………….. 83

5.4.4 Modulation of electronic band structure and band alignment under biaxial strain and external electric field ……………………………………………………………………... 85

5.4.5 Modulation in optical properties under biaxial strain and external electric field …..… 88

5.4 Conclusions ……………………………………………………………………… 90

Chapter 6: n-WS_2 QDs/p-Si (0D-3D) and p-WSe_2 NSs/n-WS_2 QDs/p-Si (2D-0D-3D) mixed-dimensional multilayer heterostructures based high performance broadband photodetector …………………………………………………………………………………………… 91-105

6.1 Introduction …………………………………………………………………………… 91

6.2 Experimental details ………………………………………………………………… 92

6.2.1 Chemical used ……………………………………………………………… 92

6.2.2 Synthesis of WSe_2 nanosheets …………………………………………… 92

6.2.3 Synthesis of WS_2 quantum dots ………………………………………… 94

6.2.4 Fabrication of n-WS_2 QDs/p-Si (0D-3D) and p-WSe_2 nanosheets/n-WS_2 QDs/p-Si (2D-0D-3D) heterojunction devices.. 95

6.3 Results and discussions ……………………………………………………………… 96

6.3.1 Structural and optical characterization of WSe_2 nanosheets ………… 96

6.3.2 Structural and optical characterization of WS_2 quantum dots………… 98

6.3.3 Electrical and Photodetection characteristics of the (0D-3D) and (2D-0D-3D) MD heterostructures based devices ……………………………………… 100

6.4 Conclusions ……………………………………………………………………… 105

Chapter 7: Conclusion and Future Work………………………………………........ 106-109

7.1 Major contributions ……………………………………………………........ 106

7.2 Scope of future work ………………………………………………..…..….. 109

BIBLIOGRAPHY ………………………………………………………………… 110

REFERENCES ……………………………………………………...……………….. 111-131

LIST OF FIGURES

Figure No. **Description** **Page No.**

Fig. 1.1 Schematic of the family of 2D materials ……………………………………………..…....2

Fig. 1.2 Schematic of 2D hexagonal honeycomb-like graphene structure ……………………..…......2

Fig. 1.3 shows (a) a Geometrical side view of monolayer TMDCs, where M is transition metal atom and X is chalcogenides materials (b) Hexagonal structure of monolayer TMDC materials ………….......3

Fig. 1.4 a) Geometrical side view of monolayer Metal monochalcogenides (MMC) structure (b) the Hexagonal structure (top view) of monolayer MMC, where M represents a group III element and X represents chalcogen atoms………………………………….………………..…………………4

Fig. 1.5 Schematic of substitutional doping method ………………………………………………….5

Fig. 1.6 Schematic of adsorption doping method ……………………………………………….……6

Fig. 1.7 Schematic of Charge transfer method ……………………………………………………….7

Fig. 1.8 Type 1 Straddled alignments ………………………………………………………….......8

Fig. 1.9 Type II Staggered alignments ……………………………………………………………..9

Fig. 1.10 Type III Broken gap alignment ……………………………………………………….…9

Fig. 1.11 Schematic of (a) Biaxial tensile strain (b) Biaxial compressive strain ……………...............11

Fig. 1.12 Schematic of External Electric Field ……………………………………………………11

Fig. 1.13 Structure of Transmission Electron Microscopy ……………………………………..15

Fig. 1.14 Structure of Scanning Electron Microscopy ……………………………………….…....16

Fig. 1.15 AFM working principles are depicted schematically. The AFM probe is a micro-cantilever with a sharp tip at one end. The tip's monomolecular point enables nanometer resolution imaging, and the micro-cantilever is a force sensor capable of detecting even minute deformation of a sample, enabling very high sensitivity AFM in force measurements ……………………………………...17

Fig. 1.16 Three basic working modes of AFM **(a)** In contact mode the probe is always slightly in contact with the sample and scanned in a constant force mode. (**b)** In the non-contact mode, the tip of the needle always vibrates on the surface of the sample, but it is never in contact with the sample. The scanning detector detects long-range forces such as van der Waals force or electrostatic forces that do not damage the imaged sample. **(c)** In the tapping mode, the micro cantilever is subjected to stress vibration near its resonant frequency, and the oscillating needle tip gently strikes the surface of the sample, intermittently making contact with it …………………………………………………….....17

Fig. 1.17 Bragg's Law …………………………………………………………………………......18

Fig. 1.18 Block diagram of UV-Vis Spectroscopy includes a light source, monochromator, sample and reference cells, detector, and data output …………………………………………………………....19

Fig. 1.19 Figure depicts the block diagram of photoluminescence spectroscopy. One monochromator selects an excitation wavelength, and the luminescence is observed through a second monochromator which is set at 90° positioned to the incident light……………………….……………………..20

Fig. 1.20 Structural diagram of photoluminescence spectroscopy (PL) ……………………………......20

Fig. 1.21 Schematic of a Raman spectrometer ………………………...21

Fig. 1.22 Energy-level diagram with all the states involved in Raman spectra ……………………...21

Fig. 1.23 Schematic structure of different semiconductor-based photodetectors ……………….……..22

Fig. 1.24 Photoconductor working principle under UV illumination ………………………….........22

Fig. 1.25 Schematic structure of P-n junction diode at unbiased condition ……………………………23

Fig. 1.26 Schematic diagram of Schottky junction ……………………….......................................24

Fig. 1.27 Schematic diagram of an MSM photodiode ……………………….....................................24

Fig. 1.28 Energy band diagram of I-V characteristics ……………………………………………….26

Fig. 3.1 (a) Schematic atomic structure of pristine WSe_2 monolayer (2 × 2 × 1 supercell) with a side view, showing W atoms sandwiched between two chalcogen planes (Se); The (b) side and (c) top view of Transition metal (3d, 4d, and 5d) doped at W site of WSe_2 monolayer. The blue, yellow, and violet bolls denote W, Se, and TM atoms …………………………………………..…………………40

Fig. 3.2 1H-WSe_2 monolayer (a) Band structure and (b) Total density of states (TDOS) with GGA-PBE (solid black line) and GGA-HSE06 functional (magenta dash line) along with the major symmetric directions ……………………………………………..…………………………………..…....42

Fig. 3.3 (a), (c), (e), (g) panels show the band structures of WSe_2 with 3d TM dopants (blue solid lines) and (b), (d), (f), (h) panels show the TDOS of TM doped WSe_2 system (blue solid line) with corresponding DOS of Sc, Ti, V and Cr (red solid line). In the case of V, the Fermi level shifts inside the VBM due to the lack of one electron as compared to the W atom. For Sc and Ti, acceptor states created around the Fermi level wherein the case of the Cr doped system, no shift in the Fermi level observed…………………………………………………………………………………….…...45

Fig. 3.4 (a), (c), (e) shows the band structures of Y, Zr, and Nb-doped WSe_2 monolayer, and (b), (d), (f) shows the TDOS with Y, Zr, and Nb. For Y and Zr doped WSe_2, acceptor states have created around the Fermi level, whereas for Nb and Zr doped WSe_2, the Fermi level moves inside the VBM ……………47

Fig. 3.5 (a), (c), (e), (g) shows the band structures of Ru, Rh, Pd, and Ag-doped WSe_2 system, and (b), (d), (f), (h) shows the corresponding TDOS. For Ru and Rh-doped WSe_2, the Fermi level moves deeper inside CBM, showing n-type doping characteristics, whereas the Pd and Ag-doped WSe_2 system shows metallic nature …………………………………………………………………………….....48

Fig. 3.6 (a), (c), (e), (g) and (i) shows the band structures, and (b), (d), (f), (h) and (j) shows the TDOS of Hf, Ta, Re, Ir and Au-doped WSe_2 (solid blue lines) with DOS of corresponding TM dopants (solid red line). For Re-doped WSe_2, the system becomes an n-type semiconductor, whereas, for Ta doping, the system behaves clearly as a p-type semiconductor material. In the case of Ir and Hf, some acceptor-type and donor-type defect states originate across the Fermi level. The Au-doped WSe_2 is showing metallic characteristics…..50

Fig. 4.1 Schematic atomic structure (top view) of (a) WSe_2 monolayer (b) TM-doped WSe_2 monolayer; the TM include, Nb, Ta, and Re ………………………..56

Fig. 4.2 Projected band structure of (a) pristine WSe_2 monolayer (b) Nb-doped WSe_2, (c) Ta-doped WSe_2 (d) Re-doped WSe_2, p-doping observed for Nb and Ta-dopants, where n-type doping for Re-doped WSe_2 monolayer. The blue, red, and pink dots represent the contribution of Nb-d, Ta-d, and Re-d orbitals ……………………………………………………………………………………57

Fig. 4.3 Charge density difference plot of (a) pristine (b) Nb-doped WSe_2 (c) Ta-doped WSe_2 (d) Re-doped WSe_2 ……………………………………………………………………………………58

Fig. 4.4 Variation of TM (Nb, Ta, and V)-doped WSe_2 monolayer bandgap under different biaxial strains from -5% to + 5% ……………………………………………………………………59

Fig. 4.5 Variation of K-K and Γ-K transition with tensile strain for (a) pristine WSe_2 (b) Nb-doped WSe_2 (c) Ta-doped WSe_2 (d) Re-doped WSe_2 monolayer. The arrow shows the critical strain value at which direct (K-K) to indirect bandgap (K-Γ) transition occurs ……………………………………60

Fig. 4.6 The optical properties of pristine and Nb, Ta and Re-doped WSe_2 monolayer, Panel (a)-(j) represents absorption spectra, (b)-(k) characterizes the real part of the dielectric function $\varepsilon_1(\omega)$, and (c)-(l) $\varepsilon_2(\omega)$ the imaginary part of the dielectric function …………………………………………… 63

Fig. 4.7 Biaxial tensile and compressive strain tuning of absorption spectra of (a) pristine WSe_2 (b) Nb-doped WSe_2 (c) Ta-doped WSe_2 (d) Re-doped WSe_2 monolayer ………………………………… 64

Fig. 4.8 Schematic atomic structure of transition metal (TM = Re, Nb, Ta, and V) doped WSe_2 monolayer with a top view under biaxial (a) compressive strain (b) unstrained (c) tensile strain conditions ……………………………………………………………………………………… 66

Fig. 4.9 PDOS of (a) Re doped-WSe_2 (b) Nb-doped WSe_2 (c) Ta-doped WSe_2 (d) V-doped WSe_2 monolayer ……………………………………………………………………………………67

Fig. 4.10 (a) Comparison of total energy versus V curve for WSe_2 and Re-doped WSe_2 monolayer, the ΔV is the net change in volume between host and dopant atom (b) E_{form} (=ΔE_T) versus strain curve for Re-dopant, shows the parabolic behaviour ……………………………………………………68

Fig. 4.11 (a, c) The total energy versus V curve and (b, d) E_{form} (=ΔE_T) versus strain plot for Nb, Ta, and V dopants, A linear relation of E_{form} with strain observed for Nb and Ta, whereas a parabolic behaviour observed for V dopant …………………………………………………………… 69

Fig. 4.12 Schematic atomic structure of 4×4×1 g-AZO monolayer (a) top and (b) side view shows the hexagonal arrangement of the g-AZO monolayer, where Zn, O, and Al are represented by grey, red, and green balls respectively ……………………………………………………………………70

Fig. 4.13 Band structures and PDOS of (a), (b) g-ZnO monolayer and (c), (d) g-AZO monolayer along with high symmetric directions (Γ-M-K-Γ) obtained by HSE06 calculations; the g-ZnO monolayer has a bandgap of 3.98 eV, whereas g-AZO monolayer has a bandgap of 3.8 eV, the Fermi level (E_F) presented by a green dashed line …………………………………………………………………… 71

Fig. 4.14 (a) The total energy versus V plot for g-ZnO and g-AZO monolayer, the ΔV is negligible (b) E_{form} vs. biaxial strain, the value of the E_{form} in the unstrained (0 %) g-ZnO monolayer is set as a reference ……………………………………………………………………………………… 73

Fig 4.15 Electronic band structure of the g-AZO monolayer at (a) +5%, (b) +10%, (c) -5%, and (d) -10% biaxial strain values ……………………………………………………………………74

Fig. 4.16 Variation of bandgap energy with different biaxial tensile and compressive strain …………...74

Fig. 4.17 Optical absorption spectra of the g-AZO monolayer (a) under tensile strain (b) enlarged optical spectra to show a shifting of wavelength (c) under compressive strain (d) enlarged version shows the shift of wavelength ……………………..76

Fig. 5.1 Schematic atomic structure of (a) GaTe and (b) $MoTe_2$ monolayer; and the electronic band structures of (c) GaTe and (d) $MoTe_2$ monolayer, using PBE (dash line) and HSE06 (solid lines) functionals ………………………...81

Fig. 5.2 The top and side views of stacking patterns of the GaTe/$MoTe_2$ heterostructures (a) A, where the Ga atom is on the top of the Te atom, (b) B, where Te atom on the Te atom (c) C, where Te atom on top of Mo atom, and (d) D, where Ga atom on the top of Mo atom ……………………………........... 82

Fig. 5.3 (a) The E_b versus the d_{in} for the GaTe/$MoTe_2$ heterostructure of C stacking pattern (b) Effective potential plot at GaTe/$MoTe_2$ heterostructures, showing an ΔV ~ 15.3 eV (c) Band alignment of individual GaTe and $MoTe_2$ monolayer in GaTe/$MoTe_2$ heterostructure. It is observed that GaTe/$MoTe_2$ heterostructure has typical type-I band alignment ……………………………………………...83

Fig. 5.4 The projected (a) band structure and DOS of the GaTe/$MoTe_2$ heterostructure determined from HSE06 functional; Red and blue solid lines represent the GaTe and $MoTe_2$ components, respectively. The band structure shows indirect bandgap type-I heterostructure, where CBM and VBM both have a contribution from the $MoTe_2$ monolayer; Fermi level is indicated by a dashed green line, the orbital contribution from Mo (4d), Ga (4p) and Te (5p) are included …………………………....................84

Fig. 5.5 Comparison of the absorption spectra of the GaTe monolayer (red dot line), $MoTe_2$ monolayer (blue dash line), and GaTe/$MoTe_2$ heterostructure (black solid line) using HSE06 functional ………......84

Fig. 5.6 Variation of (a) interlayer distance and (b) E_b of GaTe/$MoTe_2$ vdW heterostructure with biaxial strain ………………………..85

Fig. 5.7 The projected band structures of the GaTe/$MoTe_2$ heterostructure for different tensile (+) and compressive (-) strains; (a) 1 % (b) 3% (c) 5% (d) 9% and (e) -1% (f) -4% (g) -5% and (h) -9%. The contributions of GaTe and $MoTe_2$ layers are described by the red and blue lines, respectively ……..... 86

Fig. 5.8 The projected band structures of the GaTe/$MoTe_2$ vdW heterostructure for different positive and negative E_{ext}. The contributions of GaTe and $MoTe_2$ layers are described by the red and blue lines, respectively ………………………...87

Fig. 5.9 The variations of the bandgap of GaTe/$MoTe_2$ vdW heterostructure with (a) biaxial tensile and compressive strain (b) different (+) and (-) E_{ext} ………………………...88

Fig. 5.10 Optical absorption spectra of the GaTe/$MoTe_2$ vdW heterostructure with different values of (a) tensile strain (b) compressive strain (c) (+) E_{ext} and (d) (-) E_{ext} ………………………................ 89

Fig. 5.11 Schematic illustration of the (a) Type-I and (b) Type- II conventional photocatalytic GaTe/$MoTe_2$ heterojunction ………………………..90

Fig. 6.1 Schematic diagram of Colloidal synthesis process for WSe_2 Nanosheets ……………….…... 93

Fig: 6.2 (a) Solution of as-prepared WSe_2-NSs before annealing (b) WSe_2 NSs powder after annealing at 200°C for 2 hrs (c) WSe_2 NSs powder dispersed in IPA for further use. (d) WSe_2 NSs final solution under UV light to show the luminescence ……………………………………………………...93

Fig.6.3 Schematic diagram of Colloidal synthesis process for WS_2 Quantum dots …………………..…..94

Fig: 6.4 (a) Solution of as-prepared WS_2-QDs (b) WS_2 QDs solution after filtration by dialysis bag for 2-3 days. (c) WS_2 QDs solution under UV light to show the luminescence……………………………94

Fig. 6.5 Schematic diagram of the mixed-dimensional heterostructures based on (a) (0D-3D) n-WS_2 QDs/p-Si (b) (2D-0D-3D) p-WSe_2 NSs/n-WS_2 QDs/p-Si ……………………………………….……...95

Fig. 6.6 (a) SEM images and (b) high-magnification SEM image of graphene-like WSe_2 nanosheet….96

Fig. 6.7 (a) TEM images of graphene-like WSe_2 nanosheets (b, c) HRTEM image of the selected region (d) shows the corresponding SAED pattern ……………………………………………………......96

Fig. 6.8 (a) The XRD pattern and (b) the Raman spectrum of graphene-like WSe_2 nanosheets ……......97

Fig. 6.9 (a) UV-visible absorbance spectra of the WSe_2 NSs (b) Photoluminescence spectra of pristine WSe_2 NSs with different excitation wavelengths, (c) photoluminescence excitation (PLE) spectra of WSe_2 NSs ………………………...98

Fig. 6.10 (a) HRTEM image of WS_2 QDs, (b) Size distribution histogram plot of WS_2 QDs ……….…...98

Fig. 6.11 (a) the XRD pattern and (b) the XPS of WS_2 quantum dots …………………………….....99

Fig. 6.12 (a) UV-visible absorbance spectra (b) PL spectra of pristine WS_2 QDs with different excitation wavelengths…………………………………………………………………………….....99

Fig. 6.13 Room temperature I-V characteristics of the (a) (0D-3D) n-WS_2 QDs/p-Si (b) (2D-0D-3D) p-WSe_2 NSs/n-WS_2 QDs/p-Si at dark and under the illumination of white light with a power intensity of 21.98 mW/cm^2 ………………………………………………………………………….…….……..101

Fig. 6.14 The wavelength-dependent R, D^* and EQE of the (a, c) n-WS_2 (0D-3D) QDs/p-Si (b, d) (2D-0D-3D) p-WSe_2 NSs/n-WS_2 QDs/p-Si heterostructures photodetectors……………………….……....103

Fig. 6.15 (a, b) Transient photo response and (c, d) magnified image of single pulse for measurement of rise time and decay time of n.WS_2 QDs/p-Si heterojunction with (a, c) before and (b, d) after p.WSe_2 NS deposition under the illumination of white light with a power intensity of 21.98 mW/cm^2 at -3 V bias voltage ……………………………………………………………………………………………104

LIST OF TABLES

Table No **Description** **Page No**

Table 3.1: The optimized lattice parameters for pure and TM-doped WSe_2 monolayer, where a and c are lattice constant, and $d_{X\text{-}Se}$ describes the bond length in the vicinity of metal impurity, E_{form} is the formation energy of TM-doped WSe_2 monolayer in W-rich and Se-rich conditions, Eg is the bandgap TM doped WSe_2 and ΔQ is the charge transfer from TM dopants to WSe_2 monolayer ……………………………………..41

Table 4.1: The lattice constant, bond length, formation energy, bandgap, ΔQ is the charge transfer and doping-type for pristine and Nb, Ta, and Re-doped WSe_2 monolayer…………………...58

Table 4.2: The slope of the K-K (A) and Γ-K (I) bandgaps with respect to biaxial tensile strain (in unite of meV/%) for pristine WSe_2 and Nb, Ta, and Re-doped WSe_2 monolayer……….…..... 61

Table 4.3: The doping type, bond length (between TM dopant and Se atom), ionic radii, formation energy (E_{form}), and change in volume (ΔV) due to substitutional TM doping……......67

Table 6.1: Comparison of device performance of n-WS_2 QDs/p-Si and p-WSe_2 NSs/n-WS_2 QDs/p-Si heterostructure with Ag as top contact based photodetectors………………………..101

LIST OF ABBREVIATIONS

Abbreviation	Details
2D	Two Dimensional
TMDC	Transition Metal Dichalcogenides
MMC	Metal monochalcogenides
WSe_2	Tungsten diselenide
WS_2	Tungsten disulfide
ZnO	Zinc Oxide
GaTe	Gallium telluride
$MoTe_2$	Molybdenum telluride
TM	Transition Metal
0-D	Zero Dimensional
2-D	Two Dimensional
3-D	Three Dimensional
J-V	Current density - Voltage
I-V	Current-Voltage
C-V	Capacitance -Voltage
CVD	Chemical Vapor Deposition
DI	Deionized
DOS	Density of States
PDOS	projected density of states
E_b	Binding Energy
E_{form}	Formation Energy
E_{ext}	Electric field
ε_{xy}	Biaxial strain
LCAO	Linear combination of atomic orbitals
DFT	Density Functional Theory
GGA	Generalized Gradient Approximation
PBE	Perdew–Burke–Ernzerhof
PAW	Projected Augmented Wave
HSE06	Heyd-Scuseria-Ernzerhof
CBM	Conduction Band Minima
VBM	Valance Band Maxima
MSM	Metal Semiconductor Metal
NSs	Nanosheets
QDs	Quantum dots
NPs	Nanoparticles
PDs	Photodetector
SEM	Scanning Electron Microscope
SAED	Selected Area Electron Diffraction
TEM	Transmission Electron Microscopy
HRTEM	High-resolution transmission electron microscopy
XRD	X-ray diffraction
PL	Photoluminescence
UV	Ultra violet
PLE	photoluminescence excitation
AFM	Atomic Force Microscopy
EQE	External Quantum Efficiency
R	Responsivity
D^*	Detectivity

Chapter 1

INTRODUCTION AND BASIC CONCEPT BEHIND THE THESIS

1.1 Introduction of Two-Dimensional (2D) Materials:

2D Materials are crystalline materials consisting of a single layer of atoms with a thickness of a few nanometers or less. Graphene was the first 2D material discovered in the year 2004 by mechanical exfoliation from graphite using the scotch tape method [1-4]. In 2D materials, electrons can move freely in two dimensions, but their motion is restricted in the third dimension. The 2D materials family consists of Graphene, Black phosphorus (BP), hexagonal boron nitride (h-BN), Transition Metal Dichalcogenides (TMDCs), Metal monochalcogenides (MMCs), 2D oxides and MXenes, etc. [5-9]. Among these materials, Graphene has zero band gap energy due to which it behaves as a semimetal [10]. Insulating hexagonal boron nitride (h-BN) is an insulator [11]. BP has a lower effective mass than TMDC due to which it has a high ON current [12]. Despite having the above advantages, BP shows less stability as compared to TMDCs. The semiconducting TMDC materials (MoS_2, WSe_2, WS_2, $SnSe_2$, etc.) have a tunable bandgap which is attractive for optoelectronics applications [13]. Due to the tunable bandgaps of TMDCs, it shows semiconducting properties as well, like Silicon (Si) and Germanium (Ge). 2D metal oxides have attracted its attention due to their ultra-thin nature, high air stability, and high environment-friendly synthesis, such as ZnO, MoO_2, Sb_2O_3, etc. induces various application in the field of optoelectronics, sensing, and electrochemical storage [14-16]. 2D- MMC semiconductors such as InSe, GaTe, GaS, etc. have emerging applications in the nanoelectronics field due to their layer-dependent tunable bandgap, high mobility, and quantum emission [16-18]. 2D materials have emerging applications in the nanoelectronics industry such as photodetectors, sensing, spintronics, ultrafast lasers, batteries, supercapacitors, and thermoelectric etc. [19, 20]. **Fig.1.1** shows the schematic of the 2D materials family including the main popular components of 2D materials such as Graphene, TMDCs, BP, h-BN, 2D oxides and MMC family as discussed above.

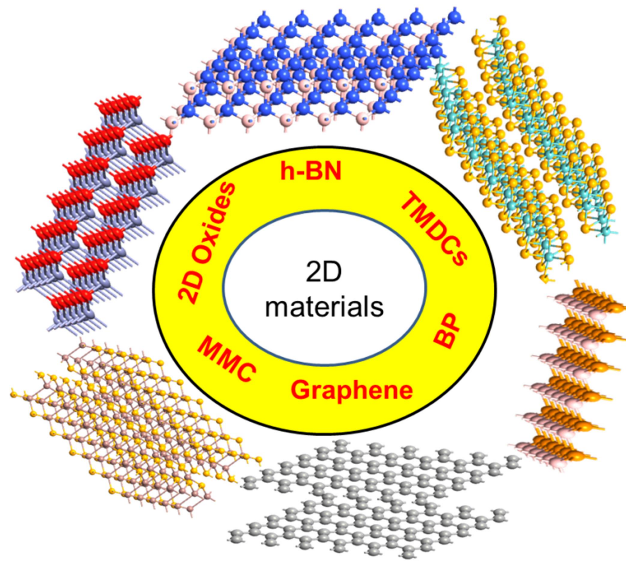

Fig. 1.1 Schematic illustration showing popular 2D materials family

1.1.1 Graphene

The very first discovered 2D material was Graphene which is a combination of carbon atoms arranged in a hexagonal honeycomb lattice structure as shown in **Fig. 1.2**. It has zero band gap energy with semi-metal structure linear band dispersion joining at the Fermi level of K points in the Brillouin zone. Graphene is composed of hexagonally arranged sp^2 hybridized atoms that have extraordinary strength and optical properties, excellent carrier mobility (15,000 $cm^2V^{-1}s^{-1}$), and high thermal conductivity [1][21, 22]. Graphene's exceptional properties and single-layer atomic structure allow it to be used in a wide variety of field-effect transistors (FETs), photodetectors, flexible composite materials, and storage of energy precise sensors.

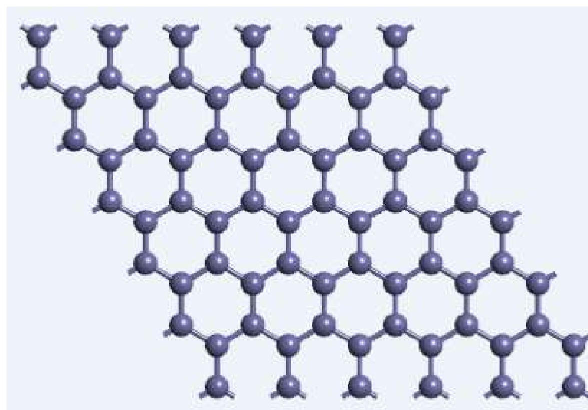

Fig. 1.2 Schematic of 2D hexagonal honeycomb-like graphene structure

1.1.2 Transition metal dichalcogenide (TMDCs)

TMDCs are a kind of 2D material consisting of a single layer of atoms with a thickness of a few nanometers or less [13, 23, 24]. TMDCs monolayers are atomically thin semiconductors of the type MX_2, where M is a transition metal atom (Mo, W, Sn, etc.) and X is a chalcogen atom (S, Se, or Te). One layer of the M atom is sandwiched between two layers of X atoms [2][25]. One of the biggest advantages of TMDCs material is their tunable band gap, they have an indirect band gap in the bulk form whereas in monolayer form the gap becomes direct and is located in the K points [26]. They have high carrier mobilities, the absence of dangling bonds, high crystallinity, and good thermal stability [13, 27]. This varying band gap in TMDCs is accompanied by strong photoluminescence (PL) and large exciton binding energy [28, 29]. The bandgap of TMDCs material changes with their thickness which allows the detection of light at different wavelengths. Other than tunable optical band gap, TMDCs have various advantages such as strong light-matter interactions, high exciton binding energy [30], and large specific surface area due to reduced dimensionality [31, 32]. TMDC semiconductors such as MoS_2, WS_2, $MoSe_2$, WSe_2, etc. have attracted significant attention for future optoelectronic applications owing to their unique electrical [33], optical [34], and mechanical properties [35, 36]. Nowadays, electronic devices based on these 2D TMDCs materials with silicon (Si) are at the forefront of current research due to their potential applications as p-n junctions, solar cells, light-emitting Diodes (LEDs), photodetectors, and photovoltaic cells. The geometrical side and top view of TMDCs monolayer has been shown in **Fig. 1.3.**

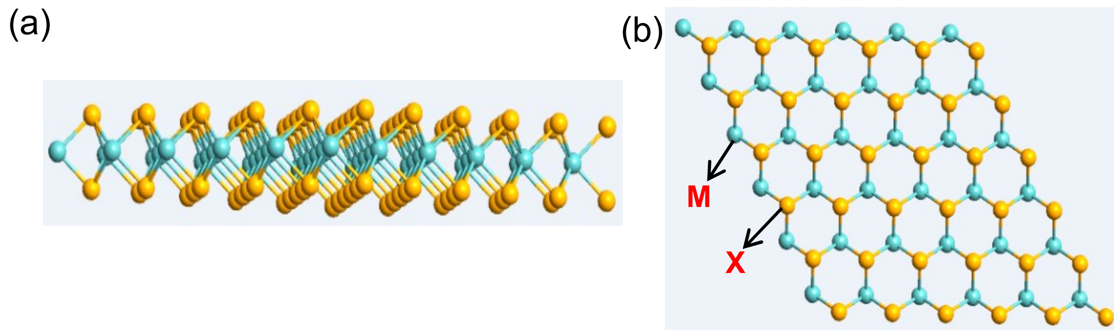

Fig. 1.3 shows (a) the Geometrical side view of monolayer TMDCs (b) the Hexagonal structure (top view) of monolayer TMDC materials, where M is a transition metal atom and X is chalcogenides materials

1.1.3 Metal monochalcogenides (MMCs)

MMCs having the chemical formula of MX, where M = Ga, In, and Sn, etc. and X = Te, Se, S, etc.) have been grown as popular 2D materials due to their low-cost, eco-friendly, and anisotropic electronic and optical properties [18, 37, 38]. They have good chemical stability, bandgap tunability, high carrier mobility, and polarization properties [39, 40]. MMCs have various applications in the field of field effect transistors (FETs), photovoltaic cells, photocatalysis, and optoelectronics devices [41-43]. In 2019, C. Ren *et. al.* [44] reported the electronic properties and band alignment of group III monochalcogenides ($M_{III}X$) which includes GaS, GaSe, GaTe, and InSe, etc. are useful in nanoelectronics, photocatalysis, and photovoltaics application. $M_{III}X$ monolayers are indirect-bandgap semiconductors and they have interesting properties of band convergence. There are many systematic studies reported on the possibility of forming type-II heterostructures by combining $M_{III}Xs$ with other popular 2D semiconducting materials, including MoS_2, $MoTe_2$, WS_2, WTe_2, black phosphorene (BlackP) and graphene, etc. which are very useful for optoelectronics and photocatalysis applications [45-48]. The geometrical side and top view of the MMCs monolayer has been shown in **Fig. 1.4.**

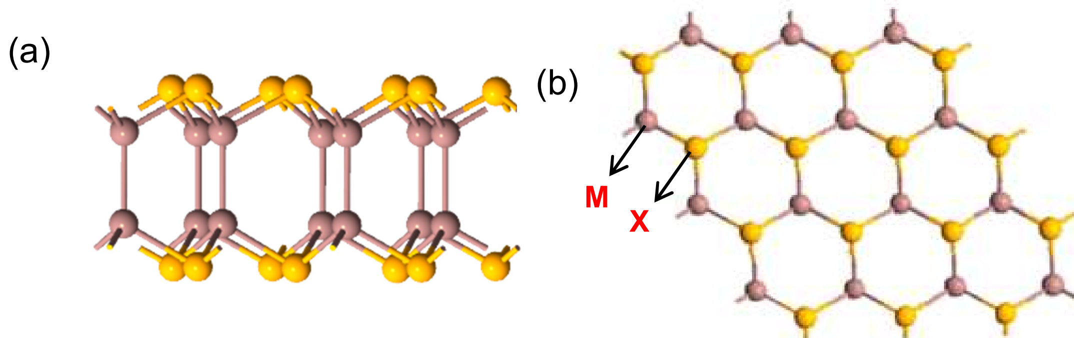

Fig. 1.4 a) Geometrical side view of monolayer Metal monochalcogenides (MMC) structure (b) the Hexagonal structure (top view) of monolayer MMC, where M represents a group III element and X represents a chalcogen atoms

1.2 Doping of 2D Materials

Doping is the intentional introduction of impurities into intrinsic semiconductor materials, used to increase the number of mobile electrons/holes [49]. For doping in 2D materials, mainly three types of doping techniques are studied by researchers across the world such as adsorption doping [50-53], substitutional doping [54-56], and charge transfer method [57, 58]. In 2D materials, impurities doping, adatom adsorption, and charge transfer are possible because of their high surface area. Intrinsic monolayer 2D materials have low free charge density, low standby power dissipation, and drive current [59]. The doping

concentration of 2D materials can be enhanced by the substitution of suitable impurities or the adsorption of surface adatoms. In 2013, Dolui *et. al*. [53] reported the doping strategies of MoS_2 monolayers with possible dopants by substitution of S/Mo atoms or as adsorbents for device applications. In 2014, Rastogi *et. al*. [60] reported a systematic study on MoS_2 monolayer by surface adsorption of different atoms. Sun *et. al.* [61] investigated the electronic and optical properties of ZnO monolayer doped with different concentrations of Al, Ga, and In atoms.

Types of doping methods:

(a) Substitutional doping
(b) Adsorption doping effect
(c) Charge transfer method

(a) Substitutional doping:

Substitutional doping can be considered the best doping technique in Si because it provides long-term stability without degrading the performance and controllability of the doping level [62]. Substitutional doping is the key to modulating the conductivity of 2D materials, enabling their electronic devices for future applications [23, 63-66]. It can be done through direct synthesis and post-treatment methods like chemical vapor deposition (CVD), solvothermal methods, etc. [67, 68]. Therefore homogeneous doping is possible via the Substitutional doping method. Typically, in substitutional doping, atoms of the host metal are replaced by foreign (dopant) atoms. When the host atom replaces by a dopant atom, an internal strain induces due to the size differences between the host and the dopant [69]. **Fig. 1.5** shows a schematic of the substitutional doping of dopants in Place of the W (host) atom in the WSe_2 monolayer.

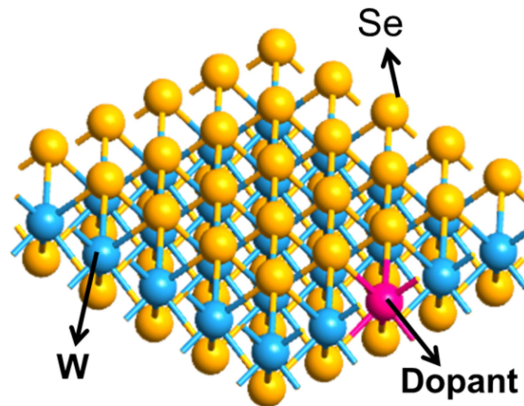

Fig. 1.5 Schematic of substitutional doping method

To analyze the stability of dopants in 2D materials, the formation energy (E_{form}) is calculated, which is given by the following relation [70-72].

The formation energy of a particular substitutional dopant, E_{form}, is defined as

$$E_{form} = E_{tot}[WSe_2 + X] - E_{tot}[WSe_2] + \mu_{host} - \mu_X \quad \textbf{(1.1)}$$

Where, $E_{tot}[WSe_2 + X]$is the total energy of the system including the substitutional atom X, E_{tot} [WSe_2] is the total energy of the corresponding pristine WSe_2 monolayer, while μ_X and μ_{host} are respectively the chemical potentials of the substitutional atom X and the substituted W (Se) host atom. The chemical potentials of the X dopants are calculated concerning bulk reference levels for W (Se) substitution. When the system has more negative energy that means the system is more stable.

(b) Adsorption doping effect:

Adsorption is a physical process in which the accumulation of a molecule happens from a substance when it interacts with the surface of the adsorbent [50, 73, 74]. It is a low-temperature exothermic process [75]. In this process, the molecules are loosely held on the surface and can be easily removed. **Fig. 1.6** shows the schematic of the adsorption doping method where the dopant adsorped at the Se site. There are two types of adsorption processes such as physisorption and chemisorption which corresponds to weak van der Waals forces and covalent bonding respectively.

The binding energy for an adsorbate E_{ads} can be written as [60]

$$E_{ads} = E_{tot}[WSe_2 + Y] - E_{tot}[WSe_2] + E_{bulk}[Y] \quad \textbf{(1.2)}$$

Where $E_{tot}[WSe_2 + Y]$ refers to the total energy with adsorbate atom Y, $E_{bulk}[Y]$ is the energy of the adsorbate Y in its bulk form.

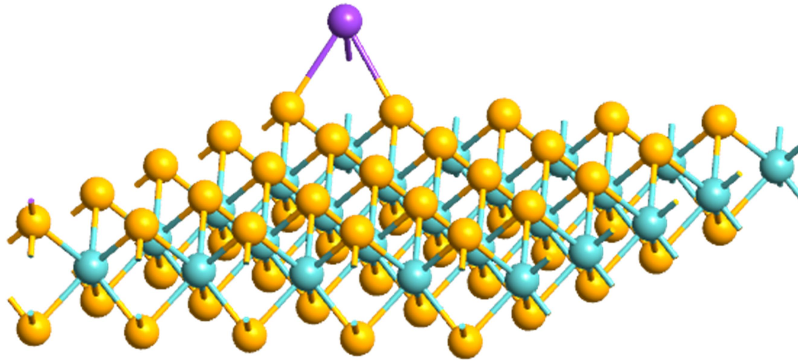

Fig. 1.6 Schematic of adsorption doping method

(c) Surface charge transfer doping (SCTD):

Charge-transfer doping has been done by thermal deposition of organic or inorganic layers of thin film on the top of the 2D semiconductors [76]. The charge transfer amount is determined by the intrinsic properties of the dopant molecules such as relative frontier orbital positions and their spin configurations [58]. SCTD involves the physisorption of dopants (e.g. Al_2O_3) on the surface of 2D materials as shown in **Fig. 1.7**, which induces a charge transfer across the surface/dopant interface [77]. 2D TMDC materials have a large surface-to-volume ratio which makes them highly sensitive to the surface-attached dopants. SCTD is a comparatively non-destructive process. In SCTD, the selection of materials for dopants is diverse by molecular reductants (oxidants) for n (p)-type doping because of their high molecular degree of freedom [78]. Therefore, several studies reported on molecular SCTD in 2D material-based electronic devices for reducing contact resistance and controlling the carrier type for complementary logic applications [79, 80].

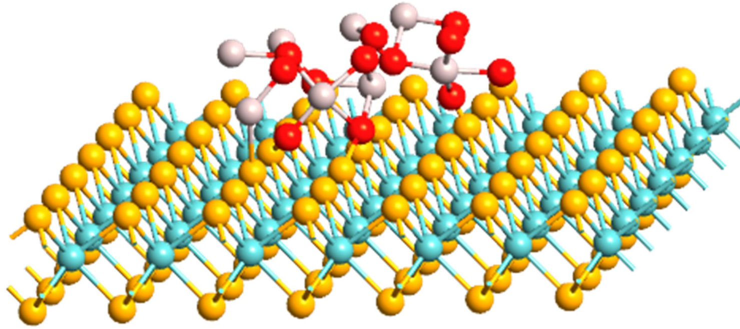

Fig. 1.7 Schematic of Charge transfer method

1.3 Formation of Heterostructures

Heterostructures are formed between two dissimilar semiconductor materials of different bandgaps and lattice constants, and the first successful heterojunction structure of Ge/GaAs was developed by Anderson in 1960 [81]. He established the well-known Anderson model to determine the energy band diagram of heterojunctions at the interface for the prediction of the current flow [81]. The Anderson model was based on the assumption of the ideal heterojunctions where the interface states are assumed to be zero at the interface and current transport occurs by injection of carriers over the band offsets into the quasi-neutral region of the semiconductors [81].

Heterostructures have namely three types of band alignment depending on the valance band and conduction band of the two different semiconductors as given below:

(i) Type I or Straddled alignment,

(ii) Type II or Staggered alignment,

(iii) Type III or Broken gap alignment.

1.3.1 Type I or Straddled alignment:

When the band gap of one material overlaps with the other band gap material, the narrower band gap is enclosed within the wider band gap [45, 82]. In this case, $E_{V2}>E_{V1}$ and $E_{C1}>E_{C2,}$ and the signs of band offsets for the two bands are opposite. E.g. WS_2/PtS_2 [82], $GaTe/MoTe_2$ [45], MoS_2/ReS_2 [83] etc. The schematic diagram of type-I band alignment has been shown in **Fig. 1.8**.

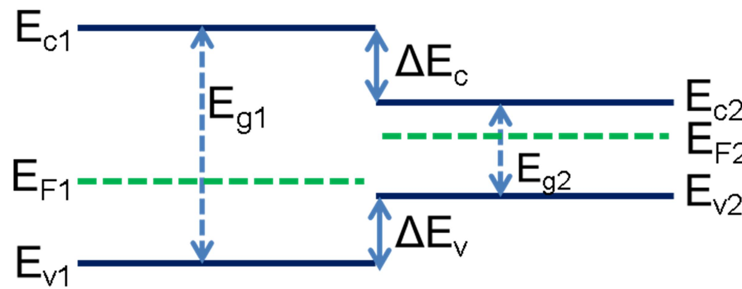

Fig. 1.8 Type 1 Straddled band alignment of heterostructures

1.3.2 Type II or Staggered alignment:

The band gap of one semiconductor material entirely overlaps with the other band gap of the material with $E_{V2}>E_{V1}$, $E_{C2}>E_{C1,}$ and $\Delta E_C<E_{g1}$. In this case, the band offsets have the same sign. Both the conduction band edge and valance band edge of one material are lower than the equivalent band edges of other material. E.g. $GaTe/MoS_2$ [47], MoS_2/WS_2 [84], $MnPSe_3/MoTe_2$ [85], $InSe/WTe_2$ [86] etc. The Type II band alignment has been shown in **Fig. 1.9.**

Type II band alignment is very important for optoelectronic and light harvesting applications due to their unique ability to separate and collection of electron-hole (e^--h^+) pairs [87]. There are many works reported on type-II "staggered gap" band alignment of 2D-heterostructures which can imply the electrons and holes into two different layers of materials for optoelectronics application [46, 47, 85, 86, 88].

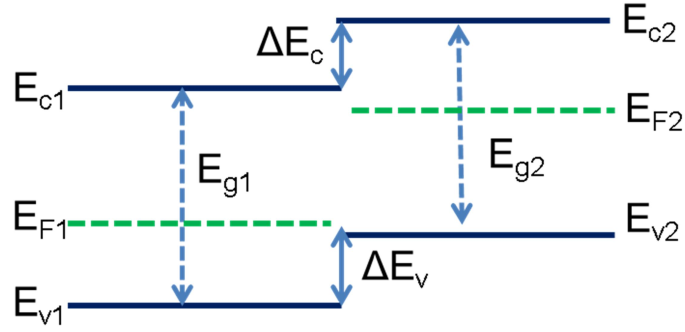

Fig. 1.9 Type II Staggered band alignment of heterostructure

We can calculate the Conduction band (ΔE_C) and Valence band (ΔE_V) offsets by using the following equations:

$$\Delta E_c = \chi_1 - \chi_2 \quad \textbf{(1.3)}$$

Where χ is the electron affinity of the materials.

$$\Delta E_c + E_{g1} = \Delta E_V + E_{g2}$$

$$\text{So, } \Delta E_V = \Delta E_g - \Delta E_c \quad \textbf{(1.4)}$$

1.3.3 Type III or Broken gap alignment:

In this kind of band alignment, the band gap of one material does not overlap with the other band gap of material because $E_{V1}>E_{V2}$, $E_{C1}>E_{C2}$, and $\Delta E_C>E_{g1}$. In this case, the band offsets have the same sign [89]. Both the conduction band edge and valance band edge of one material are separately lower than the band edges of the other material. E.g. $MoTe_2/SnSe_2$ [90], WTe_2/HfS_2 [91], etc.

The schematic diagram of type III band alignment has been shown in **Fig. 1.10**.

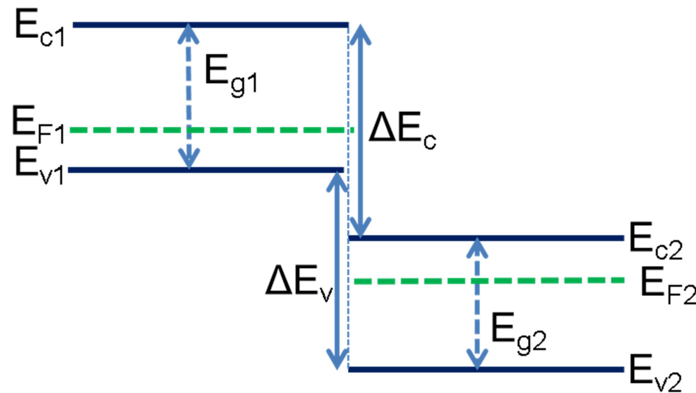

Fig. 1.10 Type III Broken gap alignment of heterostructures

1.4 Role of External Factors on 2D Materials

The electronic structure and optical properties of 2D materials can be modulated by various external factors such as mechanical strain, external electric field, twist angle, etc. [45, 92, 93] Here, in our thesis work, we will discuss mainly two external factors such as biaxial strain and External electric field in detail.

1.4.1 Mechanical Strain

Mechanical strain (ε) is a geometrical measurement of distortion or deformation in a material, which represents the relative displacement between particles in a material system when it is subjected to applied mechanical stress [40, 94, 95].
The magnitude of ε is defined as $\boldsymbol{\varepsilon = (a_0 - a)/a \times 100\%}$, where a and a_0 are the lattice constants of the unstrained and strained materials, respectively. The four different types of strain are longitudinal strain, lateral strain, volumetric strain, and shear strain.

Longitudinal strain is expressed as the ratio of change in length (ΔL) to the original length (L) of the material.

$$\varepsilon = \text{Strain} = \frac{Change\ in\ lengt}{Original\ length} = \frac{\Delta L}{L} \qquad \textbf{(1.5)}$$

It measures how much a material elongates or shortens along its length when it is subjected to tensile or compressive stress, respectively. When longitudinal strain is positive, the material is elongated and it is known as **tensile strain**. Whereas; if the longitudinal strain is negative, the material is compressed and it is known as **compressive strain**. In our work, we focused on the modulation of electronic and optical properties of 2D materials by applying biaxial tensile and compressive strain [55, 96, 97]. **Fig. 1.11** shows the schematic of 2D materials under biaxial tensile and compressive strain.

The 2D semiconductors have outstanding stretchability and resilience to mechanical deformations of the order of 10-11%, while traditional semiconductors break at a small value of deformations of ~ 1.5 % [98-100]. The application of strain to modulate the electronic [36, 56, 101, 102], optical [98, 103, 104], and magnetic [105, 106] properties of 2D semiconductors are well explored in the 2D materials community. Due to applying strain, the original state of atomic bonding changes by stretching or shortening the distance of chemical bonds [107]. As a result, the electronic structure of the material is reformed, and a series of new properties emerge [36, 100, 108].

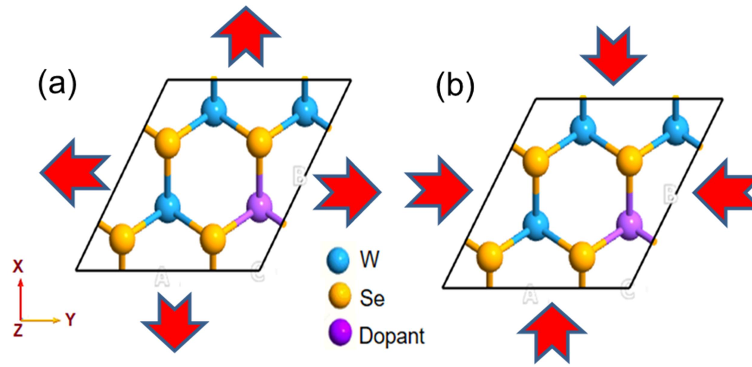

Fig. 1.11 Schematic of 2D materials under (a) biaxial tensile strain (b) biaxial compressive strain

1.4.2 External Electric Field

When an electric field surrounds the electrically charged particles and exerts force on all other charged particles in the field, by either attracting or repelling them [109]. **External Electric field** (E_{ext}) can be applied to a given materials system in various ways and considered as an electric property related to each point. There are several studies reported on the modulation of electronic and optical properties of 2D materials with the application of E_{ext} [110, 111]. **Fig. 1.12** shows 2D bilayer materials under an external electric field.

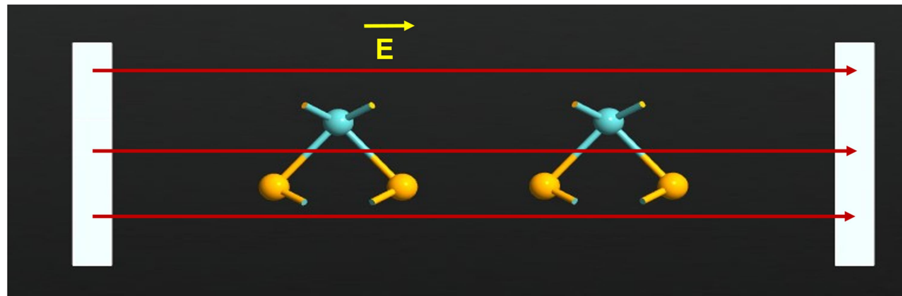

Fig. 1.12 Schematic of 2D bilayer material under External Electric Field

1.5 Synthesis of 2D Materials

The route of synthesis processes of 2D materials has been categorized into two methods: (a) top-down methods and (b) bottom-up methods. Top-down methods involve the formation of one or a few atomic layers of 2D nano-sized particles by breaking down the bulk material using external energy [13, 112]. Top-down methods consist of Micromechanical exfoliation, chemical or liquid exfoliation, laser ablation and thinning, etching, sputtering, and electron beam lithography [113]. On the other hand, bottom-up methods are the process in which materials are deposited on a substrate via thermal and/or chemical reactions to synthesize 2D nanostructures [114, 115]. Bottom-up methods include solvothermal and hydrothermal methods, chemical vapor deposition (CVD), sol-gel method, and Soft and hard

templating methods which are used to synthesize 2D nanostructures [116]. This section will discuss the different synthesis processes for 2D nanostructures.

1.5.1 Micromechanical Exfoliation (MME)

The MME process was first discovered by Geim and Novoselov in 2004 [117]. The Graphene monolayer was first time exfoliated from graphite peeled off by scotch tape and placed on the surface of the photoresist [118]. There are various materials reported by the scotch tape method such as MoS_2 [119], and WS_2 [120] monolayers, and cleavage of these materials are possible because of weak van-der walls attraction. Mechanical exfoliation is not a suitable method for industrial-scale production of monolayer materials because the majority of the flakes are smaller than 20 m in diameter although it has high speed and low loss. The monolayer formed by this method is highly crystalline and retains its structural integrity due to a lack of chemical interaction. This monolayer can be stable at ambient temperatures for months [13].

1.5.2 Liquid Exfoliation

Liquid exfoliation can produce mono or a few layers of 2D materials on a large scale such as $MoSe_2$, $MoTe_2$, BN, WSe_2, and MoS_2, etc. [121, 122]. This method is classified into four types: oxidation, ion exchange, ultrasonic cleavage, and intercalation [123]. Graphene oxide can be synthesized via the oxidation method by treating graphite flakes with potassium permanganate, potassium chlorate, nitric acid, sulfuric acid, or a mixture of these acids [124]. The oxidation method is also known as the Hummers method [125]. In liquid exfoliation, oxidative form is preferable for layered materials with low reduction potential. Ultrasonic cleavage is another method of liquid exfoliation for obtaining single- or few-layered 2D materials. In this method, the bulk materials consisting of weak interlayer bonding have been dispersed in a suitable solvent followed by ultrasonication for 1-3 hrs, the cavitation bubbles are formed in the solvent as a result of high-energy ultrasonic waves. Then the layered exfoliation is performed by bursting of cavitation bubbles via releasing the pressure and then the crystals are separated using centrifugation. The intercalation technique works very well with TMDCs and Graphene. In this method, interlayer force is reduced because of the intercalation of ionic or organic molecules which results in lower energy required for exfoliation [126].

1.5.3 Chemical Vapour Deposition (CVD)

CVD is a bottom-up technique that allows 2D thin film synthesis on a large-scale substrate with uniform thickness and makes it suitable for optoelectronics and electronic device applications [127, 128]. In this process, gas molecules are combined in a reaction chamber at ambient temperature and when it comes into contact with the substrate, a gaseous reaction occurs that creates a material film deposited on the substrate surface. Then the waste gases have been pumped out from the reaction chamber. The quality of the resulting materials is very high, pure, and fine-grained. CVD is the finest process of film deposition on substrates for application in the semiconductor industry as well as the optoelectronics field [68, 128, 129]. The precursors that have been chosen for the CVD method should have high purity, volatility, cost-effectiveness, high stability, and non-hazardous nature. There are most recent developments of CVD synthesis of 2D nanostructured MoS_2 sheets on an oxidized silicon substrate published in several studies [130, 131]. Other 2D materials produced using CVD techniques include TiS_2 [132], VSe_2 [133], WSe_2 [134], WS_2 [135], $MoSe_2$ [136] nanostructures, etc.

1.5.4 Hydrothermal and Solvothermal synthesis method

The hydrothermal method is the synthesis of single crystals from an aqueous solution in an autoclave under high temperature and pressure. Due to the harsh conditions, this method is only suitable for precursors that can withstand them. It is a liquid medium bottom-up synthesis process that produces 2D layered nanostructured materials deposited on substrates via chemical reactions [114]. When water is used as a medium, the synthesis is referred to as hydrothermal. The solvothermal method is a synthesis method that can be done via a chemical reaction of precursors in the presence of a solvent in a closed system at a temperature higher than the boiling temperature of the solvent. It is a low-cost scalable chemical synthesis technique. For example, single-layered $MoSe_2$ and MoS_2 nanostructures were created by chemically reacting Se/S with $(NH_4)_6Mo_7O_{24}4H_2O$ (ammonium molybdate) in hydrazine monohydrate solution for 48 hours at 150–180°C [137]. Metal chloride in oleylamine was used to create 2D nanostructures of TMDCs (groups IV and V) [138]. The selenium (Se), sulfur (S), or compounds CS_2 are used as chalcogen sources in this process. There are various types of 2D nanostructures of TMDCs (MoS_2, WSe_2, WS_2, etc.) like nanosheets, nanorods, and quantum dots, etc. can be produced via hydrothermal and solvothermal methods [115, 139, 140].

1.6 Characterization Methods

Spectroscopy techniques have been used to characterize nanomaterials as well as other materials for a long time in the chemical, biological, and engineering fields. In our work, we have used some most effective spectroscopy methods for characterizing various nanomaterials of various dimensional such as 0D/1D/2D/3D. These techniques are used to provide important information about the chemical structure and properties of nanomaterials. Spectroscopy techniques are used jointly with various microscopy techniques to provide a comprehensive picture of the nanomaterials.

1.6.1 Transmission Electron Microscopy (TEM):

Transmission electron microscopy (TEM) is a microscopy technique in which an electron beam is passed through an ultra-thin specimen less than 100 nm [141]. Interaction of electrons happens when it passes through the specimen and it produces a magnified image that is focused on a layer of photographic sensor like a CCD camera. This interaction between the electrons and the specimen atoms can be observed in various features like crystal structure, grain boundaries, and chemical analysis. TEM has a very high-resolution limit of 0.2 um because it can magnify a small particle of about 2-3 nm. **Fig. 1.13** shows the internal configuration of Transmission Electron Microscopy. TEM is used to operate with an electron beam which focuses on the specimen and produces an image whereas a light microscope uses light rays to focus and produce an image. TEM has been used to study material composition, growth of layers, surface image, and thickness. Their working mechanism is enabled by the high-resolution power, allowing it to be used in a wide range of fields. It has three working parts, which are as follows:

- The electron gun
- Image producing system
- Image recording system

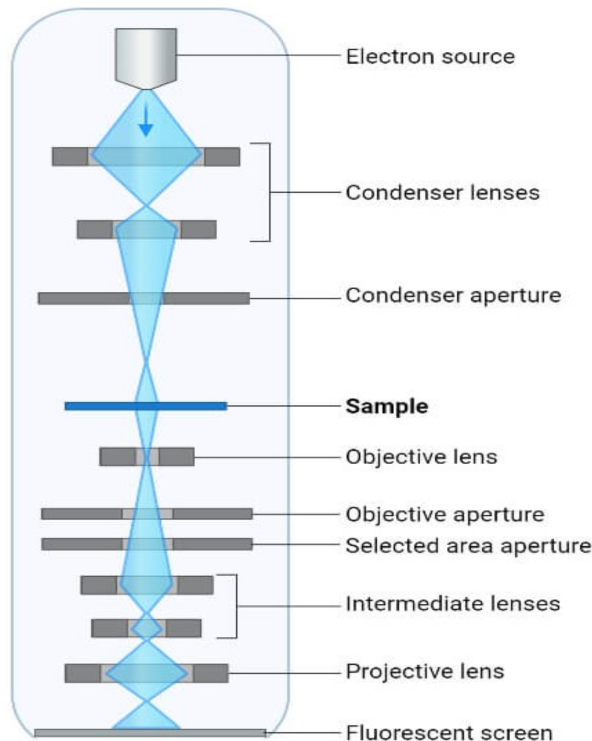

Fig. 1.13 Internal Configuration of Transmission Electron Microscopy; Reproduced from Ref. [141]

1.6.2 Scanning Electron Microscopy (SEM):

A scanning electron microscope (SEM) is a microscopy technique which uses to produce an image by focusing electron beams on the surface. When the electrons interact with the sample, it produces a variety of signals which use to give information about the topography and composition of the surface and crystalline structure. The data has been collected over a specific area of the sample's surface and provides a 2D image. SEM analysis has been useful in determining chemical compositions, crystalline structure, and orientations and it has a wide range of scanning modes from 1 cm to 5 microns [142]. **Fig. 1.14** shows the structure of SEM. The following are the main SEM components:

- Electron generator
- Electrons travel down a column using electromagnetic lenses.
- Electron detector
- Sample chamber
- Computer and display to view the images

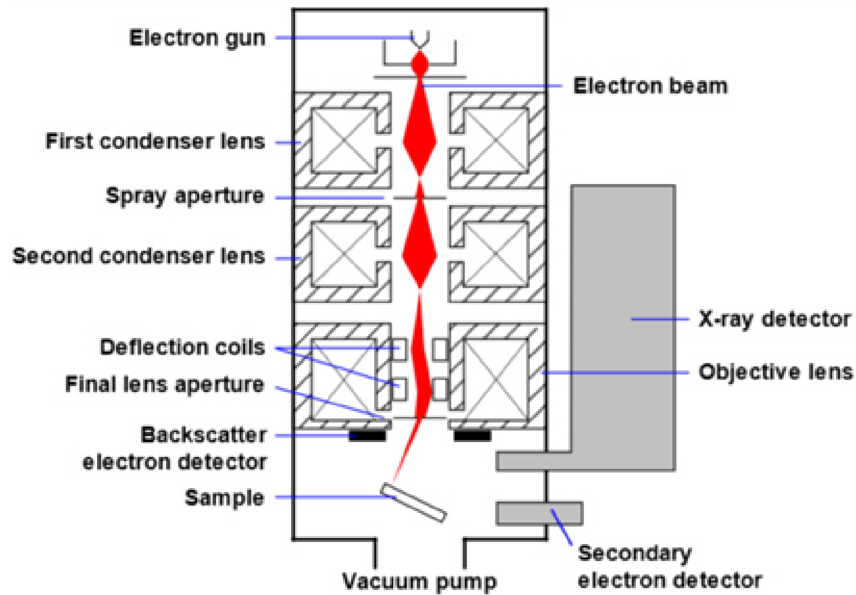

Fig. 1.14 Structure of Scanning Electron Microscopy; Reproduced from Ref. [142]

1.6.3 Atomic Force Microscopy (AFM):

AFM is a very high-resolution scanning probe microscopy on the order of fractions of nanometers, 1000 times better than the optical diffraction limit. AFM is used to produce images with atomic resolutions of 10^{-10} m, or one-tenth of a nanometer used in the field of polymers to investigate the surface properties of a polymer sample. AFM system includes various components such as a micro-cantilever with a probe, a motion detection device, a feedback loop for monitoring micro-cantilever motion, a piezoelectric ceramic scanning device for sample scanning, and a computer-controlled image acquisition, display, and processing system. AFM detects very weak interatomic interactions between the sample surface and the probe tip to study the surface structure and properties of the sample. The principle of AFM operation is to fix one end of a micro cantilever, which is extremely sensitive to the weak force, while the other end of the cantilever is situated in the probe which is close to the sample [143]. Once this is accomplished, a very weak force exists between the probe's tip atom and the atoms of the sample surface, which can be either repulsive or attractive. The magnitude of this force alters the deformation or motion state of the micro cantilever. Sensors detect these changes and obtain force distribution information when the sample is scanned, allowing the user to obtain surface structure information with nanometer resolution. **Fig. 1.15** shows the working principal of AFM schematically and **Fig. 1.16** shows the three basic working modes of AFM. The AFM scanner can move in three directions: X, Y, and Z. While the X and Y directions vary depending on the scanner; the vertical Z

direction is typically limited to a few microns. Simultaneously, the morphology of the scanning area sample can be obtained by reconstructing the position of the piezoelectric ceramic scanning tube in the Z and X-Y planes. AFM's force-distance curve reflects the quantitative force between the tip and the sample. AFM can measure the nano-indentation of micro-regions using corresponding probes equipped with dedicated software, and force-displacement curves drawn on this basis [144] which can be used for the quantitative measurement of a material's elastic modulus, adhesion, and stiffness. During the test, each force curve is saved for later quantitative analysis [145].

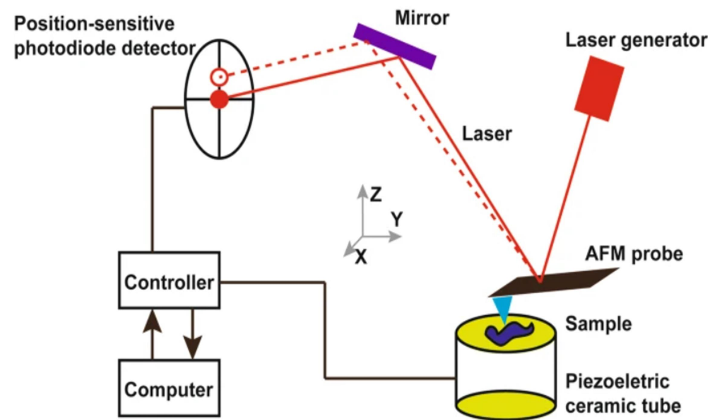

Fig. 1.15 AFM working principles are depicted schematically. The AFM probe is a micro-cantilever with a sharp tip at one end. The tip's monomolecular point enables nanometer resolution imaging, and the micro-cantilever is a force sensor capable of detecting even minute deformation of a sample, enabling very high sensitivity AFM in force measurements; Reproduced from Ref. [145]

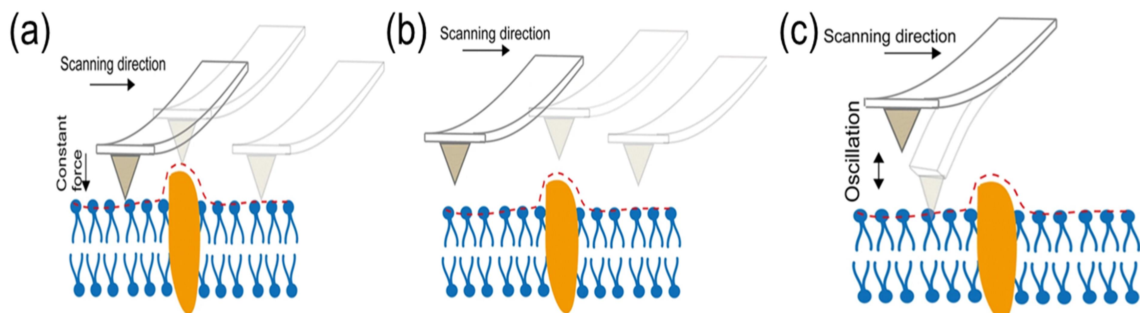

Fig. 1.16 Three basic working modes of AFM **(a)** In contact mode the probe is always slightly in contact with the sample and scanned in a constant force mode. (**b)** In the non-contact mode, the tip of the needle always vibrates on the surface of the sample, but it is never in contact with the sample. The scanning detector detects long-range forces such as van der Waals force or electrostatic forces that do not damage the imaged sample. **(c)** In the tapping mode, the microcantilever is subjected to stress vibration near its resonant frequency, and the oscillating needle tip gently strikes the surface of the sample, intermittently making contact with it; Reproduced from Ref. [145].

1.6.4 X-ray Diffraction (XRD):

XRD is a technique used in materials science to determine the crystallographic structure of the material, atomic spacing, and phase identification. It also provides information on the difference between the actual structures and the ideal structure due to internal stresses and defects. XRD analysis provides the identification of materials based on their diffraction pattern. The working principle of XRD is based on the interaction of the monochromatic X-rays with a crystalline sample and to produce a constructive interference if the condition of Bragg's Law is satisfied ($n\lambda = 2d \sin\theta$) [146]. These monochromatic X-rays have been generated from a cathode ray tube and filtered to monochromatic radiation which is collimated before being directed towards the sample. **Fig. 1.17** shows the principle of Bragg's Law.

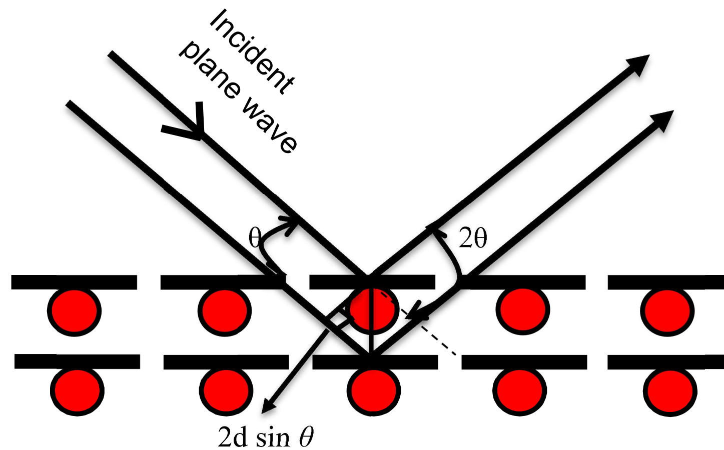

Fig. 1.17 Bragg's Law

X-ray diffractometers are made up of three basic components: an X-ray tube, a sample holder, and an X-ray detector. The intensity of the reflected X-rays is measured as the sample and detectors are rotated. This X-ray signal is recorded and processed by a detector and then produces a device output as a count rate. An X-ray diffractometer's geometry is such that the sample rotates at an angle θ in the path of the collimated X-ray beam, while the X-ray detector is mounted on an arm to collect the diffracted X-rays and rotates at an angle of 2θ. A goniometer is an instrument used to maintain the angle and rotate the sample. For typical powder patterns, data is collected at 2θ angles ranging from 5° to 70°, which are predefined in the X-ray scan [147].

1.6.5 UV-Vis Spectroscopy:

UV-Vis Spectroscopy is the measurement of electromagnetic radiation absorbed or emitted when molecules, atoms, or ions in a sample change energy state. It is a type of absorption spectroscopy in which incident light has been absorbed by molecules in the ultra-violet-visible region (200-800 nm) where electrons are excited from the ground state to a higher energy state [148]. The principle of absorption has been followed by Beer's Law. When light has been absorbed by matter, the energy consists of the atoms or molecules with electrons or non-bonding electrons that have been increased and excite these electrons to higher anti-bonding molecular orbitals. The longer the wavelength of light that electrons can absorb, the more easily they can be excited. There are four types of transitions (π–π*, n–π*, σ–σ*, and n–σ*) which can be ordered as follows: σ–σ* > n–σ* > π–π*> n–π* [148]. The absorption of ultraviolet light by a chemical compound produces a distinct spectrum that helps in the identification of the compound and provides information about the concentration of the sample. UV-Vis spectroscopy is an analytical technique that compares the number of discrete wavelengths of UV or visible light absorbed by or transmitted through a sample to a reference or blank sample. UV spectrometer includes a light source, excitation monochromator, sample and reference cells, detector, amplifier, and recording devices [149]. **Fig. 1.18** shows the block diagram of UV-Vis spectroscopy.

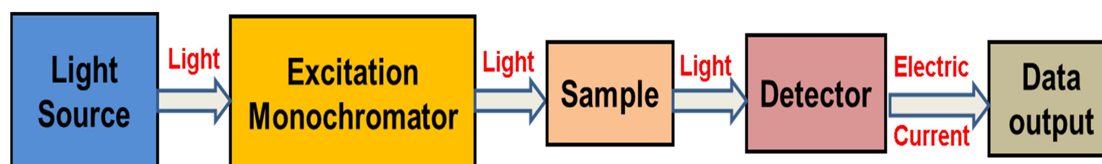

Fig. 1.18 Block diagram of UV-Vis Spectroscopy includes a light source, monochromator, sample and reference cells, detector, and data output.

1.6.6 Photoluminescence (PL) Spectroscopy

Photoluminescence spectroscopy is a nondestructive, contactless process of analyzing the electronic structure of materials. In this process, when photo-excitation light is incident onto a sample, it dissipates excess energy by emitting light which is known as photoluminescence. Electrons within a material move into permissible excited states as a result of photo-excitation. These excited electrons back to their stable state (ground state) by dissipating the extra energy in the form of light through a radiative process or non-radiative process. The portion of the radiative process decides the quantity of light emitted [150, 151].

A spectrofluorometer is an analytical device that records and measures the fluorescence of a sample, where the excitation, emission, or both wavelengths were scanned. The block diagram of a fluorescence spectrometer is shown in **Fig. 1.19**. Fluorescence spectrometers use monochromators, laser sources, amplifiers, detectors, and corrected spectrums [152]. The structural diagram of photoluminescence spectroscopy is shown in **Fig. 1.20**.

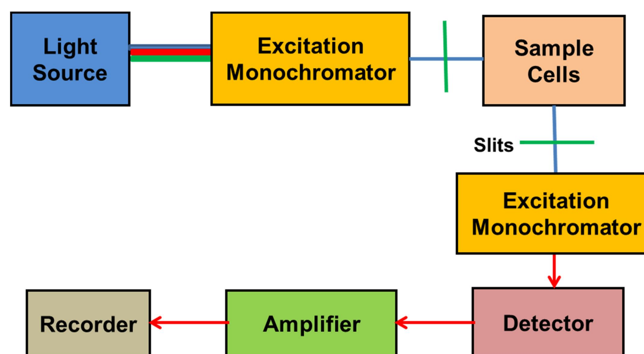

Fig. 1.19 Figure depicts the block diagram of photoluminescence spectroscopy. One monochromator selects an excitation wavelength, and the luminescence is observed through a second monochromator which is set at 90° positioned to the incident light.

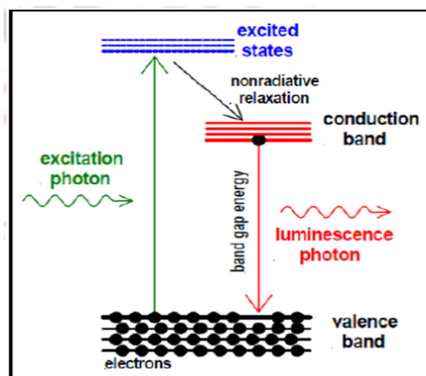

Fig. 1.20 Structural diagram of photoluminescence spectroscopy (PL); Reproduced from Ref. [152]

1.6.7 Raman Spectroscopy

Raman spectroscopy is a vibrational technique that yields detailed information about molecular vibrations, chemical structure, phase and polymorph, crystallinity, and molecular interactions. This technique uses a laser light source to irradiate a sample and generate a RAMAN scattered light which is detected using a CCD camera as a Raman spectrum. Raman spectroscopy was first discovered by Indian physicist 'Chandrasekhara Venkata Raman' in 1928 which is formed on the Raman Effect. The Raman effect is based on light scattering, which includes elastic (Rayleigh) scattering at the same wavelength and inelastic (Raman)

scattering at different wavelengths caused by molecular vibrations [153]. Raman spectra are obtained by exciting a sample with a high-intensity laser beam and the resulting scattered light passes through a spectrometer [153]. **Fig. 1.21** shows the schematic diagram of the Raman spectrometer setup.

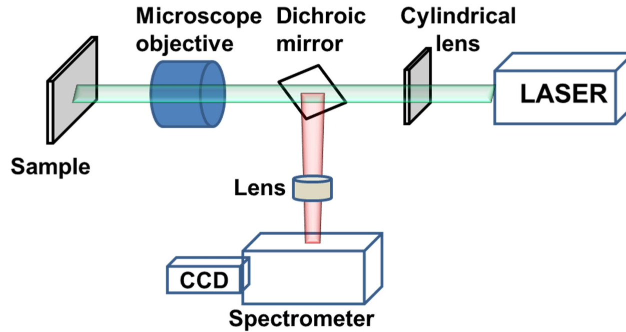

Fig. 1.21 Schematic diagram of a Raman spectrometer

The Raman shift is the difference in energy between an incident and scattered light. Stokes-Raman scattering refers to the shift at wavelengths greater than those of the incident light whereas anti-Stokes-Raman scattering refers to the shift at wavelengths shorter than those of the incident light. Stokes scattering is observed at lower wavenumbers (longer wavelengths) and anti-Stokes scattering at higher wavenumbers (shorter wavelengths) [154]. The energy diagram of Raman spectra with all the states has been shown in **Fig. 1.22**.

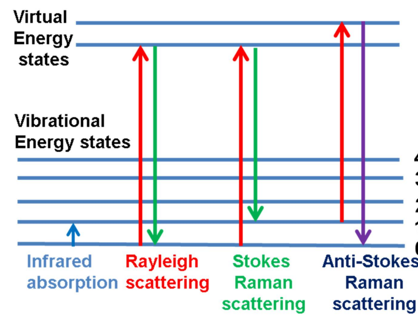

Fig. 1.22 Energy-level diagram with all the states involved in Raman spectra

1.7 Basics of Photodetectors

Photodetectors are electronic devices that convert the optical energy of light to an electrical signal which is used for the detection of light [155-158]. The photodetection capability depends on the semiconductor material and type of device structure used for the photodetector [159]. There are different types of photodetectors structures such as photoconductor [160, 161], p-n junction diode [162, 163], Schottky photodiode [164], MSM photodiode [165], and phototransistor [166] as shown in **Fig. 1.23** have been reported by various researchers briefly discussed as follows.

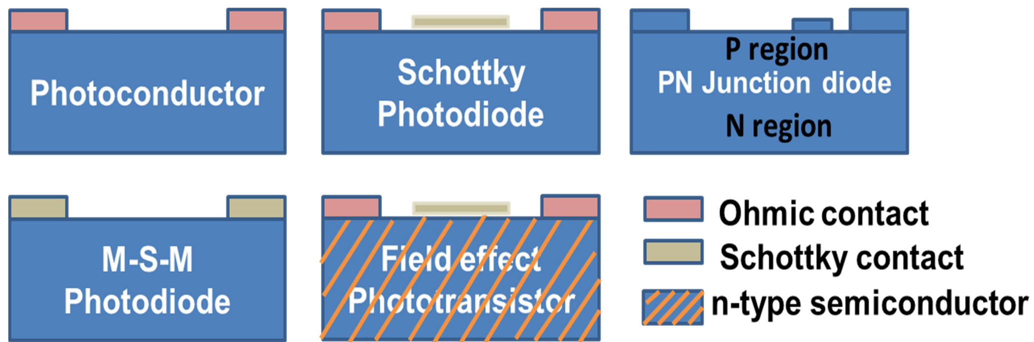

Fig. 1.23 Schematic structure of different semiconductor-based photodetectors

1.7.1 Photo conductor

Photoconductors are two terminal-based photodetectors that can create photo-excited electron-hole pairs to change the conductivity of a semiconductor owing to the absorption of electromagnetic radiation [160, 161]. When the photons of energy are larger than the band gap energy of the active semiconductor, electrons are excited from the valence band to the conduction band thereby creating holes in the valence band and free electrons in the conduction band due to the photoelectric effect. The photogenerated electron-hole pairs increase the conductivity and reduce the resistance of the active semiconductor material. As a result, the current flowing through the semiconductor bar increases with incident photon flux density for any fixed bias voltage applied between the two Ohmic electrodes as shown in **Fig. 1.24**.

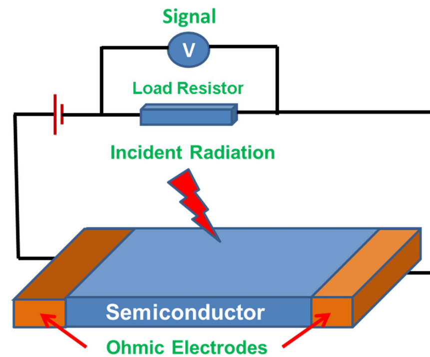

Fig. 1.24 Photoconductor working principle under UV illumination

1.7.2 Photodiode

Photodiodes are two terminal devices that consume light energy to produce an electric current. There are four different types of Photodiodes present 1) p-n photodiodes 2) PIN photodiodes 3) Schottky-type photodiodes 4) Avalanche photodiodes. Mainly we will discuss the p-n junction diode and Schottky photodiode.

1.7.2.1 p-n junction

A p-n junction photodiode is an interface between the p-type and the n-type materials inside a semiconductor [162, 163] as shown in **Fig. 1.25**. It is a bipolar device having two types of charge carriers i.e. electrons and holes. The p-n junction is created by the doping method in a semiconductor. The positive side of the semiconductor has an excess of holes, and the negative side has an excess of electrons. It is a two-terminal semiconductor device that allows current flow in one direction at forward-biased conditions. In reverse-biased conditions, it blocks the electric current flow.

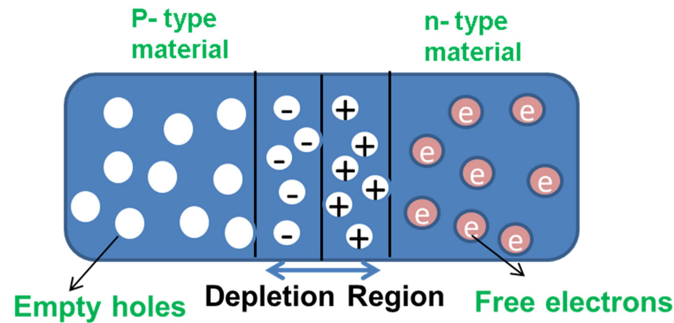

Fig. 1.25 Schematic structure of p-n junction diode at the unbiased condition

The processes that follow after forming a p-n junction are of two types - diffusion and drift [167]. There is a difference in the concentration of holes and electrons at the two sides of a junction. The holes from the p-side diffuse to the n-side, and the electrons from the n-side diffuse to the p-side. These give rise to a diffusion current across the junction.

The formula used in the p-n junction depends upon the built-in potential difference created by the electric field is given as:

$$E_0 = V_T ln[\frac{N_D N_A}{n_i^2}] \quad \textbf{(1.6)}$$

Where, E_0, V_T is the zero bias junction voltage, thermal voltage of 26 mV at room temperature, N_D and N_A are the impurity concentrations and n_i is the intrinsic concentration.

For the p^+n junction, the depletion width (w) formed under a reverse bias voltage of V_R,

$$W = \sqrt{\frac{2\varepsilon\,(V_{bi}+V_R)}{qN_d}} \quad \textbf{(1.7)}$$

Where, ε, q, N_d represent the effective dielectric constant, electronic charge, donor concentration, and V_{bi} is the built-in potential developed across the depletion region at the thermal equilibrium of the junction.

1.7.2.2 Schottky junction

The Schottky diode is a metal-semiconductor junction diode that has less forward voltage drop (0.2 - 0.3 eV) than the p-n junction diode [168-170]. It is also known as a hot-carrier diode. It is a unipolar device and the conduction of current occurs due to the movement of electrons only [171]. It has low junction capacitance, fast reverse recovery time, high current density and high efficiency, and less unwanted noise and it can be used in high-speed switching applications [172]. **Fig. 1.26** shows the symbol of the Schottky diode and the schematic diagram of the Schottky junction.

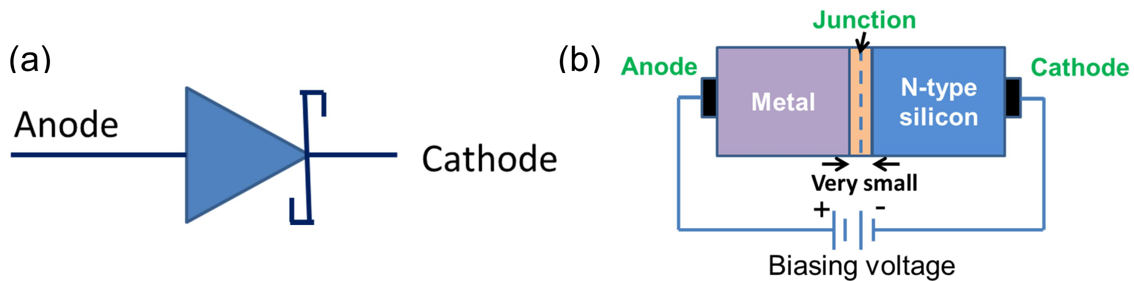

Fig. 1.26 (a) Symbol of Schottky diode, (b) Schematic diagram of Schottky junction

1.7.3 MSM photodiode

A metal-semiconductor-metal (MSM) photodiode is a photodetector device that consists of two Schottky contacts, i.e., two metallic electrodes on a semiconductor material as shown in **Fig. 1.27** [173, 174]. Thus, it is a kind of Schottky barrier detector with two Schottky junctions [165]. When light falls on the semiconductor between the two electrodes, it generates charge carriers (electrons and holes), which are collected by the electric field and thus it can produce a photocurrent. MSM photodetectors have high detection bandwidth (hundreds of gigahertz) and are faster than other photodiodes which makes them suitable for high-speed optical fiber communications.

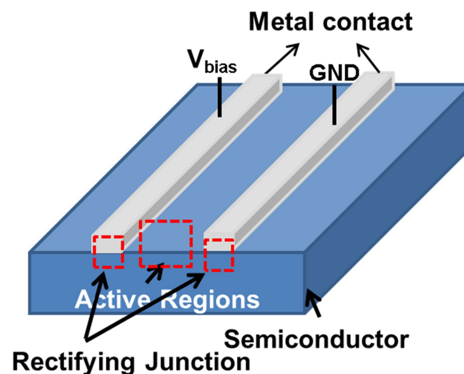

Fig. 1.27 Schematic diagram of an MSM photodiode

1.8 Performance Parameters of Photodetector

1.8.1 Responsivity

Responsivity (R) is defined as the ratio of the generated photocurrent (I- I_0) per effective area (A) to the incident optical power density of the device at a given wavelength of incident light and is expressed by A/W. The R is expressed as [175, 176]

$$R = \frac{\text{Change in Current/Effective Area of Device}}{\text{incident Power Density of the Device}} = \frac{I_{ph}/_{A}}{P_{opt}} \quad \textbf{(1.8)}$$

1.8.2 Detectivity

The detectivity (D^*) of the device has been calculated to measure the performance of the device due to the major contribution from shot noise and it is linearly proportional to the 'R' of the device [177]. It is also defined as the inverse of the noise-equivalent power (NEP). The greater the detectivity of a photodetector, the better it can detect the weak signals that compete with detector noise.

The D^* of the proposed device is calculated using the following equation [175, 176]

$$D^* = \frac{R}{\sqrt{2 \times e^- \times J_d}} \quad \textbf{(1.9)}$$

Where R is responsivity, e^- is the charge of an electron, and J_d is the dark current density.

1.8.3 External Quantum Efficiency (EQE)

The EQE is defined as the ratio of the number of charge carriers collected at the external terminal to the number of photons of an incident wavelength on the device which is expressed as [175, 178]

$$EQE\ \% = \frac{1240 \times R}{\lambda(nm)} \times 100 \quad (\mathbf{1.10})$$

Where R is responsivity and λ is the incident wavelength in nm.

1.8.4 Rise time and fall time

The most crucial figures of merit of switching devices are the rise time and fall time. The response time of the photodetector has been measured by the rise time (τ_r) and fall time (τ_d) using a pulsed light of a particular wavelength with an equal ON-OFF time [179].

Rise time is defined as the time required for the pulse to rise from 10% to 90% of its final value and fall time is defined as the time required for the pulse to drop from 90% to 10% of the final value.

1.9 Current-Voltage (I-V) characteristics

A current-voltage (I-V) characteristic is a relationship between the electric current through a device or circuit and the corresponding voltage across it. The selection of components for voltage-current characteristics allows us to set the voltages and currents in a circuit so that the circuit performs the desired function. **Fig. 1.28** shows the I-V characteristics of a semiconductor diode.

The current-voltage characteristic of a diode is described by the diode equation [180, 181],

$$\mathbf{I = I_S\,(exp\,(\frac{qV}{\eta kT})-1)} \qquad \textbf{(1.11)}$$

Where I_S is the saturation current, q is the elementary charge, V is the applied voltage, η is the ideality factor, k is Boltzmann constant and T is room temperature.

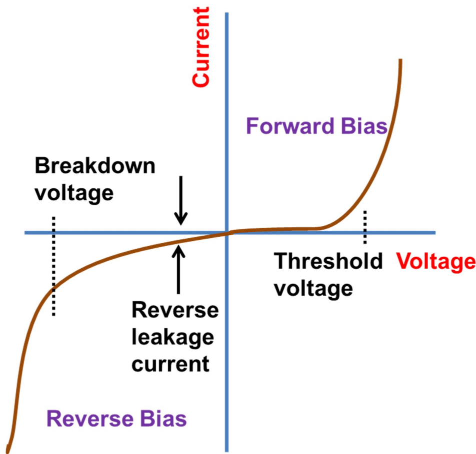

Fig. 1.28 The I-V characteristics of a semiconductor diode.

In our work, the room temperature current (I)-Voltage (V) characteristics of the devices have been measured by the semiconductor parameter analyzer (Agilent B1500A) in a particular voltage range. From I-V characteristics, we can measure the ideality factor, rectification ratio, and Barrier height of the as-fabricated heterojunction diodes. The rectification ratio is the ratio of the forward current and reverse current (I_F/I_R) at the same bias voltage.

The ideality factor and the barrier height can be expressed by following formulas:

$$\text{Ideality factor, } \eta = \frac{q}{kT}\left[\frac{x_2-x_1}{y_2-y_1}\right] \qquad \textbf{(1.12)}$$

$$\text{Barrier height, } \phi_B = \frac{KT}{q}\ln\left[\frac{A^*T^2}{J_S}\right] \qquad \textbf{(1.13)}$$

Where, T=300 k, KT/q= 0.026, $A^*$is the Richardson's constant and J_S is the current density.

1.10 Density Functional theory (DFT)

In Quantum-mechanics, the quantum mechanical wave function contains all the information about a given system. For the case of a simple 2D material or even a hydrogen atom, we can solve the Schrödinger equation exactly in order to get the wave function of the system. We can then determine the allowed energy states of the system [182, 183].

$$H (r_1, r_2, \ldots, R_1, R_2, \ldots) = E (r_1, r_2, \ldots , R_1, R_2, \ldots), \quad \textbf{(1.14)}$$

Where $(r_1, r_2, \ldots R_1, R_2 \ldots)$ is a wavefunction, which corresponds to the positions of electrons, r_i, and the nuclei R_I.

Unfortunately, it is impossible to solve the Schrödinger equation for an N-body system. Evidently, we must involve some approximations to reduce the complications of the above problem. Here, we have our simplest method called **Density functional theory (DFT)** which is a method of obtaining an approximate solution to the Schrödinger equation of a many-body system [184, 185]. The foundation of DFT is based on the fact that the properties of interacting many electrons system can be described by a **functional of the electron density** which is a function of space and time [186]. The electron density is used as a main fundamental property in DFT [48]. DFT allows all properties to determine by the electron density n (r), a function of just three variables r = (x, y, z). DFT was first theoretically proposed by **Walter Kohn and Pierre Hohenberg** in 1964, which states that the Ground state energy, E of a many-electron system is a unique functional of the electron density which is very useful for DFT calculations [187]. Later, **Kohm and Sham** in 1965 stated that the electron density that minimizes the energy of the overall functional is the true ground state electron density [187]**.**

There are two most important fundamental theorems of DFT such as the Hohenberg-Kohn theorem (1964) and the Kohn-Sham theorem (1965) which clearly state the relation of total energy with electron density.

Theorem-1: The Hohenberg-Kohn theorem states that "the ground state of any interacting many-particle systems with a given fixed interparticle interaction is a unique functional of the electron density n(r)" [188]. It asserts that the density of any system determines all ground-state properties of the system. In this case, the total ground state energy of a many-electron system is a functional of the density. i.e.,

$$\mathbf{E = E\,[n(r)].}$$

Theorem-2: Kohn-Sham theory the introduction of the non-interacting kinetic energy functional T_s into the energy expression leads, upon functional differentiation, to a collection

of one-particle equations whose solutions are the Kohn-Sham orbitals [50]. It states that "The electron density that minimizes the energy of the overall functional is the true ground state electron density" i.e.,

$$\mathbf{E\ [n(r)] > E_0\ [n_0(r)]}$$

DFT is a powerful tool to theoretically simulate the physical and optical properties of 2D materials [40, 187, 189]. All theoretical calculations will be performed by using the Quantum-ATK package [190] based on DFT within the Projector-Augmented Wave (PAW) framework. The exchange-correlation energy will be treated by the **Local density approximations (LDA) or General gradient approximation (GGA) method.** The exchange-correlation functionals were described within GGA in the Perdew-Burke-Ernzerhof (PBE) form [191, 192]. The PBE functionals underestimate the bandgap calculations, therefore hybrid -DFT functionals are used to correct the error. All structures are fully optimized until the force on each atom is less than 0.01 eV/Å, the maximum displacement of 0.001 eV/$Å^3$, with a tolerance limit of 10^{-5} and a maximum of 100 steps, using the Pulay mixer algorithm for the iteration control parameter.

1.10.1 Local Density Approximations (LDA):

LDA is a class of approximations to the exchange-correlation (XC) energy functional in DFT that depend solely upon the value of electronic density at each point in space. It is defined by the following equation [193]:

$$E_{xc}^{LDA}\ [\rho] = \int \rho\ (r)\ E_{xc}^{HEG}[\rho\ (r)] \qquad \mathbf{(1.15)}$$

Where ρ (r) is the electron density and E_{xc}^{HEG} is the exchange-correlation energy per particle of a uniform system of density ρ (r).

1.10.2 General Gradient Approximation (GGA):

GGA denotes a variety of ways proposed for functions that modify the behaviour at large gradients in such a way as to preserve desired properties. It can be defined as [193]

$$E_{xc}^{GGA}\ [\rho] = \int \rho\ (r)\ E_{xc}^{HEG}\ [\rho\ (r), \Delta\ \rho\ (r)] \qquad \mathbf{(1.16)}$$

Where Δ ρ (r) is the gradient of the charge density,

Chapter 2

LITERATURE REVIEW & ORGANIZATION OF THE THESIS

2.1 Literature review

2.1.1 Substitutional doping of 2D materials

The 2D-TMDCs are promising materials for future electronic device applications [5, 156, 187]. In previous work, Ataca *et. al.* [194] performed an extensive stability analysis of 88 monolayer TMDCs and TMOs using DFT in the local density approximation (LDA) and identified 52 stable compounds including both metals and semiconductors. Doping in 2D materials is very attractive and challenging work nowadays. Doping can be of various types such as substitutional doping [54, 195, 196], adsorption doping [50, 51, 53, 60] and charge transfer doping [57, 58]. However, the lack of a suitable doping technique is a major obstacle to its practical use as a channel material in field effect transistors (FET). Conventional substitutional doping is considered one of the best techniques as it provides long-term stability without degrading performance and controllability of doping level [53, 62, 70]. Transition metals (TM) are a popular choice of substitutional dopants in TMDCs materials [62, 72, 195, 197-199]. Several works reported the direct substitution of TM metal at the W atomic site of the WSe_2 monolayer [72, 198, 200, 201]. In 2013, Dolui *et. al*. [53] reported the possible doping strategies for MoS_2 monolayers which concluded that molecule adsorption can lead to both *n*- and *p*-type conductivity, depending on the charge polarity of the adsorbed species. Pandey *et. al*. [62] reported p-type substitutional doping in large-area monolayer WSe_2 crystals grown by chemical vapor deposition using acceptor Niobium (Nb) TM metal. Zhao *et al*. [72] reported electronic and magnetic properties on 3d TM-doped WSe_2 using first-principle calculations. Recently, Mabelet *et al.* [195] also reported a WSe_2 monolayer doped with pnictogens, halogens, and TM atoms. Based on the literature review, it is observed that there is enough scope to study in doping of various 2D TMDCs materials, which have unique properties and potential applications in nanoelectronics. Although studies are available on doping of WSe_2 using specific TM dopants. A systematic theoretical study

on substitutional doping of 3d, 4d, and 5d group TM dopants has not been reported yet, particularly for FET applications. Therefore **in Chapter 3**, we have studied the electronic properties of the WSe_2 monolayer by doping various TM (3d, 4d, 5d group) metals. We have studied the changes in electronic band structures, density of states, E_{form} and charge density of TM doped WSe_2 monolayer.

2.1.2 Strain engineering of 2D materials

Strain engineering of 2D monolayers has been intensively studied towards modulating their electrical, optical, and magnetic properties [97, 98, 100, 103, 104, 107]. Conventional three-dimensional (3D) semiconductors are quite brittle and typically break under strains larger than ~1.5 % due to defects and dislocations. However, the 2Ds monolayer can resist mechanical deformations up to ~10 % before rupture [202-205]. Due to applying strain, the original state of atomic bonding changes by stretching or shortening the distance of chemical bonds [107]. It is expected that external mechanical strain that deforms the host lattice may reduce the dopant-induced internal strain, further increasing dopant solubility [69, 106, 206]. As a result, the electronic structure of the material is reformed, and a series of new properties emerge [36, 100, 108, 207]. The strain-tuning of electronic structure and optical properties of pristine WSe_2 monolayers is well studied in the literature [208-210]. However, studies on the strain-tuning of electrical and optical properties of Nb, Ta, and Re-doped WSe_2 monolayer are not reported yet. We believe that knowledge of these properties is very crucial for their further use in emerging device applications. Graphene-like ZnO (g-ZnO) is a 2D monolayer having excellent electronic and optical properties, with high mechanical stability [211-213]. Aluminium (Al) is considered one of the most efficient dopants used to produce conducting ZnO thin films; in the g-ZnO monolayer, the substitution of the Al atom at the Zn site is energetically favorable [214]. Ma *et. al*. [212] reported CO catalytic oxidation on Al-doped graphene-like ZnO (g-AZO) monolayer sheets. Wu *et. al.* [215] reported the Al doping concentration-dependent optical properties of the g-AZO monolayer. Zhu *et. al*. [216] demonstrated enhanced p-type doping in Li-doped ZnO using external strain. Zhang *et. al.* [217] demonstrated experimentally that the high concentration of Al dopants (> 20 %) shows excellent visible absorption which leads to high photocatalytic activity of AZO monolayer. However, synthesis of ZnO with high Al doping concentration is difficult due to the high dopant E_{form} of the Al atom in ZnO and the reduction of E_{form} is a challenging task. The E_{form} is a critical parameter that primarily influences the doping concentration; thus, it is very important to understand how to control that in 2D materials. Control and enhancement of

doping concentration in 2D semiconductors is a critical issue. Therefore, **in Chapter 4**, we have studied the strain-dependent doping, electronic structure and optical properties of transition metal-doped 2D semiconductors. We theoretically determine the variation of bandgap with biaxial strain and optical properties of Nb, Ta, and Re-doped WSe_2 monolayer under biaxial strain varying from -5% to +5%. We determine the rate of bandgap tunability for K-K and, Γ–K transition, corresponding to A and I peak in PL and absorption spectroscopy. We also explore the possibility of enhancing doping concentration by application of mechanical strain in TM-doped WSe_2 monolayer using DFT calculations. The variation of E_{form} with biaxial strain varying from −5% to +5% is studied in detail. Further, we investigated biaxial strain varying from -10% to +10 % on the E_{form}, electronic structure, and optical absorption of the g-AZO monolayer.

2.1.3 2D heterostructures

In recent years, the 2D heterostructures are highly explored by the device community due to their atomically thin nature, large surface area, and various degrees of freedom [218-220]. The electronic, transport, and optical properties of 2D heterostructures with different stacking modes have been carried out using the DFT [47, 85]. Heterostructures of 2D materials are divided mainly into vertical and lateral heterostructures, among which vertical stacking of 2D vdW heterostructures attracts more consideration [221-224]. The application of 2D heterostructure mainly depends upon atomic commensurability, interlayer interaction, charge transfer, and band alignment between constituent 2D materials when heterostructure is formed [225-227]. Many technologies can effectively improve the electronic and photoelectric performance of heterostructures devices, such as doping of inverse layer, electrostatic self-assembled layer-by-layer technology, surface modification, and various external perturbation methods [228-232]. Kim *et. al.* [233] demonstrated that vertical heterostructures built from WS_2/MoS_2 and MoS_2/WS_2 hetero-bilayers are promising for high-efficiency ultrathin photovoltaic devices. In 2013, Kosmider *et. al*. [84] reported the electronic properties of the MoS_2/WS_2 heterojunction with the lowest energy electron and highest energy hole states in the optically active *K* point are localized on different monolayers and the Mo-W bilayer forms a type II heterostructure. Yin *et. al*. [110] reported a $PtS_2/MoTe_2$ heterostructure with adjustable electronic and optical properties using strain and electric field. Similarly, Wang *et al*. [172] explored tunable electronic properties of $MoTe_2/XS_2$ (X = Hf, Sn, Zr), and Bai *et al*. [234] reported C_2N/GaTe heterostructure for photocatalytic water splitting for hydrogen production applications. Li *et. al.* [47] reported GaTe/MoS_2

heterostructure by modulating electronic and optical properties using strain for nanoelectronics and optoelectronic devices applications. However, so far no work is reported on the modulation of electronic structure and optical properties of GaTe/$MoTe_2$ vdW heterostructures under various external perturbations such as external biaxial strain and electric field. Therefore, **in Chapter 5**, we have studied the modulation of electronic band Structure and optical properties of GaTe/$MoTe_2$ heterostructure under different strain and electric fields for optoelectronic applications.

2.1.4 Mixed dimensional (MD) heterostructures-based photodetectors

Apart from atomistic simulations, several experimental results were also reported for various 2D materials-based heterostructures which always pose a significant influence in research fields for device applications [235-240]. After the first introduction of MD heterostructures by Jariwala *et al*. [241], many works reported on MD heterostructures-based photodetectors [235, 236, 242-245]. In 2016, Xu *et. al*. [246] reported a monolayer MoS_2/GaAs heterostructure self-driven photodetector with extremely high responsivity and detectivity. In 2016, Mukherjee *et. al*. [247] demonstrate n-MoS_2/p-Si 0D/3D heterojunctions which exhibited excellent rectification behaviour for multifunctional optoelectronic devices. In 2017, Huo *et. al*. [248] reported an ultrasensitive 2D photodetector employing an in-plane phototransistor with an out-of-plane vertical MoS_2 p–n junction as a sensitizing scheme. The hybrid detector yields an R of 7×10^4 AW^{-1} and a record measured D* of 3.5×10^{14} Jones with a time response on the order of 10 ms demonstrating the highest sensitivity of a 2D-based photodetector. In the same year, Dhyani *et. al.* [249] has been reported a high-performance broadband photodetector based on MoS_2/porous silicon heterojunction with high responsivity and detectivity of 9 A/W (550–850 nm) and $\sim 10^{14}$ Jones, respectively. Pataniya *et. al*. [239] demonstrated flexible 2D-WSe_2 NSs/Graphite MD heterostructures-based photodetector for optoelectronic devices applications. Selamneni *et. al*. [240] demonstrates 0D–2D n-WS_2-QDs/p-SnS hybrid heterostructures for highly responsive flexible broadband photodetectors. However, so far, no experimental reports are available on multilayer MD heterostructures-based photodetectors. **In chapter 6**, we have synthesized and characterized the WSe_2 nanosheets and WS_2 quantum dots and fabricated the p.WSe_2 NS/n.WS_2 QDs/p.Si (2D-0D-3D) multilayer MD heterostructures-based high-performance broadband photodetector.

2.2 Motivation

The main motivation of this thesis is to perform atomistic simulation, synthesis, and characterization of 2D materials for various electronic and optoelectronic devices applications.

2D Materials are layered crystalline materials consisting of a single layer of atoms with a thickness of a few nanometers or less. DFT is a powerful tool to theoretically simulate the structural, optical, and electronic properties of 2D materials [183]. DFT calculations will be performed using the projector-augmented wave method. The crystal structure is optimized using the Quasi-Newton method [250]. The exchange-correlation energy is treated by Local density approximations (LDA) or General gradient approximation (GGA) method depending upon the material system [182]. The vdWs interactions are adopted by the semi-empirical DFT-D2 dispersion-correction approach.

Now a day, doping in 2D materials has gained tremendous research interest in optoelectronics applications [196, 251, 252]. However, the lack of a suitable doping technique is a major obstacle to its practical use as a channel material in field effect transistors (FETs). Conventional substitutional doping is considered one of the best techniques as it provides long-term stability without degrading performance [53, 62, 70]. TM is a popular choice of substitutional dopants in TMDCs materials [62, 72, 195, 197-200]. The atomic substitution of TM at metal-site in 2D monolayers is well studied using first-principal calculations [63, 253, 254] as well as via experimental synthesis [62, 255, 256]. WSe_2 monolayer is one of the most important TMDC materials with great potential due to its ambipolar behavior. WSe_2 has a direct optical bandgap of ~1.6 eV [257-259], and exciton binding energy of ~0.79 eV [28] with high photoluminescence yield and absorption coefficient [62, 260]. Therefore, in this work, we have systematically studied the electronic structure of 3d, 4d, and 5d TM-doped WSe_2 monolayers using DFT calculations. The TM dopants mainly include Niobium (Nb), Tantalum (Ta), Vanadium (V), and Rhenium (Re), which are popular choice for p and n-type doping.

Mechanical strain is an effective and practical way to tune the physical and optical properties of 2D materials, as they can sustain a mechanical strain of greater than ~10 % [96, 97, 202, 213, 261-263]. Strain engineering is abruptly used in the semiconductor industry for manufacturing various devices to improve efficiency and performance [264]. Now a day, bandgap engineering on 2D materials using biaxial strain gained promising research interest in optoelectronic fields [265]. In this work, we theoretically investigated the electronic

structure, bandgap tunability, and optical properties of Nb, Ta, and Re-doped WSe_2 monolayer by applying biaxial tensile and compressive strain. Strain can modulate the doping concentration of many semiconducting materials [55, 69, 216]. Control and enhancement of doping concentration in 2D semiconductors is a critical issue. The dopant E_{form} is a critical parameter that primarily influences the doping concentration; thus, it is very important to understand how to control that in 2D materials. Therefore, we investigate the strain-dependent behaviour of E_{form} for Nb, Ta, V, and Re doped-WSe_2 monolayer using DFT calculations. Further, Graphene-like ZnO (g-ZnO) is a 2D monolayer having excellent electronic and optical properties, with high mechanical stability [211-213]. Aluminium (Al) is considered one of the most efficient dopants used to produce conducting ZnO thin films; in the g-ZnO monolayer, the substitution of the Al atom at the Zn site is energetically favorable [214]. However, synthesis of ZnO with high Al doping concentration is difficult due to the high E_{form} of the Al atom in ZnO and the reduction of E_{form} is a challenging task. Therefore, we systematically studied the strain-dependent doping behaviour and optical absorption of the g-AZO monolayer under the application of ε_{xy} by using hybrid DFT calculations.

Now a day, vdWHs heterostructures fabricated by various 2D materials have gained attractive research interest [266, 267]. The tuning of electronic and optical properties of 2D heterostructures is very important to extend their applications in the next-generation nanoelectronic and optoelectronic devices [268, 269]. When the vdWHs have type II band arrangement then only electron-hole separation is possible which very important factor to establish the device designs. This is a vast area to explore new vdWHs heterostructure for multi-device purposes [87]. There are many vdWHs reported on the modulation of electronic properties by applying external strain and electric field [47, 85, 92, 111]. Therefore, we investigated the structural, electronic, and optical properties of a GaTe/$MoTe_2$-based vdW heterostructure under mechanical strain and external electric fields. The tunability of the band alignment and optical spectra of GaTe/$MoTe_2$ heterostructure are examined under ε_{xy} varying from -9% to +9%, and the E_{ext} between -1V/Å to +1V/Å using hybrid -DFT calculations.

The 2D-TMDC materials provide an excellent opportunity to design high-performance electronic devices for various applications in photonics, electronics, and optoelectronics [270-272]. Among all 2D materials, TMDC semiconductors have attracted significant attention because of their rich electronic and optical properties such as tunable optical band gap, strong light-matter interactions, high exciton binding energy, and large specific surface area due to reduced dimensionality [23]. Nowadays, heterostructures based on these 2D TMDCs

materials are at the forefront of current research due to their potential applications as a p–n junctions, FETs, tunneling transistors, solar cells, LEDs, photodetectors, sensors, and photovoltaic cells [122, 243, 273, 274]. The photodetectors with all broadband response, high photoconductive gain, high response speed, and high detectivity are hard challenges to realize using one photo-active material. Building photodetectors composed of two or more semiconductor materials of different band gaps was an efficient route to realize high-performance light detection due to the efficient charge separation at the interface, and fast charge transfer process because of high carrier mobility. Due to the absence of a dangling bond in 2D materials, it is possible to combine 2D semiconductors with materials of other dimensional (i.e. 0D, 1D, and 3D) to form MD-heterostructures. These MD heterostructures provide a distinctive platform for next-generation 2D electronics and optoelectronic fields. Photodetectors based on Mixed-dimensional heterostructures perform beyond existing technologies enable very high sensitivities for the broadband region, and achieve high photodetection gain [176, 275-277]. Therefore, we will fabricate a MD heterojunction-based photodetector device using different TMDC materials. In this work, we have taken WSe_2/WS_2 bilayers of different dimensionality on p-Si substrate to fabricate (2D-0D-3D) multilayer MD heterostructures for photodetection applications.

Based on the above literature review, I have been inspired to work on "**Atomistic Simulation, Synthesis, and Characterization of 2D materials for Optoelectronic Device applications**" as there is still a dearth of scope for work in this area.

2.3 Scope of the Thesis

The basic objectives of the present thesis are to perform atomistic simulation, synthesis, and characterization of the 2D materials and to explore their electronic and optoelectronic applications. The present thesis consists of seven chapters including four main working chapters. The contents of the seven chapters are given as follows:

Chapter 1 presents a brief introduction to the 2D materials family, various doping techniques such as substitutional doping, adsorption doping, and charge transfer doping, the role of external factors such as biaxial strain and external electric field on 2D materials, formation of heterostructures, synthesis and characterization methods for 2D materials and basics of photodetectors. The various performance parameters of photodetectors to characterize the overall performance of the devices are also briefly discussed. The fundamental concepts behind DFT calculations are discussed in detail.

Chapter 2 presents a brief literature survey on substitutional doping of 2D materials, strain engineering of 2D materials, 2D heterostructures, and MD heterostructures-based photodetectors has been discussed. Based on the observations from the literature survey, the motivation and the scope of the Thesis have been detailed and outlined at the end of this Chapter.

Chapter 3 reports a systematic study on the electronic structure of 3d (Sc, Ti, V, Cr), 4d (Y, Zr, Nb, Ru, Rh, Pd, and Ag), and 5d (Hf, Ta, Re, Ir, Au) group of TM-doped WSe_2 monolayer using DFT calculations. The TM dopants are substituted at the W-site of the WSe_2 monolayer. Here, we studied the changes in electronic band structures, the density of states (DoS), E_{form}, and charge transfer due to TM-dopants in the WSe_2 monolayer.

Chapter 4 reports the electronic structure and optical properties of Nb, Ta, and Re-doped WSe_2 monolayer under varying biaxial strain using DFT calculations. We determine the rate of bandgap tunability for K-K and, Γ–K transition, corresponding to A and I peak in PL and absorption spectroscopy. We also determined the critical tensile strain value at which crossover from direct to indirect bandgap takes place. We also explore the possibility of enhancing doping concentration by application of mechanical strain in Nb, Ta, V, and Re-doped WSe_2 monolayer using DFT calculations. The variation of E_{form} with biaxial strain varying from -5% to +5% is studied in detail. Moreover, in this chapter, we have studied the strain-dependent doping behavior and optical absorption of the Al-doped ZnO (AZO) monolayer under the application of biaxial tensile and compressive strain using hybrid DFT

calculations. We investigated the biaxial strain varying from -10% to +10 % on the E_{form}, electronic structure, and optical absorption of the g-AZO monolayer. This study opens various applications in electronic and optoelectronic fields.

Chapter 5 presents the modulation of electronic band Structure and optical properties of GaTe/$MoTe_2$ heterostructure under different strain and electric fields for optoelectronic applications. We have constructed four different heterostructure configurations of GaTe/$MoTe_2$, and find the most stable GaTe/$MoTe_2$ heterostructure by calculating minimum binding energy. Then we studied the effect of biaxial strain and external electric fields on the bandgap, band alignment type, and optical spectra of the GaTe/$MoTe_2$ heterostructure in detail. The biaxial strain ranges from -9% to +9%, and electric field values between ±1V/Å have been studied in detail by using DFT calculations. Our finding suggests that the GaTe/$MoTe_2$ vdWs heterostructure has attractive potential for various optoelectronics and photocatalytic device applications.

Chapter 6 reports the synthesis process of WSe_2 nanosheets (NSs) and WS_2 quantum dots (QDs) by using solvothermal and hydrothermal methods and then fabricated n-WS_2 QDs/p-Si (0D-3D) and p-WSe_2 NSs/n-WS_2 QDs/p-Si (2D-0D-3D) multi-layer mixed-dimensional (MD) heterostructures based broadband photodetectors by using silver (Ag) as top contacts. The morphological and structural characteristics of WSe_2 NSs and WS_2 QDs were measured by Transmission Electron Microscopy (TEM), Scanning Electron Microscopy (SEM), Atomic Force Microscopy (AFM), X-ray Diffraction (XRD), and Raman Spectroscopy. The optical characteristics were measured by UV-Visible Spectroscopy and Photoluminescence Spectroscopy (PL). Further, the current-voltage (I-V) under dark and light illumination conditions and photoresponse characteristics of the (0D-3D) n-WS_2 QDs/p-Si and (2D-0D-3D) p-WSe_2 NS/n-WS_2 QDs/p-Si heterostructures investigated in details. It is observed that the device has high photoresponse characteristics in broadband photodetection range from UV to near-IR (300 to 1100 nm).

Chapter 7 is devoted to summarizing the major findings of the research works presented in various chapters of the thesis. Finally, some future scopes of research in the related area of the thesis are outlined at the end of this Chapter.

Chapter 3

ELECTRONIC STRUCTURE OF 3d, 4d, AND 5d TRANSITION METAL (TM) - DOPED WSe_2 MONOLAYER

3.1 Introduction

The TMDCs materials provide an excellent opportunity to design high-performance electronic devices for various applications [270, 271]. Due to their unique fundamental properties, TMDCs materials emerge as a replacement for Silicon (Si) in next-generation devices technology [272, 278, 279]. However, precise control of the doping of TMDCs is a prerequisite for its practical use in nanoscale devices [65]. TMDCs materials like MoS_2, WS_2, WSe_2, $MoSe_2$, etc. have a tunable bandgap and are being investigated experimentally [62, 271, 272] and theoretically using DFT calculations [65, 70, 258, 280, 281]. WSe_2 monolayer is a potential candidate as a channel material for FETs [282, 283]. It has a direct optical bandgap of ~1.6 eV [257-259], and exciton binding energy of ~0.79 eV [28] with high photoluminescence yield and absorption coefficient [62, 260, 272]. It has been shown to exhibit both n-type [282] and p-type [283] conductivities with different metal contacts.

Conventional substitutional doping is considered one of the best techniques as it provides long-term stability without degrading performance [53, 62, 70]. TMs are a popular choice of substitutional dopants in TMDCs materials [62, 72, 195, 197-200]. Several works reported the direct substitution of TM metal at the W atomic site of the WSe_2 monolayer [72, 198, 200, 201]. Recently, Mabelet *et. al*. [195] also reported a WSe_2 monolayer doped with pnictogens, halogens, and TM atoms. Although studies are available on the doping of WSe_2 using specific TM dopants. A systematic theoretical study on substitutional doping of 3d, 4d, and 5d group TM dopants has not been reported yet, particularly for FET applications.

Our primary goal is to identify potential TM dopants that can induce p-type and n-type doping in the WSe_2 monolayer. Therefore, in this work, we are studying the effect of 3d, 4d, and 5d TM dopants on the electronic structure of the WSe_2 monolayer using DFT calculations. First, we relaxed the atomic structure of undoped and 3d, 4d, and 5d TM-doped WSe_2 monolayer. The energetics of TM doped WSe_2 monolayer has been determined by using E_{form} calculations. Next, the TM-doped WSe_2 monolayer with the 3d (Sc, Ti, V, Cr), 4d (Y, Zr, Nb, Ru, Rh, Pd, and Ag), and 5d (Hf, Ta, Re, Ir, Au) group of metals has been analyzed by the band structure and density of electronic state calculations. Due to the strain induced by the atomic radius difference between W atom and TM dopants, a significant change in lattice parameters and bond lengths has been observed. Among all TM dopants, the V, Nb, and Ta are useful p-type, and Re is only an effective n-type dopant for the WSe_2 monolayer.

3.2 Computation Methods

DFT calculations were performed with projected augmented wave (PAW) pseudopotentials using the Virtual Nano lab Quantum ATK Tool Kit [284]. The exchange-correlation functionals were described within generalized gradient approximation (GGA) in the Perdew-Burke-Ernzerhof (PBE) form [191]. We have used a plane-wave basis with an energy cut-off of 550 eV. The Brillouin-zone integrations were performed with Monkhorst-Pack k-points with a grid sampling of 9×9×1 [285]. Structures were fully relaxed to minimize the system's total energy until the force on each atom is less than 0.01 eV/Å using a limited memory Broyden–Fletcher–Goldfarb–Shannon (LBFGS) method. The iteration control parameters consisted of a Pulay mixer algorithm with a maximum of 100 steps with a tolerance limit of 10^{-5}. A 2×2×1 hexagonal supercell of monolayer WSe_2 was appropriate to study the effect of doping by substitutional atoms, supported by earlier reports [70, 198, 286]. A vacuum space of more than 12 Å is included perpendicular to the monolayer surface to eliminate the coupling between neighboring cells. In the band structure calculation, k-points with high symmetry directions (Γ-M- K- Γ) were used. Here, our goal is to find the suitable TM dopants that induced n or p-type doping in WSe_2 monolayer for FET applications. This study mainly analyzes the formation of acceptor and donor states in the bandgap and Fermi level shift due to TM dopants, which leads to the doping of a WSe_2 monolayer by electrons/ holes. Therefore, we have not taken spin polarization into account. It is noted that spin polarization is necessary to understand the magnetic properties of TM doped WSe_2.

3.3. Results and discussions

3.3.1. Electronic structure of WSe_2 monolayer

The 1H-WSe_2 monolayer crystallizes in the hexagonal lattice structure with $P6_3/mmc$ space group symmetry [287]. The W atom has bonded to six neighboring Se atoms in each unit cell, with a trigonal prismatic configuration. The schematic atomic structure of the pristine WSe_2 monolayer (side view) is shown in **Fig. 3.1 (a).** The optimized lattice parameters of the WSe_2 are a = b = 3.31 Å and c = 12.96 Å, with the bond length ($d_{W\text{-}Se}$) of 2.55 Å, very close to the experimentally reported values [287]. We have selected various TM metal (X) atoms from 3d, 4d, and 5d groups of the periodic table for substitution doping, as listed in **Table 3.1**. In this work, only one W atom is substituted by the TM dopant in the 2 × 2 × 1 WSe_2 supercell. The side and top view of TM metal-doped WSe_2 supercell at W site is shown in **Fig. 3.1 (b) and (c).** After the structural relaxation, a little contraction in $d_{X\text{-}Se}$ was observed for V, Cr, Ru, Re, Ir, doped WSe_2 monolayer. However, an extension in $d_{X\text{-}Se}$ observed for Sc, Nb, Y, Zr, Hf, Ta, Pd, Ag, and Au doped WSe_2 system. A significant change in lattice parameters has also been noted after TM doping. All the values of $d_{X\text{-}Se}$ and lattice parameters are listed in **Table 3.1.**

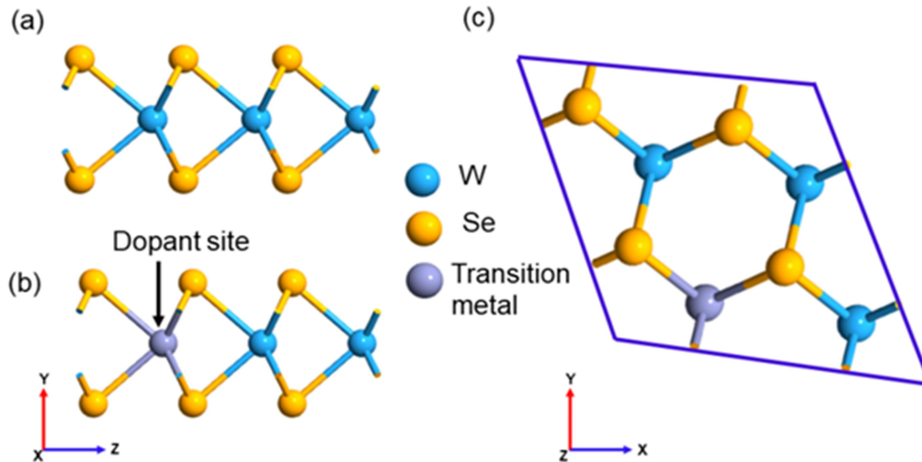

Fig. 3.1 (a) Schematic atomic structure of pristine WSe_2 monolayer (2 × 2 × 1 supercell) with a side view, showing W atoms sandwiched between two chalcogen planes (Se); The (b) side and (c) top view of Transition metal (3d, 4d, and 5d) doped at W site of WSe_2 monolayer. The blue, yellow, and violet bolls denote W, Se, and TM atoms.

Table 3.1: The optimized lattice parameters for pure and TM-doped WSe_2 monolayer, where a and c are lattice constant, and $d_{X\text{-}Se}$ describes the bond length in the vicinity of metal impurity, E_{form} is the formation energy of TM-doped WSe_2 monolayer in W-rich and Se-rich conditions, E_g is the bandgap TM doped WSe_2 monolayer and ΔQ is the charge transfer from TM dopants to WSe_2 monolayer

Dopants	System	Lattice parameter		$d_{X\text{-}Se}$ (Å)	$E_{tot}[WSe_2 + X]$	μ_X	E_{form} (eV)		Eg (eV)	Δ Q (eV)
		a (Å)	c (Å)				W-rich	Se-rich		
Pure		6.63	12.96	2.55	-	-	-	-	1.55	
3d-metals	Sc-doped	6.85	12.94	2.65	-200.27098	7.42069	-0.09	-2.43	0.85	-0.01e
	Ti-doped	6.74	12.93	2.55	-201.87422	8.38541	-0.80	-3.14	1.22	-0.06e
	V-doped	6.64	12.93	2.50	-202.13818	9.08401	-0.29	-2.64	1.23	-0.31e
	Cr-doped	6.60	12.92	2.47	-205.69034	13.54960	0.61	-1.73	1.04	-0.04e
4d - metals	Y-doped	6.97	12.95	2.71	-217.22018	24.36314	-0.09	-2.44	0.74	-0.041e
	Zr-doped	6.85	12.94	2.65	-202.84639	8.78704	-1.30	-3.64	1.16	-0.64e
	Nb-doped	6.72	12.94	2.59	-204.42623	10.39960	-1.26	-3.61	1.43	-0.08e
	Ru-doped	6.75	12.88	2.50	-200.47300	9.66822	1.95	-0.39	0.97	0.57e
	Rh-doped	6.76	12.90	2.55	-198.07322	7.90038	2.58	0.23	1.07	0.61e
	Pd-doped	6.80	12.92	2.61	-258.46602	69.14213	3.43	1.08	------	0.72e
	Ag-doped	6.87	12.92	2.67	-239.17	51.833	5.42	3.07	0.72	0.67e
5d - metals	Hf-doped	6.84	12.94	2.63	-201.52750	8.52640	-0.24	-2.59	1.31	-0.61e
	Ta-doped	6.72	12.95	2.58	-601.25830	407.8325	-0.66	-3.01	1.42	-0.12e
	Re-doped	6.65	12.91	2.52	-203.58738	11.72348	0.89	-1.45	1.01	0.36e
	Ir-doped	6.81	12.88	2.54	-199.01	10.02942	3.77	1.42	0.96	0.88e
	Au-doped	6.88	12.92	2.68	-191.98291	5.25039	6.02	3.67	0.49	0.59e

It is due to the difference in the atomic radius between the W atom and TM dopants. This difference also induces a strain within the lattice, which causes the bandgap reduction in the TM-doped WSe_2 monolayer [65]. A decrease in lattice parameters was also observed as we move individually in each 3d (Sc to Cr), 4d (Y to Ag), and 5d (Hf to Au) TM group of Table 3.1 from top to bottom. It is mainly due to the atomic radius's shrinkage in a similar manner in the Periodic table. **Fig. 3.2** represents the band structure and density of states (DOS) of the WSe_2 monolayer with GGA-PBE and GGA-HSE06 functionals. As determined GGA-PBE bandgap (solid black line) of the WSe_2 monolayer is 1.55 eV (direct bandgap) shown in Fig. 3.2 (a), which is in good agreement with previous results [258, 281]. The valence-band maximum (VBM) and the conduction band minimum (CBM) are located at K point which has been induced by quantum-confinement effect [260]. It is noted that the PBE exchange-correlation potential underestimates the band gaps; therefore, various

correction schemes have been proposed so far [288, 289]. The hybrid functional of Heyd-Scuseria Ernzerhof (HSE06) with the PAW pseudopotential results is in good agreement with the experimental results for TMDCs materials [65]. Therefore, we used the HSE06 hybrid functional for more accurate bandgap calculation [289]. The determined direct bandgap from the GGA-HSE06 functional is 1.98 eV, shown in Fig. 3.2 (a) (magenta dash line). The bandgap of the WSe_2 monolayer was corrected by ~20% using HSE06 functional [281, 290]. The bandgap values from band structure calculations are consistent with the DOS of WSe_2 monolayer from GGA-PBE and GGA-HSE06 functional, as shown in Fig. 3.2 (b). The Fermi level (E_F), is the highest occupied state within a continuous energy band aligned to zero energy level and indicated by a dashed (green) line (see Fig. 3.2). However, that energy scale is completely arbitrary and has no physical meaning. The actual value of Fermi level is measured always with respect to vacuum level (zero level), also given as output in the text form. In our calculation, we have used value of Fermi level calculated using Fermi-Dirac occupation method with respect to vacuum level.

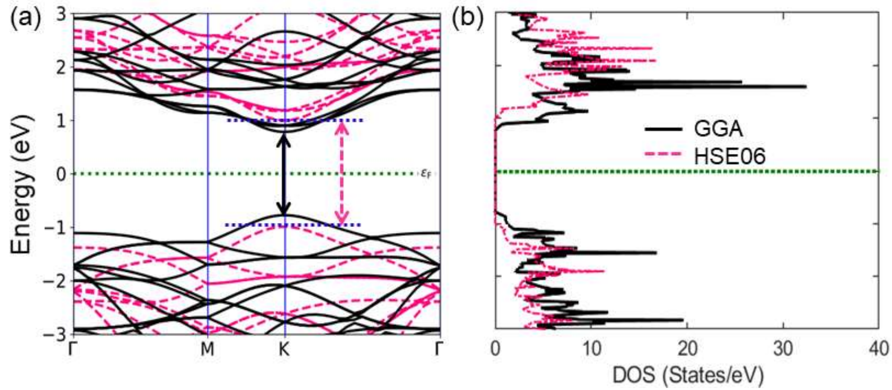

Fig. 3.2 1H-WSe_2 monolayer (a) Band structure and (b) Total density of states (TDOS) with GGA-PBE (solid black line) and GGA-HSE06 functional (magenta dash line) along with the major symmetric directions.

3.3.2 Formation energy calculations

The formation energy is the key parameter to understanding the feasibility and stability of dopants in materials, which is defined as [70, 72, 198]

$$E_{form} = E_{tot}[WSe_2 + X] - E_{tot}[WSe_2] + \mu_{host} - \mu_X \quad \textbf{(3.1)}$$

Where, $E_{tot}[WSe_2 + X]$ is the total energy of the WSe_2 supercell with the substitutional TM dopant X, $E_{tot}[WSe_2]$ is the total energy of the pristine WSe_2 supercell, μ_X and μ_{host} are the chemical potentials of the substitutional dopant atom X and the substituted host atom W. The values of $E_{tot}[WSe_2]$ and μ_{host} are same for different dopant metals in E_{form}calculation which are -204.98327 eV and -12.22496 eV, respectively. The values of $E_{tot}[WSe_2 + X]$ and μ_X are different for different dopant atoms in E_{form} calculation which are given in Table. 3.1.

The chemical potentials in Eq. (3.1) are subject to a series of thermodynamic constraints under the equilibrium growth condition. To maintain the stability of WSe_2 during growth, the chemical potentials of W and Se should satisfy Eq. (3.2) as given below

$$\mu_W + 2\mu_{Se} = \Delta E_{form}(WSe_2) \quad \textbf{(3.2)}$$

The formation energy of such a reaction is given as

$$E_{form}[WSe_2] = \mu_{WSe_2} - \mu_{W,bulk} - 2\mu_{Se,bulk} \quad \textbf{(3.3)}$$

Where $\mu_{W,bulk}$ and $\mu_{Se,bulk}$ are the energy per atom of W bulk in the bcc structure and Se in the molecular crystal (phase) of Se_6 molecules and μ_{WSe_2} is the energy per unit cell of WSe_2. The E_{form} of WSe_2 is determined as -2.34 eV/atom, which is in good agreement with the experimental value of ΔH_f for bulk WSe_2 material ~ -1.92 eV/atom [291]. There could be an excessive amount of constituent atoms of a product compound in the surroundings depending on different synthesis routes in the practical experimental condition. To take this factor into account, in DFT calculations, we consider W-rich (Se-poor) and the W-poor (Se-rich) conditions for monolayer WSe_2. Under W-rich condition

$$\mu_W = \mu_{W,bulk} \text{ and} \quad \textbf{(3.4)}$$

$$\mu_{Se} = \mu_{Se,bulk} + \frac{1}{2}\Delta E_{form}(WSe_2) \quad \textbf{(3.5)}$$

In contrast, in the Se-rich condition

$$\mu_W = \mu_{W,bulk} + \Delta E_{form}(WSe_2) \text{ and} \quad \textbf{(3.6)}$$

$$\mu_{Se} = \mu_{Se,bulk} \quad \textbf{(3.7)}$$

The E_{form} of all TM-doped WSe_2 systems is listed in Table 3.1. It is observed that in Se-rich conditions, all the doped systems have a negative value of E_{form} except for Pd, Ag, Au, Ir, and Rh. A negative E_{form} indicates an exothermic reaction and a stable doped system. It also suggests that it is energetically more favorable and relatively easier to incorporate with TM atom under Se-rich experimental conditions.

We have also calculated the charge transfer (ΔQ) between the TM dopant and WSe_2 monolayer using the Bader charge analysis [292, 293]. The negative value of charge transfer indicates that electrons transferred from the WSe_2 monolayer to the TM dopants; all the ΔQ values are listed in Table 3.1. Charge transfer values for Sc, Ti, V, Cr, Y, Zr, Nb, Hf, and Ta doped WSe_2 show that the nearest neighbor Se atoms lost electrons in favor of the doped TM atom. However, for Ru, Rh, Pd, Ag, Re, Ir, and Au-doped WSe_2, the nearest neighbor Se atoms gain electrons from the corresponding TM dopants.

3.3.3. Substitutional doping at W site using 3d, 4d, and 5d transition metals

3.3.3.1. 3d TM-doped WSe_2 monolayer

Here, in this section, we investigate the possibility of p-type and n-type doping in the WSe_2 monolayer by substitution of 3d TMs dopants at the W atomic site. The band structures and total density of states (TDOS) of the 3d TM, i.e., Sc, Ti, V, and Cr doped WSe_2, are shown in **Fig. 3.3.** First, we will discuss WSe_2 monolayer with the 3d TM dopants having less d-orbital occupancy than W atom. In this case, when Sc ($3d^1$ $4s^2$) is substituted in place of the W ($5d^4$ $6s^2$) atom in the WSe_2 supercell, the Fermi level moves inside the VBM, and acceptor-type defect states appear crossing the Fermi level as shown in Fig. 3.3 (a). These defects state around the VBM originate from the hybridized d orbitals of W and Sc, as confirmed by the DOS plot in Fig. 3.3 (b). Similar metallic nature of band structure and DOS was also observed for Ti ($3d^2$ $4s^2$) doped WSe_2, as shown in Fig. 3.3 (c) and (d). However, due to the additional one electron, the acceptor-type defect states are more hybridized with the VBM in the Ti-doped WSe_2 than the Sc. Comparable observations for Sc and Ti-doped WSe_2 were also reported by Zhao *et al.* [72]. Both Sc and Ti-doped systems have negative E_{form} in W and Se-rich conditions; therefore, the synthesis of these materials will be energy favorable. For V ($3d^3$ $4s^2$) dopant, this has one electron less than the W atom, Fermi level shifts just below VBM without the creation of any defect level, as shown in Fig. 3.3 (e) and (f). Therefore, the V-doped WSe_2 works as a p-type semiconductor with a reduced direct band gap of 1.23 eV. The E_{form} calculations also indicate that it is thermodynamically favorable to substitute the V atom in the WSe_2 monolayer in Se-rich experimental conditions (Table 3.1). Recently, Yun *et. al*. [294] reported an experimental study of p-type doping in WSe_2 via V substitutional doping. A quantum tunneling in V-doped WSe_2/$SnSe_2$ heterostructures has been reported by Fan *et. al*. [295]. The Cr ($3d^5$ $4s^1$) dopant has equal d-orbital occupancy the same as the W atom and is located in the same subgroup of the periodic table. For Cr-doped WSe_2, the direct bandgap semiconducting nature remains unchanged, as shown in Fig. 3.3 (g) with a narrower bandgap of ~1.04 eV. The two clear broad peaks are observed close to the CBM, contributed by the Cr dopant shown in Fig. 3.3 (h). Overall, among 3d TM dopants, Sc, Ti, V, and Cr, only V is a possible dopant for p-type doping in WSe_2 monolayer for FET applications.

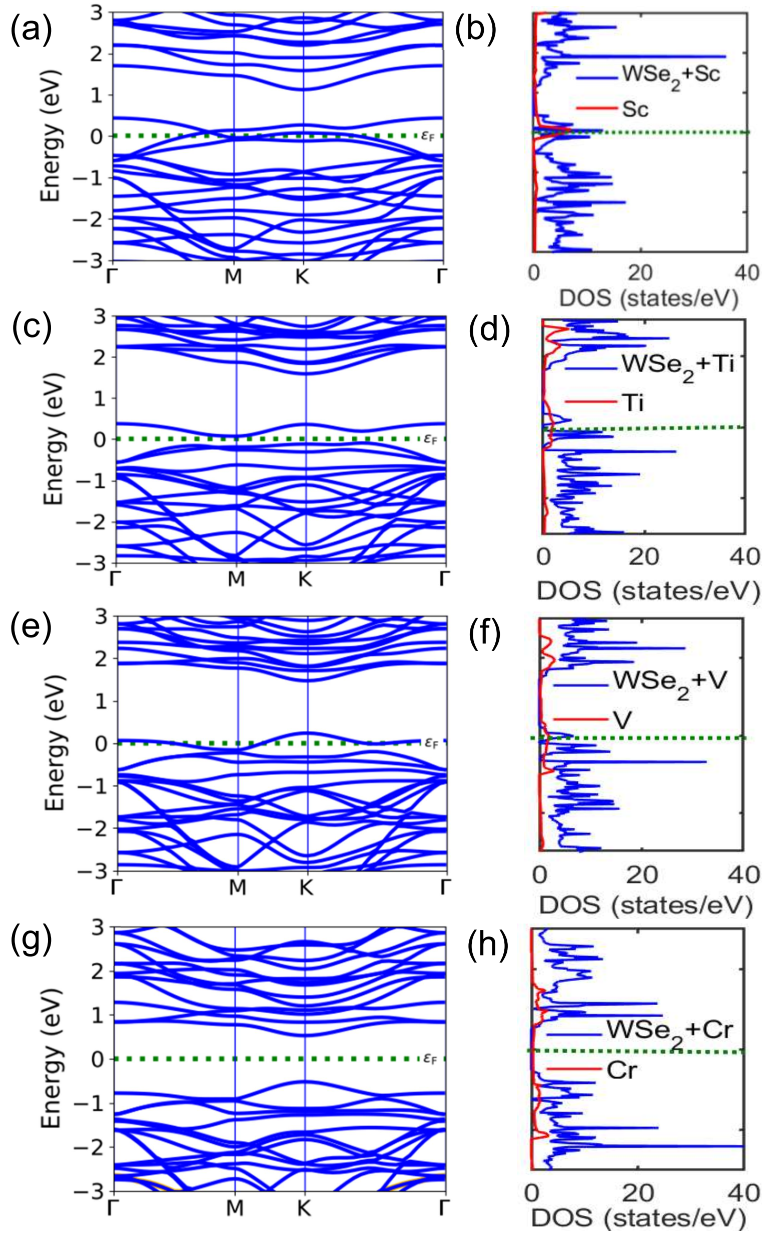

Fig. 3.3 (a), (c), (e), (g) panels show the band structures of WSe_2 with 3d TM dopants (blue solid lines) and (b), (d), (f), (h) panels show the TDOS of TM doped WSe_2 system (blue solid line) with corresponding DOS of Sc, Ti, V and Cr (red solid line). In the case of V, the Fermi level shifts inside the VBM due to the lack of one electron as compared to the W atom. For Sc and Ti, acceptor states were created around the Fermi level wherein the case of the Cr doped system, no shift in the Fermi level was observed.

3.3.3.2. 4d TM-doped WSe_2 monolayer

Next, we consider substitutional doping at the W site with 4d TM group metals, i.e., Y, Zr, Nb, Ru, Rh, Pd, and Ag. The band structure and DOS for the 4d TM doped WSe_2 monolayer having d-occupancy less than the W atom has shown in **Fig. 3.4**. Let us start with Y ($4d^1$ $5s^2$) dopant, which has the lowest d-orbital occupancy in the 4d-TM group. For the Y-doped WSe_2 system, the Fermi level shifts inside the VBM, and acceptor-type defects states emerge surrounding the Fermi level showing metallic behavior, as shown in Fig. 3.4 (a) and (b). The band structure of Y-doped WSe_2 resembles the Sc-doped WSe_2 system due to a similar number of valance electrons in the outermost orbital. The E_{form} of Y-doped WSe_2 is -2.44 eV in Se-rich conditions, which suggests that the synthesis process is thermodynamically preferred. For Zr ($4d^2$ $5s^2$) doped system, the Fermi level shifts just below the VBM, as shown in Fig. 3.4 (c). Acceptor defect states originated above the VBM, as shown in Fig. 3.4 (d), similar to the case of Y. However, the density of defect states is lesser in Zr doped system than in the Y-doped WSe_2. We are now moving our discussion to the next dopant in the 4d TM group, i.e., Nb metal, a popular choice of p-type doping among all the TM dopants for TMDC materials [53]. Like the V dopants in the 3d-TM group, the Nb ($4d^5$, $5s^1$) dopant also has one electron less than the W atom. Thus, the Fermi level shifts below VBM and the system behaves like a p-type semiconductor, as shown in Fig. 3.4 (e). A reduced direct bandgap of 1.43 eV was observed for the Nb-doped WSe_2 monolayer. The states around the VBM mainly originate from hybridized d orbitals of Nb and W atoms, as confirmed by aligned DOS distribution in Fig. 3.4 (f). The Nb and Zr doped systems also have the E_{form} of -3.61 eV and -3.64 eV (Table 3.1) in Se-rich condition, which suggests that it is highly energy favorable. As calculated, E_{form} for the Nb-doped system is well-matched with recent work reported by Mabelet *et al.* [195].

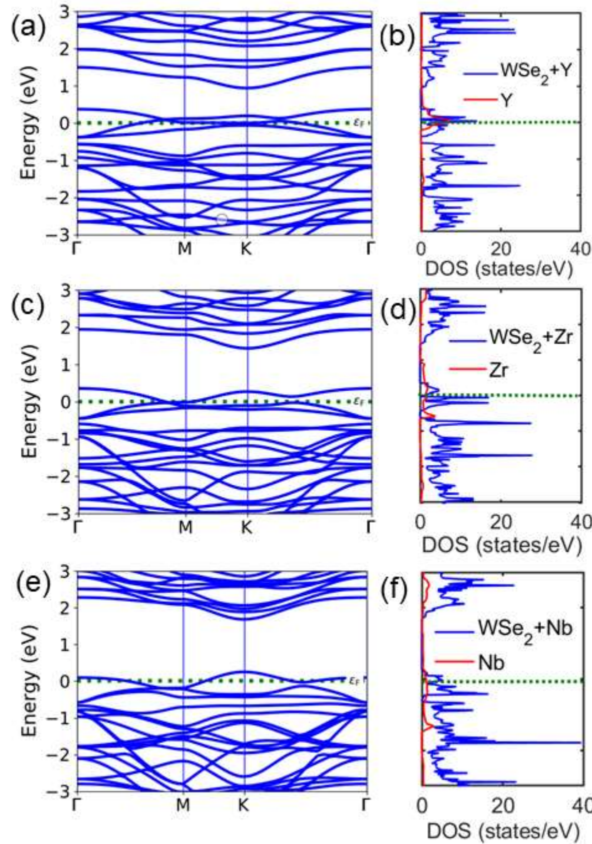

Fig. 3.4 (a), (c), (e) shows the band structures of Y, Zr, and Nb-doped (4d dopants) WSe_2, and (b), (d), (f) shows the TDOS with Y, Zr, and Nb. For Y and Zr doped WSe_2, acceptor states have been created around the Fermi level, whereas for Nb and Zr doped WSe_2, the Fermi level moves inside the VBM.

Now, we discuss the case of dopants has higher d-orbital occupancy than the W atom in the WSe_2 monolayer has shown in **Fig. 3.5**. For Ru ($4d^7 5s^1$) and Rh ($4d^8 5s^1$) dopants with an excess of two and three electrons, the Fermi level shifts deep inside the CBM, as shown in Fig. 3.5 (a) and (c). Only one defect state appears across the bandgap, offering the possibility of n-type doping in the WSe_2 confirmed by the DOS in Fig. 3.5 (b) and (d). However, the E_{form} of both Ru and Rh-doped WSe_2 is not thermodynamically favourable (See Table 3.1).

In the case of the Pd ($4d^{10}$) and Ag ($4d^{10}$ $5s^1$) doped WSe_2, the Fermi level position remains unaffected, and several defect states appear in the bandgap crossing the Fermi level (Fig. 3.5 (e) and (g)). Thus, the Pd and Ag-doped WSe_2 become metallic in nature. Fig. 3.5 (f) and (h) show the density of metallic state distribution for the Pd and Ag-doped WSe_2 monolayer. Both dopants also have positive E_{form} in both (W-rich and Se-rich) conditions, suggesting that it is not a favorable energy-doped system. Therefore, among all the 4d-TM dopants, Nb is the only potential dopant for p-type doping in the WSe_2 monolayer.

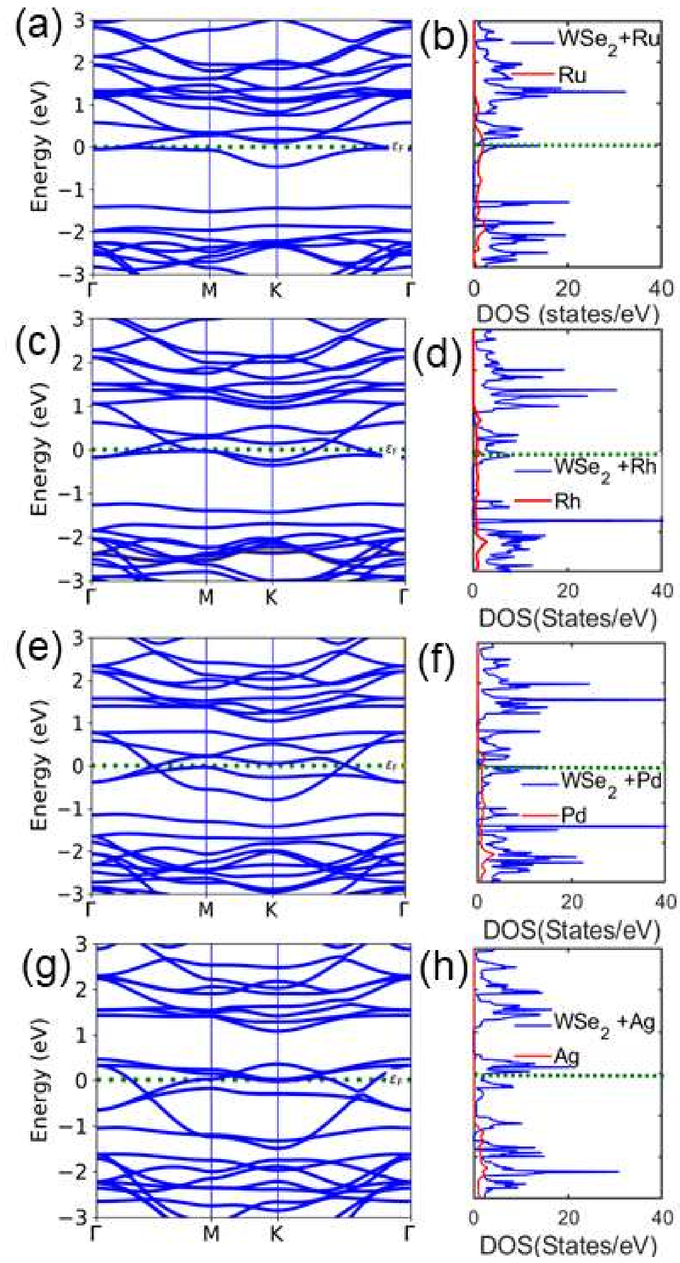

Fig. 3.5 (a), (c), (e), (g) shows the band structures of Ru, Rh, Pd, and Ag-doped WSe_2 system, and (b), (d), (f), (h) shows the corresponding TDOS. For Ru and Rh-doped WSe_2, the Fermi level moves deeper inside CBM, showing n-type doping characteristics, whereas the Pd and Ag-doped WSe_2 system shows metallic nature.

3.3.3.3. 5d TM-doped WSe_2 monolayer

Finally, we investigate the substitutional doping of 5d TM dopants, i.e., Hf, Ta, Re, Ir, and Au. The band structure and TDOS of the 5d TM doped WSe_2 have shown in **Fig. 3.6.** We start the discussion with Hf ($5d^2$ $6s^2$) dopant having lesser d orbital occupancy than the W atom. For Hf-doped WSe_2, the Fermi level moves deeper inside VBM due to the lack of two valance electrons, which shows p-type doping characteristics, as shown in Fig. 3.6 (a). The newly created defect states of the doped system are weekly hybridized with VBM and create a split-off level, as shown in the DOS plot in Fig. 3.6 (b). A lower E_{form} = -2.59 eV observed in Se-rich condition, suggests that it is the thermodynamically preferable doped system. Due to the lack of one electron in Ta ($5d^3$ $6s^2$) doped WSe_2, the Fermi level shift below the VBM, as shown in Fig. 3.6 (c). The defect states are localized around the Fermi level, as demonstrated in DOS in Fig. 3.6 (d). The holes introduced into the valence band contribute to the increase of the hole carrier concentration, and Ta-doped WSe_2 becomes a p-type semiconductor. The Ta-doped WSe_2 has a direct bandgap of 1.42 eV observed close to the pristine WSe_2. The high value of E_{form} -3.01 eV in Se-rich condition also indicated its energy favorable to incorporate Ta in WSe_2. Ta-doped WSe_2 crystals are already synthesized by the chemical vapor transport (CVT) method for FET devices application by Fu *et. al.* [201].

Let us move to the case where the dopant has higher d-orbital occupancy than the W atom, i.e., Re, Ir, and Au. When Re ($5d^5$ $6s^2$) substitutes the W atom, an extra electron is added to the system. Due to this one extra donor electron, Fermi level shifts inside the CBM, and Re-doped WSe_2 became an n-type semiconductor. The band structure and DOS of Re doped WSe_2 have shown in Fig. 3.6 (e) and (f). The E_{form} of Re-doped WSe_2 is -1.45 eV in Se-rich condition, suggesting that it is energetically favorable for synthesis. Our results are consistent with experimental work reported by Mukherjee *et. al.* [296]. By substituting W with Ir ($5d^7$ $6s^2$), the Fermi level moves deeper in CBM and it has tendency to make n-type. However, due to an excess of 3 electrons than the W atom, some acceptor states are also created in the bandgap, which is working as a trap state, as shown in Fig. 3.6 (g) and (h). In the case of Au ($5d^{10}$, $6s^1$) dopant, due to an excess of 5 valance electrons than the W atom, the several defects states created in the bandgap, and the Au-doped WSe_2 system become metallic in nature (Fig. 3.6 (i) and (j)). However, the energetics of both the Ir and Au-doped WSe_2 show its synthesis is not energy-favorable (Table 3.1). Among all the 5d TM dopants, the Ta and Re are potential p-type and n-type dopants for the WSe_2 monolayer. Also, both Ta and Re dopants are the nearest neighbor of the W atom in the periodic table. Therefore, they are the natural choice of suitable substitutional dopants at the W-site.

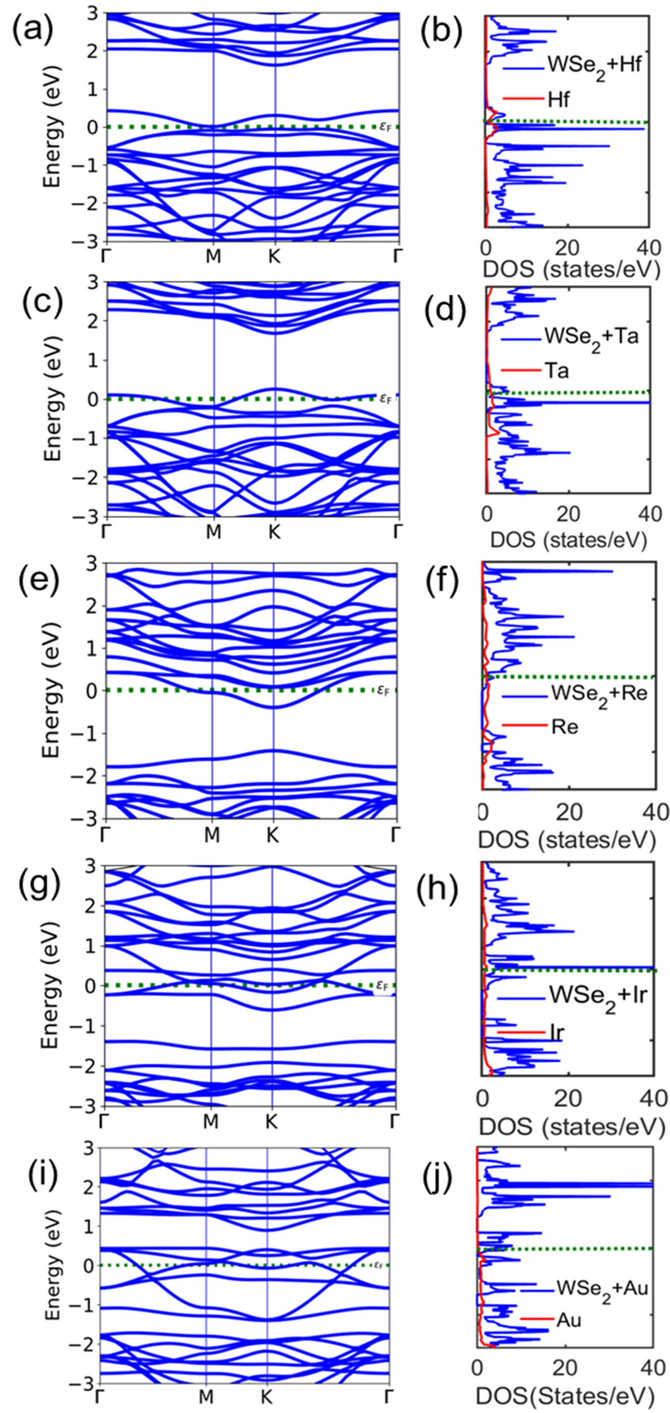

Fig. 3.6 (a), (c), (e), (g) and (i) shows the band structures, and (b), (d), (f), (h) and (j) shows the TDOS of Hf, Ta, Re, Ir and Au-doped WSe_2 (solid blue lines) with DOS of corresponding TM dopants (solid red line). For Re-doped WSe_2, the system becomes an n-type semiconductor, whereas, for Ta doping, the system behaves clearly as a p-type semiconductor material. In the case of Ir and Hf, some acceptor-type and donor-type defect states originate across the Fermi level. The Au-doped WSe_2 is showing metallic characteristics.

3.4 Conclusions

In this work, we have done a systematic study on the electronic structure of 3d, 4d, and 5d TM-doped WSe_2 monolayers based on DFT calculations. A significant change in bond length and lattice parameters was observed for TM-doped WSe_2. The E_{form} calculations suggested that TM-doped WSe_2 is thermodynamically favorable in Se-rich conditions. The energy bandgap of the TM-doped WSe_2 monolayer is decreasing due to induced strain. The Pd, Ag, and Au-doped WSe_2 show purely metallic characteristics, whereas the Cr-doped WSe_2 retains its pristine semiconducting nature with reduced direct bandgap. The V, Nb, and Ta dopants are only potential p-type dopants, and Re as an n-type dopant for the WSe_2 monolayer. The reduced direct bandgap of V, Nb, Ta, and Re doped WSe_2 semiconductors is 1.23 eV, 1.43 eV, 1.42 eV, and 1.01 eV.

Chapter 4

STRAIN-DEPENDENT DOPING, ELECTRONIC STRUCTURE AND OPTICAL PROPERTIES OF TM-DOPED 2D SEMICONDUCTORS

4.1 Introduction

The atomically thin two-dimensional (2D) semiconducting materials are extensively explored for next-generation optoelectronics [5, 297, 298], nano-mechanics [299, 300], solar cells [301, 302], and photocatalytic water splitting research [303-305]. The electronic and optical absorption behaviours of transition metals doped systems are reported by various doping methods such as adsorption [50-52], substitutional doping [54-56], and charge transfer methods [57, 58]. Substitutional doping is an effective approach to modulate the conductivity of atomically thin 2D materials so that they can electrically functionalize as the key component in various electronic and optoelectronic devices [63, 64, 253, 306]. Graphene-like ZnO (g-ZnO) is a 2D monolayer having excellent electronic and optical properties, with high mechanical stability [211-213]. It is a structural analogue of h-BN where the Zn and O atoms are arranged in a planar sheet in a honeycomb structure [307]. However, the g-ZnO monolayer has the main absorption in the ultraviolet (UV) region, limiting its capability to utilize solar energy, which hinders its use in various applications [213]. It is noted that UV light only covers 4% of the energy in the solar spectrum, while visible light embodies 43% part of the solar spectrum [213]. Aluminium (Al) is considered one of the most efficient dopants used to produce conducting ZnO thin films; in the g-ZnO monolayer, the substitution of the Al atom at the Zn site is energetically favorable [214]. However, synthesis of ZnO with high Al doping concentration is difficult due to the high E_{form} of the Al atom in ZnO and the reduction of E_{form} is a challenging task.

TMDC monolayers such as MoS_2, WS_2, $MoSe_2$, WSe_2, etc. have attracted significant attention for future electronics owing to their unique electrical [308], optical [34], and mechanical properties [35, 36]. As one of the most extensively used TMDCs, WSe_2 monolayer has a direct optical bandgap (~ 1.6 eV) [309, 310], strong photoluminescence [311], large optical absorption (~ 10^5 cm^{-1}, visible range) [309, 311], good thermal stability [312] and excellent mechanical properties [98] with both n-type [313] and p-type [283] transport ambipolar behavior with a different metal contact. While experimental research on substitutional doping in WSe_2 monolayer is at an early stage; several theoretical calculations predicted transition metals (TM) can effectively control the Fermi level to acts as potential n- or p-type dopants [63, 253, 314, 315]. Among all the TM, Niobium (Nb) [62, 296], Tantalum (Ta) [255], Vanadium (V) are popular choices for p-type dopants, whereas and Rhenium (Re) [256] is the n-type dopant in the WSe_2 monolayer. The Nb, Ta, V, and Re-doped WSe_2 monolayer are predicted to have negative E_{form} from the thermodynamics perspective, implying a stable doped system for practical applications [314, 316].

Strain engineering of TMDCs monolayers has been intensively studied towards modulating their electrical, optical, and magnetic properties [97, 98, 100, 103, 104, 107]. Due to the application of strain, the original state of atomic bonding changes by stretching or shortening the distance of chemical bonds [107]. As a result, the electronic structure of the material is reformed, and a series of new properties emerge [36, 100, 108, 207]. The strain-tuning of electronic structure and optical properties of pristine WSe_2 monolayers is well studied in the literature [55, 56, 208, 210]. However, studies on the strain-tuning of electrical and optical properties of Nb, Ta, and Re-doped WSe_2 are not reported yet.

The E_{form} is a critical parameter that primarily influences the doping concentration; thus, it is very important to understand how to control that in 2D materials. Controlled enhancement of doping concentration in substitutional doping is one of the most important challenges for advancing 2D-materials-based technology [63, 317, 318]. This bottleneck represents a critical obstacle to the full utilization of 2D materials as novel electronic materials for next-generation electronic devices [64, 253, 319]. Typically, in substitutional doping when the host atom replaces by a dopant atom, an internal strain induces due to the size differences between the host and the dopant [69]. It is expected that external mechanical strain that deforms the host lattice may reduce the dopant-induced internal strain, further increasing dopant solubility [69, 106, 206]. The application of strain to modulate the electronic [36, 101], optical [98, 103, 104], and magnetic [105, 106] properties of 2D

semiconductors are well explored in the 2D materials community. However, reports on the effect of strain on doping behavior are scarce. Although strain-dependent doping behavior has been well studied for traditional semiconductor materials [69, 106, 216, 320, 321]. This encourages us to explore strain as an external parameter to enhance the doping concentration of 2D semiconductors for future applications. Therefore, we have chosen the Re, Nb, Ta, and *V* dopants to understand strain-dependent doping behavior in the WSe_2 monolayer.

Therefore, in this work, we theoretically analyze the modulation of bandgap and optical properties of Nb, Ta, and Re-doped WSe_2 monolayer under biaxial strain varying from -5% to +5%. We analyze the rate of bandgap tunability and determine the critical value of strain at which direct (K-K transition) to indirect (Γ-K transition) band gap transition occurs. The optical spectra are determined by analyzing the dielectric function of the TM doped-WSe_2 monolayer. Further, the optical properties are determined by analyzing the dielectric function of the TM doped-WSe_2 monolayer in detail.

We also explore the possibility of enhancing doping concentration by application of mechanical strain in TM-doped WSe_2 monolayer using DFT calculations. The variation of E_{form} with biaxial strain varying from -5% to +5% is studied in detail. We found out the E_{form} has parabolic relation with biaxial strain for the dopants (Re and *V*) where the change in ΔV due to substitution is negligible. However, the E_{form} has a monotonic linear relation with energetically more favorable under tensile strain for the dopants (Nb and Ta) where the ΔV is significantly larger. A significant reduction in the E_{form} of TM-doped WSe_2 was observed under different mechanical strain conditions, which leads to the enhancement of dopant concentration.

We also investigated biaxial strain varying from -10% to +10 % on the E_{form}, electronic structure, and optical absorption of the g-AZO monolayer. We observed that up to the ε_{xy} of +5%, the E_{form} varies linearly with strain, whereas at $\varepsilon_{xy} > +5\%$, a sudden drop in the value of E_{form} is observed which enhances the concentration of Al dopants in the g-ZnO monolayer. Although under the ε_{xy} up to -10%, the change in the E_{form} is visible, it is not sufficient to induce higher Al doping concentration in the g-ZnO monolayer. We find that the due to lowest E_{form} at $\varepsilon_{xy} = +10\%$, a higher absorption in the visible region is observed for the g-AZO monolayer, which is also well-matched with the experimental observations.

4.2 Computational Methods

Our DFT calculations are performed with the Virtual Nano lab Quantum Atomistic tool kit [322], with projected augmented wave (PAW) pseudopotentials. The exchange-correlation functionals are defined within GGA using PBE form [323]. In case of TM-doped WSe_2 monolayer, the electron wave functions are represented by a plane-wave basis of an energy cut-off of 550 eV with grid sampling of 9 × 9 × 1. Whereas for the AZO monolayer, the electron wave functions are represented by a Linear combination of atomic orbitals (LCAO) basis with an energy cut-off of 125 Hartree with a grid sampling of 25×25×1. Atomic structures were fully relaxed to minimize the system's total energy until the force on each atom is less than 0.01 eV/Å using a limited memory Broyden-Fletcher-Goldfarb-Shannon (LBFGS) method. A vacuum space of more than 12 Å is included perpendicular to the monolayer surface to avoid the physical interaction between neighboring unit cells. To improve the accuracy of the band gap and absorption coefficient, all electronic and optical properties of the g-AZO monolayer were evaluated using the Heyd-Scuseria-Ernzerhof (HSE06) hybrid functional [289].

4.3 Results and Discussions

4.3.1 Electronic structure of pristine and Nb, Ta, and Re-doped WSe_2 monolayer

The pristine WSe_2 monolayer has a hexagonal lattice structure with P63/mmc space group symmetry, with the W atoms having a trigonal prismatic configuration with six neighboring Se atoms [310]. The relaxed lattice parameters of the WSe_2 monolayer are a = b = 3.31 Å and c = 12.96 Å, with a bond length ($d_{W\text{-}Se}$) of 2.55 Å [63, 324]. We have substitutionally doped 2 × 2 × 1 supercell of WSe_2 with Nb, Ta, and Re atoms by replacing one W atom using periodic boundary conditions. It is noted that the 2×2×1 supercell of WSe_2 was appropriate to study the effect of doping by substitutional atoms, supported by previous reports [325, 326]. It is well known that the WSe_2 monolayer is a non-magnetic semiconductor [327]. However, after Nb, Ta, and Re doping, we checked the ground state of the WSe_2 monolayer by taking spin polarization into account. The minority spin is aligned with the majority spin in all cases, revealing that the systems are non-magnetic, matching the reported results [316]. Therefore, for further calculations, we have not taken spin polarization into account. The atomic structure of pristine WSe_2 monolayer and Nb, Ta, and Re-doped WSe_2 monolayer is shown in **Fig. 4.1.**

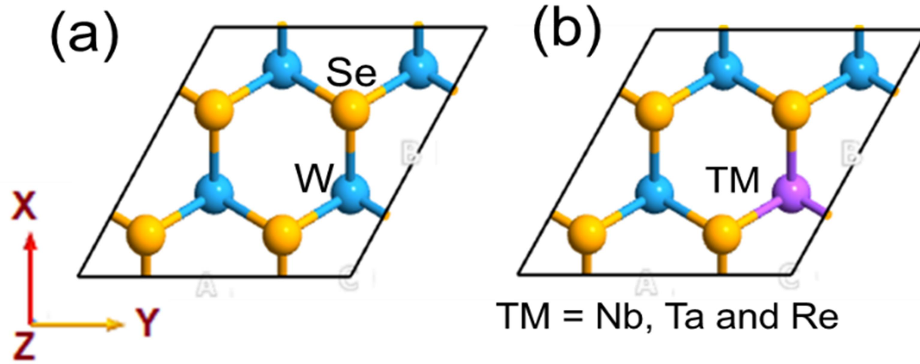

Fig. 4.1 Schematic atomic structure (top view) of (a) WSe_2 monolayer (b) TM-doped WSe_2 monolayer; the TM includes, Nb, Ta, and Re.

We have applied a biaxial strain ($\varepsilon = \varepsilon_x = \varepsilon_y$) to study the tunability of electronic and optical properties of WSe_2 monolayer doped with Nb, Ta, and Re metals. It may be mentioned here that the biaxial strain is more effective than uniaxial and shear strain for tuning the bandgap because of the larger lattice deformation in both crystal orientations [328-330]. The magnitude of ε is defined as $\varepsilon = (a_0 - a)/a \times 100\%$, where a_0 and a are the lattice constants of the strained and unstrained doped WSe_2 monolayer, respectively. The ε varies from -5% to +5%, where + and - signs represent the tensile and compressive strain, respectively.

The projected electronic band structure of the Nb, Ta, and Re-doped WSe_2 monolayer was analyzed and compared to the pristine WSe_2 monolayer as shown in **Fig. 4.2**. The pristine WSe_2 monolayer has a direct bandgap of 1.55 eV, matching previous DFT-PBE results [327] as shown in Fig. 4.2 (a). Due to removing one electron from the WSe_2, the Nb-doped WSe_2 system becomes electron-deficit and behaves as a p-type semiconductor with a direct bandgap of 1.43 eV (Fig. 4.2(b)). Similarly, doping behaviour was also observed with the Ta-doped $WSe_{2,}$ with little variation in bandgap value ~ 1.42 eV (Fig. 4.2 (c)). This is due to similar d orbital occupancy of Nb and Ta dopants. For the Re dopant in the WSe_2 monolayer, an extra electron has been added to the system. Due to this, Fermi level-shifted inside the CBM and became an electron-rich, n-type semiconductor with a bandgap of 1.01 eV (Fig. 4.2 (d)).

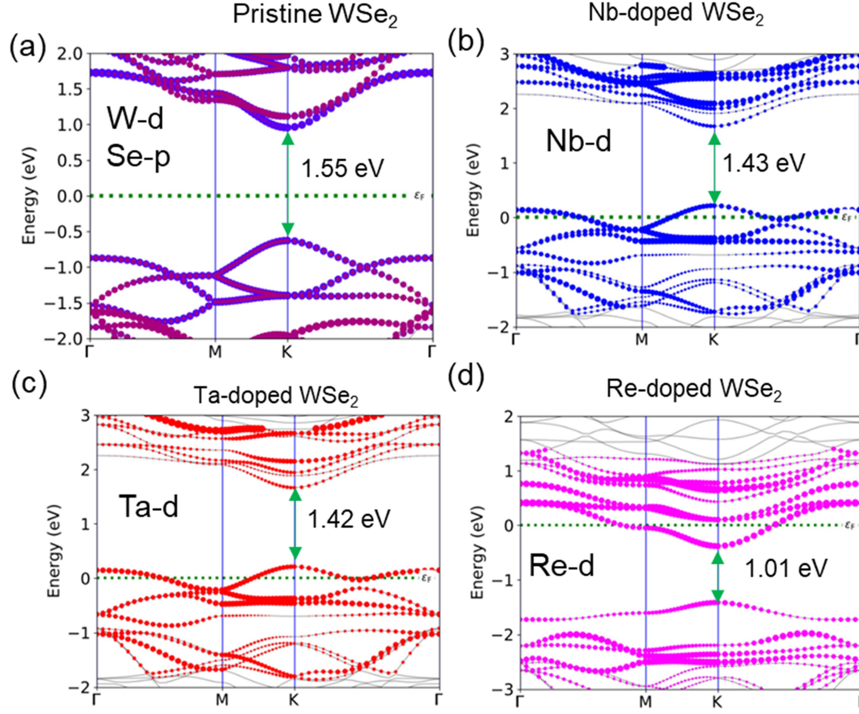

Fig. 4.2 Projected band structure of (a) pristine WSe_2 monolayer (b) Nb-doped WSe_2, (c) Ta-doped WSe_2 (d) Re-doped WSe_2, p-doping observed for Nb and Ta-dopants, where n-type doping for Re-doped WSe_2 monolayer. The blue, red, and pink dots represent the contribution of Nb-d, Ta-d, and Re-d orbitals

Further, we calculated the E_{form} to understand the stability of dopants in the WSe_2 monolayer. It can be calculated according to the following relation [254, 331]

$$E_{form} = E_{\text{tot}}[WSe_2 + X] - E_{tot}[WSe_2] + \mu_{host} - \mu_X \qquad \textbf{(4.1)}$$

where, $E_{\text{tot}}[WSe_2 + X]$ is the total energy of the WSe_2 supercell with the substitutional TM dopant X= Nb, Ta and Re, $E_{tot}[WSe_2]$ is the total energy of the pristine WSe_2 supercell, while μ_X and μ_{host} are the chemical potentials of the substitutional dopant atom X and substituted host atom W. All Nb, Ta, and Re-doped WSe_2 systems have a negative value of E_{form} in Se-rich conditions which shows a stable doped system. This also indicates that it is energetically more favorable and relatively easier to incorporate with TM atom under Se-rich experimental conditions. The E_{form} of Nb, Ta, Re doped WSe_2 monolayer are calculated as -3.61 eV, -3.01 eV, and -1.45 eV respectively under Se- rich condition which is well matched with the previous reports [316]. We also performed Bader charge analysis [292] to know the nature and amount of charge transfer between dopants and the nearest neighbor atoms. Charge transfer values (ΔQ) for Nb-doped WSe_2 ~ -0.08e and Ta-doped WSe_2 ~ -0.12 e, which show that the nearest neighbor Se atoms lost electrons in favor of the doped TM atom.

However, Re-doped WSe_2, the nearest neighbour Se atoms gains +0.36e electrons from the Re dopant. The negative value of charge transfer indicates that electrons transferred from WSe_2 to the TM dopants; all the ΔQ values are listed in Table. 4.1. **Fig. 4.3** shows the charge density difference plot of pristine and doped WSe_2 systems, which further supports our results on charge transfer (ΔQ) analysis. All the values of lattice constant, bond length, E_{form}, bandgap, charge transfer (ΔQ) and doping-type for pristine and Nb, Ta and Re-doped WSe_2 monolayer are mentioned in **Table. 4.1.**

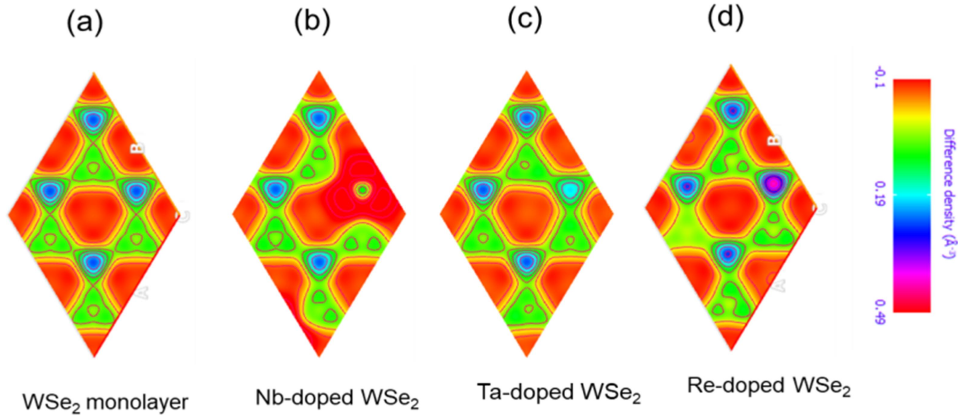

Fig. 4.3 Charge density difference plot of (a) pristine (b) Nb-doped WSe_2 (c) Ta-doped WSe_2 (d) Re-doped WSe_2

Table 4.1: The lattice constant, bond length, formation energy, bandgap, ΔQ is the charge transfer and doping type for pristine and Nb, Ta, and Re-doped WSe_2 monolayer

Monolayer system	**Lattice constant a (Å)**	**Bond length (Å)**	**E_{form} (eV) (Se-rich)**	**Bandgap (eV)**	**ΔQ (e)**	**Doping type**
Pristine WSe_2	3.31	2.55 (W-Se)	-	1.55	-	intrinsic
Nb-doped WSe_2	3.36	2.59 (Nb-Se)	-3.61	1.43	-0.08	p-type
Ta-doped WSe_2	3.36	2.58 (Ta-Se)	-3.01	1.42	-0.12	p-type
Re-doped WSe_2	3.325	2.52 (Re-Se)	-1.45	1.01	0.36	n-type

4.3.2. Biaxial strain tuning of the electronic structure of pristine and Nb, Ta, and Re doped WSe_2 monolayer

Here, we investigate the change of electronic structure of pristine and Nb, Ta, and Re-doped WSe_2 monolayer under the influence of biaxial strain varies from -5% to +5%. **Fig. 4.4** shows the bandgap variation for pristine and Nb, Ta, and the Re-doped WSe_2 monolayer under the application of biaxial strain. The band gap value of the pristine WSe_2 monolayer

linearly decreases with increasing tensile strain. However, it increases up to some critical strain value for the compressive strain and then further decreases. The Nb-doped WSe_2 and Ta-doped WSe_2 monolayer also followed a similar bandgap variation with strain. However, for the Re-doped WSe_2 monolayer, the bandgap increases up to a particular tensile strain value and decreases. A continuous decrease in bandgap was observed for the compressive strain, utterly different from both Nb and Ta-doped WSe_2 monolayer cases.

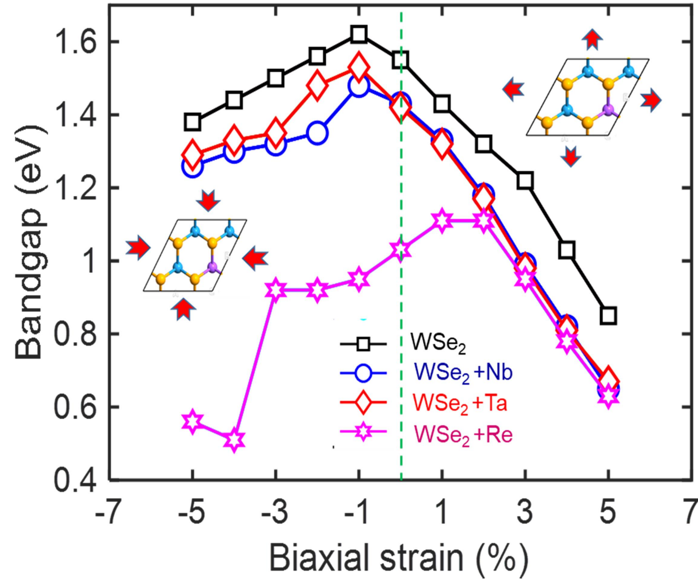

Fig. 4.4 Variation of TM (Nb, Ta, and Re)-doped WSe_2 monolayer bandgap under different biaxial strains from -5% to + 5%

Further, we determined the tunability of the bandgap with the biaxial tensile strain (slope between E_g and ε, i. e. $\Delta E_g/\Delta \varepsilon$) is determined using the simple linear fitting. It is noted that in the tensile strain domain, the K-K and Γ-K energy gaps correspond to the A and I peak in PL and absorption spectroscopies [103, 332]. Therefore, we have plotted K-K and Γ–K bandgap transition with biaxial tensile strain for all the pristine and doped WSe_2 monolayers as shown in **Fig. 4.5** (a)-(d). The critical value of biaxial tensile strain at which the crossover from direct (K-K) bandgap to indirect (Γ-K) bandgap occurs, marked by an arrow in each figure. When the strain value >+2.9 %, the valance band maximum (VBM) shifts from K to Γ point of the reciprocal space and the bandgap becomes indirect in nature for the pristine WSe_2 monolayer. The $\Delta E_g/\Delta \varepsilon$ equal to -114 meV/% for the K-K transition whereas it is -204 meV/% for Γ–K transition.

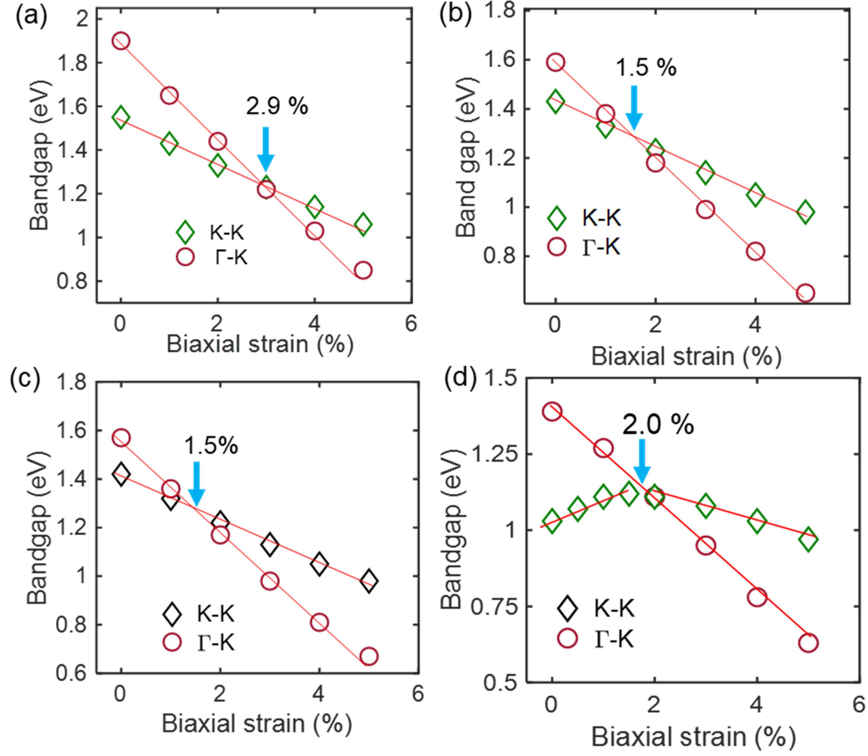

Fig. 4.5 Variation of K-K and Γ-K transition with tensile strain for (a) pristine WSe_2 (b) Nb-doped WSe_2 (c) Ta-doped WSe_2 (d) Re-doped WSe_2 monolayer. The arrow shows the critical strain value at which the direct (K-K) to indirect bandgap (K-Γ) transition occurs.

This slope of A and I energy gaps with strain for the WSe_2 monolayer agrees well with the available experimental and theoretical results [98, 103]. For Nb-doped WSe_2 monolayer, $\Delta E_g/\Delta\varepsilon \sim -90$ meV/% for K-K transition whereas the $\Delta E_g/\Delta\varepsilon \sim -187$ meV/% for Γ-K transition. It is clear that the Nb-doped WSe_2 monolayer has lower bandgap tunability with strain as compared to the pristine WSe_2 monolayer. Similarly, for Ta-doped WSe_2 monolayer, $\Delta E_g/\Delta\varepsilon \sim -88$ meV/ % for K-K transition, whereas $\Delta E_g/\Delta\varepsilon \sim -181$ meV/ % for Γ-K transition. The close bandgap tunability with strain for both Nb and Ta-doped WSe_2 is mainly due to the similar nature of electronic structure and atomic radius. For Re-doped WSe_2, the variations of bandgap are different from other dopants. For K-K transition, $\Delta E_g/\Delta\varepsilon \sim 62$ meV/% up to +1.5% and $\Delta E_g/\Delta\varepsilon$ -147 meV/% for further decreasing bandgap up to 5%, also for Γ-K transition, the $\Delta E_g/\Delta\varepsilon \sim -155$ meV/%. **Table 4.2** shows the value of $\Delta E_g/\Delta\varepsilon$ for pristine WSe_2, Nb, Ta, and Re-doped WSe_2 monolayer for K-K (A peak) and Γ-K (I peak). We observe that the magnitude of the bandgap tunability is the largest with the pristine WSe_2 monolayer and lowest for the Re-doped WSe_2 monolayer. We can write the shift following the order of WSe_2 > Nb-doped WSe_2 > Ta-doped WSe_2 > Re-doped WSe_2.

Table 4.2: The slope of the K-K (A) and Γ-K (I) bandgaps with respect to biaxial tensile strain (in unit of meV/%) for pristine WSe_2 and Nb, Ta, and Re-doped WSe_2 monolayer.

Bandgap Transition	$\Delta E_g/\Delta \varepsilon$ (meV/%)			
	WSe_2 monolayer	Nb-doped WSe_2	Ta-doped WSe_2	Re-doped WSe_2
K-K (A)	114	90	88	62 (0-1.5%) 147 (1.5-5%)
Γ-K (I)	204	187	181	155

4.3.3 Optical properties of pristine and Nb, Re, and Ta-doped WSe_2 monolayer under biaxial strain

Here, we first investigate the optical properties of pristine and Nb, Ta, and Re-doped WSe_2 monolayer from the real and imaginary parts of the dielectric function in detail. In this work, we have analyzed the optical properties of the doped and pristine WSe_2 monolayers without considering excitonic effects. The excitonic effects can only be considered by the approaches outside the standard DFT formalism, such as GW approaches that were not part of this present study. The frequency-dependent complex dielectric function can be expressed as

$$\varepsilon(\omega) = \varepsilon_1(\omega) + i\varepsilon_2(\omega) \qquad \textbf{(4.2)}$$

which is the measure of the light absorption and emission of material. The imaginary part of the dielectric constant $\varepsilon_2(\omega)$ is an important parameter to measure the optical absorption in materials and can be computed by using the following expression [333]:

$$\varepsilon_2 = \frac{2\pi e^2}{V\varepsilon_0}\sum_{k,V,c}\left|\langle\psi_k^c|\hat{u}.r|\psi_k^V\rangle\right|^2\delta[E_k^c - E_k^v - \hbar\omega] \qquad \textbf{(4.3)}$$

where ω is the frequency of light, ε_0 is the dielectric constant of vacuum, ψ_k^c and ψ_k^V are the conduction and valance band wave functions, respectively, V is the volume of the unit cell, $\hat{u}$ is the vector defining the polarization of the E_{ext} of incident light. It is essential to mention that two different directions of E_{ext} polarizations of the incident light, namely (i) the E ∥ xy-plane (in-plane) and (ii) the E ⊥ xy-plane (out-plane). It is noted that in 2D materials, the in-plane dielectric constant is larger than in the out-of-plane direction [334]. Thus, in this work, we have mainly discussed optical properties in the in-plane direction.

The real part of the dielectric function $\varepsilon_1(\omega)$ is associated with dispersion in materials and, can be obtained using the Kramer-Kronig relation, and is given by [335]

$$\varepsilon_1(\omega) = 1 + \left(\frac{2}{\pi}\right)\int_0^\infty d\omega' \frac{(\omega')^2\,\varepsilon_2(\omega)}{(\omega')^2 - \omega^2} \qquad \textbf{(4.4)}$$

The energy-dependent absorption coefficient $\alpha(\omega)$, can be deduced from ε_1 and ε_2 and mathematically, can be calculated as:

$$\alpha(\omega) = \sqrt{2}\omega\left[\sqrt{\varepsilon_1^2(\omega)+\varepsilon_2^2(\omega)}-\varepsilon_1(\omega)\right]^{1/2} = \frac{2\kappa}{c} \quad \textbf{(4.5)}$$

Where, κ is the extinction coefficient, and c is the velocity of light.

Fig. 4.6 shows that absorption spectra, $\varepsilon_1(\omega)$ and, $\varepsilon_2(\omega)$ the plot of pristine and Nb, Ta, and Re-doped WSe_2 monolayer for the energies from 0 to 3 eV. The WSe_2 monolayer shows an absorption edge at ~ 1.55 eV, close to the DFT-PBE bandgap of the material. Also, the absorption spectra have one peak in the lower energy range at ~ 1.8 eV, and another peak at the higher energy of 2.7 eV shown in Fig. 4.6(a). The peaks for the WSe_2 monolayer primarily lie among the visible light range (400–800 nm), which is well-matched with previous experimental results [98, 311, 336]. The experimental absorption spectra of WSe_2 consist of two peaks in lower energy corresponding to A exciton, and B exciton and, one peak at the high energy region [336-338]. The absence of some peaks between the DFT-PBE absorption spectra and the experiment can be attributed to the excited states not being taken into account. As shown plot of $\varepsilon_1(\omega)$ and $\varepsilon_2(\omega)$ also matched with experimental dielectric response function of the WSe_2 monolayer [207, 338]. The peaks in the imaginary part of the dielectric function represent inter-band transitions. The absorption spectra get modified when the WSe_2 monolayer is doped with Nb, Ta, and Re, resulting in changes to its optical response. A redshift in the absorption band edge was observed for Nb, Ta, and Re-doped WSe_2 monolayer. The absorption peak around ~ 1.8 eV disappears on doping with Nb and Ta-dopants, whereas a small broadening was observed for an energy range below 1 eV. However, for the Re-doped WSe_2 monolayer, a slightly broadened peak is present at ~ 1.8 eV, whereas a significant peak is observed in the infrared region at energy < 1 eV. This suggests that different impurity states are introduced in the materials that give rise to different absorption features in the absorption spectra of doped WSe_2 monolayer due to doping. This also suggests that Nb, Ta, and Re-doping have an insightful influence on the optical properties of the host WSe_2 monolayer. A similar observation has been reported for the cases of TM-doping in phosphorene by Kong *et al*. [339]. The redshift in the absorption spectra due to TM-doping makes the WSe_2 monolayer highly applicable for broadband photodetection and photocatalytic applications.

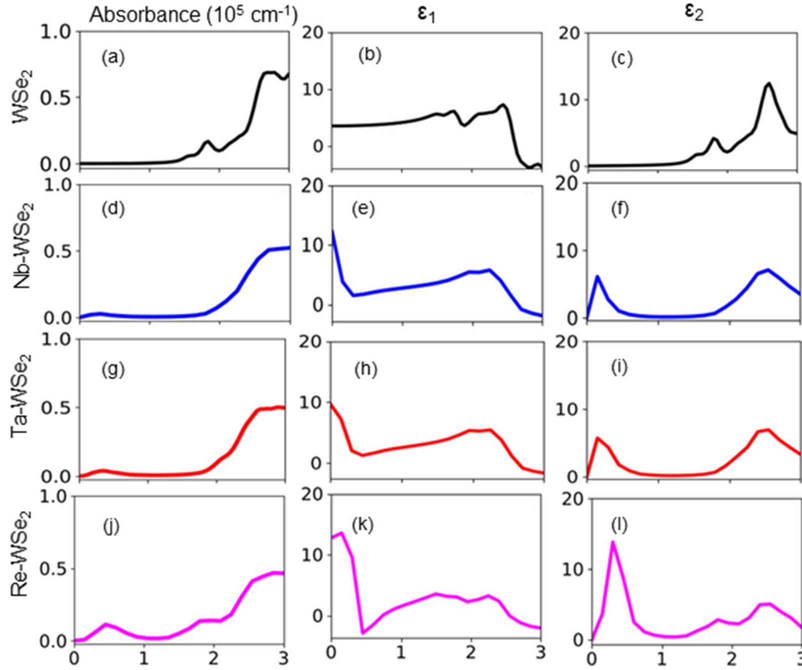

Fig. 4.6 The optical properties of pristine and Nb, Ta and Re-doped WSe_2 monolayer, Panel (a)-(j) represents absorption spectra, (b)-(k) characterizes the real part of the dielectric function $\varepsilon_1(\omega)$, and (c)-(l) $\varepsilon_2(\omega)$ the imaginary part of the dielectric function

Now, we investigate the tuning of absorption spectra of WSe_2 and Nb, Ta, and Re-doped WSe_2 monolayer by applying a biaxial strain. The absorption spectra of the pristine and doped-WSe_2 monolayer with the tensile and compressive strain of +5% (violet) and -5% (green) are shown in **Fig. 4.7.** Upon application of tensile strain (+5%), a redshift in the absorption spectrum of the WSe_2 monolayer was observed with no other significant changes in spectra shape. However, for compressive strain, a blue shift in spectra was observed with the disappearance of peaks at lower energy. Although at higher energy, the nature of spectra almost remains the same. This can be interpreted in a higher value $\Delta Eg/\Delta \varepsilon$ for tensile strain than compressive strain (see Table. 2). In Nb and Ta-doped WSe_2 monolayer, a redshift in spectra was observed at +5%, with no broadening in the lower energy region. Interestingly, an absorption peak around ~ 1.3 eV appears very close to the native peak in the WSe_2 monolayer. A blue shift was observed with enhanced absorption in the infrared region at -5% for both Nb and Ta-doped WSe_2 systems. For the Re-doped WSe_2 monolayer, no significant shift in absorption edge was observed at +5%, although suppressed broadening of a peak at lower energy <1eV and significantly enhanced absorption observed at higher energy range. At compressive strain of -5%, a significant broadening is observed in the energy range

between ~ 0.8 eV to 2 eV which is almost negligible in both unstrained and tensile strain conditions.

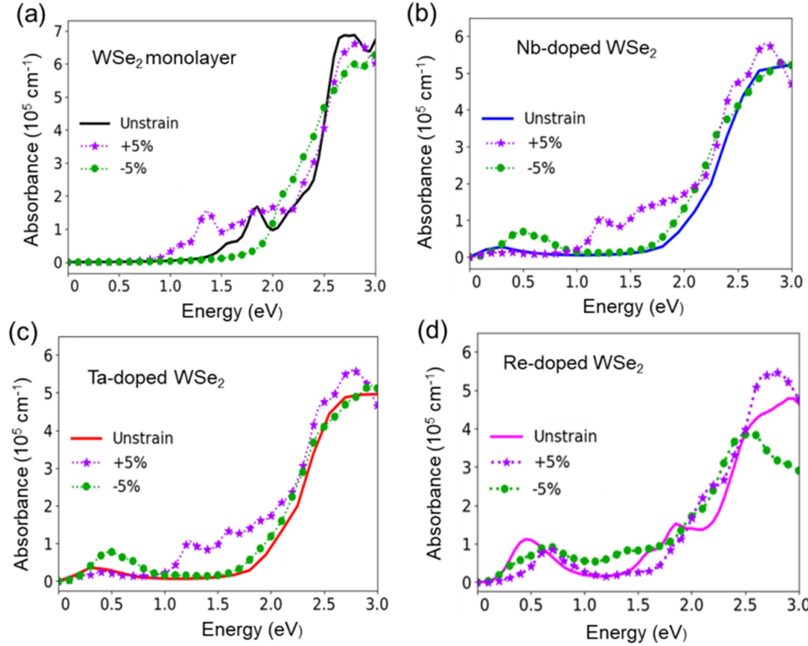

Fig. 4.7 Biaxial tensile and compressive strain tuning of absorption spectra of (a) pristine WSe_2 (b) Nb-doped WSe_2 (c) Ta-doped WSe_2 (d) Re-doped WSe_2 monolayer.

4.3.4 Strain-dependent doping behaviour of TM-doped WSe_2 monolayer

The dopants E_{form} for substitutional dopants can be defined as [254, 315]

$$E_{form}(V) = \Delta E_T\,(V) + \mu_{host} - \mu_{\mathrm{dopant}} \tag{4.6}$$

Where, $\Delta E_T = E_T^{host+dopant} - E_T^{host}$, the $E_T^{host+dopant}$ is the total energy of the doped WSe_2 monolayer and E_T^{host} is the total energy of the undoped WSe_2 monolayer, while μ_{dopant} and μ_{host} are the chemical potentials of the substitutional TM dopant and host W atom in its bulk form. For simplicity, we assume that the chemical potential difference is not much sensitive to the change in volume (V), so any values of them do not change our results. Therefore, we can see that the E_{form} and ΔE_T follow the same variation with V. We note that under equilibrium conditions, the dopants concentration N_d at the temperature T related to E_{form} by the given relation

$$N_d = N_0 \exp\left(-\frac{E_{form}(N_d)}{k_B T}\right) \tag{4.7}$$

Where N_0 the concentration without any dopants and k_B is the Boltzmann constant. Typically, for any pristine semiconductor the total energy (E_T^{host}) as a function of V can be expressed as [69].

$$E_T^{host}(V) = \alpha_0(V - V_0)^2 \quad \textbf{(4.8)}$$

Where, V_0 is the volume of host material under equilibrium and $\alpha_0 = \frac{1}{2}\frac{B_0}{V_0}$, with B_0 being the bulk modulus [69]. However, for a host system with a dopant, its total energy can be written as:

$$E_T^{host+dopant}(V) = (\alpha_0 + \Delta\alpha)[V - (V_0 + \Delta V)]^2 \quad \textbf{(4.9)}$$

Where $\Delta\alpha$ and ΔV are changed in α_0 and V_0 due to the dopants. The net change in total energy as a function of V can be expressed as:

$$\Delta E_T(V) = E_T^{host+dopants}(V) - E_T^{host}(V)$$
$$= -2\alpha_0 \Delta V\,(V - V_0) + \Delta\alpha(V - V_0)^2 \quad \textbf{(4.10)}$$

From Eq. 5, it is clear that the behavior of ΔE_T with V depends upon the value of ΔV and $\Delta\alpha$. Now, we have two cases, *Case-1*: If ΔV is large and $\Delta\alpha$ negligible, then ΔE_T mostly varies linearly with V (first term in eq.5). *Case-2*: However, if ΔV is very small and $\Delta\alpha$ has significant value, then the high-order second term in Eq. (5) could become dominant, giving a parabolic dependence of ΔE_T *to* V under strain.

It may be noted that in substitutional doping, the net volume change ΔV due to dopants depends upon the atomic size and electronic environment between the host and dopants [69]. In general, a common perception is that the small dopants induce a volume shrinkage and whereas large ones induce a volume expansion. However, the ΔV is also affected by the electronic environment surrounding the dopant and host. A p-type dopant atom induces an electronic environment that has negative global volume change, whereas the opposite will be true if the system is doped by an n-type dopant with an extra valence electron. Typically, the value of $\Delta\alpha$ in substitutional doping is very small.

The calculated bond lengths of Nb-Se and Ta-Se bonds are 2.59 Å and 2.58 Å respectively which are slightly larger than the W-Se. In contrast, the bond length of Re-Se and *V*-Se are 2.52 Å and 2.50 Å smaller than the W-Se bond in the WSe_2 monolayer. We have carried out spin-polarized calculations to check the magnetic ground state The Nb, Ta, and Re-doped WSe_2 remain nonmagnetic [316] whereas *V*-doped WSe_2 is a magnetic semiconductor in nature, well-matched with the reported works [294]. However, the inclusion of spin polarization neither affects the calculation for E_{form}, nor the change in its value at any strain condition. Therefore, we have not considered spin-polarization into account. At unstrained conditions, all the TM-doped WSe_2 systems have a negative E_{form} in Se-rich conditions, indicating a stable doped system (the values are listed in Table. 4.3).

The biaxial strain ($\varepsilon = \varepsilon_x = \varepsilon_y$) varying from -5% to +5% is applied to study the strain-dependent doping behavior of the WSe_2 monolayer. The magnitude of biaxial strain is defined as $\varepsilon = (a_0 - a)/a \times 100\%$, where a_0 and a are the lattice constants of the TM-doped WSe_2 monolayer with and without applied biaxial strain. **Fig. 4.8** (a)-(c) shows the schematic atomic structure of TM-doped WSe_2 monolayer under compressive, unstrain, and tensile strain conditions.

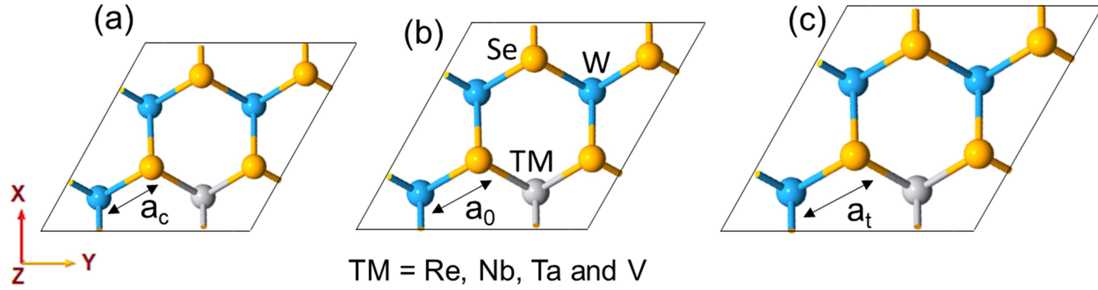

Fig. 4.8 Schematic atomic structure of transition metal (TM = Re, Nb, Ta, and *V*) doped WSe_2 monolayer with a top view under biaxial (a) compressive strain (b) unstrain (c) tensile strain conditions.

First, we analyzed the effect of TM dopants on the electronic structure of the WSe_2 monolayer in detail. **Fig. 4.9** (a)-(d) presents the projected density of states (PDOS) of the TM-doped WSe_2 monolayer. We observed that the density of states of the TM (Re, Nb, Ta, and *V*)-dopants in both conduction and valence band are mainly characterized by d-orbitals. When one W atom substitutionally replaced by a Re atom, an extra electron has added to the system. Due to one extra electron, the Fermi level (E_F) moves inside the conduction band minimum (CBM), and Re-doped-WSe_2 became an n-type semiconductor as shown in Fig. 4.9 (a). In the case of the Nb, Ta, and *V* dopants in the WSe_2 monolayer, E_F shifts inside the valance band maximum (VBM) due to the removal of one electron from the system without the creation of any mid-gap states. Consequently, Nb, Ta, and *V*-doped WSe_2 systems behave as p-type semiconductors. We have noted that no hole-localized or electron-localized states are observed in the middle of the bandgap and therefore the holes or electrons can be readily released from each dopant to the valance (conduction) band and contribute to the free carrier concentration. These observations well matched with the other theoretical and experimental results on TM-doped WSe_2 monolayer [253, 314, 315]. **Table 4.3** lists all the calculated parameters for TM atoms in the present study.

Table 4.3: The doping type, bond length (between TM dopant and Se atom), ionic radii, formation energy (E_{form}), and change in volume (ΔV) due to substitutional TM doping

Transition metal	Doping type	Bond length (Å) (TM-Se)	Ionic radius [340] (Å)	E_{form} (Se-rich) (eV)	Δ V ($Å^3$)
W (host)	-	2.56	0.66	-	-
Re	n	2.52	0.63	-1.45	+0.4
Nb	p-	2.59	0.72	-3.61	+13
Ta	p	2.58	0.72	-3.01	+13.8
V	p	2.50	0.79	-2.64	+2.3

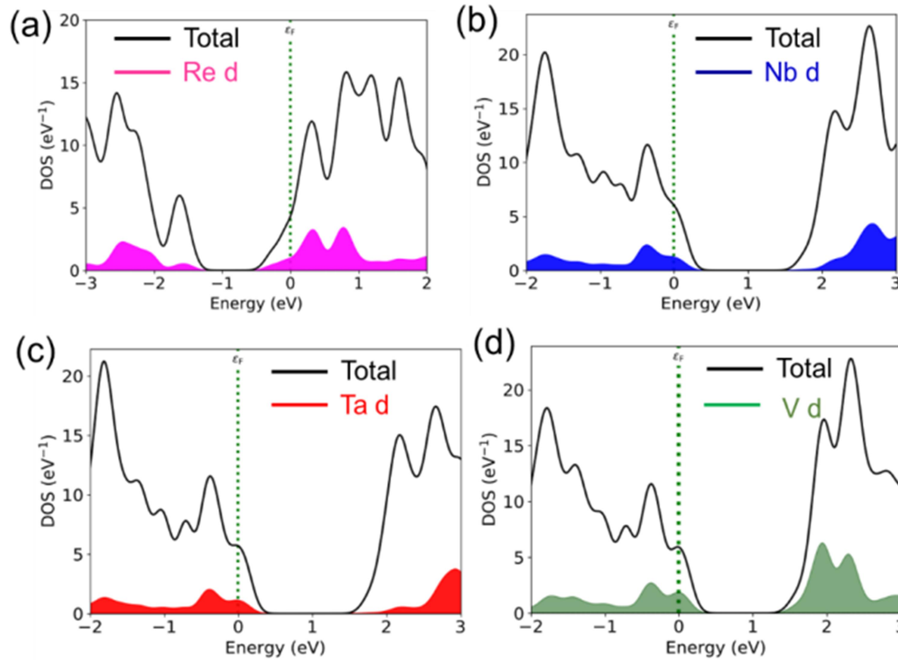

Fig. 4.9 PDOS of (a) Re doped-WSe_2 (b) Nb-doped WSe_2 (c) Ta-doped WSe_2 (d) *V*-doped WSe_2 monolayer

Now we will discuss the variation of E_{form} with biaxial strain for Re, Nb, Ta, and *V* dopants in the WSe_2 monolayer in detail. First, let us consider the case of Re which is an n-type dopant in the WSe_2 monolayer. **Fig. 4.10 (a)** compares variation in total energy as a function of V of pristine WSe_2 monolayer and Re doped-WSe_2 monolayer. We note that Re^{+4} has a smaller ionic radius (0.63 Å) than the W^{+4} (0.66 Å) host atom [41]. But due to the n-type electronic environment, a volume expansion also materializes which resulted in a negligible value of ΔV due to Re substitution. **Fig. 4.10 (b)** shows the variation of E_{form} (=ΔE_T) with applied biaxial strain for the Re dopant. As expected, the variation of E_{form} with biaxial strain is dominated by the second term in eq. 4.10, and it is parabolic in nature. The

value of E_{form} decreases under the application of both compressive as well as tensile strain. From Fig. 4.10 (b), it is observed that the change in E_{form} up to +3% tensile strain is ~ 0.2 eV, much higher than the E_{form} value at -3%. Although, by further increasing strain value up to +5%, compressive strain is more dominant in reducing E_{form} as compared to tensile. This suggests that the dopability of Re dopant can be controlled and enhanced under the application of suitable biaxial strain, which could lead to the desired contents in monolayer WSe_2 for various electronic device applications.

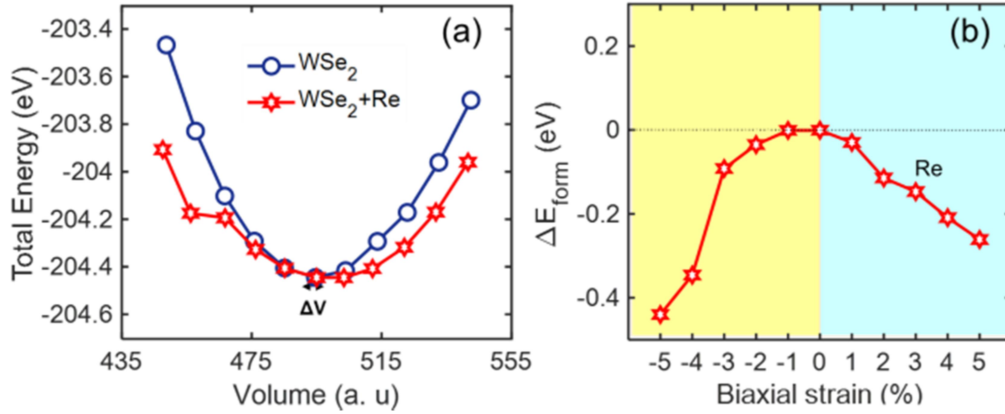

Fig. 4.10 (a) Comparison of total energy versus V curve for WSe_2 and Re-doped WSe_2 monolayer, the ΔV is the net change in volume between host and dopant atom (b) E_{form} (=ΔE_T) versus strain curve for Re-dopant, shows the parabolic behavior.

Now, let us consider the p-type dopants i.e. Nb, Ta, and *V* in the WSe_2 monolayer. The Nb^{+3} (0.72 Å) and Ta^{+3} (0.72 Å) dopants have a similar ionic radius [341] which is larger than the host W^{+4} (0.66 Å) atom. Although due to p-type doping behavior, it induces a volume contraction, although still a positive value of ΔV ~ 13Å^3 is observed. This large change in ΔV gives a right shift in its total energy versus the V curve as shown in **Fig. 4.11 (a).** The E_{form} of Nb and Ta dopants is plotted as a function of biaxial strain as shown in **Fig. 4.11 (b)** which is dominated by the first term in eq. 4.10. Due to having monotonic linear relation with strain, the doping concentration will increase under tensile strain as compared to compressive strain. The change in E_{form} at 2% strain value is 0.09 eV, whereas by further increasing strain at 4%, a very small reduction is observed. This shows it is harder to enhance doping concentration at a higher strain value. A similar observation for Nb and Ta dopants in the MoS_2 monolayer is also reported by Choi *et al*. [341].

In the case of *V* dopants, a very small change in ΔV~ 2.3 Å^3 is observed. Since the ionic radius of V^{+2} (0.79 Å) is much larger than the W, but due to volume reduction, a small ΔV was observed. The variation of total energy with V is plotted in **Fig. 4.11 (c). Fig. 4.11 (d)**

shows a plot between E_{form} and biaxial strain, which is parabolic in nature. This behaviour can be similarly analyzed as Re dopants. However, by comparing E_{form} at a given strain (±5%) value, it is observed that the change in E_{form} is higher for Re as compared to the *V* dopant. While, for Nb, Ta, and *V* p-type dopants, the change in E_{form} at any value of tensile strain value is quite similar.

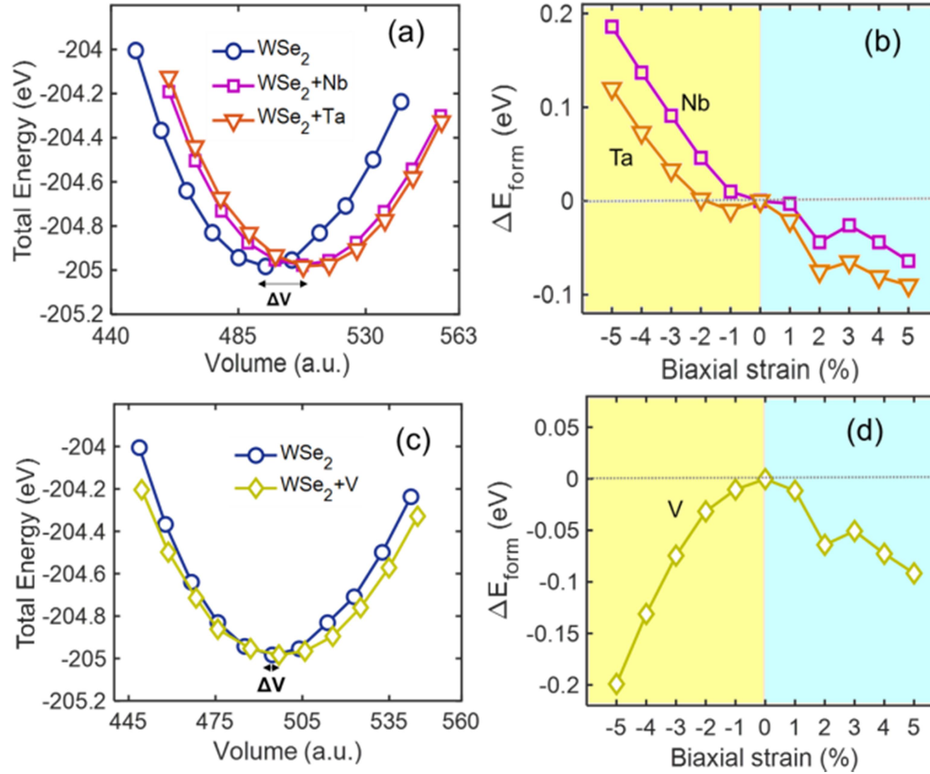

Fig. 4.11 (a, c) The total energy versus V curve and (b, d) E_{form} (=ΔE_T) versus strain plot for Nb, Ta, and *V* dopants, A linear relation of E_{form} with strain observed for Nb and Ta, whereas a parabolic behavior observed for *V* dopant.

4.3.5 Electronic structure of Al doped g-ZnO (g-AZO) monolayer

The g-ZnO monolayer has a planar honeycomb structure with lattice constant a = 3.27 Å, and $d_{Zn\text{-}O}$ = 1.89 Å which is in good agreement with the previous studies [342]. In this work, we have taken a 4×4×1 supercell of g-ZnO monolayer where one Zn atom has been replaced by one Al dopant by the substitutional doping method which corresponds to a 6.25% doping concentration of Al atom in ZnO monolayer. The doping process between the Al atom and the Zn hosts atoms in AZO thin films is a charge transfer type as reported in the literature [343, 344]. The optimized geometrical structure of the g-AZO monolayer with the top and side views is shown in **Fig. 4.12 (a) and (b).** The optimized lattice constant and bond length

for the g-AZO monolayer obtained from GGA calculations are determined as a = 3.29 Å, and d_{Al-O} = 1.77 Å, which agrees with previous reports [345]. The electronic band structure and projected density of states (PDOS) of the pristine g-ZnO and g-AZO monolayer are compared as shown in **Fig. 4.13 (a) and (b).**

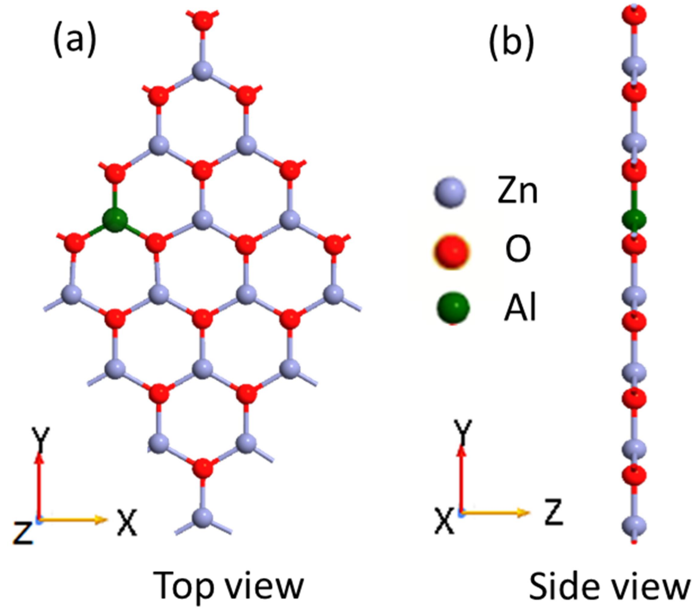

Fig. 4.12 Schematic atomic structure of 4×4×1 g-AZO monolayer (a) top and (b) side view shows the hexagonal arrangement of the g-AZO monolayer, where Zn, O, and Al are represented by grey, red, and green balls respectively.

The band structure of g-ZnO and g-AZO monolayer are found to be direct (Γ- Γ) in nature with the band gap (E_g) values of 3.98 eV and 3.8 eV respectively [345, 346]. It is observed that upon Al doping, the Fermi level (E_F) shifts inside the conduction band minima (CBM), therefore showing an n-type doping effect that is similar to Al doping in the bulk ZnO layer. It is noted that the band gap of the g-ZnO monolayer is larger than that of the ZnO bulk counterpart; this is due to the quantum confinement effect [215, 347]. From PDOS as shown in Fig. 4.13 (b) and (d), it is observed that the main contribution of VBM is mainly derived from the O- 2p and Zn-3d orbital, and for CBM, the energy states from Zn-4s orbital are the main contributors. The enlarged DOS in Fig. 4.13 (b) clearly indicates all the contributions of the s, p, and d orbitals of the Zn atom.

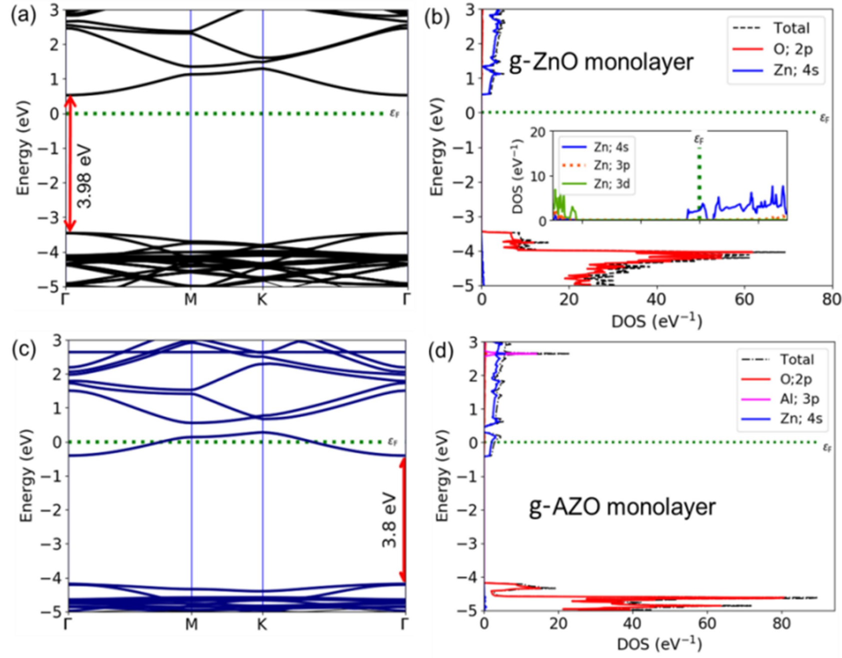

Fig. 4.13 Band structures and PDOS of (a), (b) g-ZnO monolayer and (c), (d) g-AZO monolayer along with high symmetric directions (Γ-M-K-Γ) obtained by HSE06 calculations; the g-ZnO monolayer has a bandgap of 3.98 eV, whereas g-AZO monolayer has a bandgap of 3.8 eV, the Fermi level (E_F) presented by a green dashed line.

4.3.6 The formation energy of Al dopant in ZnO monolayer under biaxial strain

To determine the stability of Al dopants in the g-ZnO monolayer, the E_{form} of the g-AZO monolayer is calculated by using the following relation [72, 198]

$$E_{form} = E_{host+dopant} - E_{host} + \mu_{host} - \mu_{dopant} \quad \textbf{(4.11)}$$

Where, $E_{host+dopant}$ and E_{host} are the total energy of the pure g-ZnO and g-AZO monolayer, μ_{host} and μ_{dopant} represent the chemical potentials of the Zn and Al atom, respectively. The E_{form} of the g-AZO monolayer is obtained as -2.98 eV in Zn-rich conditions [54] which indicates that the chemical reaction is exothermic in nature, and the g-AZO monolayer is thermodynamically stable. Now, we determine the variation of E_{form} under the application of biaxial strain varying from -10% to +10%. We observed that upon application of biaxial strain, the size of the monolayer increases (decreases) in tensile (compressive) strain. However, the value of chemical potential remains constant, since it is the intensive quantity of the system. So, the changes in the value of chemical potential difference i. e. ($\mu_{host} - \mu_{dopant}$) with respect to strain or volume (V) remain negligible. Thus, it is assumed that the ($\mu_{host} - \mu_{dopant}$) is not much sensitive to the change in strain or V. Therefore, at a particular value of the biaxial strain, the value of E_{form} is given by

$$E_{form} = E_{host+dopan} - E_{host} \quad \textbf{(4.12)}$$

We note that the value of E_{form} also tends to increase/decrease under tensile and compressive biaxial strain, depending upon the net volume change (ΔV) in the material due to dopants substitution. However, the ΔV not only depends upon the atomic size of dopants but also on the electronic environment between the host and the dopants [55, 216, 321]. Here, in this work, the ionic radius of Al^{+3} (0.54 Å) is smaller than Zn^{+2} (0.74 Å) [348], but due to the n-type electronic environment, a volume expansion also materializes. Therefore, the value of ΔV due to Al substitution in the g-ZnO monolayer is negligible. **Fig. 4.14(a)** compares the plot of total energy versus volume (V) for g-ZnO and g-AZO monolayer, which clearly shows the negligible value of ΔV. **Fig. 4.14(b)** shows the plot of change in E_{form} (w.r.t to unstrained g-AZO) of g-AZO monolayer under biaxial strain varying from -10 % to +10 %. It is observed that for ε_{xy} range ~ 0 to +5%, the relation between E_{form} and biaxial strain is almost linear and the value of E_{form} becomes more positive with biaxial strain. However, at ε_{xy} > +5% up to +9% an inverse parabolic behavior is observed. It is to be mentioned here that the sign of the E_{form} defines the stability of materials after doping, whereas the (-) E_{form} means stability at the dopants site, and the (+) E_{form} implies instability at the dopants site [71]. From Fig. 4.14(b), it is clear that upto ε_{xy} ~ +9% there are no increases in Al doping concentration in the g-ZnO monolayer due to strain. However, at ε_{xy} = +10%, a sudden decrease in the value of E_{form} is observed and the value of E_{form} becomes more negative, as compared to an unstrained g-AZO monolayer. It indicates that the concentration of Al dopants is very high in the g-ZnO monolayer at ε_{xy} = +10%. Now, the variation of E_{form} under compressive strain is studied and it is found that ε_{xy} between -1% to -8%, a small reduction in E_{form} is observed which suggested that g-AZO monolayer is thermodynamic stable and small increases in Al doping concentration is expected. However, after ε_{xy} > -9% further increases in the value of E_{form} are observed. This suggests that by using compressive strain, the reduction in E_{form} is visible, but it is not sufficient to induce a high doping concentration of the Al atom in the g-ZnO monolayer.

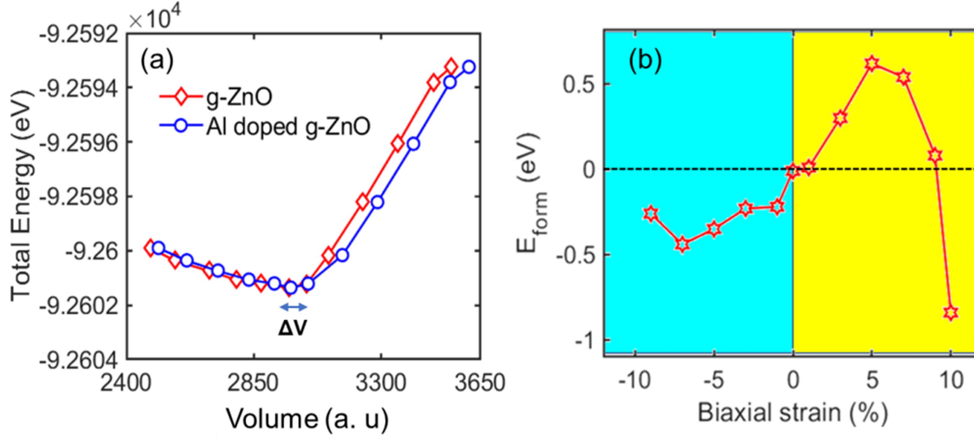

Fig. 4.14 (a) The total energy versus V plot for g-ZnO and g-AZO monolayer, the ΔV is negligible (b) E_{form} (= $E_{g\text{-}ZnO+Al} - E_{g\text{-}ZnO}$) vs. biaxial strain, the value of the E_{form} in the unstrained (0 %) g-ZnO monolayer is set as a reference

4.3.7 The electronic band structures of g-AZO monolayer under biaxial strain

Here, we have studied the effect of biaxial strain on the electronic band structure of the g-AZO monolayer. Since the biaxial strain on pristine g-ZnO is already reported by Chen *et. al.* [213], it is not included in this work. An increase in lattice constant and volume observed as strain varies from -10% to +10%, mainly, due to the changing of coupling between the Zn-O and Al-O atoms during the tensile and compressive strain. The electronic band structure of the g-AZO monolayer at different values of biaxial strain is shown in **Fig. 4.15 (a)-(d).** The bandgap of the g-AZO monolayer is 3.8 eV at unstrained (ε_{xy} = 0%) conditions, and it decreases to 3.48 eV at +5% of tensile strain shown in Fig. 4.15 (a). Further, it continues to decrease up to +9% strain and the obtained bandgap value for +9% is 2.89 eV, by further increasing at +10%, a little increase in value of bandgap i. e 2.91 eV obtained as shown in Fig. 4.15 (b). In the case of compressive strain, the bandgap initially increases up to a certain strain range, and then it started to decrease. Firstly, the bandgap energy increases to 3.83 eV at -1% strain, and then it decreases to 3.76 eV at -5% compressive strain as shown in Fig. 4.15 (c). The bandgap value further decreases to 3.58 eV at -10% compressive strain as shown in Fig. 4.15 (d). We also observed that the nature of bandgap always remains direct at the Γ point for both tensile as well as compressive strain. Therefore, the g-AZO monolayer remains a direct (Γ- Γ) bandgap semiconductor after applying biaxial strains -10 % to +10 %. We note that the band gap energy must exceed the free energy of water splitting of 1.23 eV and be smaller than about 3 eV to enhance solar absorption [349]. Since the band gap of the g-AZO monolayer (3.8 eV) exceeds the value of 3 eV, it does not satisfy the criterion for

photocatalytic application. Therefore, we applied a biaxial strain to tune the electronic band structure of the g-AZO monolayer. We observe an increase in lattice constant and volume as strain varies from -10% to +10%. Mainly, it is due to the changing of coupling between the Zn-O and Al-O atoms during the tensile and compressive strain.

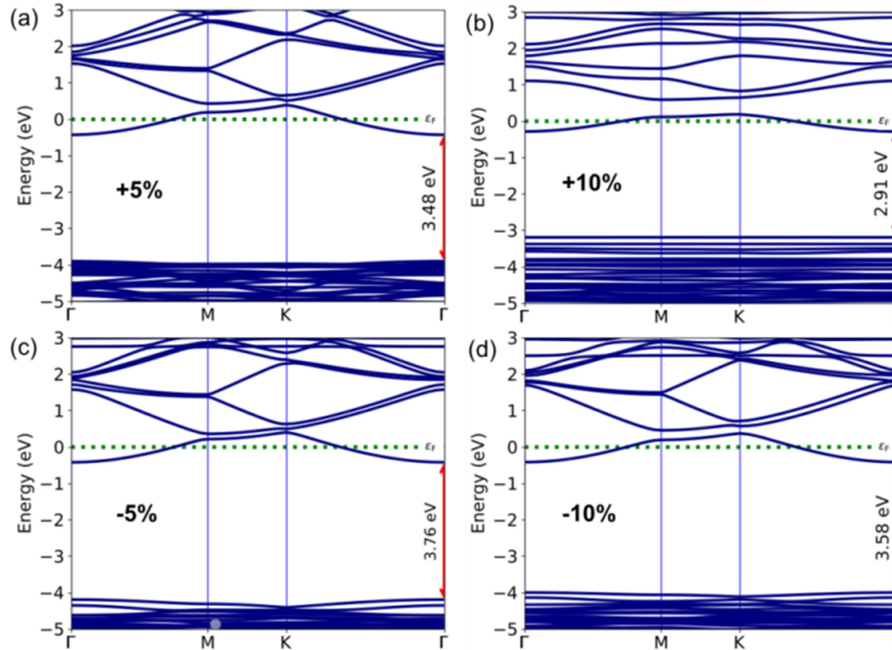

Fig 4.15 Electronic band structure of the g-AZO monolayer at (a) +5%, (b) +10%, (c) -5%, and (d) -10% biaxial strain values

The variation of the bandgap of the g-AZO monolayer with biaxial tensile and compressive strain has been shown in **Fig. 4.16**. The bandgap almost linearly decreases with tensile strain up to +9% and then slightly increases at +10%. For compressive strain, it initially increases up to -1% strain and then started decreasing continuously up to -10%. Therefore, it is noted that the biaxial tensile strain at +9% and +10% has a suitable bandgap value for a photocatalytic water-splitting reaction.

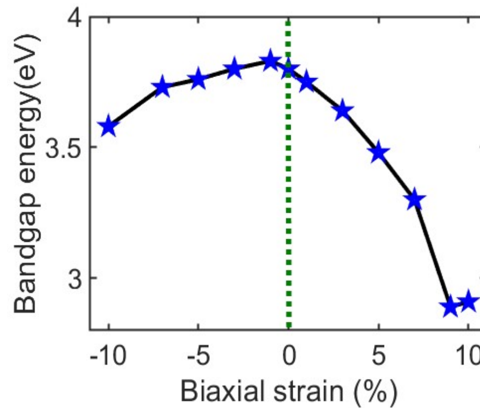

Fig. 4.16 Variation of bandgap energy with different biaxial tensile and compressive strain

4.3.8 The absorption spectra of g-AZO monolayer under application of biaxial strain

For photocatalytic water splitting, the materials must capture a significant portion of the visible spectrum. The absorption coefficient is defined as the decay of light intensity dispersed in a unit length of the given materials and it is calculated by using the frequency-dependent complex dielectric function

$$\varepsilon(\omega) = \varepsilon_1(\omega) + \varepsilon_2(\omega) \quad \textbf{(4.13)}$$

The energy-dependent absorption coefficient $\alpha(\omega)$ can be deduced from ε_1 and ε_2 and mathematically written as

$$\alpha(\omega) = \sqrt{2}\omega\,[\sqrt{(\varepsilon_1^2(\omega)+\varepsilon_2^2(\omega))}-\varepsilon_1(\omega)]^{1/2} = \frac{2k\omega}{C} \quad \textbf{(4.14)}$$

Where ω is the frequency of light, c is the velocity of light κ is the extinction coefficient. The imaginary part $\varepsilon_2(\omega)$ is used to measure the optical absorption in materials and the real part $\varepsilon_1(\omega)$ is associated with dispersion in materials deduced from the imaginary part ε_2 by the well-known Kramer-Kronig relation.

The absorption spectra of the g-AZO monolayer under biaxial tensile and compressive strain are shown in **Fig. 4.17(a) and (c**), and the enlarged version of the wavelength range from 300 nm to 400 nm is shown in **Fig. 4.17(b) and (d)** for the sake of better clarity. For comparison, the absorption spectra of the g-ZnO monolayer are also included in the spectra (black dashed line). The absorption spectra can be calculated by using the frequency-dependent complex dielectric function [236, 350, 351]. As visible from Fig. 4.17(a)-(d), the g-ZnO monolayer has only absorption within the UV region, in unstrained conditions. When the g-ZnO monolayer is doped with an Al atom (g-AZO), the absorption coefficient decreases, and shifts to a lower wavelength region in the UV region while absorption increases in the visible and infrared (IR) region as shown by the blue solid line. A similar observation for g-AZO bulk and monolayer was also reported by Wu *et. al.* [215] at a higher doping concentration of > 18.75 %. This phenomenon can be well explained by the strain-dependent of E_{form} as shown in Fig. 4.17 (b).

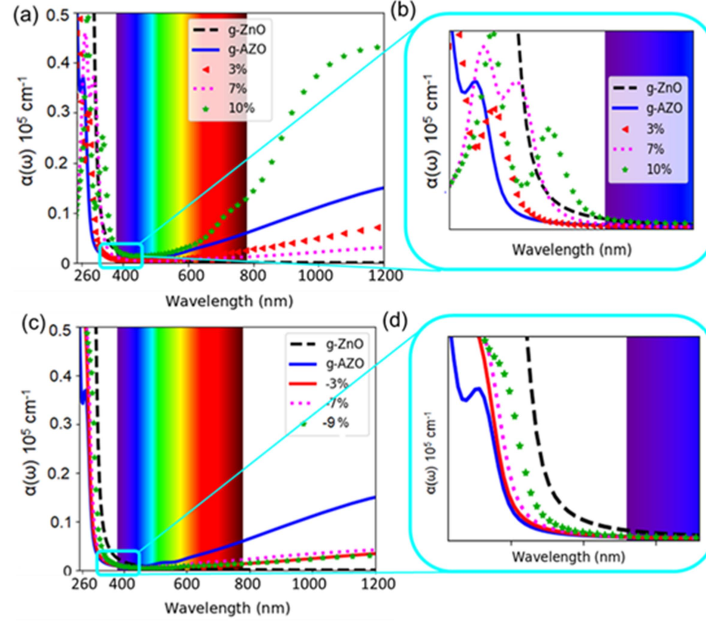

Fig. 4.17 Optical absorption spectra of the g-AZO monolayer (a) under tensile strain (b) enlarged optical spectra to show a shifting of wavelength (c) under compressive strain (d) enlarged version shows the shift of wavelength

As we increase the tensile strain from 0 % to +7%, the absorption shifted to a higher wavelength region (close to the g-ZnO monolayer) as clearly seen in Fig. 4.17 (b), and absorption suppression in visible and NIR regions is also observed. This is due to the positive increase of E_{form} in this tensile strain range, which makes doping harder and the g-AZO monolayer behaves like an undoped g-ZnO monolayer. However, at +10 % strain (green starred line), the absorption is slightly red-shifted, and an increased sharp absorption in the visible and NIR region is observed. This change in the optical spectrum at +10 % is similar to that work reported by Wu *et. al.* [215], at a higher doping concentration of > 18.75 %. This phenomenon of strain-enhanced optical absorption in g-AZO monolayer can be well explained by the strain-dependent behaviour of E_{form} as we have already discussed in detail in Fig. 4.14 (b). Although as compared to tensile strain, in the compressive strain up to -9%, there is no such enhancement in the optical absorption observed as shown in Fig. 4.17 (c). This observation can also be explained by the behavior of E_{form} in the compressive strain as shown in Fig. 4.14 (b). This suggests that the value of E_{form} decreases under compressive strain, but the doping concentration is not sufficient to improve the absorption. It may be noted here that the increase in absorption in visible ranges is only observed for doping concentrations higher than 18%. This observation is reported theoretically by Wu *et al.* [215] and experimentally verified for bulk AZO by Zhang *et al* [217].

4.4 Conclusions

We systematically analyzed the electronic and optical properties of Nb, Ta, and Re-doped WSe_2 monolayer and its tuning under the application of biaxial strain within the framework of DFT-PBE functional. We have determined the bandgap tunability rate for K-K and, Γ–K transition for biaxial tensile strain, following the given order: pristine WSe_2 > Nb-doped WSe_2 > Ta-doped WSe_2 > Re-doped WSe_2. We also determined the critical tensile strain value at which crossover from direct to indirect bandgap takes place. A redshift was observed in the optical spectra of Nb, Ta, and Re-doped WSe_2 monolayer with a significant broadening in the infrared region. By applying biaxial tensile strain, a further redshift and, in compressive strain, a blue-shift was observed in absorption spectra. Therefore, we can significantly modulate the electronic and optical properties of Nb, Ta, and Re-doped WSe_2 monolayer by using a biaxial strain. This can be well explained with higher $\Delta E_g/\Delta\varepsilon$ for tensile as compared to compressive.

Further, we systematically analyze the effect of biaxial strain on E_{form} of Re, Nb, Ta, and *V*-dopants in the WSe_2 monolayer. We propose that the strain-induced change in E_{form} can be used effectively to enhance dopant solubility in the WSe_2 monolayer. It is observed that the E_{form} shows parabolic and linear behaviour with biaxial strain; depending upon the net change in ΔV. The change ΔV is explained based on the atomic radius and induced electronic environment due to different dopant types. For Re and *V*, the calculated E_{form} is parabolic in nature and favors both tensile as well as compressive strain. However, due to the monotonic linear relation with the biaxial strain, E_{form} favors the tensile strain for Nb and Ta dopants. This suggests that strain engineering can be used as an effective tool to enhance the doping concentration of 2D semiconductors.

Further, we systematically studied the strain dependent doping behaviour and optical absorption of the g-AZO monolayer under the application of ε_{xy} by using hybrid DFT calculations. The g-AZO monolayer remains a direct bandgap semiconductor after applying ε_{xy} from -10 % to +10 %. We observed that E_{form} increases linearly upto ε_{xy} = +5% of tensile strain, whereas after ε_{xy} > 5% an inverse parabolic relation with ε_{xy} is observed. However, there is no drastic change in the E_{form} observed for compressive strain range. Due to the lowest value of E_{form} at ε_{xy} = +10%, a higher doping concentration of Al dopants is expected. Moreover, the g-AZO monolayer at ε_{xy} +10% biaxial strains has the highest absorption in the visible range, which further confirms the higher doping concentration of Al dopants in g-ZnO monolayer. As obtained results are well matched with the reported experimental results on AZO thin films for doping concentrations higher than 18%.

Chapter 5

ELECTRONIC BAND STRUCTURE AND OPTICAL PROPERTIES OF GaTe/$MoTe_2$ HETEROSTRUCTURE UNDER DIFFERENT BIAXIAL STRAIN AND ELECTRIC FIELDS

5.1 Introduction

The atomically thin 2D semiconductors are attracting significant attention nowadays for various electronic and optoelectronic applications such as field-effect transistors (FETs), photodetectors [352, 353], p-n junction diodes [354, 355], photovoltaic cells [356, 357], light-emitting devices [358], etc. However, all intrinsic 2D-monolayer materials are limited by their inherent properties which restricted their use in applications that demand controllable electronic and optical properties [319, 359, 360]. To overcome this issue, one solution is to construct 2D van der Waals (vdW) heterostructures by assembling different 2D materials of different bandgaps [218, 226]. In recent years, the 2D heterostructures are highly explored by the device community due to their atomically thin nature, large surface area, and various degrees of freedom [218-220]. It is also expected that some new phenomena/properties can emerge by the weak vdW interaction among heterostructure bilayers. They are divided mainly into vertical and lateral heterostructures, among which vertical stacking of 2D vdW heterostructures attracts more consideration [221-224]. Many technologies can effectively improve the photoelectric properties of heterojunction, such as doping of inverse layer, electrostatic self-assembled layer-by-layer technology, and surface modification method [228-231]. The application of 2D heterostructure mainly depends upon atomic commensurability, interlayer interaction, charge transfer, and band alignment between constituent 2D materials when heterostructure is formed [225-227].

The 2H-phase $MoTe_2$ monolayer is a member of the 2D-TMDCs family with a direct bandgap (~1.1 eV) and broad absorption from ultraviolet (UV) -visible to infrared (IR) region [361, 362]. The GaTe monolayer is an emerging group-III 2D-MMC material with its

main absorption ability only in the UV (λ < 400 nm) region. However, both 2D semiconductors i.e. $MoTe_2$ and GaTe are not suitable for various applications that require strong visible absorption. Recently, Opoku *et. al*.[363] reported MTe_2/GaTe (M = Mo and W) vdW heterostructures as promising photovoltaic solar cell materials. It is noted that all the properties of vdW heterostructures such as bandgap, band alignment, and optical properties are very much sensitive to external perturbations such as mechanical strain, external electric fields, and the interlayer twist angle [110, 111, 244]. Thus, it is also very important to understand the tunability of vdW heterostructures under various external factors. Many vdW heterostructures studies reported so far involve $MoTe_2$ or GaTe as one of the constituent monolayers under various mechanical strains and external electric field values, for various optoelectronics and energy applications [47, 85, 110, 172, 234, 243]. However, so far no work is reported on the modulation of electronic structure and optical properties of GaTe/$MoTe_2$ vdW heterostructures under various external perturbations such as external biaxial strain and electric field.

Therefore in this work, we vertically stacked GaTe and $MoTe_2$ monolayers to form GaTe/$MoTe_2$ vdW heterostructures and investigate their stability, electronic structure, and optical properties using Hybrid-DFT calculations. Among four heterostructure configurations, the most stable GaTe/$MoTe_2$ heterostructure is selected based on the minimum binding energy (E_b) calculations. Further, tunability of band alignment and optical spectra are investigated under biaxial strain range from -9% to +9% and E_{ext} varying between -1 V/Å to +1 V/Å. Our finding suggests that within a practically achievable strain and E_{ext} value, a direct band gap, type-II alignment, and excellent visible response are observed in the GaTe/$MoTe_2$ vdW heterostructure. This shows that the GaTe/$MoTe_2$ vdW heterostructure is an attractive excellent candidate for various optoelectronics and energy device applications.

5.2 Computational Methods

All the DFT calculations are performed using the Synopsys Quantum-ATK package [364]. The exchange-correlation interaction is described by GGA in the PBE form [323]. The energy cut-off for the LCAO basis electron wave function expansion is set to 125 Hartree. The vdWs interactions are adopted by the semi-empirical DFT-D2 dispersion-correction approach [365]. All the structures are fully optimized to minimize the system's total energy until the force on each atom is less than 0.01 eV/Å within a tolerance of 1×10^{-6}. The Brillouin-zone integrations are sampled by Monkhorst-Pack k-mesh with a grid sampling of 5×5×1. A vacuum space set larger than 22 Å is included perpendicular to the hetero surface

to eliminate the coupling between adjacent cells. In addition, we have also calculated the bandgap of monolayers using the HSE06 hybrid functional due to the underestimation of the band gap using the PBE exchange-correlation function [289].

To study the optical absorption properties, the frequency-dependent complex dielectric function $\varepsilon(\omega) = \varepsilon_1(\omega) + \varepsilon_2(\omega)$ is calculated. The energy-dependent absorption coefficient $\alpha(\omega)$ can be deduced from ε_1 and ε_2 and mathematically written as [366]

$$\alpha(\omega) = \sqrt{2}\omega\left[\sqrt{(\varepsilon_1^2(\omega) + \varepsilon_2^2(\omega))} - \varepsilon_1(\omega)\right]^{1/2} = \frac{2k\omega}{C} \quad \textbf{(5.1)}$$

Where ω is the frequency of light, c is the velocity of light κ is the extinction coefficient. The imaginary part $\varepsilon_2(\omega)$ is used to measure the optical absorption in materials and the real part $\varepsilon_1(\omega)$ is associated with dispersion in materials deduced from the imaginary part ε_2 by the well-known Kramer-Kronig relation [367].

5.3. Results and Discussions

5.3.1 The atomic and electronic structure of $MoTe_2$ and GaTe monolayer

Before making the heterostructure, the crystal structure and electronic bandgap of individual GaTe and $MoTe_2$ monolayers are investigated using PBE and HSE06 functionals. The GaTe monolayer has a hexagonal structure with a lattice constant a = b = 4.134 Å, with a repeating unit of Te-Ga-Ga-Te sequence via covalent bonds as shown in **Fig. 5.1 (a).** Similarly, the $MoTe_2$ monolayer also has a hexagonal structure with lattice constant a = b = 3.52 Å with intralayer atoms sandwiched in the order of Te-Mo-Te shown in **Fig. 5.1 (b).** The bond lengths between Ga-Te and Mo-Te bonds are 2.71 Å and 2.72 Å [47, 85]. All the optimized lattice constants are well matching with the reported experimental and theoretical results [47, 88, 243].

Fig. 5.1 (c) and (d) show the electronic band structure of GaTe and $MoTe_2$ monolayer determined using PBE (--dash lines) and HSE06 (solid lines) functionals. The GaTe shows semiconducting nature with an indirect bandgap of 1.47 eV [368], where the valence band maximum (VBM) lies at the Γ point and conduction band minimum (CBM) located at the M point with the standard DFT-PBE results. Similarly, the $MoTe_2$ is a direct-gap semiconductor with a bandgap of 1.14 eV [361], where VBM and CBM are both located at the K point [85]. It is well known that PBE functional underestimates the bandgap; therefore, Hybrid functional is used to calculate the more accurate value of bandgap and optical properties. By using the HSE06 functional, the bandgap values are 2.12 eV for GaTe and 1.57 eV for $MoTe_2$ monolayer, respectively [85, 368].

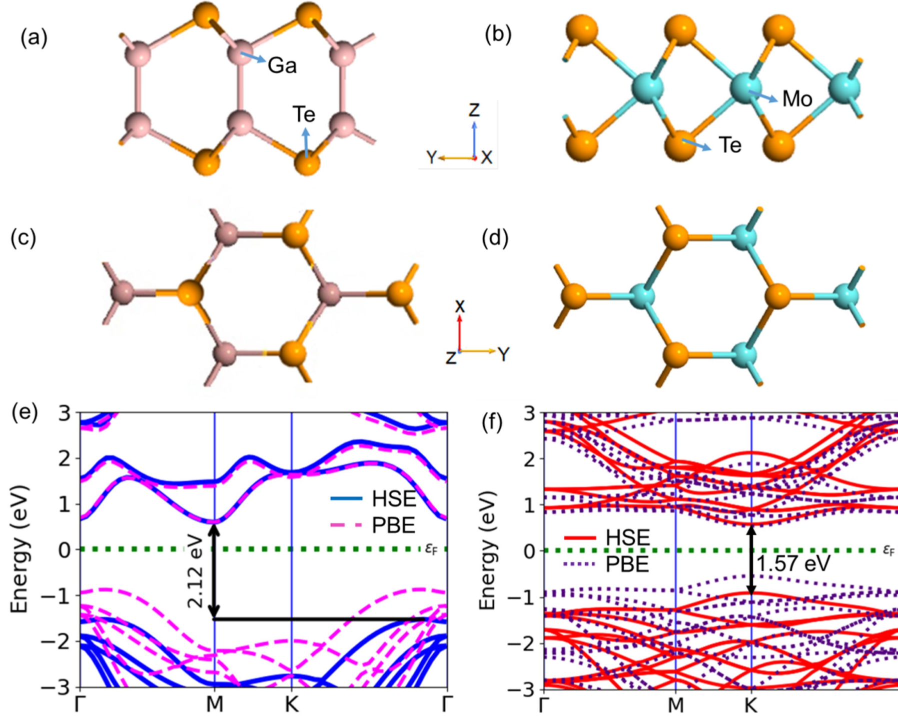

Fig. 5.1 Schematic atomic structure of (a) GaTe and (b) $MoTe_2$ monolayer side view; the top view of (c) GaTe and (d) $MoTe_2$ monolayer and the electronic band structures of (e) GaTe and (f) $MoTe_2$ monolayer, using PBE (dash line) and HSE06 (solid lines) functionals.

5.3.2 Formation and stability of GaTe/MoTe₂ heterostructures with different stacking order

The GaTe/$MoTe_2$ heterostructure is constructed by the vertical stacking of one GaTe monolayer on the top of the $MoTe_2$ monolayer in a virtual Nano lab in Quantum-ATK [87]. For the construction of the GaTe/$MoTe_2$ heterostructure, we have taken a $\sqrt{6} \times \sqrt{6} \times 1$ GaTe and 2×2×1 $MoTe_2$ supercells, with lattice mismatch of ~0.34%, where the $MoTe_2$ is strained with respect to GaTe monolayer when building the heterostructure stacking model. Further, the GaTe/$MoTe_2$ heterostructure with four different stacking patterns labeled as A, B, C, and D has been constructed to obtain the most stable configurations.

The top and side views of different stacking patterns are shown in **Fig. 5.2 (a) to (d).** To determine the relative stability, the binding energy (E_b) is calculated for each GaTe/$MoTe_2$ heterostructure configuration by using the following relation [234, 369]

$$E_b = E_{\mathrm{GaTe/MoTe2}} - E_{\mathrm{GaTe}} - E_{\mathrm{MoTe2}} \quad \textbf{(5.2)}$$

Where, $E_{\mathrm{GaTe/MoTe2,}}$ E_{GaTe} and E_{MoT} represent the total energy of the GaTe/$MoTe_2$ heterostructure, GaTe, and $MoTe_2$ monolayers, respectively. By using eq. (2), the calculated

E_b of the A, B, C, and D stacking models are given as -1.40 eV, -1.404 eV, -1.41 eV, and -1.39 eV, respectively, suggesting that these structures are energetically favorable. Based on the E_b values, the trend of stability is analyzed, which is given as C>B>A>D. The most stable stacking pattern is stacking model- C, where the Te atom locates at the top site of the Mo atom. Therefore, for further study, we have taken stacking pattern (C) into account.

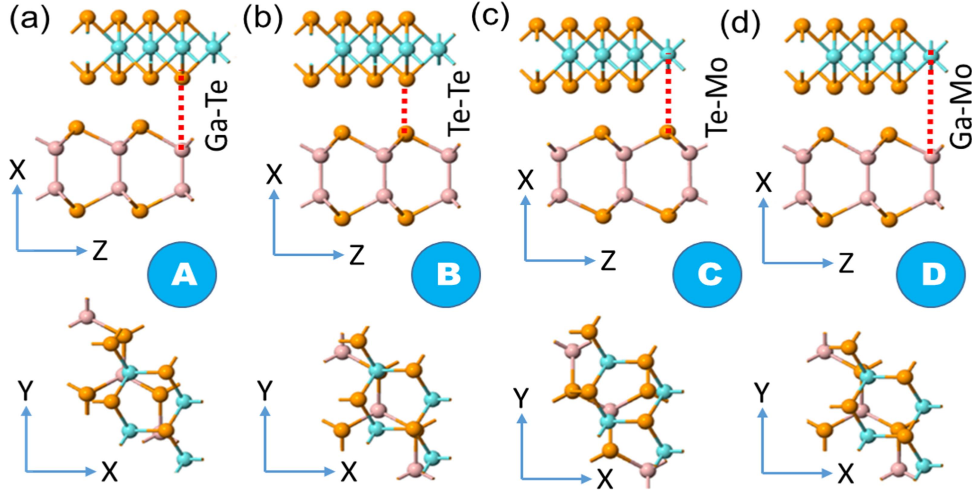

Fig. 5.2 The top and side views of stacking patterns of the $GaTe/MoTe_2$ heterostructures (a) A, where the Ga atom is on the top of the Te atom (b) B, where the Te atom is on the Te atom (c) C, where Te atom on top of Mo atom and (d) D, where Ga atom on the top of Mo atom

Furthermore, we have determined the optimized interlayer distance (d_{in}) in the $GaTe/MoTe_2$ heterostructure (Te-Mo), by calculating E_b with the varying value of d_{in} as shown in **Fig. 5.3 (a).** The lowest value of the d_{in} is ~3.7 Å for the most stable position. **Fig. 5.3 (b)** shows the effective potential plot of the $GaTe/MoTe_2$ heterostructure along the z-direction, by applying Dirichlet and Neumann boundary conditions. It can be seen that $MoTe_2$ has a deeper potential than GaTe and a large potential difference (ΔV) of ~15.3 eV across the $GaTe/MoTe_2$ heterostructures. The presence of such huge ΔV implies that the charge transfer and injection are influenced by a strong electrostatic field. The schematic diagram of the band alignment of GaTe and $MoTe_2$ monolayer in $GaTe/MoTe_2$ heterostructure is shown in **Fig. 5.3 (c),** which shows typical type-I band alignment. The electron affinity (χ) and work function are the energy difference between CBM and Fermi level (E_F) to vacuum level, as displayed in Fig. 5.3 (c). As obtained values of χ are 3.51 eV and 3.75 eV, and the value of work function are 4.16 eV and 4.26 eV for GaTe and $MoTe_2$ monolayer respectively, which is well-matched with the literature [227, 370].

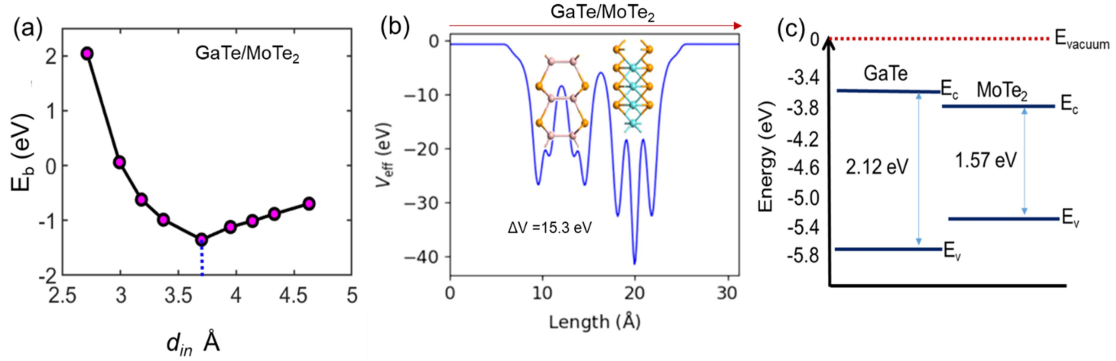

Fig. 5.3 (a) The E_b versus the d_{in} for the GaTe/MoTe$_2$ heterostructure of C stacking pattern (b) Effective potential plot at GaTe/MoTe$_2$ heterostructures, showing an ΔV ~ 15.3 eV (c) Band alignment of individual GaTe and MoTe$_2$ monolayer in GaTe/MoTe$_2$ heterostructure. It is observed that GaTe/MoTe$_2$ heterostructure has typical type-I band alignment

5.4.3 The electronic structure and the optical properties of GaTe/MoTe$_2$ vdW heterostructure

The projected electronic band structure and the density of state (PDOS) of the most stable GaTe/MoTe$_2$ heterostructure (Te-Mo) are analyzed in detail using HSE06 functional as shown in **Fig. 5.4 (a) and (b).** The calculated bandgap of GaTe/MoTe$_2$ heterostructure is 1.5 eV, which is indirect in nature with bandgap transition from K→M in the Brillouin zone. It is observed that the GaTe/MoTe$_2$ heterostructure has a typical type-I band alignment (matched with Fig. 5.3(c)), where CBM and VBM of the heterostructure both come from the MoTe$_2$ layer (blue solid line). The electrons and holes are localized in the CBM and VBM of the MoTe$_2$ layers. The PDOS of GaTe/MoTe$_2$ heterostructure shows that the CBM and VBM both are dominated by the 4d orbital of the Mo atom, and the 5p orbitals from Te mainly originated from the MoTe$_2$ monolayer. These PDOS results are consistent with the projected band structures observations.

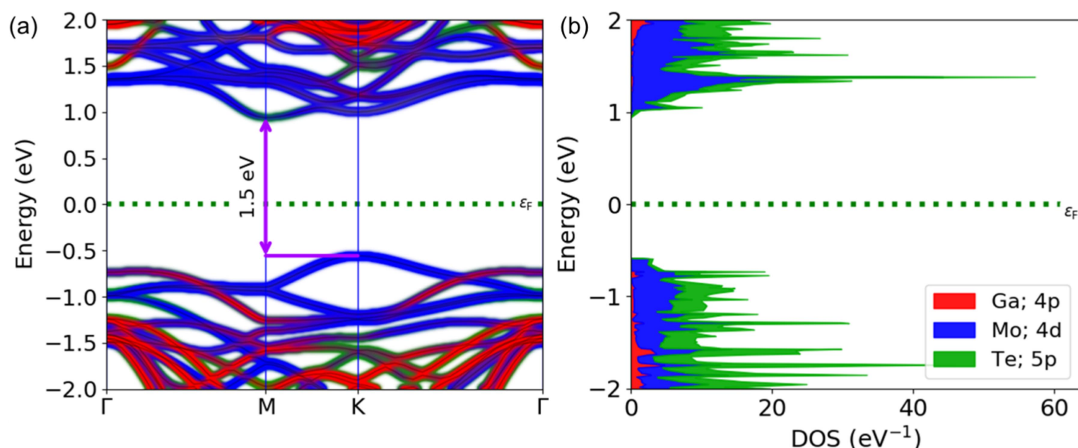

Fig. 5.4 The projected (a) band structure and DOS of the GaTe/$MoTe_2$ heterostructure determined from HSE06 functional; Red and blue solid lines represent the GaTe and $MoTe_2$ components, respectively. The band structure shows indirect bandgap type-I heterostructure, where CBM and VBM both have a contribution from the $MoTe_2$ monolayer; Fermi level is indicated by a dashed green line, the orbital contribution from Mo (4d), Ga (4p) and Te (5p) is included

The optical absorption spectra of the individual GaTe, $MoTe_2$ monolayers as well as GaTe/$MoTe_2$ heterostructure are compared as shown in Fig. 5.5. For the GaTe monolayer, the ability to absorb UV and deep UV light with a wavelength < 500 nm is stronger than absorbing visible light, whereas the $MoTe_2$ monolayer has a broad absorption spectrum covering from UV-visible to the NIR region [361]. However, as constructed GaTe/$MoTe_2$ heterostructure has excellent sharp absorption only in the visible region, which makes it a potential candidate for optoelectronics and photocatalytic water splitting reaction applications.

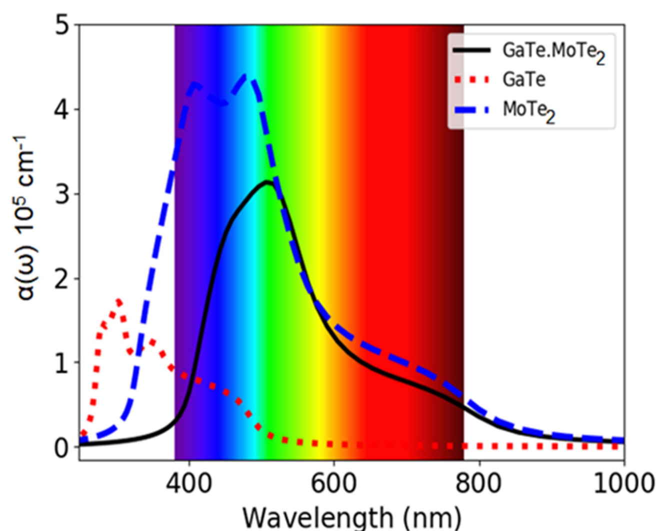

Fig. 5.5 Comparison of the absorption spectra of the GaTe monolayer (red dot line), $MoTe_2$ monolayer (blue dash line), and GaTe/$MoTe_2$ heterostructure (black solid line) using HSE06 functional

5.4.4 Modulation of electronic band structure and band alignment under biaxial strain and external electric field

Although the GaTe/$MoTe_2$ heterostructure has excellent visible absorption, due to type-I band alignment, the separation of electron and hole pair is limited, which can restrict its uses in various optoelectronics and energy applications. Therefore, we have applied ε_{xy} and E_{ext} to study the modulation of the electronic structure, band alignment, and optical spectra of the GaTe/$MoTe_2$ heterostructure.

Biaxial strain engineering has been used significantly for exploring the novel phenomenon in 2D materials and its heterostructures devices [98, 110]. Here, we used biaxial strain to study the modulation in the electronic structure, band alignment, and optical properties of GaTe/$MoTe_2$ heterostructures. It is applied by setting the lattice parameters of heterostructure in a given direction to a fixed value (smaller and larger), allowing the atomic positions to relax. The magnitude of ε is defined as $\varepsilon = (a_0 - a)/a \times 100\%$, where a_0 and a are the lattice constants of the strained and unstrained GaTe/$MoTe_2$ heterostructure respectively. The value of ε_{xy} has been taken from -9% to +9%, where + and - signs represent the tensile and compressive strain respectively. **Fig. 5.6 (a) and (b)** show the variation of interlayer distance and binding energy with biaxial strain. The interlayer distance decreases with the increase of ε_{xy} from -9% to +9%. From Fig. 5.6(b), it is clear that for higher biaxial strain values, the stability of the heterostructure decreases.

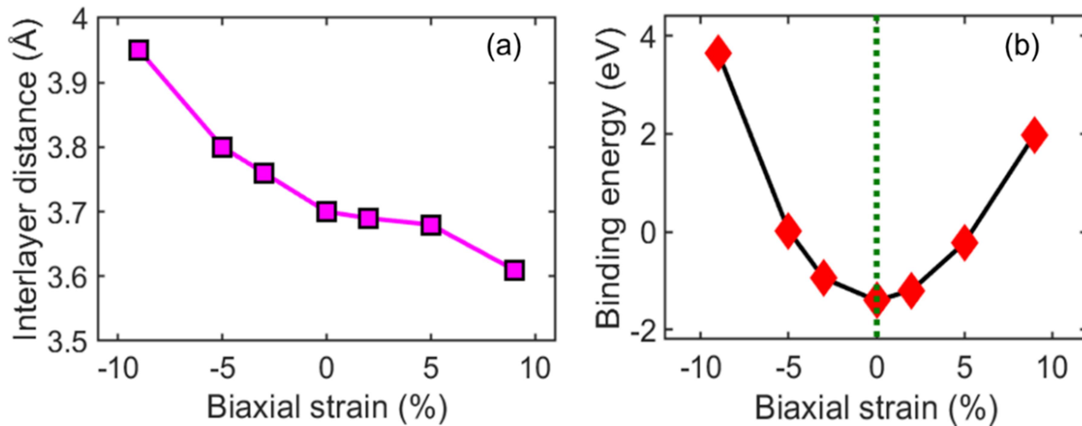

Fig. 5.6 Variation of (a) interlayer distance and (b) E_b of GaTe/$MoTe_2$ vdW heterostructure with biaxial strain.

The projected band structure of GaTe/$MoTe_2$ heterostructures at different values of ε_{xy} is shown in Fig. **5.7 (a)-(h)** respectively. At ε_{xy} = +1% tensile strain, the bandgap becomes direct (K-K) with type-I band alignment where both the CBM and VBM contributed from $MoTe_2$ layer (blue) as shown in Fig. 5.7 (a). As we increase the ε_{xy} ≥+2% to +9%, the band

alignment become type-II, where CBM is dominated by contributions from the $MoTe_2$ layer (blue) and VBM contributed from the GaTe layer (red) as shown in Fig. 5.7 (b), (c) and (d).

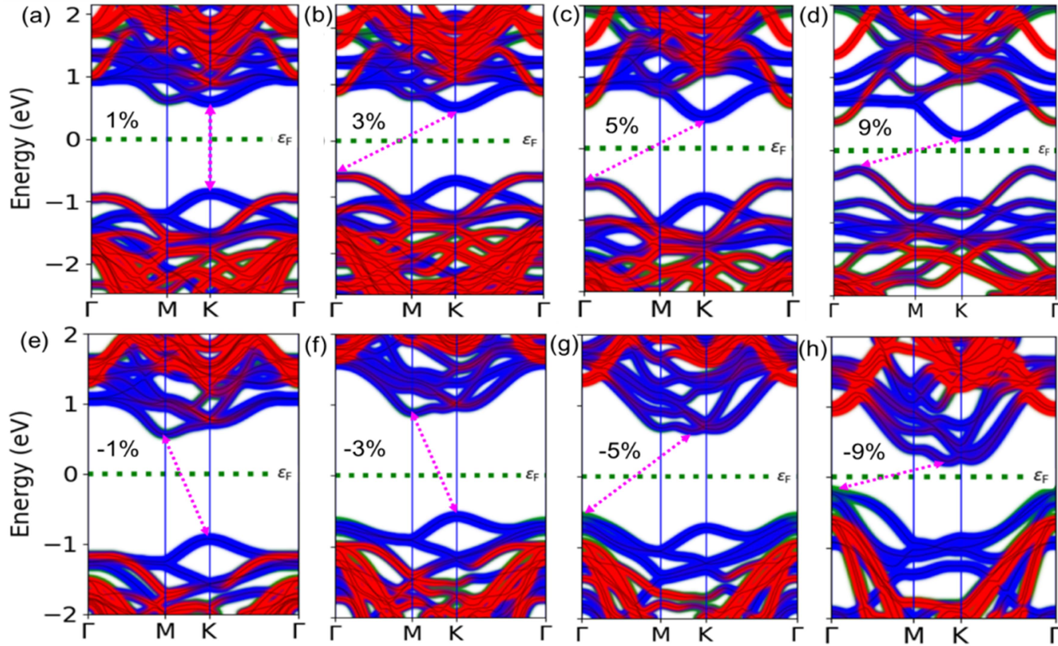

Fig. 5.7 The projected band structures of the $GaTe/MoTe_2$ heterostructure for different tensile (+) and compressive (-) strains; (a) 1 % (b) 3% (c) 5% (d) 9% and (e) -1% (f) -4% (g) -5% and (h) -9%. The contributions of GaTe and $MoTe_2$ layers are described by the red and blue lines, respectively.

By further increasing the tensile strain > +9%, a semiconductor-to-metallic transition tends to start. Further, by application of compressive strain at $\varepsilon = -1$ %, a nominal increase in the indirect bandgap (K-M) observe, while keep maintaining the type-I band alignment nature as shown in Fig. 5.7 (e). A similar behavior shows at -3% strain with a decreased indirect bandgap (Fig. 5.7 (f)). However, at $\varepsilon = -5\%$ and -9%, the VBM is shifted from K to Γ point but it maintained its type-I band alignment as shown in Fig. 5.7 (g) and (h). These variations in bandgap and band alignment are mainly attributed to the interlayer interaction and charge transfer between GaTe and $MoTe_2$ layer [110, 369]. It is seen that the bandgap linearly decreases with the increase of both tensile and compressive strains for $GaTe/MoTe_2$ vdW heterostructure. We have observed a clear band alignment transition from the type-I to type-II heterostructure in the strain range ε_{xy} = +2% to +9%.

Now, we have investigated the effect of E_{ext} varying from -1 V/Å to +1 V/Å with an interval step of 0.2 V/Å applied perpendicular along the z-direction on the $GaTe/MoTe_2$ heterostructure. The (+) ve E_{ext} direction specified from $MoTe_2$ to GaTe monolayer. **Fig. 5.8 (a)-(f)** shows the projected band structure of the $GaTe/MoTe_2$ heterostructure under various

E_{ext} -field values. The change in the interlayer distance under various E_{ext} values is not significant; therefore it is not shown here in the Thesis. As we know that at 0 V/Å, it has a typical type-I band alignment where both CBM and VBM contribute from $MoTe_2$ monolayer with indirect K-M transition. As we applied +0.2 V/Å E-field, the CBM shifts from M to K point, and typical type-I band alignment is observed with a direct bandgap as shown in Fig. 5.8 (a). However, by increasing the positive (+ve) E_{ext} -field from +0.4 V/Å to +1 V/Å, the band alignment turns to type-II with indirect bandgap where CBM contributes from $MoTe_2$ and VBM contributes from GaTe monolayer as shown in Fig. 5.8 (b), (c) and (d). While we applied the negative E_{ext} (-) field, at -0.2 V/Å it shows that the contributions of VBM and CBM both are coming from $MoTe_2$ (blue) monolayer, which implies type-I band alignment as shown in Fig. 5.8 (e). However, from -0.6 V/Å to -1 V/Å, the contribution of CBM starts to shift from $MoTe_2$ (blue) to GaTe (red) and VBM remains the same from the $MoTe_2$ layer as shown in Fig. 5.8 (f), (g) and (h). Therefore, the type of band alignment changes from type-I to II under the influence of a higher negative +E field in the GaTe/$MoTe_2$ heterostructure. A continuous decrease of bandgap was observed with the increase of both the (+) and (-) E_{ext} -fields.

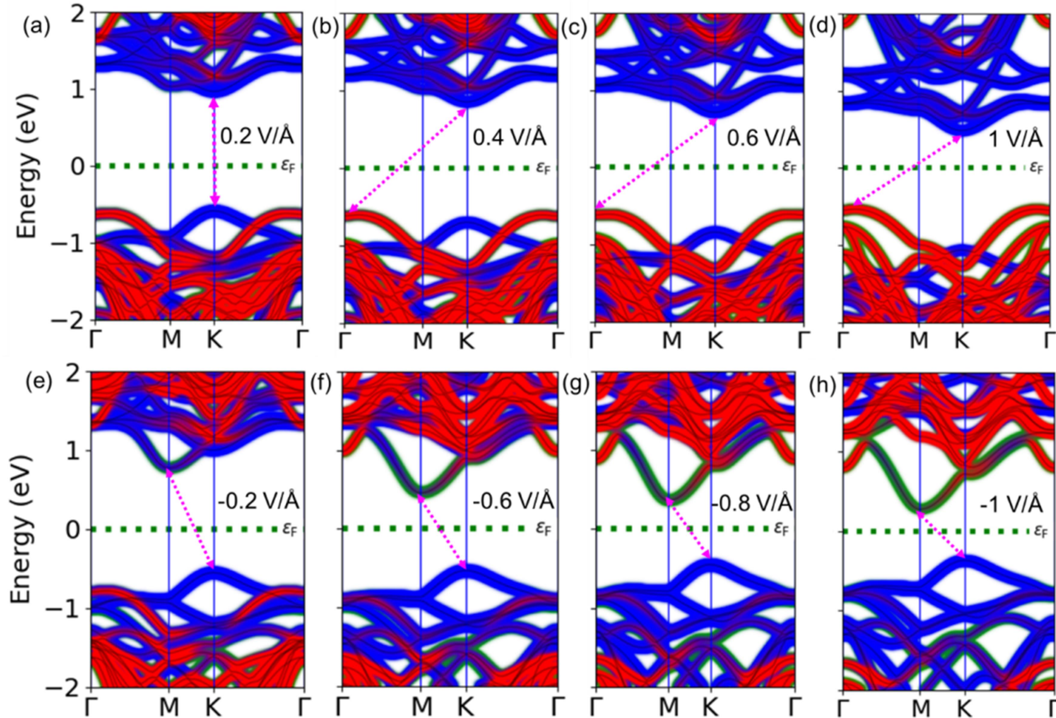

Fig. 5.8 The projected band structures of the GaTe/$MoTe_2$ vdW heterostructure for different positive and negative E_{ext}. The contributions of GaTe and $MoTe_2$ layers are described by the red and blue lines, respectively.

Further, the variation of the bandgap and band alignment of $GaTe/MoTe_2$ vdW heterostructure with different ε_{xy} and E_{ext} are shown in **Fig. 5.9 (a) and (b)** respectively. It is seen that the bandgap linearly decreases with the increase in both tensile and compressive strains for $GaTe/MoTe_2$ vdW heterostructure as shown in Fig. 5.9 (a). In the case of -9% to +1% biaxial strain, it shows type-I band alignment, although from +2% tensile strain up to +9%, the band alignment changes from type-I to type-II. The bandgap variation of the $GaTe/MoTe_2$ heterostructure as a function of E_{ext} has been presented in Fig. 5.9 (b). It is seen that the bandgap initially increases up to a certain range of +ve E_{ext} and then decreases linearly with increasing E_{ext}. In the case of +ve E-field, the band alignment is type-I up to +0.3 V/Å. However, for the applied E-field of +0.4 V/Å to +1 V/Å, the band alignment changes from type-I to type-II. In the case of negative E_{ext}, the bandgap linearly decreases with the increasing -ve values and the band alignment retains type-I from -0.1 V/ Å to -0.5 V/Å. Then from -0.6 V/Å to -1 V/Å, the band alignment again turns to type II. Therefore, in both cases, the bandgap eventually achieved a semiconductor-to-metal transition at a particular larger value of E_{ext}.

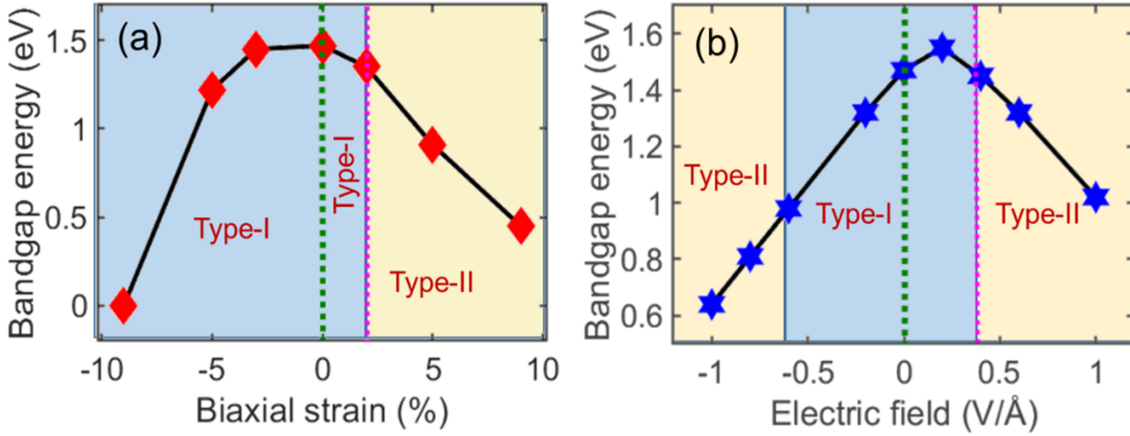

Fig. 5.9 The variations of the bandgap of $GaTe/MoTe_2$ vdW heterostructure with (a) biaxial tensile and compressive strain (b) different (+) and (-) E_{ext}.

5.4.5 Modulation in Optical Properties under biaxial strain and external electric field

Finally, we investigated the modulation of absorption spectra of $GaTe/MoTe_2$ heterostructure under the application of ε_{xy} and E_{ext} as shown in **Fig. 5.10 (a)-(d).** A clear red shift in the absorption spectra is observed for ε_{xy} up to ±9% as shown in Fig. 5.10 (a)-(b). However, under E_{ext} varying from - 1 V/Å to +1 V/Å, no such shift is visible as shown in Fig. 5.10 (c)-(d). The broadening in the optical spectra from the visible to the infrared region is

noticeable with the increase of the ε_{xy} up to ±9%. Under ε_{xy} from >+2% up to +9%, the $GaTe/MoTe_2$ heterostructure has strong optical visible absorption with type-II band alignment. Similarly, the $GaTe/MoTe_2$ heterostructure has type-II band alignment and excellent visible absorption at +0.4 V/Å to +1 V/Å, and -0.6 V/Å to -1 V/Å. By comparing band alignment and optical spectra under ε_{xy} and E_{ext}, it is clear that $GaTe/MoTe_2$ heterostructure is a potential candidate for various optoelectronics and photocatalytic water splitting reactions.

A schematic illustration showing the variation of band alignment of $GaTe/MoTe_2$ heterostructures under ε_{xy} and E_{ext} for the photocatalytic splitting reaction is shown in **Fig. 5.11.**

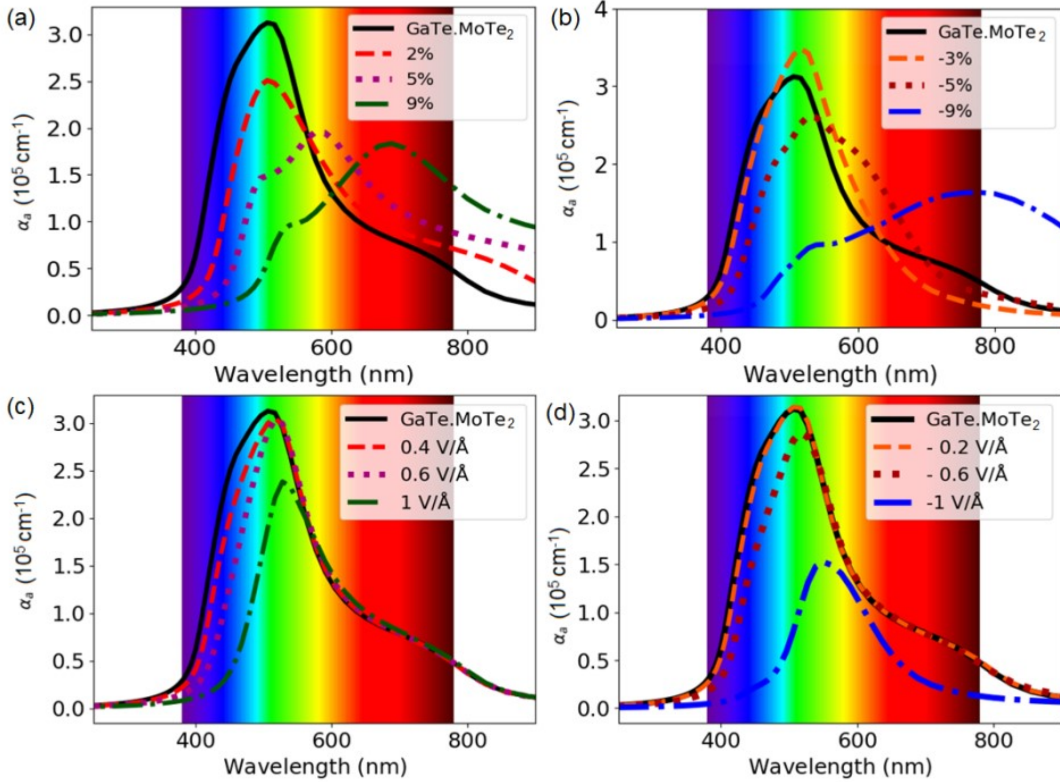

Fig. 5.10 Optical absorption spectra of the $GaTe/MoTe_2$ vdW heterostructure with different values of (a) tensile strain (b) compressive strain (c) (+) E_{ext} and (d) (-) E_{ext}.

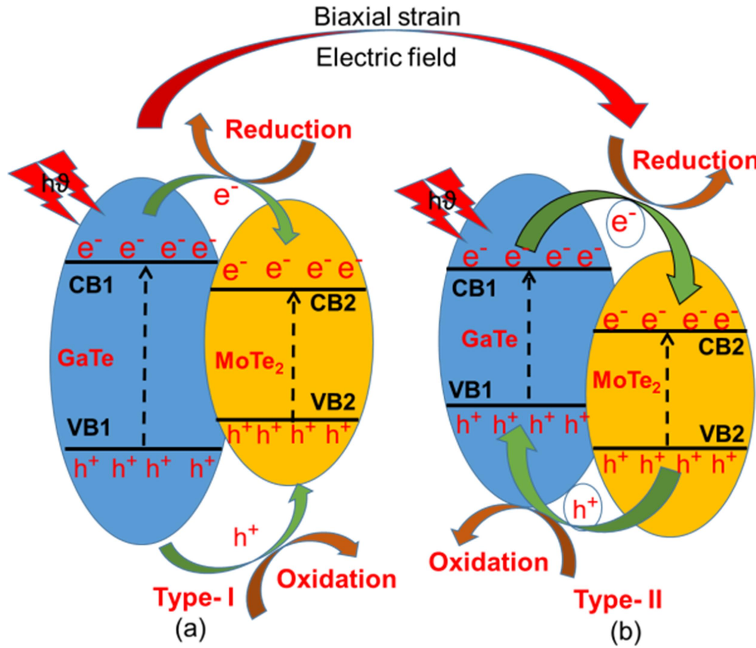

Fig. 5.11 Schematic illustration of the (a) Type-I and (b) Type-II conventional photocatalytic GaTe/$MoTe_2$ heterojunction

5.4 **Conclusions:**

In summary, we systematically investigated the design, formation, and stability of GaTe/$MoTe_2$-based 2D heterostructure using hybrid- DFT calculations. Out of the four stacking configurations of the heterostructure, the most stable configuration is selected based on the minimum E_b value. The optimized 2D-GaTe/$MoTe_2$ heterostructure has an indirect bandgap of 1.5 eV, having type-I band alignment and excellent optical absorption in the visible region. Due to the type-I alignment, electrons and holes both reside in the $MoTe_2$ monolayer, restricting its use in various optoelectronic and energy applications. Therefore, the band alignment and optical spectra of the GaTe/$MoTe_2$ heterostructure are investigated under the varying external biaxial strain and electric field. It is observed that for $\varepsilon_{xy} > +2\%$ and E_{ext} between +0.4 V/Å to +1 V/Å, and -0.6 V/Å to -1 V/Å, the band alignment changes from type-I to type-II, with the high optical visible absorption of order 10^5 cm^{-1}. All of these properties under ε_{xy} and E_{ext} make the GaTe/$MoTe_2$ heterostructure a promising multifunctional heterostructures device for next-generation 2D electronics applications.

Chapter 6

n-WS_2 QDS/p-Si (0D-3D) AND p-WSe_2 NSs/ n-WS_2 QDS/p-Si (2D-0D-3D) MIXED-DIMENSIONAL MULTILAYER HETEROSTRUCTURES BASED HIGH PERFORMANCE BROADBAND PHOTODETECTOR

6.1. Introduction

2D-TMDC semiconductors such as MoS_2, $MoSe_2$, WS_2, and WSe_2 have attracted significant attention for the next-generation optoelectronic devices due to their atomically thin nature, tunable bandgap property, zero dangling bonds, ultrahigh mobility, etc. [274, 297, 298, 371]. The absence of dangling bonds in 2D materials enables them to MD heterostructures with 0D, 1D, and 3D materials [235, 241, 276]. These MD heterostructures provide a distinctive platform for next-generation 2D electronics [297].

After the introduction of MD heterostructures by Jariwala *et al.*[241], several researchers have explored MD heterostructures for photodetection applications [235, 236, 242-245]. Mukherjee *et. al*. [238] reported a 0D/2D (PbS–MoS_2) hybrid heterostructure-based photodetector to demonstrate a broad responsivity covering the visible and Infrared (IR) regions. Pataniya *et. al*. [239] demonstrated a flexible 2D-WSe_2 NSs/Graphite MD heterostructure-based photodetector for optoelectronic device applications. Selamneni *et. al*. [240] explored 0D–2D n-WS_2-QDs/p-SnS hybrid heterostructures for highly responsive flexible broadband photodetectors. However, no significant experimental demonstrations have been reported yet on multilayer MD heterostructures-based photodetectors.

Several studies show that the WSe_2/WS_2 bilayer vdW heterostructures hold great promise for various optoelectronic device applications [275, 372, 373]. Interestingly, the bulk WSe_2 is an indirect bandgap (~1.2 eV) material [54] whereas the WSe_2 monolayer shows a direct bandgap (~1.65 eV) nature suitable for photodetection applications [374]. Among various methods reported for the synthesis of WSe_2 nanostructures, solvothermal synthesis is

considered to be a cost-effective scalable method to obtain 2D-WSe_2 nanosheets (NSs) [139, 375]. On the other hand, the WS_2 possesses excellent electronic and optical properties at room temperature [376]. The 0D-Quantum dots (QDs) of WS_2 have higher bandgap energy than that of the 2D-WSe_2 materials due to enhanced quantum-confinement effects [375, 377, 378]. The 0D-WS_2 QDs can be successfully synthesized by the low-cost hydrothermal method [115]. In this paper, we have explored different dimensional materials of WSe_2 and WS_2 to fabricate multilayer MD heterostructures for photodetection applications. Here, first, we have fabricated 0D-WS_2 QDs /3D-p-Si based MD heterostructures, and then 2D-WSe_2 NSs are deposited on the top of 0D-WS_2 QDs to fabricate 2D-0D-3D (WSe_2/WS_2/p-Si) multilayer MD heterostructures based broadband photodetectors. The WSe_2 NSs and WS_2-QDs were synthesized by solvothermal and hydrothermal methods respectively. The electrical and photo response characteristics of the 0D-WS_2 QDs /3D-p-Si and 2D-WSe_2/0D-WS_2/3D-p-Si devices have been compared and analyzed in detail.

6.2. Experimental details

6.2.1 Chemical used

Sodium tungstate dihydrate ($Na_2WO_4 \cdot 2H_2O$, Purity 99%) and N, N dimethylformamide (DMF, anhydrous, purity 99.8%) were purchased from Emparta@ Merck, Se powder (-100 mesh, purity 99.99% trace metals) was procured from Sigma-Aldrich © and Sodium borohydride ($NaBH_4$, purity 98%) was purchased from Alfa Aesar for the solvothermal synthesis of WSe_2 NSs. Here, Se powder and Sodium borohydride act as a precursor, Sodium tungstate dihydrate as a reducing agent, and N, N dimethylformamide as a solvent. All the chemicals are used in this work without any further purification.

Also, for WS_2 Quantum dots synthesis, Sodium tungstate dihydrate ($Na_2WO_4 \cdot 2H_2O$) was obtained from Emparta@ Merck, purity 99% and L-cysteine was purchased from Alfa Aesar. Here, L-cysteine is used as a sulfur source as well as a reducing agent. Throughout the synthesis, DI water was provided from the laboratory and was adopted for solution preparation. All the synthesis/fabrication work of my thesis was done at CRME lab, IIT BHU under **Dr. Satyabrata Jit**, Department of Electronics and Communication Engg., IIT BHU.

6.2.2 Synthesis of WSe_2 nanosheets

The WSe_2 nanosheets have been prepared using a solvothermal method. Firstly, 0.64 g of Se powder, 0.20 g of sodium borohydride, and 1.32 g of $Na_2WO_4{\cdot}2H_2O$ were measured in a weighing machine one by one and then all powders are mixed and dissolved in 60 ml of DMF and stirred continuously for 2 hours. Then, the mixture was transferred in a Teflon-lined stainless-steel autoclave of a capacity of 100 ml and heated in the oven at 200°C for 48 hours. Further, leave it to naturally cool down and then the solution has been centrifuged at about 5000 RPM to collect the black precipitates, and washed with distilled water and absolute ethanol several times. Following this step, the obtained black color precipitate was dried in an oven at 60° C for 24 hours. Finally, the WSe_2 nanosheets were annealed at 400°C for 2 hours to improve the crystallinity. Lastly, the final product was obtained and stored in a vacuum desiccator for further characterization purposes. The schematic diagram of the synthesis of WSe_2 NSs is shown in **Fig. 6.1**. Different forms of WSe_2 Nanosheets after synthesis are shown in **Fig. 6.2.**

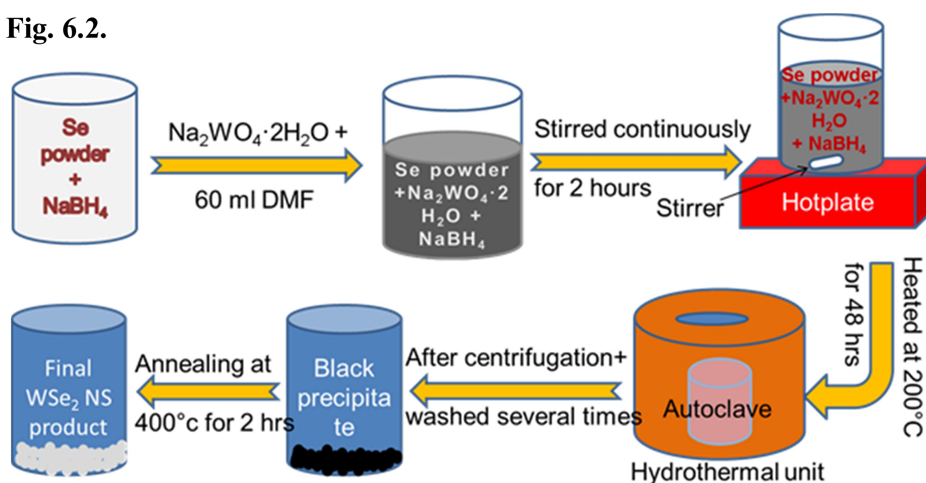

Fig. 6.1 Schematic diagram of Colloidal synthesis process for WSe_2 Nanosheets

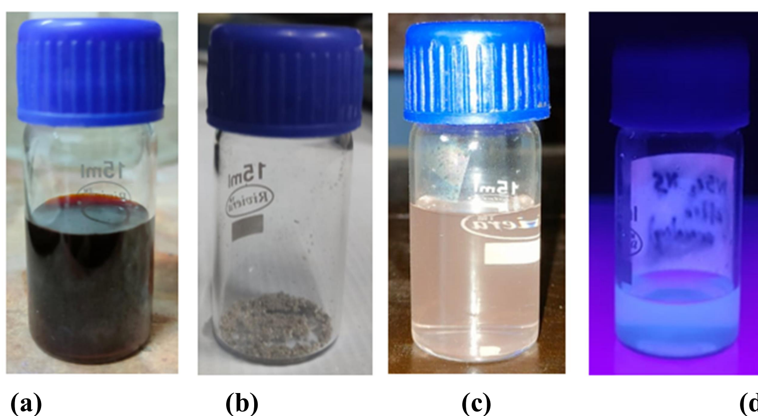

(a) **(b)** **(c)** **(d)**

Fig: 6.2 (a) Solution of as-prepared WSe_2-NSs before annealing (b) WSe_2 NSs powder after annealing at 200°C for 2 hrs (c) WSe_2 NSs powder dispersed in IPA for further use. (d) WSe_2 NSs final solution under UV light to show the luminescence.

6.2.3 Synthesis of WS_2 quantum dots

WS_2 QDs have been synthesized by the hydrothermal process. In this synthesis process, 0.25 g $Na_2WO_4 \cdot 2H_2O$ was dissolved in 25 ml of DI water and stirred for 45 minutes. Simultaneously 0.5 g L-cysteine was dissolved in 50 mL DI water and stirred continuously for 45 minutes. Both the above-prepared solutions were uniformly mixed and the pH of the resultant solution was adjusted to 3 pH level by slowly adding 0.1M HCl solution in a dropwise manner. Once the solution reached 3 pH, it was stirred for 20-30 minutes. The solution was then poured into a stainless-lined Teflon autoclave of 200 ml capacity and placed in an oven for hydrothermal reaction. Initially, the temperature was set to 120°C for 2.5 hours and then it was set to 190°C for 46 hours. After the reaction was completed, the oven was naturally cooled to room temperature, yielding a light yellowish color solution containing WS_2-QDs. The obtained solution was then filtered in a dialysis bag for 2-3 days. The schematic diagram of the synthesis of WS_2 QDs is shown in **Fig. 6.3.** Different forms of WS_2 QDs after every stage of synthesis are shown in **Fig. 6.4.**

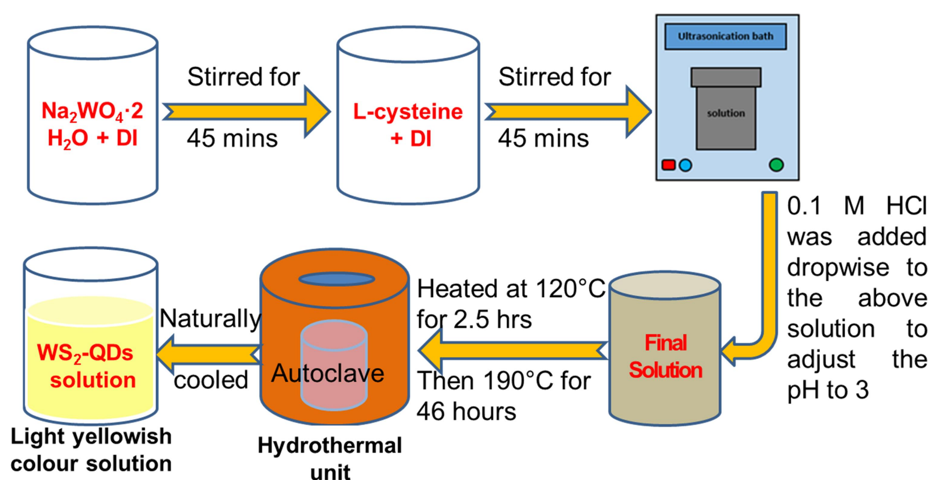

Fig.6.3 Schematic diagram of Colloidal synthesis process for WS_2 Quantum dots

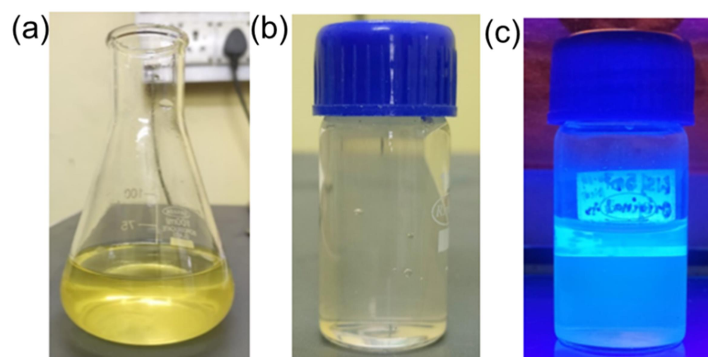

Fig: 6.4 (a) Solution of as-prepared WS_2-QDs (b) WS_2 QDs solution after filtration by dialysis bag for 2-3 days. (c) WS_2 QDs solution under UV light to show the luminescence.

6.2.4 Fabrication of n-WS_2 QDs/p-Si (0D-3D) and p-WSe_2 nanosheets/n-WS_2 QDs/p-Si (2D-0D-3D) heterojunction devices

The p-Si wafers were first cleaned by TCE, acetone, piranha solution, and HF in a sequential manner followed by drying at 60°C. The wafers were finally cleaned by Ar plasma treatment (using Femto Science Inc., CUTE, Korea). Next, the as-prepared WS_2 QDs solution was spin-coated on the cleaned p-Si substrates at 1500 rpm for 40 sec. The process was repeated 3-4 times and then the coated film was dried at 100°C to eradicate solvent residues. For WSe_2 NSs, the as-synthesized WSe_2 powder was ultra-sonicated for 1 hour. It was dissolved in the 2-propanol solvent at the rate of 1 mg/ml. The WSe_2 NSs solution was spin-coated on the n-WS_2 QDs coated p-Si substrates at 2000 rpm for 30 sec. The process was repeated twice and the resultant film was dried at 80°C to eradicate solvent residues

Both the n-WS_2 QDs/p-Si (0D-3D) and p-WSe_2 NSs/n-WS_2 QDs/p-Si (2D-0D-3D) MD heterostructures were processed for metallization for preparing two types of photodetectors. The metal contacts were deposited on the front and back sides of the MD heterostructures for device applications [379]. The Ag metal dots of size 1 mm were grown on the front side using a shadow mass technique while Al/Ti (~60/40 nm) was deposited on the back side of p-Si substrates by a thermal evaporation method using a vacuum coating method (FL400 SMART COAT 3.0 A, Hind High Vacuum, India) at a vacuum level of ~ 4×10^{-6} mbar and ~ 0.1 nm/s deposition rate. The effective area of a single Ag dot was ~ 3.14×10^{-2} cm^2. The schematic diagrams of both sets of MD heterostructures devices are shown in **Fig. 6.5 (a) and (b).**

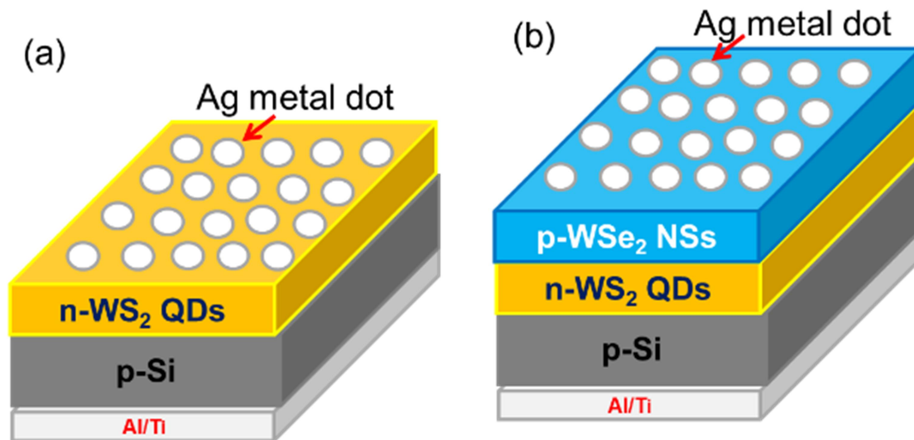

Fig. 6.5 Schematic diagram of the mixed-dimensional heterostructures based on (a) (0D-3D) n-WS_2 QDs/p-Si (b) (2D-0D-3D) p-WSe_2 NSs/n-WS_2 QDs/p-Si

6.3. Results and Discussions

6.3.1 Structural and Optical characterization of WSe_2 Nanosheets

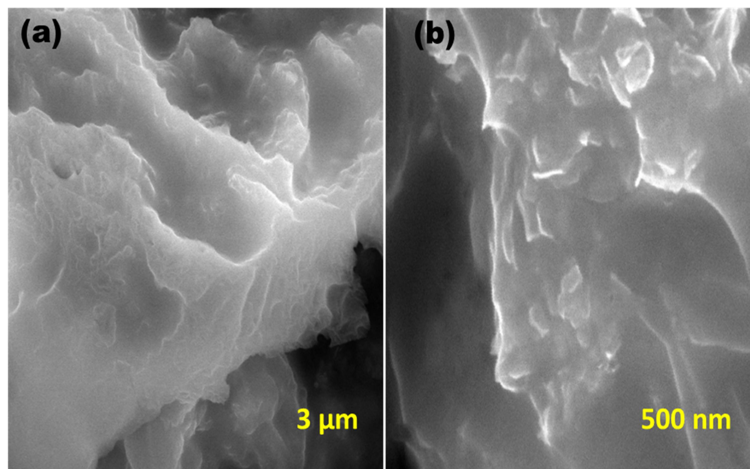

Fig. 6.6 (a) SEM images and (b) high-magnification SEM image of graphene-like WSe_2 nanosheets

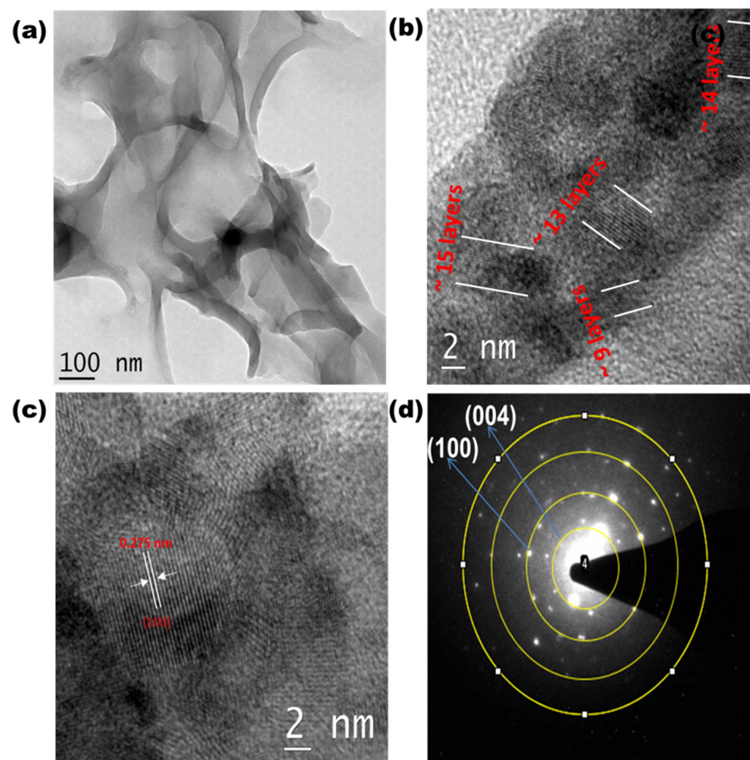

Fig. 6.7 (a) TEM images of graphene-like WSe_2 nanosheets (b, c) HRTEM image of the selected region (d) shows the corresponding SAED pattern.

The structural characterization of as-prepared WSe_2 NSs is carried out by SEM and HRTEM as shown in **Fig. 6.6 and 6.7**. The SEM images of the WSe_2 NSs sample are shown in Fig. 6.6(a) and (b). From Fig. 6.6(a) we can observe that the obtained WSe_2 possesses a clear sheet-like structure. It is seen from Fig. 6.6(b) of the high-magnification SEM image that the WSe_2 having few layers of nanosheets with some folded edges like graphene structure matches with previously reported results [380]. The TEM image shown in Fig. 6.7(a) again demonstrates that the WSe_2 nanosheets were curved and folded edges including many ultrathin layers. Fig. 6.7(b) and (b) show the HRTEM images of WSe_2 nanosheets. Fig. 6.7(b) reveals that the WSe_2 NSs consist of 9-15 layers and the interlayer spacing is found to be 0.275 nm calculated from the lattice fringes of WSe_2 which correspond to the (100) plane shown in Fig. 6.7(c). The (004) and (100) planes in the selected area electron diffraction (SAED) patterns (Fig. 6.7(d)) confirm a high crystalline quality of the as-synthesized ultrathin nanosheets of WSe_2.

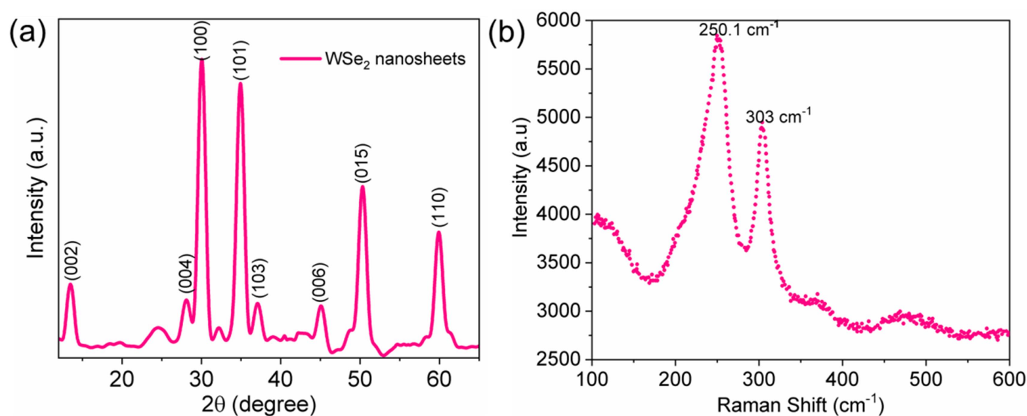

Fig. 6.8 (a) The XRD pattern and (b) the Raman spectrum of graphene-like WSe_2 nanosheets

The XRD patterns of the obtained WSe_2 NSs sample reveals the diffraction peaks at 13.5°, 28.10°, 30.16°, 34.89°, 37.11°, 45.02°, 50.31°, and 59.87° which corresponds to the (002), (004), (100), (101), (103), (006), (015) and (110) crystal planes of the hexagonal WSe_2 system [139, 140], respectively with a space group of P63/mmc (JCPDS card no. 38-1388) shown in **Fig. 6.8(a).** There are two strong peaks observed in the Raman spectrum of WSe_2 NSs as shown in **Fig. 6.8(b).** A robust peak appeared at 250.1 cm^{-1}, corresponding to the in-plane E^1_{2g} mode of WSe_2 [140, 381]. The blue shifting of the E^1_{2g} peak, as compared to the bulk WSe_2 (251.6 cm^{-1}) observed, shows the confinement of thickness in synthesized few-layer WSe_2 NSs. Another Raman peak at 303 cm^{-1} ($B_{2g}{}^1$ mode) is observed due to the interlayer interaction [381]. The sharpness of the peak in the Raman spectrum is attributed to the ordered arrangement of W and Se-atoms in the lattice structure. These RAMAN peaks are

confirms that the 2H-polymorph of WSe_2 multilayer nanosheets was successfully synthesized.

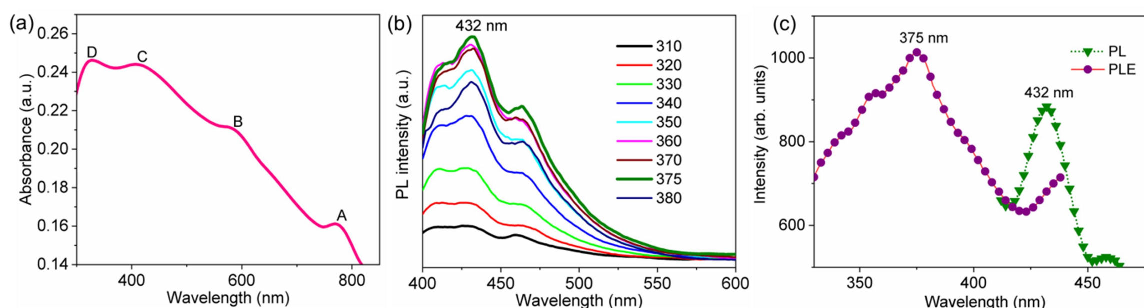

Fig. 6.9 (a) UV-visible absorbance spectra of the WSe_2 NSs (b) Photoluminescence spectra of pristine WSe_2 NSs with different excitation wavelengths, (c) photoluminescence excitation (PLE) spectra of WSe_2 NSs.

The optical properties of the as-prepared WSe_2 NSs have been measured by UV-Visible spectrum and excitation wavelength-dependent PL spectra shown in **Fig. 6.9**. In Fig. 6.9(a), shows the absorption spectrum of WSe_2 nanosheets with four resonances observed at 770 nm (A) and 583 nm (B), 408 nm (C) and 326 nm (D). The excitonic resonances peak at A and B due to inter-layer and intra-layer perturbation [260]. The 'A' peak corresponds to the band gap of about 1.61 eV of WSe_2 NSs, which matches the reported bandgap of Pataniya *et. al.* [382]. Moreover, the C and D peaks are attributed to the Van Hove singularities which lead to strong absorption. Fig. 6.9(b) depicts the excitonic wavelength-dependent photoluminescence (PL) spectrum of the WSe_2 NSs, where the highest PL peak is located at λ=432 nm under an excitation wavelength (λ_{exc}) of 375 nm [383]. Photoluminescence excitation (PLE) spectra of WSe_2 showed a maximum excitation wavelength at 375 nm, and a maximum emission wavelength at 432 nm shown in Fig. 6.9(c).

6.3.2 Structural and Optical Characterization of WS_2 quantum dots

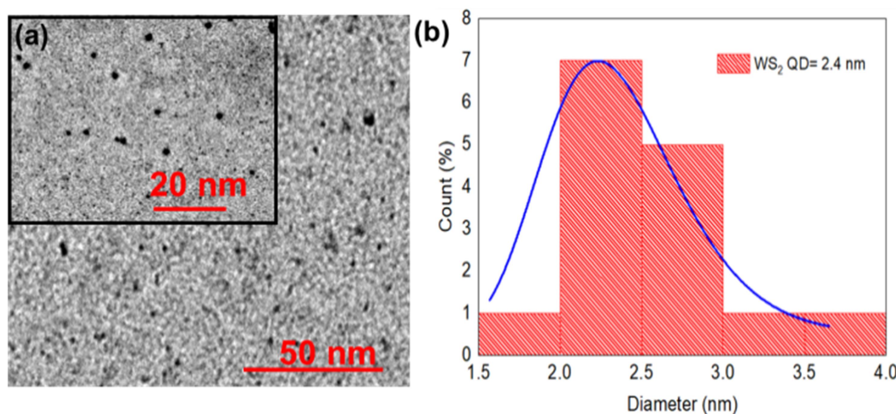

Fig. 6.10 (a) HRTEM image of WS_2 QDs, (b) Size distribution histogram plot of WS_2 QDs

The structural properties and size distribution of WS_2 quantum dots have been determined by HRTEM as shown in **Fig. 6.10**. It is observed that the size distribution of WS_2 QDs shows uniform dispersion without any apparent accumulation. The lateral size distribution of WS_2 QDs is a Gaussian profile as shown in Fig. 6.10 (b) gives the maximum size of QDs as 2.4 nm.

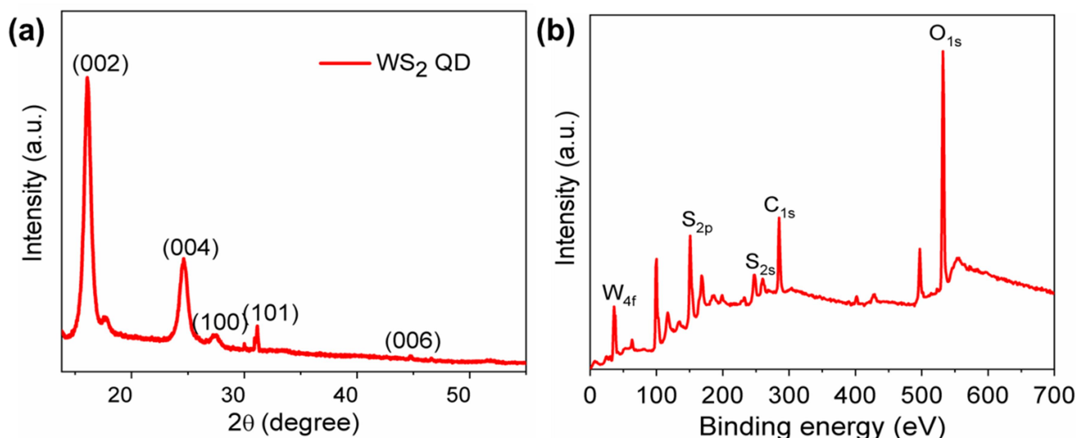

Fig. 6.11 (a) the XRD pattern and (b) the XPS of WS_2 quantum dots

The X-ray diffraction (XRD) pattern of WS_2 QDs gives peaks at 16.06°, 24.6°, 27.34°, 31.13°, and 44.76° and they can be indexed to (002), (004), (100), (101) and (006) crystal planes of the 2H-phase WS_2 crystal shown in **Fig. 6.11 (a). Fig. 6.11 (b)** shows the whole XPS survey spectra of WS_2 QDs which represent the presence of W, S, C, and O for our synthesized QDs.

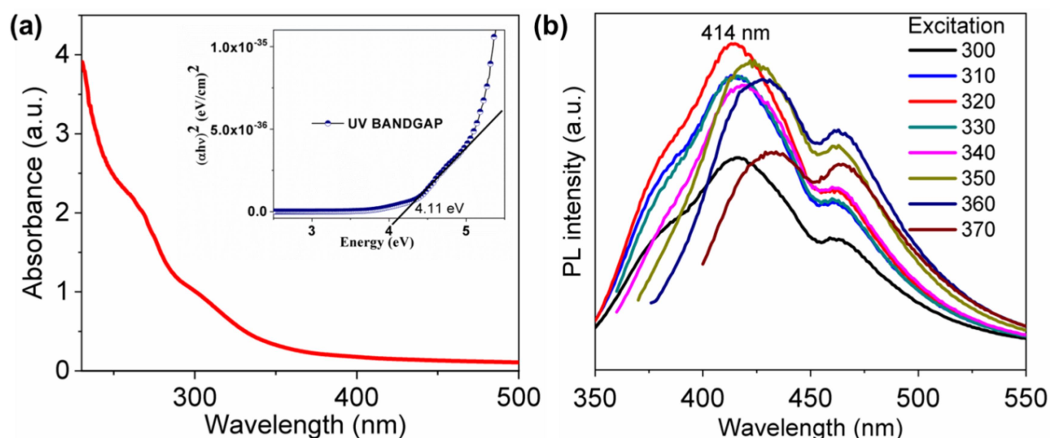

Fig. 6.12 (a) UV-visible absorbance spectra (b) PL spectra of pristine WS_2 QDs with the different excitation wavelengths

The optical characterizations of the as-prepared WS_2 QDs are investigated by UV-Visible spectroscopy and excitation wavelength-dependent PL spectra shown in **Fig. 6.12 (a) and (b)**, respectively. The UV-visible spectrum of the QDs in Fig. 6.12 (a) shows strong absorption mainly in the UV region. The inset of Fig. 6.12 (a) estimates the excitonic bandgap of ~ 414 nm. It is well known that the bandgap of QDs is dependent on their size. The smaller sizes QDs have larger bandgaps and vice versa. The enhancement in band gap due to the reduction in the size of the QDs is attributed to the enhanced effect of the quantum confinement of carriers. The average size of QDs estimated from the data shown in Fig. 6.10 (b) is around 2.4 nm. The PL spectra shown in Fig. 6.12 (b) exhibit the strongest emission at 414 nm (2.99 eV) due to the excitonic transitions between the conduction band minima (CBM) to the valence band minimum (VBM) [22] under an excitation wavelength (λ_{exc}) of 320 nm. For the λ_{exc} in 300 nm−340 nm, the WS_2 QDs demonstrated an excitation-independent emission band. However, for low-energy excitations with λ_{exc} in 360−460 nm, the emission band shows dependency on λ_{exc} as observed in Fig. 6.12 (b).

6.3.3 *Electrical and Photodetection characteristics of the (0D-3D) and (2D-0D-3D) MD heterostructures based devices*

Electrical and optical characterizations are performed using a probe station connected to a semiconductor parameter analyzer (Keysight, USA, model No. B1500) under ambient conditions at room temperature. The current-voltage (I-V) characteristics of the n-WS_2 QDs/p-Si (0D-3D) and p-WSe_2 NS/n-WS_2 QDs/p-Si (2D-0D-3D) heterostructures are compared under dark and light illumination conditions as shown in **Fig. 6.13 (a)-(b).** Both the 0D-3D and 2D-0D-3D MD devices show rectifying I-V characteristics with rectification ratios (i.e. forward bias current (I_F) to reverse bias current (I_R) ratio) of ~18.12 and 578, respectively. Thus, the use of additional 2D layers of p-WSe_2 NSs on the n-WS_2 QDs (0D) coated p-Si substrate (3D) drastically enhances the I_F/I_R ratio over the 0D-3D MD heterostructure device. This confirms the formation of a good quality p-WSe_2 NSs/n-WS_2 QDs heterojunction interface. The ideality factors (η) of the two devices are obtained as ~9.05 for the 0D-3D device and 7.5 for the 2D-0D-3D device. The high value of η (>2) of the n-WS_2 QDs/p-Si MD structure is attributed to the trapped charges at the MD heterojunction interface which play a dominant role in the current transport of MD heterostructure devices [163].

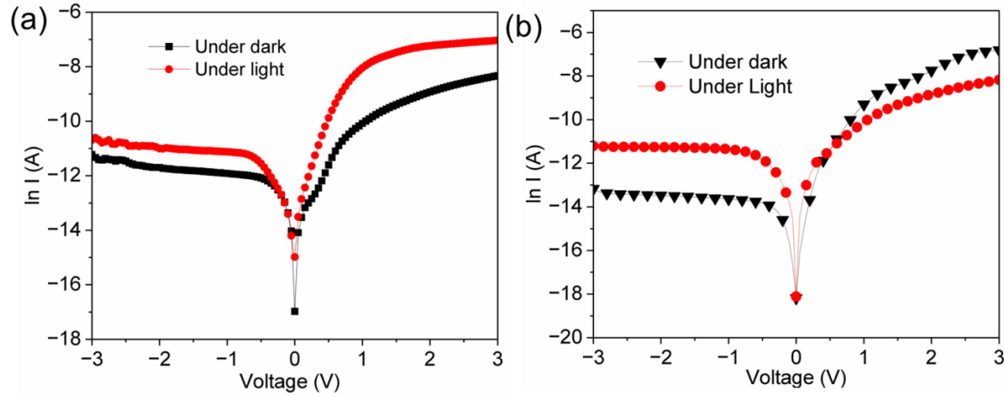

Fig. 6.13 Room temperature I-V characteristics of the (a) (0D-3D) n-WS_2 QDs/p-Si (b) (2D-0D-3D) p-WSe_2 NSs/n-WS_2 QDs/p-Si at dark and under the illumination of white light with a power intensity of 21.98 mW/cm^2

Table 6.1: Comparison of device performance of n-WS_2 QDs/p-Si and p-WSe_2 NS/n-WS_2 QDs/p-Si heterostructure with Ag as top contact-based photodetectors

Sl. no	Device structure	Responsivity (A/W)	Detectivity (Jones)	EQE (%)	Rise Time (ms)	Fall time (ms)	References
1	**Ag/n-WS_2 QDs/p-Si/Ti/Al**	**26.1 A/W**	**1.36×10^{12}**	**9768%**	**810 ms**	**800 ms**	**This work**
2	**Ag/p-WSe_2 NS/n-WS_2 QDs/p-Si/Ti/Al**	**214 A/W**	**2.35×10^{13}**	**82710%**	**24 ms**	**21 ms**	**This work**
3	CTS QDs/SnS_2 nanoflake-	53.88	3.2×10^{13}	20878%	-	-	[276]
4	n-ZnO CQDs/p-TIPS-pentacene	59.15	7.01×10^{13}	19877%	4.20 s	4.01 s	[175]
5	Au/WSe_2/ITO	0.1	-	-	0.05 ms	0.02 ms	[384]
6	GQDs/p-WSe2/n-Si	0.707	4.51×10^{9}	-	0.2 ms	-	[277]
7	WSe_2 Nanoshee ts/Graphite heterostructure	0.006	1.94×10^{8}	1.25%	0.8 sec	1.4 sec	[239]
8	WS_2/WSe_2 heter ojunction	8.4 × 102	9.7 × 1011	-	19 ms	23 ms	[275]
9	WSe_2/WS_2 heter ojunction	216 mA/W	-	50.2%	80 µs	-	[237]

Now, the responsivity (R) is defined as the ratio of the generated photocurrent density to the incident unit optical power and is expressed asNow, the wavelength-dependent R, D^*, and EQE of (0D-3D) n-WS_2 QDs/p-Si and (2D-0D-3D) p-WSe_2 NS/n-WS_2 QDs/p-Si heterostructure devices are compared and analyzed in details as shown in **Fig. 6.14 (a) and (b).** It is observed that both the devices show broadband spectral response ranging from 300 nm (ultraviolet) to 1100 nm (near infrared) region.

The responsivity (R) is defined as the ratio of the generated photocurrent density to the incident unit optical power and is expressed as [385, 386]

$$R = \frac{I_{ph}}{(P \times A)} \qquad \textbf{(6.1)}$$

Where I_{ph} is the photocurrent, P is the light intensity and A is the effective surface area of the devices.

At -3 V reverse bias voltage, the (0D-3D) n-WS_2 QDs/p-Si device gives the maximum R of 26.1 A/W under the incident intensity of 7.26 μW/cm^2 at 327 nm while the (2D-0D-3D) p-WSe_2 NS/n-WS_2 QDs/p-Si device gives the maximum value of R as 214 A/W under 6.97 μW/cm^2 intensity at 322 nm. The 2D-0D-3D shows 'R' nearly 8 times higher than that of the 0D-3D structure. Clearly, the 2D-0D-3D MD heterostructure device gives better performance than the 0D-3D MD heterostructure device.

The detectivity, D^*, is another important parameter of any photodetector device. It is directly proportional to the "R" of the device and is calculated by using the following equation [175, 176]

$$D^* = \frac{R}{\sqrt{2 \times e^- \times J_d}} \qquad \textbf{(6.2)}$$

Where R is responsivity, e^- is the charge of an electron, and J_d is the dark current density. The EQE of the device can be expressed as [385]

At -3 V reverse bias voltage, the maximum D^* of the 0D-3D structure is measured as 1.36×10^{12} Jones whereas the value of D^* for the 2D-0D-3D MD heterostructure is obtained as 2.35×10^{13} Jones at 327 nm and 322 nm with incident light intensities of 7.26 and 6.97 μW/cm^2 respectively. p-WSe_2 NSs/n-WS_2 QDs/p-Si structure shows nearly 17 times higher values of D^* as compared to its n-WS_2 QDs/p-Si (0D-3D) counterpart.

The EQE of the photodetectors can be computed using the following equation [385]

$$EQE = \frac{1240 \times R}{\lambda\ (nm)} \times 100 \qquad \textbf{(6.3)}$$

where R is responsivity, and λ is the incident wavelength in nm. **Fig. 6.14 (a-b)** shows the plot of R, D^*, and EQE with variation in wavelength.

At -3 V reverse bias voltage, the (0D-3D) n-WS_2 QDs/p-Si device gives the maximum EQE of 9768 % whereas the (2D-0D-3D) p-WSe_2 NSs/n-WS_2 QDs/p-Si structure gives the maximum EQE of 82710 % at 327 nm and 322 nm wavelengths with corresponding incident light intensities of 7.26 and 6.97 $\mu W/cm^2$, respectively.

The photo response of both devices covers the broadband spectral range of 300 nm to 1100 nm. By comparison both, it is observed that the 2D-0D-3D devices have 8× higher R, and 17× higher D^* as compared to (0D-3D) devices. All the proposed MD heterostructures photodetectors of (0D-3D) n-WS_2 QDs/p-Si and (2D-0D-3D) p-WSe_2 NSs/n-WS_2 QDs/p-Si exhibits a promising EQE of 9768 % and 82710 % respectively at 327 nm and 322 nm wavelength of the incident light of 7.26 and 6.97 $\mu W/cm^2$ intensity, respectively as shown in **Fig. 6.14 (c) and (d).** Therefore, it can be concluded that the addition of WSe_2 NSs improved R, D^*, and EQE tremendously.

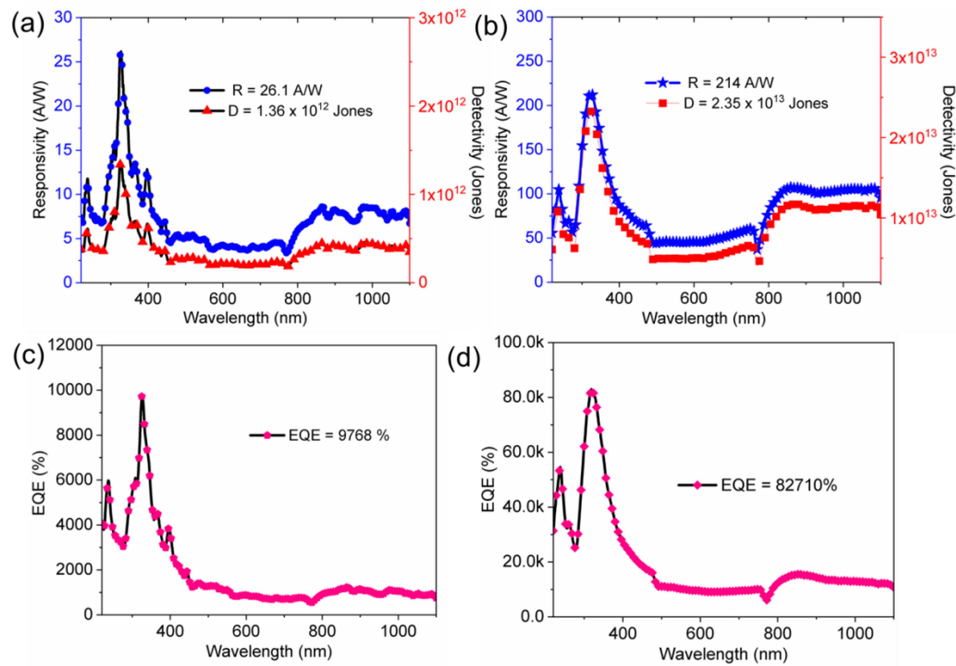

Fig. 6.14 The wavelength-dependent R, $D^*$and EQE of the (a, c) n-WS_2 (0D-3D) QDs/p-Si (b, d) (2D-0D-3D) p-WSe_2 NSs/n-WS_2 QDs/p-Si heterostructures photodetectors

The transient photo response characteristics of the (0D-3D) n-WS_2 QDs/p-Si and (2D-0D-3D) p-WSe_2 NS/n-WS_2 QDs/p-Si devices under ON and OFF state of illumination intensity of 21.98 mW/cm^2 at -3 V bias voltage are shown in **Fig. 6.15 (a) and (b),** respectively. The most crucial figures of merit of switching devices are the rise time and decay time. **Fig. 6.15 (c) and (d)** show the rise time (τ_r) and fall time (τ_f) of both devices by using a white light source at -3 V applied bias. The calculated transient responses show τ_r = 810 ms and τ_f = 800 ms for (0D-3D) n-WS_2 QDs/p-Si device and τ_r = 24 ms, whereas τ_f = 21 ms for (2D-0D-3D) p-WSe_2 NS/n-WS_2 QDs/p-Si. The values of τ_r and τ_f of the (2D-0D-3D) p-WSe_2 NS/n-WS_2 QDs/p-Si appear to be nearly 34 and 38 times smaller than their corresponding values of (0D-3D) /n-WS_2 QDs/p-Si device. The measured τ_r and τ_f of the (2D-0D-3D) p-WSe_2 NS/n-WS_2 QDs/p-Si device are also better than many other WSe_2-based broadband photodetectors [239, 387]. Various performance parameters of the proposed device have been compared with some reported devices in **Table 6.1.** Clearly, the (2D-0D-3D) p-WSe_2 NS/n-WS_2 QDs/p-Si multilayer MD heterostructure device shows better photodetection performance over the (0D-3D) n-WS_2 QDs/p-Si device.

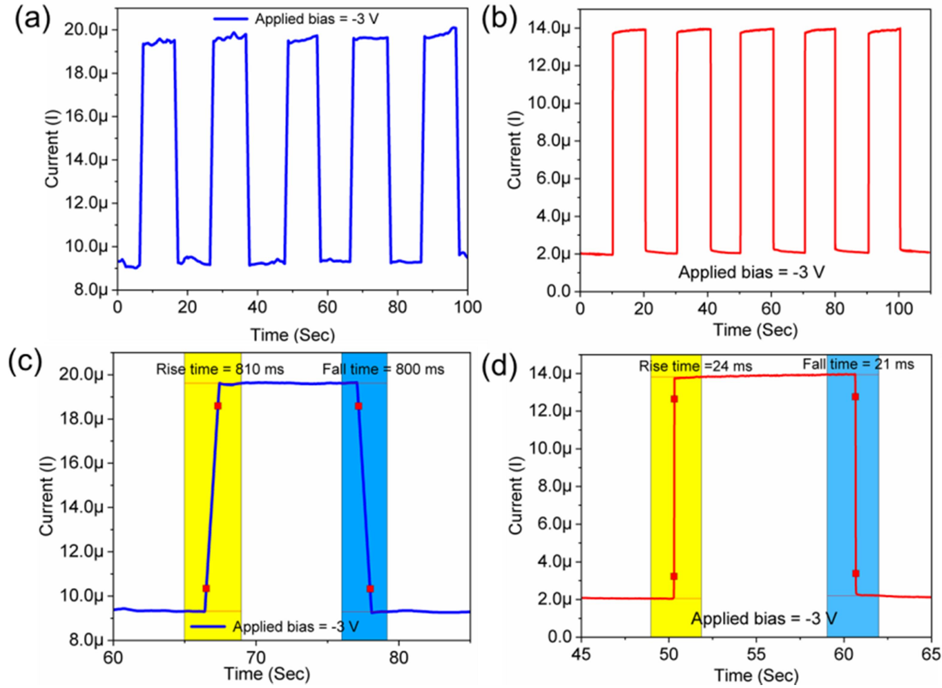

Fig. 6.15 (a, b) Transient photo response and (c, d) magnified image of single pulse for measurement of rise time and decay time of n.WS_2 QDs/p-Si heterojunction with (a, c) before and (b, d) after p.WSe_2 NS deposition under the illumination of white light with a power intensity of 21.98 mW/cm^2 at -3 V bias voltage.

6.4 Conclusions

In conclusion, we have compared the photo response characteristics of (0D-3D) n-WS_2 QDs/p-Si and (2D-0D-3D) p-WSe_2 NS/n-WS_2 QDs/p-Si MD heterostructures. The WSe_2 NSs and WS_2 QDs are synthesized using solvothermal and hydrothermal techniques respectively. Before p-WSe_2 NS deposition, the (0D-3D) n-WS_2 QDs/p-Si heterostructures-based photodetector showed R, D^* and EQE of 26.1 A/W, 1.36×10^{12} Jones and 9768% with $\tau_r = 810$ ms and $\tau_f = 800$ ms respectively. However, after p-WSe_2 NSs deposition, the (2D-0D-3D) p-WSe_2 NS/n-WS_2 QDs/p-Si showed R, D^*, and EQE of 214 A/W, 2.35×10^{13} Jones, and 82710% at 322 nm wavelength with very low τ_r and τ_f of 24 ms and 21 ms, respectively. Both devices showed a broadband photo response characteristic ranging from UV to near-IR (300 nm to 1100 nm). The results can pave the way for exploring various multilayer MD heterostructures for optoelectronic applications.

Chapter 7

CONCLUSION AND FUTURE WORK

7.1 Major contributions

The basic objective of the thesis is to study the electronic and optical properties of TM-doped 2D semiconductors and 2D heterostructures under the effect of biaxial strain using DFT calculations. Further, we fabricated and characterized 2D materials based on Mixed-dimensional heterostructures for broadband photodetection applications. The present chapter has been devoted to summarizing and concluding the major observations presented in the various chapters of this thesis. We have also outlined some scope for future works related to the areas considered in the present thesis.

Chapter 1 presents a brief introduction to the 2D materials family, various doping techniques such as substitutional doping, adsorption doping, and charge transfer doping, the formation of heterostructures, the role of external factors such as biaxial strain and external electric field on 2D materials, various synthesis and characterization methods, and fundamentals of photodetectors. The various performance parameters of photodetectors to characterize the overall performance of the devices are also briefly discussed. The fundamental concepts behind DFT calculations are discussed in detail in Chapter 1.

Chapter 2 presents a detailed literature survey on substitutional doping of 2D materials, strain engineering of 2D materials, 2D heterostructures, and mixed-dimensional (MD) heterostructures-based photodetectors has been discussed. Based on the observations from the literature survey, the motivation and the scope of the thesis have been detailed and outlined at the end of Chapter 2.

Chapter 3 presents a systematic study on the electronic structure of 3d (Sc, Ti, V, Cr), 4d (Y, Zr, Nb, Ru, Rh, Pd, and Ag), and 5d (Hf, Ta, Re, Ir, Au) group of TM-doped WSe_2 monolayer based on DFT calculations. Here, we studied the changes in electronic band structures, the density of states, E_{form}, and charge transfer due to dopants in the TM-doped WSe_2 monolayer. It is observed that due to induced strain, the energy bandgap of the TM-

doped WSe_2 monolayer has decreased. By using E_{form} calculations, we analyzed the thermal stability of the TM-doped WSe_2 monolayer. The charge transfer from TM dopants to the WSe_2 monolayer is calculated using the Bader charge analysis suggesting that the Pd, Ag, and Au-doped WSe_2 show purely metallic characteristics, whereas the Cr-doped WSe_2 retain its pristine semiconducting nature with reduced direct bandgap. The V, Nb, and Ta dopants are only potential p-type dopants, and Re is an n-type dopant for the WSe_2 monolayer. The reduced direct bandgap of V, Nb, Ta, and Re doped WSe_2 semiconductors is 1.23 eV, 1.43 eV, 1.42 eV, and 1.01 eV.

Chapter 4 reports the electronic and optical properties of Nb, Ta, and Re-doped WSe_2 monolayer under the application of biaxial strain using DFT calculations. The rate of bandgap tunability has been determined for K-K and, Γ–K transition, corresponding to A and I peak in PL and absorption spectroscopy. A redshift was observed in the optical spectra of Nb, Ta, and Re-doped WSe_2 monolayer with a significant broadening in the infrared region. By applying biaxial tensile strain, a further redshift and, in compressive strain, a blue-shift was observed in absorption spectra. Moreover, the effect of biaxial strain on the E_{form} of Re, Nb, Ta, and *V*-dopants in the WSe_2 monolayer has been analyzed in detail. It is observed that the E_{form} shows parabolic and linear behaviour with biaxial strain; depending upon the net change in ΔV. The change ΔV is explained based on the atomic radius and induced electronic environment due to different dopant types. For Re and *V*, the calculated E_{form} is parabolic in nature and favors both tensile as well as compressive strain. However, due to the monotonic linear relation with the biaxial strain, E_{form} favors the tensile strain for Nb and Ta dopants.

We also systematically studied the strain-dependent doping behaviour and optical absorption of the g-AZO monolayer under the application of ε_{xy} by using hybrid DFT calculations. We observed that E_{form} increases linearly upto $\varepsilon_{xy} = +5\%$ of tensile strain, whereas after $\varepsilon_{xy} > 5\%$ an inverse parabolic relation with ε_{xy} is observed. Due to the lowest value of E_{form} at $\varepsilon_{xy} = +10\%$, a higher doping concentration (>18%) of Al dopants is observed which further causes the improvement of optical visible absorption. Moreover, the g-AZO monolayer at $\varepsilon_{xy} =+10\%$ have the highest absorption in the Vis and NIR range.

Chapter 5 presents the modulation of electronic band structure and optical properties of $GaTe/MoTe_2$ heterostructure under different strain and electric fields for optoelectronic applications. Four different heterostructure configurations of $GaTe/MoTe_2$ are constructed the most stable $GaTe/MoTe_2$ heterostructure is determined based on minimum binding energy.

The optimized $GaTe/MoTe_2$ heterostructure has an indirect bandgap of 1.5 eV with type-I band alignment having excellent optical absorption in the visible region of the optical spectra. Our result suggests that band alignment type changes from type-I to type-II and indirect to direct by applying a particular range of biaxial strain and external electric field. It is observed that for $\varepsilon_{xy} > +2\%$ and E_{ext} between +0.4 V/Å to +1 V/Å, and -0.6 V/Å to -1 V/Å, the band alignment changes from type-I to type-II, with the high optical visible absorption of order 10^5 cm^{-1}. Moreover, for the higher value of ε_{xy} and E_{ext}-field, a semiconductor-to-metal transition is observed. All of these properties enable the $GaTe/MoTe_2$ heterostructure as a promising multifunctional device in optoelectronics and photocatalytic reaction application.

Chapter 6 presents n-WS_2 Quantum Dots/p-Si (0D-3D) and p-WSe_2 Nanosheets/n-WS_2 Quantum Dots/p-Si (2D-0D-3D) mixed-dimensional multilayer heterojunction-based high-performance broadband photodetector. The WSe_2 Nanosheets (NSs) and WS_2 quantum dots (QDs) have been synthesized via the solvothermal and hydrothermal method and then characterized by HR-TEM, AFM, XRD, Raman Spectroscopy, UV-Vis Spectroscopy, and PL spectra. The I-V characteristics and all the parameters of photodetectors such as R, D^*, EQE, and transient time (Rise time and Fall time) of the as-fabricated devices. The current-voltage (I-V) under dark and light illumination conditions and photoresponse characteristics of the (0D-3D) n-WS_2 QDs/p-Si and (2D-0D-3D) p-WSe_2 NSs/n-WS_2 QDs/p-Si heterostructures investigated in details with Ag as top contact. It is observed that the device has high photoresponse characteristics in broadband photodetection range from UV to near-IR (300 to 1100 nm). The as-fabricated Ag/p-WSe_2 NSs/n-WS_2 QDs/p-Si/Ti/Al (2D-0D-3D) mixed-dimensional heterostructure has shown the highest R, $D^*$and EQE of 214 A/W, 2.35×10^{13} Jones and 82710% at 322 nm wavelength (6.97 $\mu W/cm^2$) and -3 V reverse bias voltage with very low rise time and fall time of 24 ms and 21 ms, respectively.

7.2 Scope of Future Work

This study provided some preliminary investigations on electronic structures and optical properties of TM-doped 2D materials, 2D heterostructure, and mixed dimensional heterostructure-based broadband photodetector for optoelectronics applications. Some future works can be carried out to extend the scope of this study.

- Transport properties of the TM doped 2D materials can be studied by using DFT calculations along with Non-equalibiuirm Green Function (NEGF) approach.
- The NEGF approach further can be utilized in I-V characteristic of 2D heterostructure
- Twist-angle dependent properties of 2D bilayer and heterostructure can be studied.
- Mixed-dimensional heterostructures can be studied with 2D semiconductors

BIBLIOGRAPHY:

Sayantika Chowdhury was born on 9th December, 1991 in Udaipur city, Tripura, India. She completed her higher secondary in 2010 from M.T.B Girl's H.S. School, Agartala, Tripura, and did her bachelor's degree (B.Tech) in Electronics and Communication Engineering from Gurunanak Institute of Technology, Kolkata in 2014. Her bachelor project topic was 'Automated bot capable of stopping at traffic sensitive zones'. Then she completed her M.Tech degree in Electronics and Communication Engineering from the Heritage Institute of Technology, Kolkata in 2016. Her Master's degree thesis was entitled "Numerical analysis of photonic crystal fiber based hemoglobin sensor". Then she joined as a Junior Research Fellow in the Department of Fiber Optics and Photonics Division (FOPD), CSIR-CGCRI, Kolkata, India under the supervision of Dr. Tarun Kumar Gangopadhyay, Senior principal scientist in 2016. Her project title was "Study and development of non-invasive ambulatory respiratory and cardiac monitoring/stem for mobile health monitoring using photonic crystal fiber" from which she published one SCI journal and one conference paper**.** In 2018, she joined Jadavpur University (JU) as a project Fellow under the guidance of Dr. Divya Somvanshi, DST Inspire Faculty (Former) in the Department of Electronics and Telecommunication Engineering (ETCE). She started her journey as a Ph.D. student under the supervision of Prof. P. Venkateswaran and Dr. Divya Somvanshi in June 2019 from ETCE Dept., JU with a Thesis entitled "Atomistic Simulation, Synthesis, and Characterization of 2D materials for Optoelectronic Device applications". She has research interests in the area of semiconductor devices and 2D materials simulation.

References:

1. Rao, C.N., et al., *Graphene: the new two-dimensional nanomaterial.* Angew Chem Int Ed Engl, 2009. **48**(42): p. 7752-77.
2. Moosa, A.A. and M.S. Abed, *Graphene preparation and graphite exfoliation.* 2021. **45**(3): p. 493-519.
3. Hu, Z., Z.-B. Liu, and J.-G. Tian, *Stacking of Exfoliated Two-Dimensional Materials: A Review.* Chinese Journal of Chemistry, 2020. **38**(9): p. 981-995.
4. Edward, K., et al., *State-of-the-Art Graphene Synthesis Methods and Environmental Concerns.* Applied and Environmental Soil Science, 2023. **2023**: p. 8475504.
5. Kang, S., et al., *2D semiconducting materials for electronic and optoelectronic applications: potential and challenge.* 2D Materials, 2020. **7**(2): p. 022003.
6. Schwierz, F., J. Pezoldt, and R. Granzner, *Two-dimensional materials and their prospects in transistor electronics.* Nanoscale, 2015. **7**(18): p. 8261-8283.
7. Chaves, A., et al., *Bandgap engineering of two-dimensional semiconductor materials.* npj 2D Materials and Applications, 2020. **4**(1): p. 29.
8. Jayakumar, A., A. Surendranath, and M. Pv, *2D materials for next generation healthcare applications.* International Journal of Pharmaceutics, 2018. **551**(1): p. 309-321.
9. Derakhshi, M. and S. Daemi, *Two-Dimensional Nanomaterials beyond Graphene for Biomedical Applications.* 2022. **13**(1).
10. Lu, G., et al., *Semiconducting graphene: converting graphene from semimetal to semiconductor.* Nanoscale, 2013. **5**(4): p. 1353-1368.
11. Bhimanapati, G.R., N.R. Glavin, and J.A. Robinson, *Chapter Three - 2D Boron Nitride: Synthesis and Applications*, in *Semiconductors and Semimetals*, F. Iacopi, J.J. Boeckl, and C. Jagadish, Editors. 2016, Elsevier. p. 101-147.
12. Chanana, A. and S. Mahapatra, *First principles study of metal contacts to monolayer black phosphorous.* Journal of Applied Physics, 2014. **116**(20): p. 204302.
13. Ahmed, S. and J. Yi, *Two-Dimensional Transition Metal Dichalcogenides and Their Charge Carrier Mobilities in Field-Effect Transistors.* Nano-Micro Letters, 2017. **9**(4): p. 50.
14. Kumbhakar, P., et al., *Emerging 2D metal oxides and their applications.* Materials Today, 2021. **45**.
15. S George, N., L. Jose, and A. Aravind, *Review on Transition Metal Oxides and Their Composites for Energy Storage Application*. 2022.
16. Xie, H., et al., *Recent advances in the fabrication of 2D metal oxides.* iScience, 2022. **25**(1): p. 103598.
17. Zheng, W., et al., *Thickness- and Twist-Angle-Dependent Interlayer Excitons in Metal Monochalcogenide Heterostructures.* ACS Nano, 2022. **16**(11): p. 18695-18707.
18. Sun, H., Z. Wang, and Y. Wang, *Band alignment of two-dimensional metal monochalcogenides MXs (M=Ga,In; X=S,Se,Te).* AIP Advances, 2017. **7**(9).
19. Glavin, N.R., et al., *Emerging Applications of Elemental 2D Materials.* Advanced Materials, 2020. **32**(7): p. 1904302.
20. Li, D., et al., *Recent Progress of Two-Dimensional Thermoelectric Materials.* Nano-Micro Letters, 2020. **12**(1): p. 36.

21. Bilisik, K. and M. Akter, *Graphene nanocomposites: A review on processes, properties, and applications.* Journal of Industrial Textiles, 2021. **51**(3_suppl): p. 3718S-3766S.
22. Arikpo, J.U. and M.U. Onuu, *Graphene Growth and Characterization: Advances, Present Challenges and Prospects.* Journal of Materials Science Research, 2019.
23. Wang, Q.H., et al., *Electronics and optoelectronics of two-dimensional transition metal dichalcogenides.* Nature Nanotechnology, 2012. **7**(11): p. 699-712.
24. Ye, M., D. Zhang, and Y.K. Yap, *Recent Advances in Electronic and Optoelectronic Devices Based on Two-Dimensional Transition Metal Dichalcogenides.* Electronics, 2017. **6**(2): p. 43.
25. Vogel, E. and J. Robinson, *Two-dimensional layered transition-metal dichalcogenides for versatile properties and applications.* MRS Bulletin, 2015. **40**: p. 558-563.
26. Ahmad, S. and S. Mukherjee, *A Comparative Study of Electronic Properties of Bulk MoS2 and Its Monolayer Using DFT Technique: Application of Mechanical Strain on MoS2 Monolayer.* Graphene, 2014. **Vol.03No.04**: p. 8.
27. Rai, A., et al., *Progress in Contact, Doping and Mobility Engineering of MoS2: An Atomically Thin 2D Semiconductor.* Crystals, 2018. **8**(8): p. 316.
28. Hanbicki, A.T., et al., *Measurement of high exciton binding energy in the monolayer transition-metal dichalcogenides WS2 and WSe2.* Solid State Communications, 2015. **203**: p. 16-20.
29. Radisavljevic, B., et al., *Single-layer MoS2 transistors.* Nature Nanotechnology, 2011. **6**: p. 147.
30. Mak, K. and J. Shan, *Photonics and optoelectronics of 2D semiconductor transition metal dichalcogenides.* Nature Photonics, 2016. **10**: p. 216-226.
31. Zhang, H., *Ultrathin Two-Dimensional Nanomaterials.* ACS Nano, 2015. **9**(10): p. 9451-9469.
32. Li, X. and H. Zhu, *Two-dimensional MoS2: Properties, preparation, and applications.* Journal of Materiomics, 2015. **1**(1): p. 33-44.
33. Novoselov, K.S., et al., *Two-dimensional atomic crystals.* Proceedings of the National Academy of Sciences of the United States of America, 2005. **102**(30): p. 10451-10453.
34. Mak, K.F., et al., *Atomically Thin* MoS_2 *: A New Direct-Gap Semiconductor.* Phys. Rev. Lett., 2010. **105**(13): p. 136805.
35. Bertolazzi, S., J. Brivio, and A. Kis, *Stretching and Breaking of Ultrathin* MoS_2*.* ACS Nano, 2011. **5**(12): p. 9703-9709.
36. Peelaers, H. and C.G. Van de Walle, *Effects of strain on band structure and effective masses in* MoS_2*.* Phys. Rev. B, 2012. **86**(24): p. 241401.
37. Gomes, L.C., A. Carvalho, and A.H. Castro Neto, *Vacancies and oxidation of two-dimensional group-IV monochalcogenides.* Physical Review B, 2016. **94**(5): p. 054103.
38. Guo, Y., et al., *Oxidation Resistance of Monolayer Group-IV Monochalcogenides.* ACS Applied Materials & Interfaces, 2017. **9**(13): p. 12013-12020.
39. Li, F., et al., *Germanium monosulfide monolayer: a novel two-dimensional semiconductor with a high carrier mobility.* Journal of Materials Chemistry C, 2016. **4**(11): p. 2155-2159.
40. Vu, T.V., et al., *Enhancement of monolayer SnSe light absorption by strain engineering: A DFT calculation.* Chemical Physics, 2019. **521**: p. 5-13.
41. Liu, J., et al., *Monolayer organic field-effect transistors.* Science China Chemistry, 2019. **62**: p. 1-18.

42. Cui, Y., et al., *Two-dimensional few-layer group-III metal monochalcogenides as effective photocatalysts for overall water splitting in the visible range.* Journal of Materials Chemistry A, 2018. **6**(45): p. 22768-22777.
43. Li, W. and J. Li, *Piezoelectricity in two-dimensional group-III monochalcogenides.* Nano Research, 2015. **8**(12): p. 3796-3802.
44. Ren, C., et al., *First-principles investigation on electronic properties and band alignment of group III monochalcogenides.* Scientific Reports, 2019. **9**(1): p. 13289.
45. Chowdhury, S., et al., *Electronic structure and optical properties of GaTe/MoTe2 based vdW heterostructure under mechanical strain and external electric fields.* Materials Science in Semiconductor Processing, 2023. **163**: p. 107572.
46. Xiong, R., et al., *Direct Z-scheme WTe2/InSe van der Waals heterostructure for overall water splitting.* Catalysis Science & Technology, 2022. **12**(10): p. 3272-3280.
47. Li, Y., et al., *Strain forces tuned the electronic and optical properties in GaTe/MoS2 van der Waals heterostructures.* RSC Advances, 2020. **10**(42): p. 25136-25142.
48. Guo, H., et al., *Tunable contacts and device performances in graphene/group-III monochalcogenides MX (M = In, Ga; X = S, Se) van der Waals heterostructures.* Journal of Applied Physics, 2021. **130**(14).
49. Erwin, S., et al., *Doping Semiconductor Nanocrystals.* Nature, 2005. **436**: p. 91-4.
50. Cui, Z., et al., *Electronic, magnetism, and optical properties of transition metals adsorbed g-GaN.* Physica E: Low-dimensional Systems and Nanostructures, 2020. **118**: p. 113871.
51. Cui, Z., et al., *Electronic, magnetism and optical properties of transition metals adsorbed puckered arsenene.* Superlattices and Microstructures, 2021. **152**: p. 106852.
52. Cui, Z., et al., *Tuning the electronic properties of MoSi2N4 by molecular doping: A first principles investigation.* Physica E: Low-dimensional Systems and Nanostructures, 2021. **134**: p. 114873.
53. Dolui, K., et al., *Possible doping strategies for MoS${}_{2}$ monolayers: An ab initio study.* Physical Review B, 2013. **88**(7): p. 075420.
54. Chowdhury, S., P. Venkateswaran, and D. Somvanshi, *A systematic study on the electronic structure of 3d, 4d, and 5d transition metal-doped WSe2 monolayer.* Superlattices and Microstructures, 2020. **148**: p. 106746.
55. Chowdhury, S., P. Venkateswaran, and D. Somvanshi, *Strain-dependent doping behavior of WSe(2) monolayer: A first-principal calculations.* Europhysics Letters, 2022.
56. Chowdhury, S., P. Venkateswaran, and D. Somvanshi, *Effect of biaxial strain on the electronic structure of Nb-doped WSe2 monolayer: a theoretical study.* 2021 Devices for Integrated Circuit (DevIC), 2021: p. 79-83.
57. Wang, Y., et al., *Surface charge transfer doping for two-dimensional semiconductor-based electronic and optoelectronic devices.* Nano Research, 2021. **14**(6): p. 1682-1697.
58. Kim, J.-K., et al., *Molecular Dopant-Dependent Charge Transport in Surface-Charge-Transfer-Doped Tungsten Diselenide Field Effect Transistors.* Advanced Materials, 2021. **33**(44): p. 2101598.

59. Wu, C.-C., et al., *Elucidating the Photoresponse of Ultrathin MoS2 Field-Effect Transistors by Scanning Photocurrent Microscopy.* The Journal of Physical Chemistry Letters, 2013. **4**(15): p. 2508-2513.
60. Rastogi, P., et al., *Doping Strategies for Monolayer MoS2 via Surface Adsorption: A Systematic Study.* The Journal of Physical Chemistry C, 2014. **118**(51): p. 30309-30314.
61. Sun, D., et al., *Comparative Study on ZnO Monolayer Doped with Al, Ga and In Atoms as Transparent Electrodes.* Materials (Basel), 2017. **10**(7).
62. Pandey, S.K., et al., *Controlled p-type substitutional doping in large-area monolayer WSe2 crystals grown by chemical vapor deposition.* Nanoscale, 2018. **10**(45): p. 21374-21385.
63. Loh, L., et al., *Substitutional doping in 2D transition metal dichalcogenides.* Nano Research, 2020.
64. Luo, P., et al., *Doping engineering and functionalization of two-dimensional metal chalcogenides.* Nanoscale Horiz, 2019. **4**(1): p. 26-51.
65. Onofrio, N., D. Guzman, and A. Strachan, *Novel doping alternatives for single-layer transition metal dichalcogenides.* Journal of Applied Physics, 2017. **122**(18): p. 185102.
66. Chowdhury, S., P. Venkateswaran, and D. Somvanshi, *Strain-dependent doping and optical absorption in Al-doped graphene-like ZnO monolayer.* Solid State Communications, 2023. **365**: p. 115139.
67. Di, X., et al. *Synthesis of WSe2 by Chemical Vapor Deposition and Influence of Hydrogen on Morphology*. in *2019 China Semiconductor Technology International Conference (CSTIC)*. 2019.
68. Liu, B., et al., *Chemical Vapor Deposition Growth of Monolayer WSe2 with Tunable Device Characteristics and Growth Mechanism Study.* ACS Nano, 2015. **9**(6): p. 6119-6127.
69. Zhu, J., et al., *Strain-Enhanced Doping in Semiconductors: Effects of Dopant Size and Charge State.* Physical Review Letters, 2010. **105**(19): p. 195503.
70. Li, H., et al., *Metallic impurities induced electronic transport in WSe2: First-principle calculations.* Chemical Physics Letters, 2016. **658**: p. 83-87.
71. Choi, M., et al., *Understanding of relationship between dopant and substitutional site to develop novel phase-change materials based on In3SbTe2.* Japanese Journal of Applied Physics, 2019. **58**(SB): p. SBBB02.
72. Zhao, X., P. Chen, and T. Wang, *Controlled electronic and magnetic properties of WSe2 monolayers by doping transition-metal atoms.* Superlattices and Microstructures, 2016. **100**: p. 252-257.
73. Chang, J., et al., *Atomistic simulation of the electronic states of adatoms in monolayer MoS2.* Applied Physics Letters, 2014. **104**(14).
74. Rastogi, P., et al., *Effective Doping of Monolayer Phosphorene by Surface Adsorption of Atoms for Electronic and Spintronic Applications.* IETE Journal of Research, 2017. **63**(2): p. 205-215.
75. Pizzone, M., M.G. Grimaldi, and A. La Magna, *Study of the Molecule Adsorption Process during the Molecular Doping.* 2021. **11**(8).
76. Cho, Y., et al., *Damage-Free Charge Transfer Doping of 2D Transition Metal Dichalcogenide Channels by van der Waals Stamping of MoO(3) and LiF.* 2022. **6**(3): p. e2101073.
77. Guo, Z., F. Ambrosio, and A. Pasquarello, *Oxygen defects in amorphous Al2O3: A hybrid functional study.* Applied Physics Letters, 2016. **109**(6).

78. Gobbi, M., E. Orgiu, and P. Samorì, *When 2D Materials Meet Molecules: Opportunities and Challenges of Hybrid Organic/Inorganic van der Waals Heterostructures.* Advanced Materials, 2018. **30**(18): p. 1706103.
79. Tsai, M.-Y., et al., *Solution-Processed Doping of Trilayer WSe2 with Redox-Active Molecules.* Chemistry of Materials, 2017. **29**(17): p. 7296-7304.
80. Yu, L., et al., *High-Performance WSe2 Complementary Metal Oxide Semiconductor Technology and Integrated Circuits.* Nano Letters, 2015. **15**(8): p. 4928-4934.
81. Anderson, R.L., *Experiments on Ge-GaAs heterojunctions.* Solid-State Electronics, 1962. **5**(5): p. 341-351.
82. Wang, Z., et al., *Type-I Heterostructure Based on WS2/PtS2 for High-Performance Photodetectors.* ACS Applied Materials & Interfaces, 2022. **14**(33): p. 37926-37936.
83. Bellus, M.Z., et al., *Type-I van der Waals heterostructure formed by MoS2 and ReS2 monolayers.* Nanoscale Horizons, 2017. **2**(1): p. 31-36.
84. Kośmider, K. and J. Fernández-Rossier, *Electronic properties of the MoS2-WS2 heterojunction.* Physical Review B, 2012. **87**.
85. Limei, F., Q. Feng, and S.-N. Luo, *Tunable electronic properties of monolayer MnPSe3/MoTe2 heterostructure: A first principles study.* Journal of Physics: Condensed Matter, 2019. **31**.
86. Chowdhury, S., P. Venkateswaran, and D. Somvanshi. *Interlayer twist angle-dependent electronic structure and optical properties of InSe/WTe2 van der Waals heterostructure*. in *2022 IEEE International Conference of Electron Devices Society Kolkata Chapter (EDKCON)*. 2022.
87. Geim, A.K. and I.V. Grigorieva, *Van der Waals heterostructures.* Nature, 2013. **499**(7459): p. 419-425.
88. Yang, X., et al., *HfS2/MoTe2 vdW heterostructure: bandstructure and strain engineering based on first-principles calculation.* RSC Advances, 2020. **10**(5): p. 2615-2623.
89. Ferreira, R., *Introduction to Semiconductor Heterostructures*, in *Semiconductor Modeling Techniques*, N. Balkan and M. Xavier, Editors. 2012, Springer Berlin Heidelberg: Berlin, Heidelberg. p. 1-17.
90. Cong, X., et al., *Efficiently band-tailored type-III van der Waals heterostructure for tunnel diodes and optoelectronic devices.* Nano Research, 2022. **15**(9): p. 8442-8450.
91. Lei, C., et al., *Broken-Gap Type-III Band Alignment in WTe2/HfS2 van der Waals Heterostructure.* The Journal of Physical Chemistry C, 2019. **123**(37): p. 23089-23095.
92. Chen, H., et al., *Enhanced photocatalytic performance of ZnO monolayer for water splitting via biaxial strain and external electric field.* Applied Surface Science, 2019. **481**.
93. Zhu, J., et al., *Twisted angle modulated structural property, electronic structure and carrier transport of MoS2/AlN(0001) mixed-dimensional van der Waals heterostructure.* Applied Surface Science, 2021. **563**: p. 150330.
94. Feng, S. and Z. Xu, *Strain Characterization in Two-Dimensional Crystals.* 2021. **14**(16).
95. Andersen, M., O.S. Hopperstad, and A.H. Clausen, *Volumetric strain measurement of polymeric materials subjected to uniaxial tension.* Strain, 2019. **55**(4): p. e12314.
96. Chowdhury, S., P. Venkateswaran, and D. Somvanshi, *Biaxial strain-modulated electronic and optical properties of transition metals doped-WSe2 monolayer.* Physica B: Condensed Matter, 2023. **653**: p. 414668.

97. Chowdhury, S., P. Venkateswaran, and D. Somvanshi. *A comparative study of biaxial strain modulated electronic structure of MSe2 (M = W, Mo) monolayer*. in *2021 5th International Conference on Electronics, Materials Engineering & Nano-Technology (IEMENTech)*. 2021.
98. Frisenda, R., et al., *Biaxial strain tuning of the optical properties of single-layer transition metal dichalcogenides.* npj 2D Mater. Appli., 2017. **1**(1): p. 10.
99. Roldán, R., et al., *Strain engineering in semiconducting two-dimensional crystals.* Journal of Physics: Condensed Matter, 2015. **27**(31): p. 313201.
100. Dai, Z., L. Liu, and Z. Zhang, *Strain Engineering of 2D Materials: Issues and Opportunities at the Interface.* Adv. Mater., 2019. **31**(45): p. 1805417.
101. Yun, W.S., et al., *Thickness and strain effects on electronic structures of transition metal dichalcogenides: 2H-$M{X}_{2}$ semiconductors (M $=$ Mo, W; X $=$ S, Se, Te).* Physical Review B, 2012. **85**(3): p. 033305.
102. Chowdhury, S., P. Venkateswaran, and D. Somvanshi. *Strain-Induced Electronic Structure and Bandgap Transition in Bilayer MoSe_{2} of AB and AA Stacking Order*. in *2022 IEEE Calcutta Conference (CALCON)*. 2022.
103. Desai, S.B., et al., *Strain-Induced Indirect to Direct Bandgap Transition in Multilayer WSe_2.* Nano Lett., 2014. **14**(8): p. 4592-4597.
104. Michail, A., et al., *Biaxial strain engineering of CVD and exfoliated single- and bi-layer MoS_2 crystals.* 2D Mater, 2020. **8**(1): p. 015023.
105. Xin, Q., X. Zhao, and T. Wang, *Electronic and magnetic properties of Mn-doped WSe2 monolayer under strain.* Physica E: Low-dimensional Systems and Nanostructures, 2017. **88**: p. 11-17.
106. Kan, E., et al., *Enhancing magnetic vacancies in semiconductors by strain.* Applied Physics Letters, 2012. **100**(7): p. 072401.
107. Sun, Y. and K. Liu, *Strain engineering in functional 2-dimensional materials.* J. Appl. Phys., 2019. **125**(8): p. 082402.
108. Bissett, M.A., M. Tsuji, and H. Ago, *Strain engineering the properties of graphene and other two-dimensional crystals.* Phys. Chem. Chem. Phys.,, 2014. **16**(23): p. 11124-11138.
109. *Physics and Properties of Semiconductors—A Review*, in *Physics of Semiconductor Devices*. 2006. p. 5-75.
110. Yin, S., et al., *A type-II PtS2/MoTe2 van der Waals heterostructure with adjustable electronic and optical properties.* Results in Physics, 2022. **33**: p. 105172.
111. Li, X., et al., *Type-II InSe/MoSe2(WSe2) van der Waals heterostructures: vertical strain and electric field effects.* Journal of Materials Chemistry C, 2018. **6**(37): p. 10010-10019.
112. Takahashi, S., et al., *Direct creation of three-dimensional photonic crystals by a top-down approach.* Nature Materials, 2009. **8**(9): p. 721-725.
113. Brent, J.R., N. Savjani, and P. O'Brien, *Synthetic approaches to two-dimensional transition metal dichalcogenide nanosheets.* Progress in Materials Science, 2017. **89**: p. 411-478.
114. Kumar, S., P. Bhushan, and S. Bhattacharya, *Fabrication of Nanostructures with Bottom-up Approach and Their Utility in Diagnostics, Therapeutics, and Others*. Environmental, Chemical and Medical Sensors. 2017 Nov 18:167-98. doi: 10.1007/978-981-10-7751-7_8. eCollection 2018.

115. Hang, D.R., et al., *Facile Bottom-up Preparation of WS(2)-Based Water-Soluble Quantum Dots as Luminescent Probes for Hydrogen Peroxide and Glucose.* Nanoscale Res Lett, 2019. **14**(1): p. 271.

116. Jianghao, W., L. Guangshe, and L. Liping, *Synthesis Strategies about 2D Materials*, in *Two-dimensional Materials*, N. Pramoda Kumar, Editor. 2016, IntechOpen: Rijeka. p. Ch. 1.

117. Novoselov, K.S., et al., *Two-dimensional gas of massless Dirac fermions in graphene.* Nature, 2005. **438**(7065): p. 197-200.

118. Novoselov, K.S., et al., *Electric field effect in atomically thin carbon films.* Science, 2004. **306**(5696): p. 666-9.

119. Miremadi, B.K. and S.R. Morrison, *High activity catalyst from exfoliated MoS2.* Journal of Catalysis, 1987. **103**(2): p. 334-345.

120. Zhang, W., et al., *Role of metal contacts in high-performance phototransistors based on WSe2 monolayers.* ACS Nano, 2014. **8**(8): p. 8653-61.

121. Coleman, J.N., et al., *Two-dimensional nanosheets produced by liquid exfoliation of layered materials.* Science, 2011. **331**(6017): p. 568-71.

122. Chauhan, B., et al., *Liquid-phase exfoliation of WSe2 nanosheets for ITO/WSe2 photodetector.* Journal of Materials Science: Materials in Electronics, 2022. **33**.

123. Huo, C., et al., *2D materials via liquid exfoliation: a review on fabrication and applications.* Science Bulletin, 2015. **60**.

124. Brodie, B.C., *XIII. On the atomic weight of graphite.* Philosophical Transactions of the Royal Society of London, 1859. **149**: p. 249-259.

125. Hummers, W.S. and R.E. Offeman, *Preparation of Graphitic Oxide.* Journal of the American Chemical Society, 1958. **80**(6): p. 1339-1339.

126. Xiong, F., et al., *Li Intercalation in MoS2: In Situ Observation of Its Dynamics and Tuning Optical and Electrical Properties.* Nano Lett, 2015. **15**(10): p. 6777-84.

127. Alam, S., et al., *Synthesis of emerging two-dimensional (2D) materials – Advances, challenges and prospects.* FlatChem, 2021. **30**: p. 100305.

128. Kang, T., et al., *Strategies for Controlled Growth of Transition Metal Dichalcogenides by Chemical Vapor Deposition for Integrated Electronics.* 2022. **2**(6): p. 665-685.

129. Du, J., et al., *Advances in Flexible Optoelectronics Based on Chemical Vapor Deposition-Grown Graphene.* Advanced Functional Materials, 2022. **32**(42): p. 2203115.

130. Thomas, N., et al., *2D MoS2: structure, mechanisms, and photocatalytic applications.* Materials Today Sustainability, 2021. **13**: p. 100073.

131. Ishag, A. and Y. Sun, *Recent Advances in Two-Dimensional MoS2 Nanosheets for Environmental Application.* Industrial & Engineering Chemistry Research, 2021. **60**(22): p. 8007-8026.

132. Peters, E.S., C.J. Carmalt, and I.P. Parkin, *Dual-source chemical vapour deposition of titanium sulfide thin films from tetrakisdimethylamidotitanium and sulfur precursors.* Journal of Materials Chemistry, 2004. **14**(23): p. 3474-3477.

133. Boscher, N.D., et al., *Atmospheric pressure chemical vapour deposition of vanadium diselenide thin films.* Applied Surface Science, 2007. **253**(14): p. 6041-6046.

134. Boscher, N.D., C.J. Carmalt, and I.P. Parkin, *Atmospheric pressure chemical vapor deposition of WSe2 thin films on glass—highly hydrophobic sticky surfaces.* Journal of Materials Chemistry, 2006. **16**(1): p. 122-127.

135. Carmalt, C.J., I.P. Parkin, and E.S. Peters, *Atmospheric pressure chemical vapour deposition of WS2 thin films on glass.* Polyhedron, 2003. **22**(11): p. 1499-1505.

136. Boscher, N.D., et al., *Atmospheric Pressure CVD of Molybdenum Diselenide Films on Glass.* Chemical Vapor Deposition, 2006. **12**(11): p. 692-698.

137. Peng, Y., et al., *Hydrothermal Synthesis and Characterization of Single-Molecular-Layer MoS2 and MoSe2.* Chemistry Letters, 2001. **30**(8): p. 772-773.

138. Jeong, S., et al., *Well-defined colloidal 2-D layered transition-metal chalcogenide nanocrystals via generalized synthetic protocols.* J Am Chem Soc, 2012. **134**(44): p. 18233-6.

139. Martínez-Merino, P., et al., *WSe2 Nanosheets Synthesized by a Solvothermal Process as Advanced Nanofluids for Thermal Solar Energy.* ACS Sustainable Chemistry & Engineering, 2020. **8**(3): p. 1627-1636.

140. Wang, X., et al., *Graphene-like WSe2 nanosheets for efficient and stable hydrogen evolution.* Journal of Alloys and Compounds, 2017. **691**: p. 698-704.

141. Rukari, T. and A. Babita, *Review Article TRANSMISSION ELECTRON MICROSCOPY-AN OVERVIEW.* 2013. **1**: p. 1-7.

142. Mohammed, A. and A. Abdullah, *Scanning Electron Microscopy (SEM): A Review*. 2019.

143. Wang, Y.-a., et al., *Effects of tumor metabolic microenvironment on regulatory T cells.* Molecular Cancer, 2018. **17**(1): p. 168.

144. Dufrêne, Y.F. and A.E. Pelling, *Force nanoscopy of cell mechanics and cell adhesion.* Nanoscale, 2013. **5**(10): p. 4094-104.

145. Deng, X., et al., *Application of atomic force microscopy in cancer research.* Journal of Nanobiotechnology, 2018. **16**(1): p. 102.

146. Bunaciu, A.A., E. UdriŞTioiu, and H. Aboul-Enein, *X-Ray Diffraction: Instrumentation and Applications.* Critical reviews in analytical chemistry / CRC, 2015. **45**.

147. Foner, H.A. and N. Adan, *The Characterization of Papers by X-Ray Diffraction (XRD): Measurement of Cellulose Crystallinity and Determination of Mineral Composition.* Journal of the Forensic Science Society, 1983. **23**(4): p. 313-321.

148. Weckhuysen, B., *Ultraviolet-Visible Spectroscopy.* 2004.

149. Hussain, A., *UV-VISIBLE SPECTROMETRY.* 2019.

150. Tebyetekerwa, M., et al., *Mechanisms and Applications of Steady-State Photoluminescence Spectroscopy in Two-Dimensional Transition-Metal Dichalcogenides.* ACS Nano, 2020. **14**(11): p. 14579-14604.

151. Gfroerer, T., *Photoluminescence in Analysis of Surfaces and Interfaces*. 2006.

152. Aoki, T., *Characterization of Materials*. 2012.

153. Rostron, P. and D. Gerber, *Raman Spectroscopy, a review.* International Journal of Engineering and Technical Research, 2016. **6**: p. 50-64.

154. Bumbrah, G.S. and R.M. Sharma, *Raman spectroscopy – Basic principle, instrumentation and selected applications for the characterization of drugs of abuse.* Egyptian Journal of Forensic Sciences, 2016. **6**(3): p. 209-215.
155. Lopez-Sanchez, O., et al., *Ultrasensitive photodetectors based on monolayer MoS2.* Nat Nanotechnol, 2013. **8**(7): p. 497-501.
156. Qiao, H., et al., *Self-Powered Photodetectors Based on 2D Materials.* Advanced Optical Materials, 2020. **8**(1): p. 1900765.
157. Esmaeili-Rad, M.R. and S. Salahuddin, *High Performance Molybdenum Disulfide Amorphous Silicon Heterojunction Photodetector.* Scientific Reports, 2013. **3**(1): p. 2345.
158. Dhyani, V., et al., *High performance broadband photodetector based on MoS2/porous silicon heterojunction.* Applied Physics Letters, 2017. **111**(19).
159. Shin, J. and H. Yoo, *Photogating Effect-Driven Photodetectors and Their Emerging Applications.* 2023. **13**(5).
160. Shen, W.-C., R.-S. Chen, and Y.-S. Huang, *Photoconductivities in MoS2 Nanoflake Photoconductors.* Nanoscale Research Letters, 2016. **11**(1): p. 124.
161. Liu, K., et al., *Ultrahigh-Gain Single SnO2 Microrod Photoconductor on Flexible Substrate with Fast Recovery Speed.* Advanced Functional Materials, 2015. **25**(21): p. 3157-3163.
162. Choi, M.S., et al., *Lateral MoS2 p–n Junction Formed by Chemical Doping for Use in High-Performance Optoelectronics.* ACS Nano, 2014. **8**(9): p. 9332-9340.
163. Pal, S., et al., *WS2 Nanosheet/Si p–n Heterojunction Diodes for UV–Visible Broadband Photodetection.* ACS Applied Nano Materials, 2021. **4**(3): p. 3241-3251.
164. Katagiri, Y., et al., *Photoresponse in gate-tunable atomically thin lateral MoS2 Schottky junction patterned by electron beam.* Applied Physics Letters, 2017. **110**(14).
165. Tsai, D.-S., et al., *Few-Layer MoS2 with High Broadband Photogain and Fast Optical Switching for Use in Harsh Environments.* ACS Nano, 2013. **7**(5): p. 3905-3911.
166. Yin, Z., et al., *Single-Layer MoS2 Phototransistors.* ACS Nano, 2012. **6**(1): p. 74-80.
167. Wetzelaer, G.A.H., *Analytical description of the current-voltage relationship in organic-semiconductor diodes.* AIP Advances, 2018. **8**(3).
168. AlAhmadi, N., *Metal oxide semiconductor-based Schottky diodes: a review of recent advances.* Materials Research Express, 2020. **7**: p. 032001.
169. *Metal-Semiconductor Contacts*, in *Physics of Semiconductor Devices*. 2006. p. 134-196.
170. Zhang, M., et al., *Schottky-Contacted WSe2 Hot-Electron Photodetectors with Fast Response and High Sensitivity.* ACS Photonics, 2022. **9**(1): p. 132-137.
171. Appel, T. and H. Eckel. *Switching Losses Mechanisms of Unipolar Devices with Large Parasitic Capacitances*. in *PCIM Europe 2014; International Exhibition and Conference for Power Electronics, Intelligent Motion, Renewable Energy and Energy Management*. 2014.
172. Liu, W., Y. Wang, and J. Song, *Research on Schottky diode with high rectification efficiency for relatively weak energy wireless harvesting.* Superlattices and Microstructures, 2021. **150**: p. 106639.
173. Soole, J.B.D. and H. Schumacher, *InGaAs metal-semiconductor-metal photodetectors for long wavelength optical communications.* IEEE Journal of Quantum Electronics, 1991. **27**(3): p. 737-752.

174. Ghosh, S., et al., *Metal-Semiconductor-Metal GeSn Photodetectors on Silicon for Short-Wave Infrared Applications.* Micromachines, 2020. **11**(9): p. 795.
175. Singh, A.P., R.K. Upadhyay, and S. Jit, *High-Performance Colloidal ZnO Quantum Dots/TIPS-Pentacene Heterojunction- Based Ultraviolet Photodetectors.* IEEE Transactions on Electron Devices, 2022. **69**(6): p. 3230-3235.
176. Upadhyay, D.C., et al., *High-Performance Inverted Structure Broadband Photodetector Based on ZnO Nanorods/PCDTBT:PCBM:PbS QDs.* IEEE Transactions on Electron Devices, 2020. **67**(11): p. 4970-4976.
177. Wang, F. and T. Zhang, *How to characterize figures of merit of two-dimensional photodetectors.* 2023. **14**(1): p. 2224.
178. Wu, J.M. and W.E. Chang, *Ultrahigh Responsivity and External Quantum Efficiency of an Ultraviolet-Light Photodetector Based on a Single VO2 Microwire.* ACS Applied Materials & Interfaces, 2014. **6**(16): p. 14286-14292.
179. Zeng, L., et al., *Ultrafast and sensitive photodetector based on a PtSe2/silicon nanowire array heterojunction with a multiband spectral response from 200 to 1550 nm.* NPG Asia Materials, 2018. **10**.
180. Carlyle, T., *CHAPTER IV. CHARACTERISTICS*, in *Sartor Resartus*, L. Rodger and E. Mark, Editors. 2000, University of California Press: Berkeley. p. 22-26.
181. Piprek, J., *Chapter 2 - Electron Energy Bands*, in *Semiconductor Optoelectronic Devices*, J. Piprek, Editor. 2003, Academic Press: Boston. p. 13-48.
182. Baseden, K. and J. Tye, *Introduction to Density Functional Theory: Calculations by Hand on the Helium Atom.* Journal of Chemical Education, 2014. **91**: p. 2116-2123.
183. Bartolotti, L.J. and K. Flurchick, *An introduction to density functional theory.* Reviews in computational chemistry, 2009. **7**: p. 187-216.
184. Baseden, K.A. and J.W. Tye, *Introduction to Density Functional Theory: Calculations by Hand on the Helium Atom.* Journal of Chemical Education, 2014. **91**(12): p. 2116-2123.
185. Munakata, T., *DENSITY FUNCTIONAL THEORY AND LANGEVIN-DIFFUSION EQUATION*, in *Strongly Coupled Plasma Physics*, S. Ichimaru, Editor. 1990, Elsevier: Amsterdam. p. 695-698.
186. Noda, M., et al., *SALMON: Scalable Ab-initio Light-Matter simulator for Optics and Nanoscience.* Comput. Phys. Commun., 2018. **235**: p. 356-365.
187. QINGYUN, W., *2D materials for nanoelectronics: A first-principles investigation.* 2014.
188. Rindt, C.C.M. and S.V. Gaastra-Nedea, *15 - Modeling thermochemical reactions in thermal energy storage systems*, in *Advances in Thermal Energy Storage Systems*, L.F. Cabeza, Editor. 2015, Woodhead Publishing. p. 375-415.
189. Parandin, F., j. jalilian, and J. Jalilian, *Tuning of electronic and optical properties in ZnX (X=O, S, Se and Te) monolayer: Hybrid functional calculations.* Chemical Review and Letters, 2019. **2**: p. 76-83.
190. Smidstrup, S., et al., *QuantumATK: an integrated platform of electronic and atomic-scale modelling tools.* Journal of Physics: Condensed Matter, 2020. **32**(1): p. 015901.
191. Kohut, S.V. and V.N. Staroverov, *Apparent violation of the sum rule for exchange-correlation charges by generalized gradient approximations.* J Chem Phys, 2013. **139**(16): p. 164117.

192. Mejia-Rodriguez, D. and S.B. Trickey, *Deorbitalization strategies for meta-generalized-gradient-approximation exchange-correlation functionals.* Physical Review A, 2017. **96**: p. 052512.
193. Harrison, N., *An introduction to density functional theory.* Nato Science Series Sub Series III Computer and Systems Sciences, 2003. **187**: p. 45-70.
194. Weng, M., et al., *Wannier Koopmans Method Calculations of 2D Material Band Gaps.* The Journal of Physical Chemistry Letters, 2018. **9**(2): p. 281-285.
195. Mabelet, L.B., et al., *Energetics, electronic and magnetic properties of monolayer WSe2 doped with pnictogens, halogens and transition-metal (4d, 5d) atoms: An ab-initio study.* Physica E: Low-dimensional Systems and Nanostructures, 2020. **124**: p. 114161.
196. Chang, J., et al., *Atomistic simulation of the electronic states of adatoms in monolayer MoS2.* Applied Physics Letters, 2014. **104**(14): p. 141603.
197. Singh, N. and U. Schwingenschlögl, *Extended Moment Formation in Monolayer WS2 Doped with 3d Transition-Metals.* ACS Applied Materials & Interfaces, 2016. **8**(36): p. 23886-23890.
198. Liu, S., et al., *Tunable electronic behavior in 3d transition metal doped 2H-WSe2.* Physica E: Low-dimensional Systems and Nanostructures, 2017. **87**: p. 295-300.
199. Kanoun, M.B., *Tuning magnetic properties of two-dimensional MoTe2 monolayer by doping 3d transition metals: Insights from first principles calculations.* Journal of Alloys and Compounds, 2018. **748**: p. 938-942.
200. Ma, X., X. Zhao, and T. Wang, *Effect of strain on the electronic and magnetic properties of an Fe-doped WSe2 monolayer.* RSC Advances, 2016. **6**(74): p. 69758-69763.
201. Fu, Y., et al., *Intrinsic p-type W-based transition metal dichalcogenide by substitutional Ta-doping.* Applied Physics Letters, 2017. **111**.
202. Sa, B., et al., *Strain Engineering for Phosphorene: The Potential Application as a Photocatalyst.* The Journal of Physical Chemistry C, 2014. **118**(46): p. 26560-26568.
203. Pandey, M., et al., *Straining techniques for strain engineering of 2D materials towards flexible straintronic applications.* Nano Energy, 2023. **109**: p. 108278.
204. Peng, Z., et al., *Strain engineering of 2D semiconductors and graphene: from strain fields to band-structure tuning and photonic applications.* Light: Science & Applications, 2020. **9**(1): p. 190.
205. Roldán, R., et al., *Strain engineering in semiconducting two-dimensional crystals.* Journal of physics. Condensed matter : an Institute of Physics journal, 2015. **27**.
206. Zhu, J. and S.-H. Wei, *Overcoming doping bottleneck by using surfactant and strain.* Frontiers of Materials Science, 2011. **5**(4): p. 335-341.
207. Kumar, A. and P.K. Ahluwalia, *Tunable dielectric response of transition metals dichalcogenides MX2 (M=Mo, W; X=S, Se, Te): Effect of quantum confinement.* Physica B: Condensed Matter, 2012. **407**(24): p. 4627-4634.
208. Chen, Z., et al., *Charge Separation in Monolayer WSe2 by Strain Engineering: Implications for Strain-Induced Diode Action.* ACS Applied Nano Materials, 2022. **5**(10): p. 15095-15101.
209. Liu, X., et al., *Effect of strain on electronic and magnetic properties of n-type Cr-doped WSe2 monolayer.* Physica E: Low-dimensional Systems and Nanostructures, 2017. **87**: p. 6-9.

210. Yang, C.-x., X. Zhao, and S.-y. Wei, *Manipulation of electronic structure in WSe2 monolayer by strain.* Solid State Communications, 2016. **245**: p. 70-74.
211. Ta, H.Q., et al., *Graphene-Like ZnO: A Mini Review.* Crystals, 2016. **6**(8): p. 100.
212. Ma, D., et al., *CO catalytic oxidation on Al-doped graphene-like ZnO monolayer sheets: a first-principles study.* Journal of Materials Chemistry C, 2015. **3**(38): p. 9964-9972.
213. Chen, H., et al., *Enhanced photocatalytic performance of ZnO monolayer for water splitting via biaxial strain and external electric field.* Applied Surface Science, 2019. **481**: p. 1064-1071.
214. Saniz, R., et al., *A simplified approach to the band gap correction of defect formation energies: Al, Ga, and In-doped ZnO.* Journal of Physics and Chemistry of Solids, 2013. **74**(1): p. 45-50.
215. Wu, M., et al., *Al-Doped ZnO Monolayer as a Promising Transparent Electrode Material: A First-Principles Study.* Materials, 2017. **10**(4): p. 359.
216. Zhu, J. and S.-H. Wei, *Tuning doping site and type by strain: Enhanced p-type doping in Li doped ZnO.* Solid State Communications, 2011. **151**(20): p. 1437-1439.
217. Zhang, X., et al., *High photocatalytic performance of high concentration Al-doped ZnO nanoparticles.* Separation and Purification Technology, 2017. **172**: p. 236-241.
218. Liang, S.-J., et al., *Van der Waals Heterostructures for High-Performance Device Applications: Challenges and Opportunities.* Advanced Materials, 2020. **32**(27): p. 1903800.
219. Yu, W.J., et al., *Vertically stacked multi-heterostructures of layered materials for logic transistors and complementary inverters.* Nature Materials, 2013. **12**(3): p. 246-252.
220. Britnell, L., et al., *Strong Light-Matter Interactions in Heterostructures of Atomically Thin Films.* Science, 2013. **340**(6138): p. 1311-1314.
221. Lim, H., et al., *Stacking of Two-Dimensional Materials in Lateral and Vertical Directions.* Chemistry of Materials, 2014. **26**(17): p. 4891-4903.
222. He, J., K. Hummer, and C. Franchini, *Stacking effects on the electronic and optical properties of bilayer transition metal dichalcogenides* MoS_2*,* $MoSe_2$*,* WS_2 *and* WSe_2*.* Phys. Rev. B, 2014. **89**(7): p. 075409.
223. Somvanshi, D. and S. Jit, *Transition metal dichalcogenides based two-dimensional heterostructures for optoelectronic applications*, in *2D Nanoscale Heterostructured Materials*. 2020, Elsevier. p. 125-149.
224. Zhou, R., V. Ostwal, and J. Appenzeller, *Vertical versus Lateral Two-Dimensional Heterostructures: On the Topic of Atomically Abrupt p/n-Junctions.* Nano Letters, 2017. **17**(8): p. 4787-4792.
225. Hu, Z., et al., *Interfacial charge and energy transfer in van der Waals heterojunctions.* InfoMat, 2022. **4**(3): p. e12290.
226. Liu, Y., et al., *Van der Waals heterostructures and devices.* Nat. Rev. Mater., 2016. **1**(9): p. 16042.
227. Zhang, C., et al., *Systematic study of electronic structure and band alignment of monolayer transition metal dichalcogenides in Van der Waals heterostructures.* 2D Materials, 2016. **4**(1): p. 015026.
228. Kuang, Y., et al., *Effect of near surface inverse doping on graphene silicon heterojunction solar cell.* Optical and Quantum Electronics, 2016. **48**(3): p. 199.
229. Xie, F., et al., *Effect of* $C_{44}H_{30}N_4O_4$ *Surface Modification on the Performance of Al0.6Ga0.4N MSM Photodetectors.* IEEE Transactions on Electron Devices, 2022. **69**(8): p. 4337-4341.

230. Yang, G., et al., *Surface Modification of AlGaN Solar-Blind Ultraviolet MSM Photodetectors With Octadecanethiol.* IEEE Transactions on Electron Devices, 2022. **69**(1): p. 195-200.

231. Shao, Z.G., et al., *Ionization-Enhanced AlGaN Heterostructure Avalanche Photodiodes.* IEEE Electron Device Letters, 2017. **38**(4): p. 485-488.

232. Zhang, Z., et al., *Tunable electronic properties of an Sb/InSe van der Waals heterostructure by electric field effects.* Physical Chemistry Chemical Physics, 2019. **21**(10): p. 5627-5633.

233. Kim, B., et al., *Large Surface Photovoltage of WS2/MoS2 and MoS2/WS2 Vertical Hetero-bilayers.* ACS Applied Electronic Materials, 2021. **3**(6): p. 2601-2606.

234. Bai, Y., et al., *Efficient Carrier Separation and Band Structure Tuning of Two-Dimensional C2N/GaTe van der Waals Heterostructure.* The Journal of Physical Chemistry C, 2018. **122**(28): p. 15892-15902.

235. Ghorai, A., et al., *Highly Luminescent WS2 Quantum Dots/ZnO Heterojunctions for Light Emitting Devices.* ACS applied materials & interfaces, 2017. **9 1**: p. 558-565.

236. Hu, F., et al., *ZnO/WSe2 vdW heterostructure for photocatalytic water splitting.* Journal of Materials Chemistry C, 2019. **7**(23): p. 7104-7113.

237. Lin, P. and J. Yang, *Tunable WSe2/WS2 van der Waals heterojunction for self-powered photodetector and photovoltaics.* Journal of Alloys and Compounds, 2020. **842**: p. 155890.

238. Mukherjee, S., et al., *Infrared tunable, two colour-band photodetectors on flexible platforms using 0D/2D PbS–MoS2 hybrids.* Nanoscale Advances, 2019. **1**(8): p. 3279-3287.

239. Pataniya, P.M. and C.K. Sumesh, *Low cost and flexible photodetector based on WSe2 Nanosheets/Graphite heterostructure.* Synthetic Metals, 2020. **265**: p. 116400.

240. Selamneni, V., et al., *Hybrid 0D–2D WS2-QDs (n)/SnS (p) as Distributed Heterojunctions for Highly Responsive Flexible Broad-Band Photodetectors.* ACS Applied Electronic Materials, 2021. **3**(9): p. 4105-4114.

241. Jariwala, D., T.J. Marks, and M.C. Hersam, *Mixed-dimensional van der Waals heterostructures.* Nature Materials, 2017. **16**(2): p. 170-181.

242. Afzalian, A., et al., *Advanced DFT–NEGF Transport Techniques for Novel 2-D Material and Device Exploration Including HfS2/WSe2 van der Waals Heterojunction TFET and WTe2/WS2 Metal/Semiconductor Contact.* IEEE Transactions on Electron Devices, 2021. **68**(11): p. 5372-5379.

243. Chen, Y., et al., *High-Performance Photovoltaic Detector Based on MoTe 2 /MoS 2 Van der Waals Heterostructure.* Small, 2018. **14**: p. 1703293.

244. Chen, Z.-S., et al., *Tunable electronic structure in twisted WTe2/WSe2 heterojunction bilayer.* AIP Advances, 2022. **12**(4): p. 045315.

245. Chowdhury, S., P. Venkateswaran, and D. Somvanshi. *Optical and Electrical Characterization of n-MoS2/p-Si Heterojunction Diode*. in *2020 IEEE International IOT, Electronics and Mechatronics Conference (IEMTRONICS)*. 2020.

246. Xu, Z., et al., *Monolayer MoS2/GaAs heterostructure self-driven photodetector with extremely high detectivity*. Vol. 23. 2015.

247. Mukherjee, S., et al., *Novel Colloidal MoS2 Quantum Dot Heterojunctions on Silicon Platforms for Multifunctional Optoelectronic Devices.* Scientific reports, 2016. **6**: p. 29016-29016.

248. Huo, N. and G. Konstantatos, *Ultrasensitive all-2D MoS2 phototransistors enabled by an out-of-plane MoS2 PN homojunction.* Nature Communications, 2017. **8**(1): p. 572.

249. Dhyani, V., et al., *High performance broadband photodetector based on MoS2/porous silicon heterojunction.* Applied Physics Letters, 2017. **111**(19): p. 191107.

250. Pfrommer, B.G., et al., *Relaxation of Crystals with the Quasi-Newton Method.* Journal of Computational Physics, 1997. **131**(1): p. 233-240.

251. Commandeur, D., J. McGuckin, and Q. Chen, *Hematite coated, conductive Y doped ZnO nanorods for high efficiency solar water splitting.* Nanotechnology, 2020. **31**(26): p. 265403.

252. Duong, D.L., et al., *Long-range ferromagnetic ordering in vanadium-doped WSe2 semiconductor.* Applied Physics Letters, 2019. **115**(24): p. 242406.

253. Gao, J., et al., *Transition-Metal Substitution Doping in Synthetic Atomically Thin Semiconductors.* Adv. Mater., 2016. **28**(44): p. 9735-9743.

254. Dolui, K., et al., *Possible doping strategies for MoS_2 monolayers: An ab initio study.* Phys. Rev. B, 2013. **88**(7): p. 075420.

255. Fu, Y., et al., *Intrinsic p-type W-based transition metal dichalcogenide by substitutional Ta-doping.* Appl. Phys. Lett., 2017. **111**(4): p. 043502.

256. Hu, S.Y., et al., *The electrical and optical anisotropy of rhenium-doped WSe_2 single crystals.* J. Phy.: Condensed Matter, 2005. **17**(23): p. 3575-3583.

257. Susarla, S., et al., *Quaternary 2D Transition Metal Dichalcogenides (TMDs) with Tunable Bandgap.* Advanced Materials, 2017. **29**(35): p. 1702457.

258. Chang, C.-H., et al., *Orbital analysis of electronic structure and phonon dispersion in MoS${}_{2}$, MoSe${}_{2}$, WS${}_{2}$, and WSe${}_{2}$ monolayers under strain.* Physical Review B, 2013. **88**(19): p. 195420.

259. Bafekry, A., et al., *Tuning the bandgap and introducing magnetism into monolayer BC3 by strain/defect engineering and adatom/molecule adsorption.* Journal of Applied Physics, 2019. **126**(14): p. 144304.

260. Tonndorf, P., et al., *Photoluminescence emission and Raman response of monolayer MoS_2, $MoSe_2$, and WSe_2.* Optics Express, 2013. **21**(4): p. 4908-4916.

261. Kaewmaraya, T., et al., *Strain-induced tunability of optical and photocatalytic properties of ZnO mono-layer nanosheet.* Computational Materials Science, 2014. **91**: p. 38-42.

262. Li, Y.-L., Y. Li, and C. Tang, *Strain engineering and photocatalytic application of single-layer ReS2.* International Journal of Hydrogen Energy, 2017. **42**(1): p. 161-167.

263. Prasad, N., et al., *Microstress, strain, band gap tuning and photocatalytic properties of thermally annealed and Cu-doped ZnO nanoparticles.* Applied Physics A, 2016. **122**(6): p. 590.

264. Cho, H., et al., *Recent progress in strain-engineered elastic platforms for stretchable thin-film devices.* Materials Horizons, 2022. **9**(8): p. 2053-2075.

265. Lloyd, D., et al., *Band Gap Engineering with Ultralarge Biaxial Strains in Suspended Monolayer MoS2.* Nano Letters, 2016. **16**(9): p. 5836-5841.

266. Ren, K., et al., *Using van der Waals heterostructures based on two-dimensional blue phosphorus and XC (X = Ge, Si) for water-splitting photocatalysis: a first-principles study.* Physical Chemistry Chemical Physics, 2019. **21**(19): p. 9949-9956.
267. Xin, Y., et al., *Polarization-Sensitive Self-Powered Type-II GeSe/MoS2 van der Waals Heterojunction Photodetector.* ACS Applied Materials & Interfaces, 2020. **12**(13): p. 15406-15413.
268. Cheng, Z., et al., *2D Materials Enabled Next-Generation Integrated Optoelectronics: from Fabrication to Applications.* Advanced Science, 2021. **8**(11): p. 2003834.
269. Zhang, X., et al., *A review on optoelectronic device applications of 2D transition metal carbides and nitrides.* Materials & Design, 2021. **200**: p. 109452.
270. Fiori, G., et al., *Electronics based on two-dimensional materials.* Nature Nanotechnology, 2014. **9**(10): p. 768-779.
271. Jariwala, D., et al., *Emerging Device Applications for Semiconducting Two-Dimensional Transition Metal Dichalcogenides.* ACS Nano, 2014. **8**(2): p. 1102-1120.
272. Somvanshi, D. and S. Jit, *Transition metal dichalcogenides based two-dimensional heterostructures for optoelectronic applications.* 2D Nanoscale Heterostructured Materials: Synthesis, Properties and Applications, 2020: p. 125.
273. Chen, X., et al., *Scalable production of p-MoTe2/n-MoS2 heterostructure array and its application for self-powered photodetectors and CMOS inverters.* 2D Materials, 2022. **9**(3): p. 035015.
274. Thakar, K. and S. Lodha, *Optoelectronic and photonic devices based on transition metal dichalcogenides.* Materials Research Express, 2020. **7**(1): p. 014002.
275. Tsai, T.-H., et al., *WS2/WSe2 Nanodot Composite Photodetectors for Fast and Sensitive Light Detection.* ACS Applied Electronic Materials, 2021. **3**(10): p. 4291-4299.
276. Yadav, S.M. and A. Pandey, *Hybrid 2D–0D SnS2 Nanoflakes/CTS QDs-Based Broadband (UV-Visible-NIR) Photodetector.* IEEE Transactions on Electron Devices, 2020. **67**(5): p. 2008-2015.
277. Sun, M., et al., *Heterostructured graphene quantum dot/WSe2/Si photodetector with suppressed dark current and improved detectivity.* Nano Research, 2018. **11**(6): p. 3233-3243.
278. Bafekry, A., et al., *Van der Waals heterostructures of MoS2 and Janus MoSSe monolayers on graphitic boron-carbon-nitride (BC3, C3N, C3N4 and C4N3) nanosheets: a first-principles study.* Journal of Physics D: Applied Physics, 2020. **53**.
279. Ye, J., et al., *Defects and strain engineering the electronic structure and magnetic properties of monolayer WSe2 for 2D spintronic device.* Applied Surface Science, 2019. **497**: p. 143788.
280. Xu, R., et al., *Computational design and property predictions for two-dimensional nanostructures.* Materials Today, 2018. **21**(4): p. 391-418.
281. Roldán, R., et al., *Electronic properties of single-layer and multilayer transition metal dichalcogenides MX2 (M = Mo, W and X = S, Se).* Annalen der Physik, 2014. **526**(9-10): p. 347-357.
282. Liu, W., et al., *Role of Metal Contacts in Designing High-Performance Monolayer n-Type WSe2 Field Effect Transistors.* Nano Letters, 2013. **13**(5): p. 1983-1990.
283. Fang, H., et al., *High-Performance Single Layered WSe2 p-FETs with Chemically Doped Contacts.* Nano Letters, 2012. **12**(7): p. 3788-3792.

284. Smidstrup, S., et al., *QuantumATK: an integrated platform of electronic and atomic-scale modelling tools.* Journal of Physics: Condensed Matter, 2019. **32**(1): p. 015901.

285. Monkhorst, H.J. and J.D. Pack, *Special points for Brillouin-zone integrations.* Phys. Rev. B, 1976. **13**(12): p. 5188-5192.

286. Young, R.M., et al., *Thermal analysis of an indirectly heat pulsed non-volatile phase change material microwave switch.* Journal of Applied Physics, 2014. **116**(5): p. 054504.

287. Schutte, W.J., J.L. De Boer, and F. Jellinek, *Crystal structures of tungsten disulfide and diselenide.* Journal of Solid State Chemistry, 1987. **70**(2): p. 207-209.

288. Janesko, B.G., T.M. Henderson, and G.E. Scuseria, *Screened hybrid density functionals for solid-state chemistry and physics.* Phys. chem. chem. phys. , 2009. **11**(3): p. 443-454.

289. Heyd, J., G.E. Scuseria, and M. Ernzerhof, *Hybrid functionals based on a screened Coulomb potential.* The Journal of Chemical Physics, 2003. **118**(18): p. 8207-8215.

290. Yang, D., et al., *Electronic and Magnetic Properties of Defected Monolayer WSe2 with Vacancies.* Nanoscale Research Letters, 2019. **14**(1): p. 192.

291. O'Hare, P.A.G., B.M. Lewis, and B.A. parkinson, *Standard molar enthalpy of formation by fluorine-combustion calorimetry of tungsten diselenide (WSe2). Thermodynamics of the high-temperature vaporization of WSe2. Revised value of the standard molar enthalpy of formation of molybdenite (MoS2).* J. Chem. Thermodyn., 1988. **20**(6): p. 681-691.

292. Henkelman, G., A. Arnaldsson, and H. Jónsson, *A fast and robust algorithm for Bader decomposition of charge density.* Computational Materials Science, 2006. **36**(3): p. 354-360.

293. Yue, Q., et al., *Functionalization of monolayer MoS2 by substitutional doping: A first-principles study.* Physics Letters A, 2013. **377**(19): p. 1362-1367.

294. Yun, S.J., et al., *Ferromagnetic Order at Room Temperature in Monolayer WSe_2 Semiconductor via Vanadium Dopant.* Adv. Sci., 2020. **7**(9): p. 1903076.

295. Fan, S., et al., *Tailoring Quantum Tunneling in a Vanadium-Doped $WSe_2/SnSe_2$ Heterostructure.* Adv. Sci., 2020. **7**(3): p. 1902751.

296. Mukherjee, R., et al., *Substitutional Electron and Hole Doping of WSe_2: Synthesis, Electrical Characterization, and Observation of Band-to-Band Tunneling.* Phys. Rev. Appl., 2017. **7**(3): p. 034011.

297. Chakraborty, S.K., et al., *Challenges and opportunities in 2D heterostructures for electronic and optoelectronic devices.* iScience, 2022. **25**(3): p. 103942.

298. Lee, J.Y., et al., *Two-Dimensional Semiconductor Optoelectronics Based on van der Waals Heterostructures.* Nanomaterials, 2016. **6**(11): p. 193.

299. Sun, M. and U. Schwingenschlögl, *Structure Prototype Outperforming MXenes in Stability and Performance in Metal-Ion Batteries: A High Throughput Study.* Advanced Energy Materials, 2021. **11**(14): p. 2003633.

300. Sun, M., Y. Yan, and U. Schwingenschlögl, *Beryllene: A Promising Anode Material for Na- and K-Ion Batteries with Ultrafast Charge/Discharge and High Specific Capacity.* The Journal of Physical Chemistry Letters, 2020. **11**(21): p. 9051-9056.

301. Sun, M. and U. Schwingenschlögl, *\ensuremath{\delta}-CS: A Direct-Band-Gap Semiconductor Combining Auxeticity, Ferroelasticity, and Potential for High-Efficiency Solar Cells.* Physical Review Applied, 2020. **14**(4): p. 044015.
302. You, P., G. Tang, and F. Yan, *Two-dimensional materials in perovskite solar cells.* Materials Today Energy, 2019. **11**: p. 128-158.
303. Marschall, R., *Semiconductor Composites: Strategies for Enhancing Charge Carrier Separation to Improve Photocatalytic Activity.* Advanced Functional Materials, 2014. **24**(17): p. 2421-2440.
304. Shanker, G.S., A. Biswas, and S. Ogale, *2D materials and their heterostructures for photocatalytic water splitting and conversion of CO2 to value chemicals and fuels.* Journal of Physics: Energy, 2021. **3**(2): p. 022003.
305. Shen, S., et al., *Visible-Light-driven Photocatalytic Water Splitting on Nanostructured Semiconducting materials.* International Journal of Nanotechnology, 2011. **8**: p. 523-591.
306. Zhao, X., P. Chen, and T. Wang, *Controlled electronic and magnetic properties of WSe_2 monolayers by doping transition-metal atoms.* Superlatt. Microstruct., 2016. **100**: p. 252-257.
307. Topsakal, M., et al., *First-principles study of zinc oxide honeycomb structures.* Physical Review B, 2009. **80**(23): p. 235119.
308. Wang, Q.H., et al., *Electronics and optoelectronics of two-dimensional transition metal dichalcogenides.* Nature Nanotech., 2012. **7**: p. 699.
309. Tonndorf, P., et al., *Photoluminescence emission and Raman response of monolayer MoS_2, $MoSe_2$, and WSe_2.* Opt. Exp., 2013. **21**(4): p. 4908-4916.
310. Zhao, W., et al., *Evolution of Electronic Structure in Atomically Thin Sheets of WS_2 and WSe_2.* ACS Nano, 2013. **7**(1): p. 791-797.
311. Eftekhari, A., *Tungsten dichalcogenides (WS2, WSe2, and WTe2): materials chemistry and applications.* J. Mater. Chem. A, 2017. **5**(35): p. 18299-18325.
312. Wang, Y., et al., *Thermal Properties of Two Dimensional Layered Materials.* Adv. Funct. Mater., 2017. **27**(19): p. 1604134.
313. Liu, W., et al., *Role of Metal Contacts in Designing High-Performance Monolayer n-Type WSe_2 Field Effect Transistors.* Nano Lett., 2013. **13**(5): p. 1983-1990.
314. Chowdhury, S., P. Venkateswaran, and D. Somvanshi, *A systematic study on the electronic structure of 3d, 4d, and 5d transition metal-doped WSe_2 monolayer.* Superlatt. Microstructur, 2020. **148**: p. 106746.
315. Han, D., et al., *Chemical Trend of Transition-Metal Doping in WSe_2.* Phys. Rev. Appl., 2019. **12**(3): p. 034038.
316. Mabelet, L.B., et al., *Energetics, electronic and magnetic properties of monolayer WSe_2 doped with pnictogens, halogens and transition-metal (4d, 5d) atoms: An ab-initio study.* Physica E: Low Dimens. Syst. Nanostruct., 2020. **124**: p. 114161.
317. Schulman, D.S., A.J. Arnold, and S. Das, *Contact engineering for 2D materials and devices.* Chemical Society Reviews, 2018. **47**(9): p. 3037-3058.
318. Kang, W.T., et al., *Direct growth of doping controlled monolayer WSe2 by selenium-phosphorus substitution.* Nanoscale, 2018. **10**(24): p. 11397-11402.

319. Butler, S.Z., et al., *Progress, Challenges, and Opportunities in Two-Dimensional Materials Beyond Graphene.* ACS Nano, 2013. **7**(4): p. 2898-2926.

320. Ahn, C., et al., *Stress effects on impurity solubility in crystalline materials: A general model and density-functional calculations for dopants in silicon.* Physical Review B, 2009. **79**(7): p. 073201.

321. Yan, X., et al. *A Unified Theory and Fundamental Rules of Strain-dependent Doping Behaviors in Semiconductors*. 2020. arXiv:2008.09343.

322. Smidstrup, S., et al., *QuantumATK: an integrated platform of electronic and atomic-scale modelling tools.* J. Phys: Condensed Matter, 2019. **32**(1): p. 015901.

323. Carmona-Espíndola, J., et al., *Generalized Gradient Approximation Exchange Energy Functional with Near-Best Semilocal Performance.* J. Chem. Theory Comput., 2019. **15**(1): p. 303-310.

324. O'Hare, P.A.G., B.M. Lewis, and B.A. parkinson, *Standard molar enthalpy of formation by fluorine-combustion calorimetry of tungsten diselenide (WSe_2). Thermodynamics of the high-temperature vaporization of WSe2. Revised value of the standard molar enthalpy of formation of molybdenite (MoS_2).* J. Chem. Thermodynamics, 1988. **20**(6): p. 681-691.

325. Liu, S., et al., *Tunable electronic behavior in 3d transition metal doped 2H-WSe_2.* Physica E Low Dimens. Syst. Nanostruct., 2017. **87**: p. 295-300.

326. Li, H., et al., *Atomic structures and electronic properties of Ta-doped 2H-$NbSe_2$.* RSC Advances, 2014. **4**(101): p. 57541-57546.

327. Yang, D., et al., *Electronic and Magnetic Properties of Defected Monolayer WSe_2 with Vacancies.* Nanoscale Research Lett., 2019. **14**(1): p. 192.

328. Zhao, Q., et al., *Giant Piezoresistive Effect and Strong Bandgap Tunability in Ultrathin InSe upon Biaxial Strain.* Advanced Science, 2020. **7**(20): p. 2001645.

329. Carrascoso, F., R. Frisenda, and A. Castellanos-Gomez, *Biaxial versus uniaxial strain tuning of single-layer MoS2.* Nano Materials Science, 2022. **4**(1): p. 44-51.

330. Kumar, V. and D.R. Roy, *Strain-induced band modulation and excellent stability, transport and optical properties of penta-MP2 (M = Ni, Pd, and Pt) monolayers.* Nanoscale Advances, 2020. **2**(10): p. 4566-4580.

331. Han, D., et al., *Chemical Trend of Transition-Metal Doping in WSe_2.* Physical Review Applied, 2019. **12**(3): p. 034038.

332. Conley, H.J., et al., *Bandgap Engineering of Strained Monolayer and Bilayer MoS2.* Nano Lett., 2013. **13**(8): p. 3626-3630.

333. Li, C. and Z. Wang, *9 - Computational modelling and ab initio calculations in MAX phases – I*, in *Advances in Science and Technology of Mn+1AXn Phases*, I.M. Low, Editor. 2012, Woodhead Publishing. p. 197-222.

334. Laturia, A., M.L. Van de Put, and W.G. Vandenberghe, *Dielectric properties of hexagonal boron nitride and transition metal dichalcogenides: from monolayer to bulk.* npj 2D Materials and Applications, 2018. **2**(1): p. 6.

335. Li, Y., et al., *Measurement of the optical dielectric function of monolayer transition-metal dichalcogenides: ${\mathrm{MoS}}_{2}$, $\mathrm{Mo}\mathrm{S}{\mathrm{e}}_{2}$,*

${\mathrm{WS}}_{2}$, and $\mathrm{WS}{\mathrm{e}}_{2}$. Physical Review B, 2014. **90**(20): p. 205422.

336. Dong, N., et al., *Optical Limiting and Theoretical Modelling of Layered Transition Metal Dichalcogenide Nanosheets.* Scientific Reports, 2015. **5**(1): p. 14646.
337. Liu, H.-L., et al., *Optical properties of monolayer transition metal dichalcogenides probed by spectroscopic ellipsometry.* Appl. Phys. Lett., 2014. **105**(20): p. 201905.
338. Li, Y., et al., *Measurement of the optical dielectric function of monolayer transition-metal dichalcogenides: MoS_2, $MoSe_2$, WS_2, WSe_2.* Phys. Rev. B, 2014. **90**(20): p. 205422.
339. Kong, L.-J., G.-H. Liu, and Y.-J. Zhang, *Tuning the electronic and optical properties of phosphorene by transition-metal and nonmetallic atom co-doping.* RSC Advances, 2016. **6**(13): p. 10919-10929.
340. Shannon, R., *Revised effective ionic radii and systematic studies of interatomic distances in halides and chalcogenides.* Acta Crystallographica Section A, 1976. **32**(5): p. 751-767.
341. Choi, M., *Strain-Enhanced p Doping in Monolayer MoS_2.* Phys. Rev. Appl., 2018. **9**(2): p. 024009.
342. Topsakal, M., et al., *A First-Principles Study of Zinc Oxide Honeycomb Structures.* Physical Review B, 2009. **80**: p. 235119.
343. Papadimitriou, D.N., *Engineering of Optical and Electrical Properties of Electrodeposited Highly Doped Al:ZnO and In:ZnO for Cost-Effective Photovoltaic Device Technology.* Micromachines, 2022. **13**(11): p. 1966.
344. Liu, Y., W. Zhou, and P. Wu, *Ferromagnetism induced by the charge transfer in Al-doped ZnO nanoparticles.* Journal of Alloys and Compounds, 2014. **615**: p. 401-405.
345. Fan, Q., et al., *Electronic Structure and Optical Properties of Al-doped ZnO from Hybrid Functional Calculations.* Chemical Engineering Transactions, 2015. **46**: p. 985-990.
346. Sun, D., et al. *Comparative Study on ZnO Monolayer Doped with Al, Ga and In Atoms as Transparent Electrodes*. Materials (Basel, Switzerland), 2017. **10**, DOI: 10.3390/ma10070703.
347. Somvanshi, D., A. Pandey, and S. Jit, *Ultraviolet Detection Characteristics of Pd/n-ZnO Thin Film Schottky Photodiodes Grown on n-Si Substrates.* Journal of Nanoelectronics and Optoelectronics, 2013. **8**(4): p. 349-354.
348. Munawaroh, H., S. Wahyuningsih, and A.H. Ramelan, *Synthesis and Characterization of Al doped ZnO (AZO) by Sol-gel Method.* IOP Conference Series: Materials Science and Engineering, 2017. **176**: p. 012049.
349. Moniz, S.J.A., et al., *Visible-light driven heterojunction photocatalysts for water splitting – a critical review.* Energy & Environmental Science, 2015. **8**(3): p. 731-759.
350. Qin, H., et al., *ZnO nanorod arrays grown on g-C3N4 micro-sheets for enhanced visible light photocatalytic H2 evolution.* RSC Advances, 2019. **9**(42): p. 24483-24488.
351. Li, L., et al., *Electronic and photocatalytic properties of ZnO/GaTe heterostructure from first principles calculations.* Materials Science in Semiconductor Processing, 2023. **154**: p. 107189.
352. Yao, J. and G. Yang, *2D material broadband photodetectors.* Nanoscale, 2020. **12**(2): p. 454-476.
353. Koppens, F.H.L., et al., *Photodetectors based on graphene, other two-dimensional materials and hybrid systems*. Nature Nanotechnology, 2014. **9**(10): p. 780-793.

354. Nipane, A., et al., *Electrostatics of lateral p-n junctions in atomically thin materials.* Journal of Applied Physics, 2017. **122**(19): p. 194501.

355. Wang, Z., et al., *Electrostatically tunable lateral MoTe2 p–n junction for use in high-performance optoelectronics.* Nanoscale, 2016. **8**(27): p. 13245-13250.

356. Park, C., et al., *Photovoltaic effect in a few-layer ReS2/WSe2 heterostructure.* Nanoscale, 2018. **10**(43): p. 20306-20312.

357. Pospischil, A., M.M. Furchi, and T. Mueller, *Solar-energy conversion and light emission in an atomic monolayer p–n diode.* Nature Nanotechnology, 2014. **9**(4): p. 257-261.

358. Withers, F., et al., *Light-emitting diodes by band-structure engineering in van der Waals heterostructures.* Nature Materials, 2015. **14**(3): p. 301-306.

359. Zhu, J., et al., *Thickness-dependent bandgap tunable molybdenum disulfide films for optoelectronics.* RSC Advances, 2016. **6**(112): p. 110604-110609.

360. Huyghebaert, C., et al. *2D materials: roadmap to CMOS integration*. in *IEEE International Electron Devices Meeting (IEDM)*. 2018.

361. Ruppert, C., O.B. Aslan, and T.F. Heinz, *Optical Properties and Band Gap of Single- and Few-Layer MoTe2 Crystals.* Nano Letters, 2014. **14**(11): p. 6231-6236.

362. Duerloo, K.-A.N., Y. Li, and E.J. Reed, *Structural phase transitions in two-dimensional Mo- and W-dichalcogenide monolayers.* Nature Communications, 2014. **5**(1): p. 4214.

363. Opoku, F. and P.P. Govender, *Atomistic insight into the significantly enhanced photovoltaic cells of monolayer GaTe2 via two-dimensional van der Waals heterostructures engineering.* Physical Sciences Reviews, 2022. **7**(6): p. 629-644.

364. Smidstrup, S., et al., *QuantumATK: an integrated platform of electronic and atomic-scale modelling tools.* J. Condens. Matter Phys., 2019. **32**(1): p. 015901.

365. Grimme, S., *Semiempirical GGA-type density functional constructed with a long-range dispersion correction.* Journal of Computational Chemistry, 2006. **27**(15): p. 1787-1799.

366. Hussain, G., et al., *Electronic and optical properties of InAs/InAs$_{0.625}$Sb$_{0.375}$ superlattices and their application to far-infrared detectors*. 2022.

367. Dressel, M., et al., *Kramers-Kronig-consistent optical functions of anisotropic crystals: Generalized spectroscopic ellipsometry on pentacene.* Optics express, 2008. **16**: p. 19770-8.

368. Chen, J., et al., *Comprehensive understanding of intrinsic mobility in the monolayers of III–VI group 2D materials.* Physical Chemistry Chemical Physics, 2019. **21**(39): p. 21898-21907.

369. Wang, B., et al., *Bilayer MoTe2/XS2 (X = Hf,Sn,Zr) heterostructures with efficient carrier separation and light absorption for photocatalytic water splitting into hydrogen.* Applied Surface Science, 2021. **544**: p. 148842.

370. Kim, H.-g. and H.J. Choi, *Thickness dependence of work function, ionization energy, and electron affinity of Mo and W dichalcogenides from DFT and GW calculations.* Physical Review B, 2021. **103**(8): p. 085404.

371. Tian, H., et al., *Optoelectronic devices based on two-dimensional transition metal dichalcogenides.* Nano Research, 2016. **9**.

372. Jin, C., et al., *Observation of moiré excitons in WSe_2/WS_2 heterostructure superlattices.* Nature, 2019. **567**(7746): p. 76-80.

373. Montblanch, A.R.P., et al., *Confinement of long-lived interlayer excitons in WS_2/WSe_2 heterostructures.* Communications Physics, 2021. **4**(1): p. 119.

374. Pudasaini, P.R., et al., *High-performance multilayer WSe_2 field-effect transistors with carrier type control.* Nano Research, 2018. **11**(2): p. 722-730.

375. Eftekhari, A., *Tungsten dichalcogenides (WS_2, WSe_2, and WTe_2): materials chemistry and applications.* Journal of Materials Chemistry A, 2017. **5**(35): p. 18299-18325.

376. Iqbal, M.W., et al., *High-mobility and air-stable single-layer WS_2 field-effect transistors sandwiched between chemical vapor deposition-grown hexagonal BN films.* Scientific Reports, 2015. **5**(1): p. 10699.

377. Wang, X., et al., *Quantum dots derived from two-dimensional materials and their applications for catalysis and energy.* Chemical Society Reviews, 2016. **45**(8): p. 2239-2262.

378. Zhang, J., X. Zhang, and S. Bi, *Two-Dimensional Quantum Dot-Based Electrochemical Biosensors.* Biosensors (Basel), 2022. **12**(4), 254

379. Somvanshi, D., et al., *Nature of carrier injection in metal/2D-semiconductor interface and its implications for the limits of contact resistance.* Physical Review B, 2017. **96**(20): p. 205423.

380. Merino, P., et al., *WSe_2 Nanosheets Synthesized by a Solvothermal Process as Advanced Nanofluids for Thermal Solar Energy.* ACS Sustainable Chemistry & Engineering, 2020. **8** (3), pp. 1627–1636

381. Sierra-Castillo, A., et al. *Synthesis and Characterization of Highly Crystalline Vertically Aligned WSe_2 Nanosheets*. Applied Sciences, 2020. **10**(3), 874.

382. Pataniya, P., et al., *Photovoltaic activity of WSe_2/Si hetero junction.* Materials Research Bulletin, 2019. **120**: p. 110602.

383. Ghobadi, A., et al., *Emerging photoluminescence from defective vanadium diselenide nanosheets.* Photonics Research, 2018. **6**(4): p. 244-253.

384. Luo, M., et al., *WSe_2/Au vertical Schottky junction photodetector with low dark current and fast photoresponse.* Nanotechnology, 2018. **29**(44): p. 444001.

385. Somvanshi, D. and S. Jit, *Pd/ZnO Nanoparticles Based Schottky Ultraviolet Photodiodes Grown on Sn-Coated n-Si Substrates by Thermal Evaporation Method.* IEEE Journal of Selected Topics in Quantum Electronics, 2014. **20**(6): p. 120-125.

386. Ghimire, H., et al., *Recent Progress on Extended Wavelength and Split-Off Band Heterostructure Infrared Detectors.* Micromachines, 2020. **11**(6): p. 547.

387. Kapatel, S. and C.K. Sumesh, *Atomically thin WSe_2 nanosheets for fabrication of high-performance p-Si/WSe_2 heterostructure.* Optical Materials, 2022. **129**: p. 112537.

Sayantika Chowdhury
19/05/23